EMPIRICAL MODELS FOR STRUCTURAL EFFECTS OF A-SITE POINT DEFECTS AND ORDERING IN PEROVSKITES

by

Kevin Ross Tolman

A dissertation

submitted in partial fulfillment

of the requirements for the degree of

Doctor of Philosophy in Materials Science and Engineering

Boise State University

December 2016

BOISE STATE UNIVERSITY GRADUATE COLLEGE

DEFENSE COMMITTEE AND FINAL READING APPROVALS

of the dissertation submitted by

Kevin Ross Tolman

Dissertation Title: Empirical Models for Structural Effects of A-Site Point Defects and Ordering in Perovskites

Date of Final Oral Examination: 18 November 2016

The following individuals read and discussed the dissertation submitted by student Kevin Ross Tolman, and they evaluated his presentation and response to questions during the final oral examination. They found that the student passed the final oral examination.

Rick Ubic, Ph.D.	Chair, Supervisory Committee
Darryl Butt, Ph.D.	Member, Supervisory Committee
Dmitri Tenne, Ph.D.	Member, Supervisory Committee
Geoff Brennecka, Ph.D.	Member, Supervisory Committee

The final reading approval of the dissertation was granted by Rick Ubic, Ph.D., Chair of the Supervisory Committee. The dissertation was approved by the Graduate College.

DEDICATION

From my roots of academic rags, to my wings of unexpected academic excellence I would like to dedicate this culminating point to God, my family, colleagues and this country for freedom and opportunity of education.

ACKNOWLEDGEMENTS

I would like to extend my sincere appreciation to Dr. Rick Ubic for whom I am particularly indebted to for his vital support, guidance and profound consideration. I am very grateful for Dr. Ubic's immense efforts and intellectual support on my behalf as supervisor, mentor and advisor. It has been my great privilege to work with Dr. Ubic as his teaching assistant, editorial assistant and student research assistant. He is an outstanding professor who has continuously supported me both professionally and financially throughout my doctorate.

I would like to acknowledge and thank all of my committee members Dr. Darryl Butt, Dr. Dmitri Tenne, and Dr. Geoff L. Brennecka for their willingness, insight, comprehensive understanding, patience and for seeing this through to the end. I greatly appreciate their impact, scientific rigor and guidance. I am particularly grateful to research engineers Dr. Karthik Chinnathambi and Dr. Nick Bulloss of the Boise State Center for Materials Characterization (BSCMC) for their much appreciated time, consultations and insights regarding experimental equipment and analysis.

I would like to extend a special acknowledgement and appreciation for all of those who helped me along the way and played instrumental roles in the success of this research (*e.g.*, collaborators, co-workers, friends, visiting researchers, undergraduate researchers, etc.) for their time and resources. I acknowledge that this research was supported by the National Science Foundation (DMR-1052788) and the Micron School of Materials Science & Engineering at Boise State University.

Finally, I couldn’t have done it without the exceptional support of my beautiful bride and three wonderful children whom I express the utmost affections and love for. I would like to thank and acknowledge them for their ceaseless patience, inspiration and encouragement.

ABSTRACT

Composition-structure-property relationships are essential keys to unlocking the strength of predictive crystal chemistry. Awkwardly, the electroceramics industry largely relies on various time-consuming and expensive trial-and-error experiments to address new questions which often could otherwise be interpolated from published data. Indeed, predictive models, which can be derived from empirical evidence, can greatly aid the direction and support of future development in a meaningful, apt, and cost-effective way. Theory suggests that intrinsic properties on the scale of a unit cell may be estimated from the sizes and charges of the chemical constituents alone. Ultimately, researchers could be provided a compositional recipe for any desired structure/property; or the resulting structure/property could be readily calculated based on stoichiometry. Empirical models also lend themselves to the exploration of structure/property trends which would otherwise be virtually impossible to discover via computationally expensive first-principles methods. In order to make useful empirical models, high-quality, self-consistent data are needed; however, such composition-structure-property data pools are scarce.

Chapter one describes a material classification called perovskites which have the general formula ABX_3 and may constitute the largest range of functional materials of any other material classification, including: high-temperature insulators/capacitors, superconductors, dielectric resonators, pyroelectrics, piezoelectrics, ionic conductors, photovoltaics, *etc*. Building general processing-structure-properties models for

perovskites, involving the effects of numerous structural anomalies and extrinsic effects, is far beyond the scope of this work, which focuses primarily on the effective size of A-site vacancies and the structural effects of A-site point defect chemistry, A- and B-site cation ordering, and tetragonal distortions.

Point defects, such as vacancies, can have profound effects on crystal structure and properties. Leading up to 2013, the structural effect of extrinsic vacancies has largely been ignored in electroceramics. Chapter two explores previous system-specific studies of extrinsic vacancies in perovskites in terms of the effective sizes of vacancies. The structural effects of aliovalent doping in five typical oxide perovskite systems ($CaTiO_3$, $SrTiO_3$, $BaTiO_3$, $PbTiO_3$, and $Pb(Zr_{0.6}Ti_{0.4})O_3$) were studied. Samples synthesized via solid-state reactions were checked for phase purity using X-ray diffraction, scanning electron microscopy, and either energy dispersive spectroscopy or wavelength dispersive spectroscopy. Structural parameters were characterized using X-ray, electron, and/or time-of-flight neutron diffraction data. Quantitative diffraction data were collected and refined in order to develop empirical descriptions of the effects of A-site point defect concentrations. A predictive model for pseudocubic lattice constants was developed which relates stoichiometry to the effective sizes of ionic species and vacancies. The same model can be used to calculate values of tolerance factor which better predicts perovskite stability and structure in terms of octahedral tilting than does the traditional definition.

Chapter three examines complex perovskites which contain cation ordering. Perovskites with multiple cation species sharing the A or B sites may form superstructures in which the A- and/or B-site is non-randomly shared by more than one ionic species. Ordering generally involves a lowering of symmetry; however, such ordering is not always complete or spatially extensive. It can exist in varying degrees from perfectly ordered to near completely random (*i.e.*, disordered) and can extend uniformly throughout an entire crystal or exist only in short-range nanodomains. The model developed in chapter two is used to predict cation ordering. Several well-known examples of B-site ordered perovskites were examined and shown to result in volume shrinkage upon ordering. Furthermore, four samples in the $Na_{(1-3x)/2}La_{(1+x)/2}TiO_3$ system (x = 0.0, 0.0533, 0.1733 and 0.225) were synthesized using a conventional solid-state mixed-oxide method. The structure of the x = 0 end-member ($Na_{0.5}La_{0.5}TiO_3$) has been reported in various space groups, but always with a random distribution of Na^+ and La^{3+} on the A site; however, empirical modeling suggests that it is not only ordered but also that an unexpected volume increase accompanies the ordering process.

Chapter four proposes a predictive model for tetragonality. Samples of $[(Pb_yBa_{1-y})_{(1-3x)}La_{(2x)}]TiO_3$ were synthesized and X-ray diffraction refinements were conducted in order to measure lattice constants. Further data from open literature were used in order to reveal tetragonality trends. These trends were combined with a model for unit-cell volume in order to derive a generalized empirical predictive model for tetragonal lattice constants of perovskites in either *P*4*mm* or *P*4*/mmm*, based solely on published ionic radii data. This model was extended to include the resultant unit-cell dipole moment.

TABLE OF CONTENTS

LIST OF TABLES

LIST OF FIGURES

LIST OF ABBREVIATIONS

a_{pc}	Pseudocubic lattice constant calculated using unit-cell volume
$a^{'}$	Pseudocubic lattice constant calculated using A-X bond length
$a^{''}$	Pseudocubic lattice constant calculated using B-X bond length
t_*	Conventional tolerance factor
t_1	Calculated tolerance factor as a function of a_{pc}
t'	Empirical model tolerance factor as a function of t_*

CHAPTER ONE: INTRODUCTION

1.1 Perovskite

Perovskites, which are prevalent in modern devices, are increasing in global importance, as evidenced by the number of publications featuring perovskites (Figure 1.1), and essential to several multibillion dollar industries.[1-3] They are ubiquitous in modern devices because their wide compositional range and structural variability [2] gives rise to useful properties like piezoelectricity (*e.g.*, $PbZr_xTi_{1-x}O_3$), pyroelectricity (*e.g.*, $LiTaO_3$), ferroelectricity (*e.g.*, $BaTiO_3$), superconductivity (*e.g.*, $MgCNi_3$, $YBa_2Cu_3O_{7-\delta}$,[*] *etc.*), colossal magnetoresistance (*e.g.*, $Pr_{0.7}Ca_{0.3}MnO_3$), magneto-dielectricity (*e.g.*, $SrCu_3Ti_4O_{12}$), half metallicity (*e.g.*, Pb_2CoReO_6), proton conduction (*e.g.*, $BaCe_{0.9}Gd_{0.1}O_3$), catalysis (*e.g.*, $LaFe_{0.77}Co_{0.17}Pd_{0.06}O_3$), spin-dependent transport (*e.g.*, Sr_2CrWO_6), as well as microwave resonance (*e.g.*, $Ba_3MgTa_2O_9$). They are also of interest as passive components in wireless telecommunications devices, substrates or buffer layers for compound semiconductor heteroepitaxy, and films in tunable ferroelectric superlattice structures, in which a variation in lattice constant results in strain-induced ferroelectric thick films.

---

[*] Technically this compound is a perovskite *derivative*.

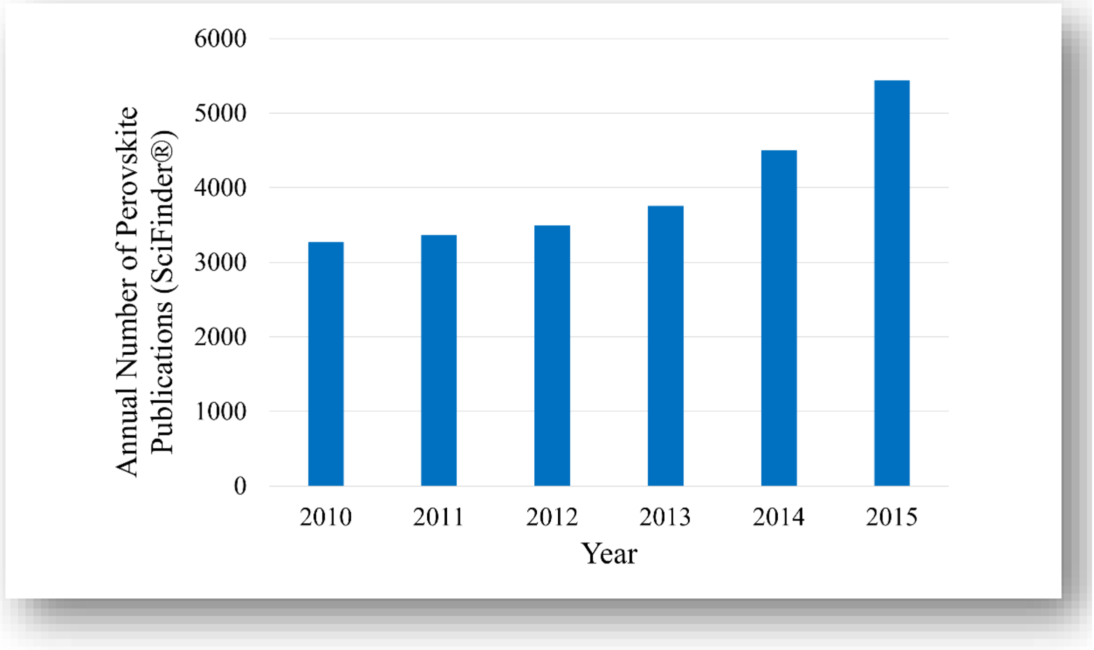

Figure 1.1. **Annual number of peer-reviewed perovskite articles per year for the past six years (data from SciFinder®).**

1.2 Perovskite Origins

In 1829 Gustav Rose, a professor of mineralogy and chemistry at the University of Berlin, [4] took part in a scientific expedition to Imperial Russia, performing mineralogical studies in the Altai and Ural Mountains. Ten years later Rose was sent a piece of chlorite-rich skarn (calcium-bearing siliceous rock produced by the metamorphic alteration of limestone or dolomite) from the Akhmatovskaya Kop' (Akhmatov's Pit) in the Urals by his Russian colleague and notable mineral collector, August Alexander Kämmerer. At Kämmerer's request the new mineral, once identified, was named *Perowskit* in honor of the decorated Napoleonic Wars veteran and mineralogist Count Lev A. Perovskiy, who was then the Assistant Minister of the Interior and later became Imperial Russia's longest serving Minister of Internal Affairs (1841 - 1852). [1, 5]

Figure 1.2 shows a skarn with $CaTiO_3$ crystals, which was discovered in the Ural Mountains and may look similar to Gustav Rose's skarn. Rose's 1839 manuscript titled *Certain New Minerals Discovered in the Ural Mountains* reported this mineral's crystalline habits, hardness values (Mohs scale), densities, and chemical compositions.[5]

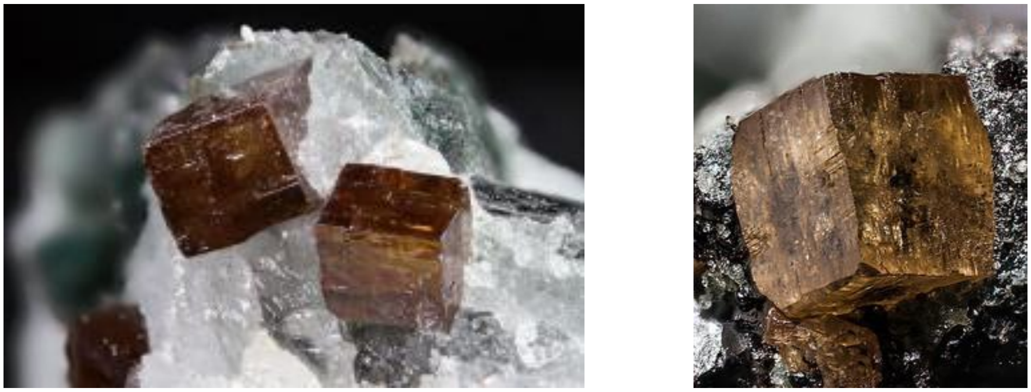

Figure 1.2. Skarn with calcium titanate (mineral perovskite) crystals found in the Ural Mountains.[6]

During the century following Rose's work, perovskite studies began to spread across Russia, Europe, and the United States. Ebelmen [1] was the first to report perovskite synthesis, which he achieved via a flux-growth method. Knop [1] introduced elemental substitutions into perovskites. Synthesis and substitutions were pivotal in Goldschmidt's [1, 7, 8] structural studies of perovskites; which led to patenting perovskite-based paint pigments. The first hundred years of perovskite structural metrology was primarily based on physically measuring the crystal's geometry, termed crystal habit, with goniometers. These macrostructural observations were refined by the advent of X-ray crystallography, which transformed the way crystal structures were characterized. For example, calcium titanate was thought to be cubic (Figure 1.2); however, Bowman [9] questioned how a cubic perovskite could have a biaxial optical character (only possible in orthorhombic, monoclinic, ort triclinic crystals). Then in 1957, Kay and Bailey [10] proved using X-ray diffraction that calcium titanate was actually orthorhombic, giving rise to the idea of almost-cubic or pseudocubic symmetry.

1.3 Perovskite Structure: The Aristotype

The aristotype or ideal perovskite structure is defined as a centrosymmetric cubic structure in space group $Pm\bar{3}m$ (Figure 1.4), which means that all of the unit-cell sides are equal in length, $a = b = c$; all of the angles are orthogonal, $\alpha = \beta = \gamma = 90°$; and all of the ions are centered in their respective coordination environments. Perovskites are typically largely ionic compounds and have the general chemical formula ABX_3, where A and B are cation species and X is the anion. The ions in perovskites can be modeled as spheres with the ionic radii of r_A, r_B, and r_X.[2] For monovalent anions the A cation must also be monovalent and the B cation divalent; whereas, for divalent anions the sum of A- and B-cation valences must be exactly six to retain charge neutrality (Table 1.1). In the unusual case of ReO_3 the A site is completely vacant in order to retain charge neutrality (see Chapter 2).

Table 1.1. For divalent anions, such as perovskite oxides, the sum of A- and B-cation valences must equal six.

(A+B)	Example:
(0+6)	ReO_3
(1+5)	$KNbO_3$
(2+4)	$SrTiO_3$
(3+3)	$LaFeO_3$

It is noteworthy that it is $SrTiO_3$, not $CaTiO_3$, which adopts the ideal cubic perovskite structure, even though the latter is the actual mineral perovskite. The mineral $CaTiO_3$ crystalizes in orthorhombic space group *Pnma*. Figure 1.3 shows a hard-sphere model illustrating the ideal perovskite structure patterned after $SrTiO_3$,[11] where the eight A cations are positioned at the cube corners, the B cation is positioned at the body center, and the six anions are positioned at the face centers. The coordinations are important when identifying whether or not a compound is a perovskite or not. For example, $MgSiO_3$ is a perovskite and has the general formula ABX_3; whereas, $MgTiO_3$ is an ilmenite at ambient conditions even though the chemical formula is ABX_3; therefore, the structural class cannot be inferred from the chemical formula alone. Figure 1.3 shows the ionic sizes for $SrTiO_3$ (r_A = 1.44 Å, r_B = 0.605 Å, and r_X =1.35 Å), which are the conventional or ideal sizes from Shannon's 1976 determination of effective ionic radii [12] (Appendix I). Figure 1.3 illustrates why the A-X bond length is:

$$r_{\text{A-X}} = \left(\frac{a}{\sqrt{2}}\right) \tag{1.1}$$

and the B-X bond length is:

$$r_{\text{B-X}} = \left(\frac{a}{2}\right) \tag{1.2}$$

A-site cations and the anions pack along the <100> directions, and their bond length is related to the lattice constant such that $a = a'$ (Equation 1.3, Figure 1.3). The B cations and anions pack along the <001> directions and their bond length is also related to the lattice constant such that $a = a''$ (Equation 1.4, Figure 1.3). If the unit cell is not exactly cubic in space group $Pm\bar{3}m$, then the lattice constant (or even pseudocubic lattice constant) is no longer exactly equal to the solutions for *a'* nor *a''* ($a \neq a' \neq a''$).

$$a' = \sqrt{2}(r^{XII}_{A(Shannon)} + r^{II}_{X(Shannon)}) \tag{1.3}$$

$$a'' = 2(r^{VI}_{B(Shannon)} + r^{II}_{X(Shannon)}) \tag{1.4}$$

where $r^{XII}_{A(Shannon)}$, $r^{VI}_{B(Shannon)}$, and $r^{II}_{X(Shannon)}$ are the effective ionic radii of A, B, and X ions in their ideal/respective coordinations.

Shannon derived effective ionic radii based on coordination and formal oxidation states, but there are at least *three* additional factors that affect ionic radii: covalency, polyhedral distortion, and ionic occupancies (*e.g.*, cation ordering, vacancies, *etc.*). It should be pointed out that effective radii essentially describe a global average rather than a single radius for each individual ion. Kassan-Ogly and Naish [13] refer to the ionic radii of Shannon's tables as "beyond doubt the best grounded and most reliable… [yet] unsatisfactory" because every case is not satisfied. Curiously, Shannon thought that his crystal radius (CR) values, which were based on Fumi & Tosi's values for sixfold oxygen and fluoride, $r\left(O^{2-}_{VI}\right) = 1.26$ Å and $r\left(F^{1-}_{VI}\right) = 1.19$ Å, more closely corresponded to the physical size of ions in a solid than did his effective ionic radii (IR), which were based on Pauling's "crystal radius" of oxygen, $r\left(O^{2-}_{VI}\right) = 1.40$ Å; nevertheless, CR values have been universally ignored in favor of IR. Still, as IR = CR - 0.14 Å, the difference in size ratios is probably negligible.

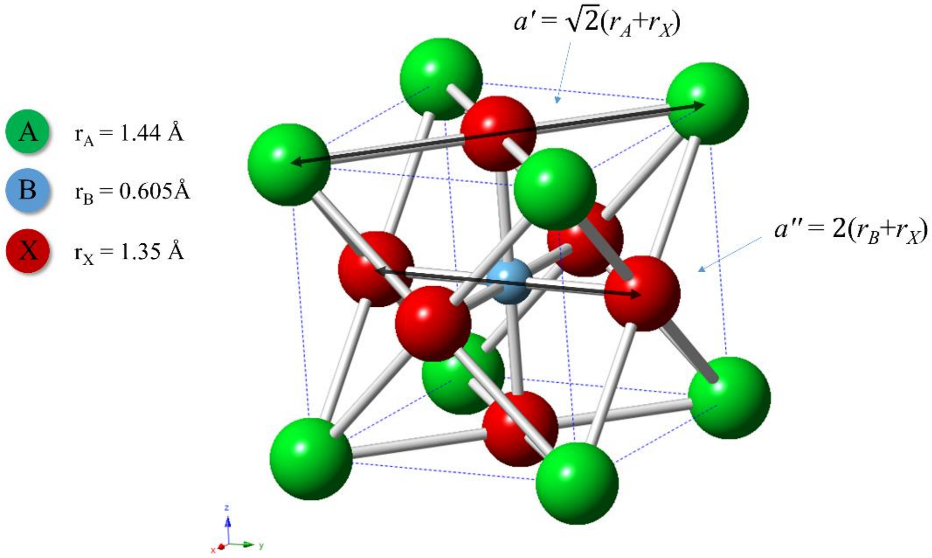

Figure 1.3. Hard-sphere space-filling/close-packed model illustrating the ideal perovskite structure patterned after $SrTiO_3$,[11] where the eight A cations are positioned at the corners, the B cation is positioned at the body-center, and the six anions are positioned at the middle of all six sides of the cube.

Figure 1.4 shows the coordination polyhedra for A, B, and X ions. The commonly used setting in Figure 1.4 (B) shows the corner-sharing of octahedra, with A, B, and X ions in Wyckoff positions 1a, 1b, and 3c, respectively. The polyhedra of the ideal perovskite structure are unique in that the ratio of polyhedral volumes is exactly five (Equation 1.5):

$$\frac{V_A}{V_B} = 5 \tag{1.5}$$

where V_A is the volume of the AX_{XII} cubooctahedron (Figure 1.4A), and V_B is the volume of the BX_{VI} octahedron (Figure 1.4B); therefore, this ratio can be a useful measure of the degree of distortion in a perovskite.

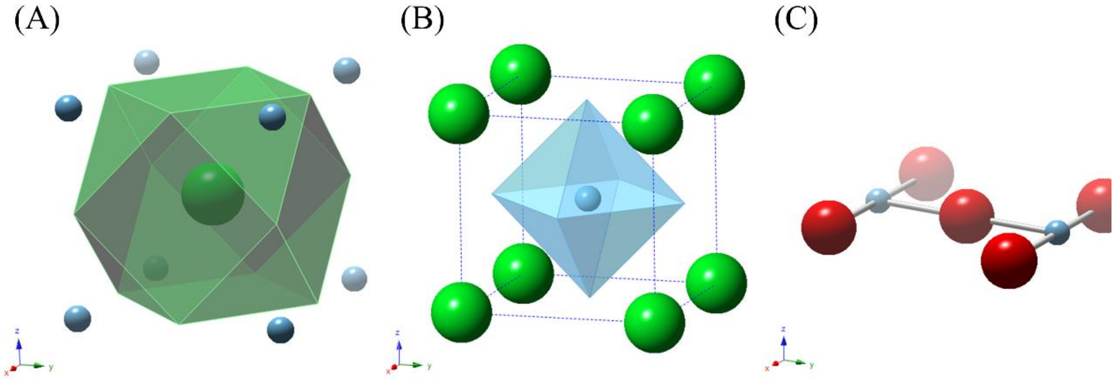

Figure 1.4. There are different coordination polyhedra in the aristotype/ideal perovskite structure: (A) A cations lie within cubooctahedral polyhedra with XII-fold coordination; (B) B cations lie within octahedral polyhedra with VI-fold coordination; and (C) X anions are coordinated to two B cations. The four nearest A cations are ~41% further away and are not shown but must still be considered crystalochemically (*e.g.*, in bond valence calculations). The anions are not shown for (A) and (B) in order for the polyhedra to be clearly illustrated.

Although most perovskites do not have the aristotype (ideal) structure due to distortions and are instead hettotypes, the ideal perovskite structure is important to define and clearly understand so it can be used as a control or base line for structural studies. A useful technique to empirically relate the hettotypes to the aristotype is to use the pseudocubic relationship (Equation 1.6):

$$a_{pc} = \left(\frac{V}{Z}\right)^{1/3} \tag{1.6}$$

where a_{pc} is the pseudocubic lattice constant, V is the unit-cell volume, and Z is the number of formula units per unit cell.

For example, $BaTiO_3$ was thought to be cubic [14] until 1945 when Helen D. Megaw [15] determined using X-ray crystallography that it is has a slight (~1%) tetragonality, which helps explain its ferroelectric behavior.[16] The stable form of $BaTiO_3$ at room temperature is tetragonal with space group *P*4*mm*, but it can still be approximately described as pseudocubic with an a_{pc} as defined in Equation 1.2.

Goldschmidt [17] semi-empirically determined that if the A cation is about the same size as the anion then the A site has a symmetrical XII-fold cubooctahedral coordination. Later Zachariasen [2] developed this relationship with all three site sizes:

$$(r_A + r_X) = \sqrt{2}(r_B + r_X) \tag{1.7}$$

This site-size relationship, derived from the geometry of a cube, is the basis for what has become known as the conventional tolerance factor, t_* (Equation 1.8), which is also a useful measure of the degree of distortion and perovskite stability:

$$t_* = \frac{a'}{a''} = \frac{(r_A + r_X)}{\sqrt{2}(r_B + r_X)} \tag{1.8}$$

Only for the ideal perovskite structure does $a' = a''$ and $t = 1$.

Tolerance factor is based on ionic sizes and can be a measure of perovskite structural stability. For example, in tetragonal $BaTiO_3$ (*P*4*mm*) at room temperature the Ba^{2+} cation is displaced from its aristotype/ideal position in the [001] direction by about 0.034 Å (~0.8%), which corresponds to a conventional tolerance factor of $t = 1.07$; however, the structure is still perovskite nonetheless. Cubic perovskite structures can have tolerance factors in the range 0.9 - 1.05. If the A cation is significantly smaller than the anion then $t << 1$ and the structure becomes ilmenite (*i.e.*, “collapsed perovskite”) as in the cases of $Mg^{2+}Ti^{4+}O_3^{2-}$ ($r_{Mg} = 0.715$ Å and $t = 0.747$) and $Fe^{2+}Ti^{4+}O_3^{2-}$ ($r_{Fe} = 0.649$ Å and $t = 0.723$); however, tolerance factor cannot be used on its own as a reliable predictor of space group because it ignores all variables except for ideal ionic sizes and doesn’t account for defects such as vacancies.

In 2001, Lufaso and Woodward [37] used the bond-valence method to back-calculate ionic radii to calculate a so-called bond-valence tolerance factor. The bond valence tolerance factor (Equation 1.9) may be a powerful method for predicting perovskite stability, but foreknowledge of the bond valence parameters are needed. It also fails to account for stoichiometric structural vacancies. In 2009, Ubic [68] derived a tolerance factor model as a function of the cubic/pseudocubic lattice constant, r_B and r_X (Equation 1.10), which accounts for A-site point defects.

$$t_{BV} = \frac{R_{0(A-X)} - B\ln\left(V_A / N_A\right)}{\sqrt{2}R_{0(B-X)} - B\ln\left(V_B / N_B\right)} \tag{1.9}$$

$$t_1 = \frac{a_c - 0.05444}{0.66046(r_B + r_X)} - 1.981012 \tag{1.10}$$

where $R_{0(A\text{-}X)}$ and $R_{0(B\text{-}X)}$ are the unit valence bond lengths of the A-X and B-X bonds, V_A and V_B are the ideal valence states of the A and B cations, N_A and N_B are their coordinations, and B = 0.37.

The chemical bonds of the ions directly impact the perovskite structure; however, it can be challenging to directly link experimental results to theoretical calculations. Consequently, I. D. Brown [18] developed *bond valence theory* as a way of linking empirical bond lengths to theoretical bond valences. Bond valence theory also apparently predicts both bond length and stability (Equation 1.11). The number resulting from Equation 1.11 is the total bond valence sum of that ion:

$$BV = \sum_{N} \exp\left[\frac{R_0 - R_{(A-X\ or\ B-X)}}{b}\right] \tag{1.11}$$

where BV is the valence of the A-X or B-X bond, R_0 and b are empirically determined parameters, and $R_{(\text{A-X or B-X})}$ is the experimentally determined A-X or B-X bond length.

1.4 Perovskite Structure: The Hettotypes

Most perovskites don’t have the aristotype/ideal structure due to differences in ionic sizes, second-order Jahn-Teller (SOJT) effects, or antiferrodistortive (AFD) instabilities (see section 1.5). Furthermore, it is increasingly important for researchers and industry to be able to predict lattice constants for lattice matching substrates used in heteroepitaxy, buffer layers for complex semiconductor epitaxy, and strain layers in superlattice structures (*e.g.*, alternating layers of $BaTiO_3$ and $SrTiO_3$), *etc*. [19-24] Consequently, much time and money is spent in structural determination because there is no universal composition-structure predictive model available.

With the advancement of analytical techniques and technology over the past century, structural determination of perovskites has evolved into several analytical techniques, including diffraction. There are three main diffraction sources available, namely X-rays, electrons, and neutrons. X-ray diffraction data can be used to determine lattice constants and cation positions and to estimate phase purity (to a few vol%), but they are insensitive to anions such as oxygen. Synchrotron X-ray sources use the angular acceleration of electrons to emit precisely-controlled monochromatic X-rays in order to achieve higher resolution diffraction data, but the problem with insensitivity to oxygen largely remains. Characteristic X-rays generated within a specimen can be used for spectroscopic chemical analysis. Electron diffraction can provide information about crystal symmetry and defects, whereas neutron diffraction is generally sensitive to phase assemblage, magnetic moments, and the positions of both cations and anions. Neutron-scattering powers of atoms vary irregularly with atomic number. Two elements may differ in atomic number by only one unit and yet their neutron scattering powers may be entirely different. Also, some light elements, like carbon or oxygen, scatter neutrons more intensely than some heavy elements, like tungsten. Neutrons can distinguish between elements which scatter x-rays with almost equal intensity and are particularly good at detecting order in alloys and compounds. These diffraction methods together have led to the elucidation of perovskite structures.

There are six different perovskite lattice systems that make up the 15 possible space groups of tilted simple perovskites (see Section 1.4.1).[25-28] Figure 1.5 shows four of these six lattice systems (hettotypes), which have unique pseudocubic unit cell relationships.

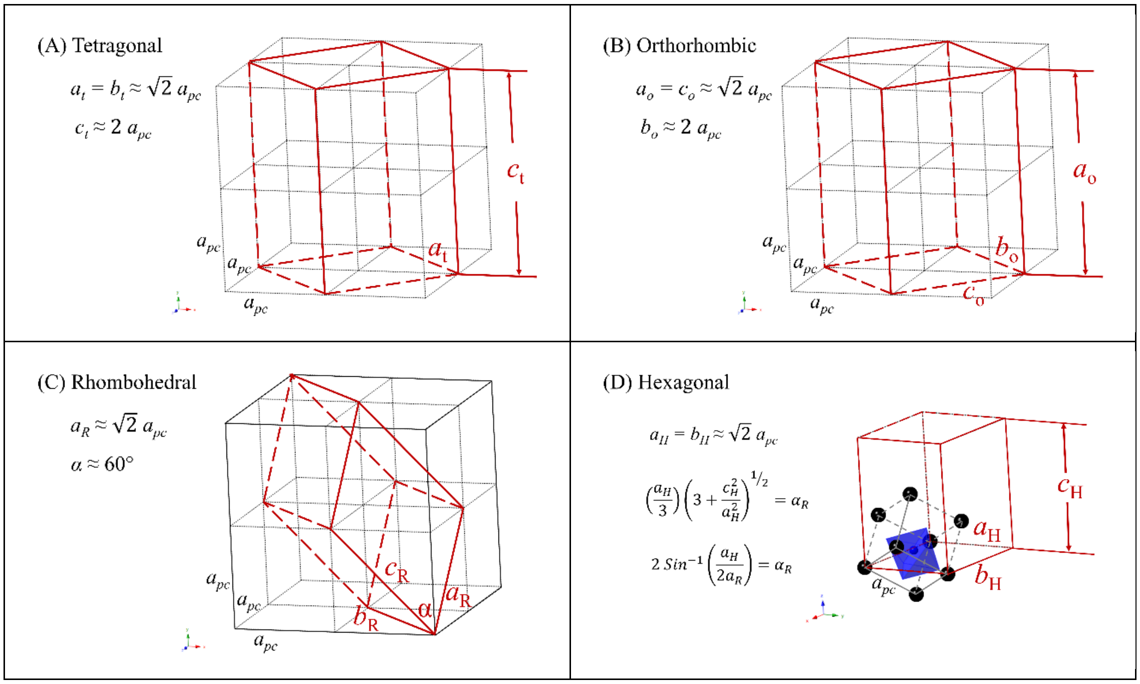

Figure 1.5. Common hettotype to pseudocubic relationships. (A) Tetragonal to pseudocubic unit cell relationship; (B) Orthorhombic to pseudocubic unit cell relationship; (C) Rhombohedral to pseudocubic unit cell relationship; (D) Hexagonal to pseudocubic unit cell and rhombohedral alpha angle relationships.

1.5 Perovskite Distortional Considerations

The majority of perovskites are distorted where the polyhedral volume ratio (Equation 1.1) is not equal to five, $a' \neq a''$, and $t \neq 1$. For a majority of defective perovskites, it is crucial to gain a clear understanding of the specific defects and their impact on composition-structure relationships. It is possible to estimate bulk and nano materials properties, but the numerous variables involved don’t always behave predictably when considering defects and distortions. As a result, synthesizing materials can lead to mixed or undesirable outcomes. Predictions based on empirical modeling can significantly reduce the time and cost required to discover and develop new perovskite dielectrics.

Although credit for the term "dielectric" is often incorrectly given to William Whewell (no doubt thanks to misinformation in Wikipedia), it was probably first used by Michael Faraday, Lord Kelvin, or even Carl Gauss. In 1845 Michael Faraday discovered that the state of polarization of light passing through a piece of lead borosilicate glass could be changed by a magnet. The transparent bodies which he found displayed this property he first called 'dimagnetics' in analogy to dielectrics, but consulted his learned friend, William Whewell, for a second opinion. Whewell proposed altering the term to “dia-magnetic”, from the Greek “dia” meaning “through”, since the bodies through (dia) which electricity passes would have been called "diaelectric" but for the fact that “dielectric” was easier to pronounce. He further proposed the term "paramagnetic" to indicate previously known magnetic properties, thereby dividing magnetic phenomena into two classes. Ferromagnetic, antiferromagnetic, and ferrimagnetic phenomena, among others, have since been added to the list.

It should be emphasized that, while electric fields can exist in dielectrics, magnetic fields are expelled from diamagnetics. The analogy is nonetheless made by both Faraday and Maxwell by superimposing a velocity-dependent resistance such that current, upon encountering a large resistance in the dielectric, would find an alternate path just as a notional magnetic current would flow around a diamagnet. Because of the induced flow of electrons which act to counter the effect of an applied magnetic field, diamagnets have $\mu_r < 1$, expel magnetic fields, and are repelled by strong magnetic fields. There is no direct analogy for electric fields in dielectrics because magnetic monopoles (the magnetic equivalent of electrons and protons) do not exist.

To maintain the analogy, the term "paraelectric" should properly refer to polar dielectrics, which consist of grains with polar regions oriented randomly in the solid so as to result in no net dipole moment (*i.e.*, no net polarization). This phenomenon is the electrical equivalent of paramagnetism and generally describes the condition of virgin (unpoled) ferroelectrics *below* the Curie temperature, T_C. Because the grains/domains are polar, they are also piezoelectric. All but one of the 21 non-centrosymmetric crystallographic point groups are piezoelectric (the symmetry elements combine in the cubic group 432 to yield no net piezoelectric effect).

Ten of the 21 non-centrosymmetric groups contain a unique polar axis and are therefore spontaneously polarized. These are the "pyroelectric" groups, in which a change in temperature produces a change in polarization. The reverse process is termed the "electrocaloric" effect. A number of pyroelectric materials have the additional property that the direction of spontaneous polarization can be changed by an applied electric field or mechanical stress. Where the change is primarily due to an electric field, the material is "ferroelectric"; when it is primarily due to stress, it is "ferroelastic". All ferroelectric materials are also piezoelectric and pyroelectric, but a piezoelectric or pyroelectric is not necessarily a ferroelectric.

Ferroelectric materials *above* their T_C are generally called "paraelectric", even though the analogy between ferromagnetism and ferroelectricity falls apart here. Although a ferromagnet would become paramagnetic above T_C (the magnetic dipoles don't go away, they just become misaligned by the thermal energy), a ferroelectric would lose its dipoles altogether above T_C and become simply a non-polar dielectric.

Such a material is centrosymmetric and so contains no dipoles at all; however, polarization can be *induced* by an external field in such a way as to reduce or expel the electrostatic energy from the solid. This phenomenon is essentially the electrical equivalent of diamagnetism except that diamagnets would also have negative susceptibilities. Some authors define a dielectric as anything which becomes polarized when exposed to an external electric field; however, that definition is so broad as to encompass pretty much everything. Curiously, this is the same definition often given for the term paraelectric!

Nonpolar dielectrics would show linear polarization-field (P-E) behavior[*] up to breakdown, whereas paraelectrics (or polar dielectrics) would show generally greater polarization and non-linear P-E behavior. Of course, as well as being non-linear, ferroelectrics have a spontaneous polarization and so show hysteresis in their P-E graphs (loops). The slope of the P-E curve ($\varepsilon_0\chi_e$) is proportional to the electric susceptibility, $\chi_e = \varepsilon_r - 1$. A superparaelectric material would show a P-E "loop" with an area of 0 and so no hysteresis.

Figure 1.6 shows an illustration of the relationships between various electroceramic types. Composition, structure, and defects all play a profound role in these properties and many others (Table 1.2). In addition, point-defect crystal chemistry causes small crystallographic changes which result in substantial differences in electrical properties. For example, Sundell *et al*. [29, 30] and Pushpa *et al*. [30] found

---

[*] The assumption of a linear relationship between ***P*** and ***E*** is valid only if the field strengths encountered in practice (typically < 10^6 V/m) are small compared to those that bind electrons in atoms (about 10^{11} V/m); however, the linear response is an approximation.

that slight cation doping in lanthanum ferrite and/or barium zirconate completely changed the ionic and electrical character of the material.

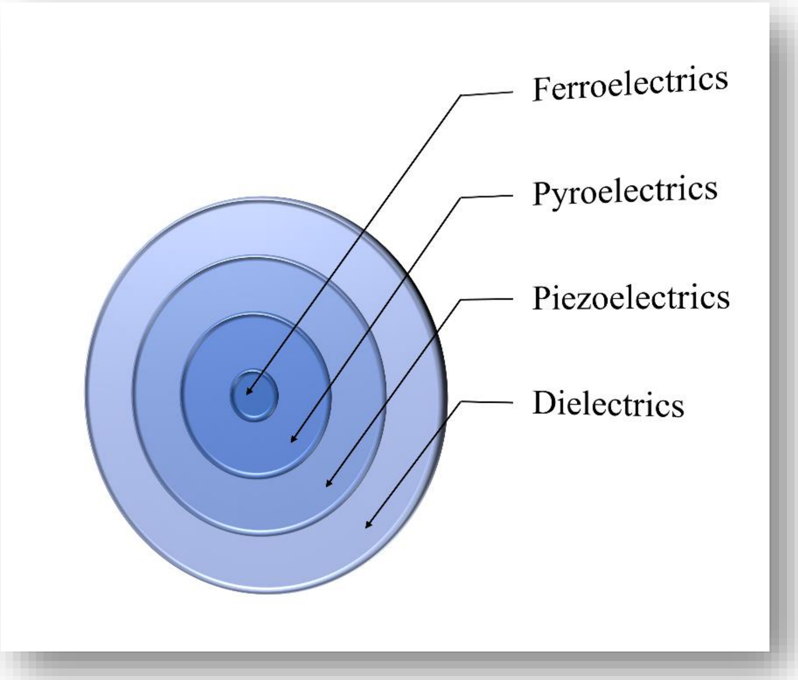

Figure 1.6. Illustration showing functional relationships. All piezoelectrics are dielectrics, but not all dielectrics are necessarily piezoelectrics.

Table 1.2. Perovskite examples:

Reference	Material	Application
[31]	$Ba(Tb_{1/2}Nb_{1/2})O_3$	Capacitor (High-k)
[32]	$YBa_2Cu_3O_{7-\delta}$ $(0.7 < \delta)$	Insulator
[32]	$YBa_2Cu_3O_{7-\delta}$ $(0 < \delta < 0.7)$	Superconductor
[33]	$Sr_2HoRu_{1-x}Cu_xO_6$	Superconductor
[34]	$BaLa_4Cu_5O_{13.4}$	Metal (Conductor)
[35]	$BaZn_{1/3}Ta_{2/3}O_3$	Dielectric Resonator
[36]	$Pb(Zn_{1-x}Ti_x)O_3$	Piezoelectric
[36]	$Pb(Zn_{1/3}Nb_{2/3})O_3$-$PbTiO_3$	Piezoelectric
[37]	Sr_2FeMoO_3	Magnetoresistor
[38]	$La_{1-x}Sr_xMnO_3$	Catalyst (Hydrogen Peroxide)
[39]	$La_{1-x}Sr_xCoO_3$	Catalyst (Diesel Oxidation)
[40]	$BaTiO_3$	Ferroelectric (Discovery)
[36]	$Pb(Zn_{1/3}Nb_{2/3})O_{3-x}$-$PbTiO_3$	Ferroelectric
[41]	$LaFeO_3$-$LaCrO_3$	Ferromagnetic
[42]	$SrCe_{1-x}REE_xO_{3-\delta}$	Proton-conductor
[43]	$Na_{1/2}Bi_{1/2}TiO_3$	Ion-conductor
[44]	$CH_3NH_3PbBr_3$	Photoelectric
[45]	$LiTaO_3$	Pyroelectric
[46]	$PbMg_{1/3}Nb_{2/3}O_3$	Relaxor

1.5.1 Octahedral Tilting

Perovskites with $t < 0.985$ will generally have tilting of the BX_6 octahedra [47] along at least one of the pseudocubic axes. Tilting will happen if the A cation is relatively small compared to the anion (*e.g.*, at ambient conditions the octahedra in $SrTiO_3$ are untilted, whereas those in $CaTiO_3$ are tilted) and equal A–X bond lengths no longer yield the lowest energy state. In 1927, Glazer [48] invented the now-conventional notation for 23 octahedral tilt systems using three Cartesian axes *a*, *b*, and *c*; where a 0 superscript indicates no tilting along an assigned axis, a positive + superscript indicates in-phase tilting (Figure 1.7), and a negative superscript "-" indicates antiphase tilting along an assigned axis. If the degree of tilt is equal along two (or three) axes, then a single symbol (*a* or *b*) is used for those axes. In 1997, Woodward [49, 50] further related tilt systems and space groups to cation ordering, and Howard and Stokes [25-28], using group theory, reduced the number of total space groups for the tilt systems from 16 to 15 (Figure 1.8) by eliminating space group *Pmmn* (No. 59).

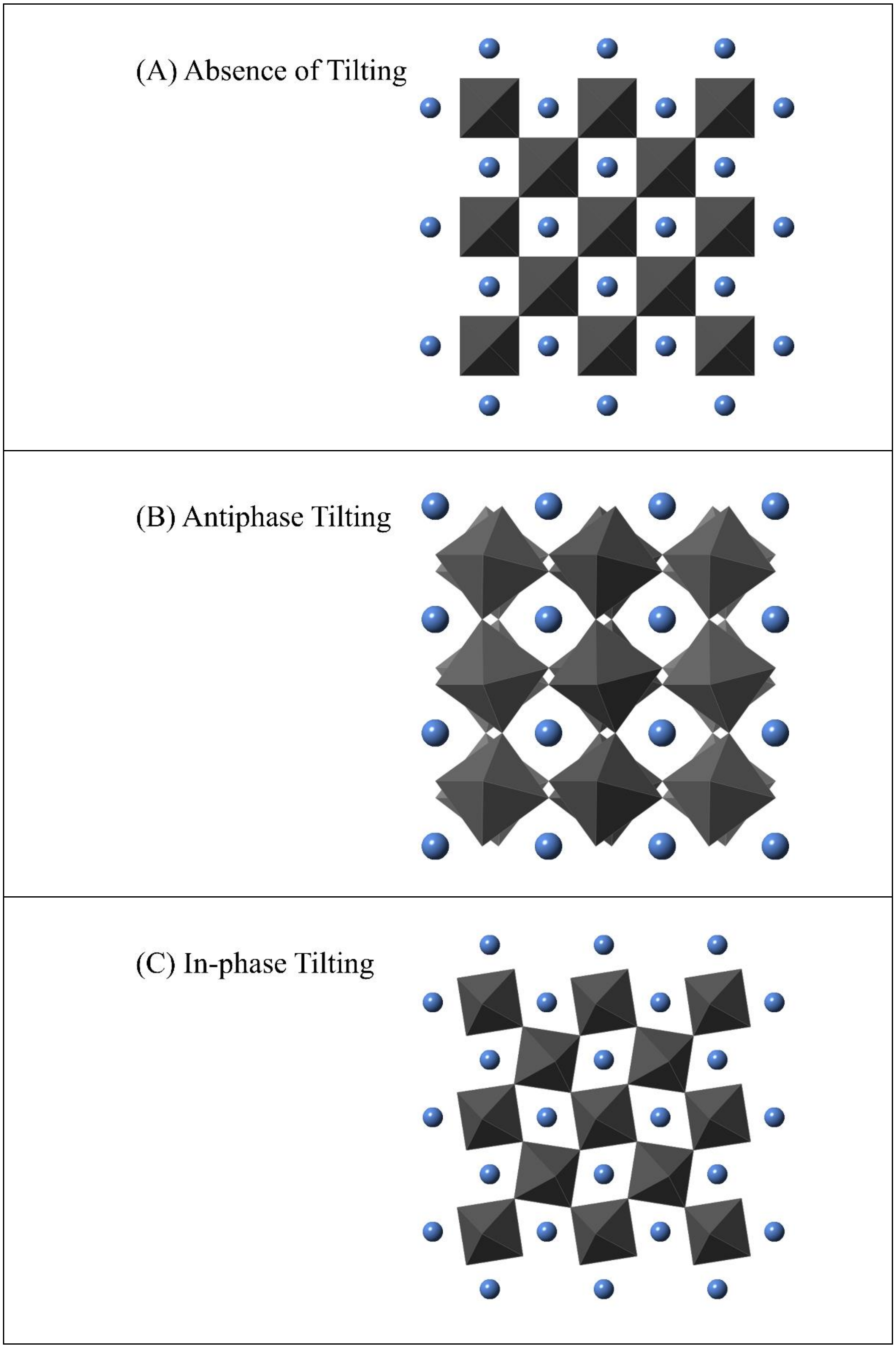

Figure 1.7. Tilting depictions. (A) absence of tilting, aristotype $a^0a^0a^0$; (B) antiphase tilting, $a^-a^-a^-$; and (C) in-phase tilting, $a^+a^+a^+$.

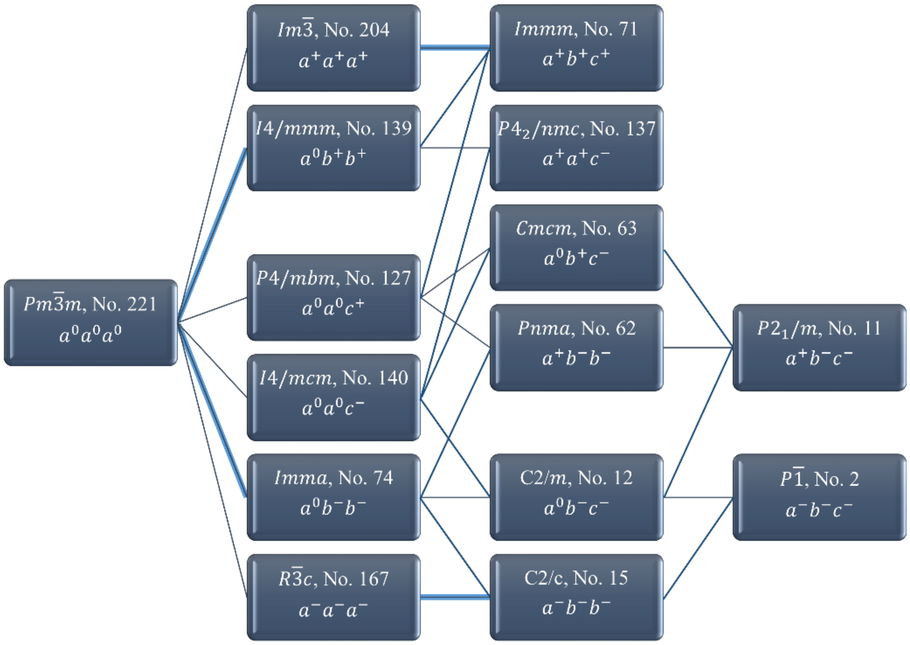

Figure 1.8. The 15 realistic tilt systems and their associated space groups, [25-28] where the bold lines show first-order transitions and thin lines show second-order transitions.

1.5.2 Jahn-Teller Distortions

According to band theory, inner electron orbitals become spherical even if not broadened, thus metals can be described by packing of spherical atoms. Indeed, the relaxation of the electron density due to bond formation is only about 1%. [51] First-order Jahn-Teller (FOJT) distortions are due to incompletely filled electron shells, which are doubly or triply degenerate molecular orbitals. The nature of the FOJT effect is such that distortions are inevitably so weak as to be negligible. On the other hand, second-order Jahn-Teller (SOJT) distortions occur when a molecule has filled shells, but where there is only a small energy difference between the highest filled orbital and the lowest empty one. These distortions result in measurable antiparallel (therefore polar) ionic displacements of cation and anion sublattices and typically yield piezoelectric or ferroelectric behavior. They occur when the gap between the highest occupied and lowest unoccupied molecular orbitals (*i.e.*, the HOMO-LUMO gap[*]) is small and there is a symmetry-allowed distortion which gives rise to mixing between the two. This distortion is favored because it stabilizes the HOMO while destabilizing the LUMO. SOJT distortions are typically observed for two classes of cations: octahedrally coordinated high-valent d^0 cations (*e.g.*, Ti^{4+}, V^{4+}) and cations containing filled valence s shells (*e.g.*, Pb^{2+}), so-called lone-pair species. [52, 53] In the case of $SrTiO_3$, Ti^{4+} is driven off-center within the octahedron as strontium is increasingly replaced with lead. In the extreme case of $PbVO_3$, the d^0 V^{4+} distorts to such an extent that its coordination environment changes to five-fold whilst the Pb^{2+} shifts from the center of its cuboctahedral coordination geometry by 19%.[51, 54]

1.6 Modeling Composition–Structure Relationships in Perovskites

Early attempts of composition-structure relationships include Roth's [55] 1957 compilation of empirical data from several $A^{2+}B^{4+}O_3^{2-}$ systems that links both cation radii to a particular structural system (*i.e.*, cubic, pseudocubic, tetragonal, rhombohedral, or orthorhombic) using two- and three-dimensional plots. Giaquinta and Loye [56] improved Roth's work with structure-composition diagrams and added $A^{3+}B^{3+}O_3^{2-}$ systems. These structure-composition diagrams are among those that are referred to as structure-field maps. In 1986, Kassan-Ogly and Naish [13, 57-59] published a series of four articles that addressed the problem of perovskite defects, tilting, and ionic shifting. Li *et al*. [60] used 197 oxides to derive an empirical structure

---

[*] In cubic perovskite with d^0 B cations, the bottom of the conduction band is a non-bonding B t_{2g} molecular orbital, and the top of the valence band is a non-bonding anion 2p.

map for simple perovskite oxides based on the radius of both cations and showed which combinations of sizes do not yield perovskites (Figure 1.9). Later, Zhang *et al*. [61] used 376 simple perovskite oxides to develop bond-valence structure maps.

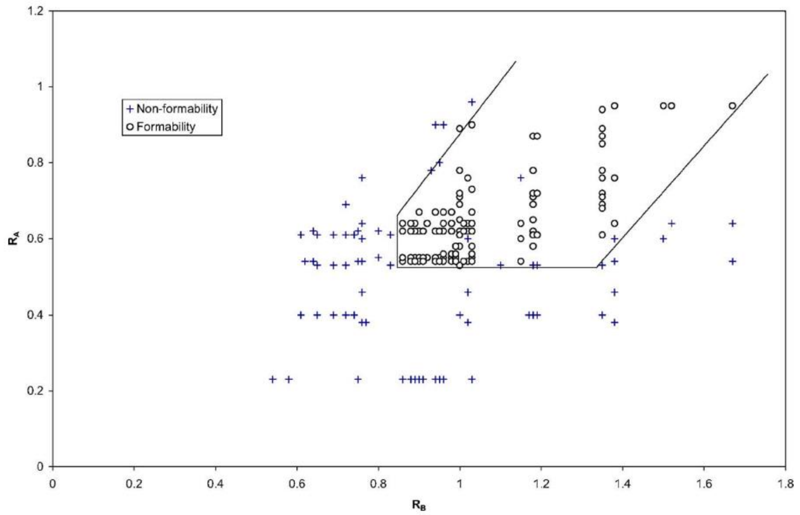

Figure 1.9. Perovskite structural boundaries proposed by Li *et al*. based on r_A and r_B. [60]

In 1992, Salinas-Sanchez derived what they termed the global-instability-index or *GII* (Equation 1.9), which can be used to determine the likelihood of perovskite formation from various ionic components. The global-instability-index was derived from the bond valence sums averaged over all the atoms within the unit; however, the accuracy of the predicted structures was quite often poor, especially for $GII > 0.2$, which would necessarily correspond to non-perovskite formation. Furthermore, Adams [62] extended bond valence sums to those systems that have asymmetric coordinations and claimed that the bond valence softness parameter, b, is not a constant. As a result, Adams used the bond-valence approach to revise the global-instability-index as:

$$GII = \sqrt{\frac{\sum_{i=1}^{j}\left(\sum_{N} BV \sum_{N} BV\right)^{2}}{N}} \tag{1.12}$$

Reaney *et al.* [47] showed the dependence of the temperature coefficient of the dielectric permittivity (τ_ε) as a function of tolerance factor for a variety of Sr- and Ba-based niobates and tantalates (Figure 1.10). The result illustrated the effect of octahedral tilting on τ_ε.

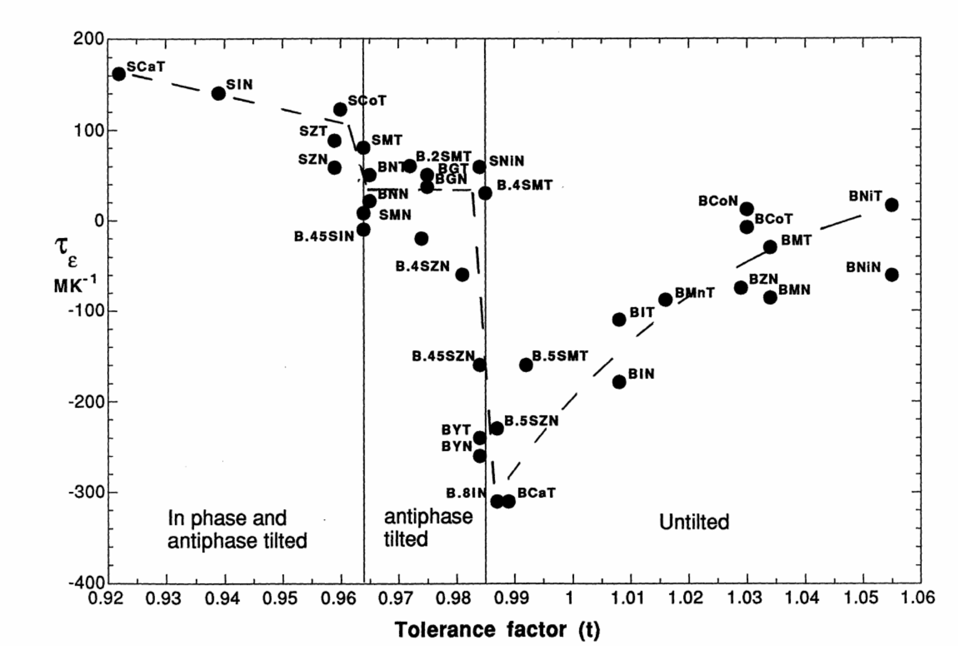

Figure 1.10. The temperature coefficient of the dielectric permittivity as a function of tolerance factor for Sr- and Ba-based compounds. [47]

In 1997, Woodward [63] built the first predictive software program, POTATO, to predict perovskite structure based on Glazer's tilt systems. POTATO was written in Fortran77 and operated by tilting a given individual octahedron by 0.01° increments in a three-dimensional network; however, the A cation was arbitrarily positioned at the center of eight nearest ions. Later, Lufaso and Woodward [64] developed another predictive software program, SPuDS, which was based on the global-instability index.

SPuDS outputs lattice constants, tilt system, tolerance factor, bond valence sums, bond lengths, and bond angles. SPuDS is a powerful tool for predicting ideal structures of perovskites; however, because it relies solely on *GII*, in many cases (including $CaTiO_3$, $SrTiO_3$, $BaTiO_3$, and $PbTiO_3$) it is unable to unambiguously predict the most stable perovskite structures and does not support some species (*e.g.*, Pm^{3+}) or any polyatomic ions apart from NH_4^+, and even then only when bonded to O^{2-}, F^-, or Cl^-.

Using the *pattern recognition atomic parameter method* and a database of 489 perovskite oxides, Ye *et al*. [65] derived an empirical model for ideal cubic perovskite oxides (Equation 1.13):

$$a = 0.3166R_A + 1.422R_B - 0.1708X_A + 0.0562X_B - 0.0066(Z_B - Z_A) + 2.706 \qquad (1.13)$$

where a is the cubic lattice constant, R_A and R_B are the cations' Shannon radii, X_A and X_B are the cations' covalency, and Z_A and Z_B are the cation's formal charges. The inclusion of covalency terms was the first attempt at accounting for bond deformations (*i.e.*, non-ideality of ionic sizes).

In 2006, Jiang *et al*. [66] reported an empirical model for simple cubic perovskites based on 132 perovskites - a mixture of oxides and non-oxides and including some with polyatomic ionic components; however, they incorrectly assumed sixfold coordination for *all* ionic species. Ubic [67, 68] revised and improved upon this model using the same 132 perovskites (Equations 1.14) and later [69] further developed this model to predict lattice constants of orthorhombic perovskites.

$$a_c = 0.05444 + 0.467016(r_A + r_O) + 1.30838(r_B + r_O) \tag{1.14}$$

Miller and Tidrow [70, 71] studied thermal effects on cation radii (*e.g.*, A-site Ca^{2+}_{XII}, Sr^{2+}_{XII}, Ba^{2+}_{XII}, Pb^{2+}_{XII} and La^{3+}_{XII}; and B-site Al^{3+}_{VI}, and Ti^{4+}_{VI}) in ideal perovskites to improve the accuracy of modeling lattice constants. They developed five geometrical relationships for cubic perovskites based on ionic radii (Figure 1.11). Not all of these geometrical relationships exist in real perovskites because the perovskite structure becomes unstable if anion-anion or cation-cation distances become too small. For example, cases 1, 3, and 5 in Figure 1.11 would represent the limits of stability; where case (1) shows that if the B site is any smaller than it would result in A cation-cation overlap, or case (5) anion-anion overlap, and anion sizes any smaller in case (3) would cause A cation-cation overlap.

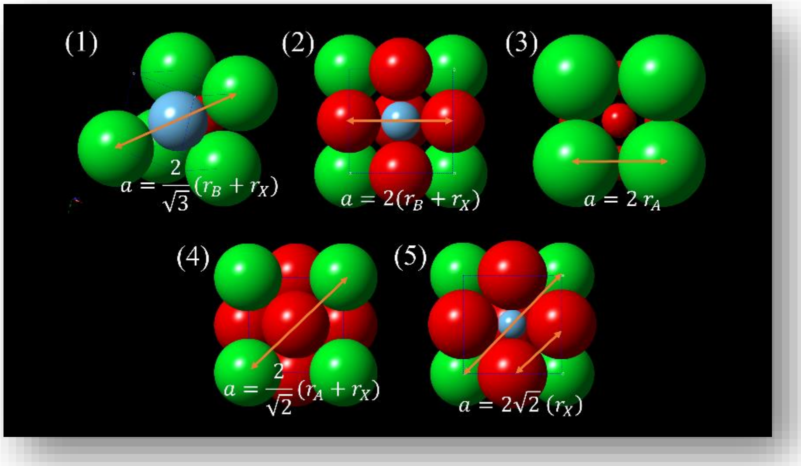

Figure 1.11. The five geometric cubic perovskite relationships developed by Miller and Tidrow. [70, 71] (1) large B (blue) cations are in contact with A (green) cations, (2) small B cations only contact anions, (3) anions (red) are much smaller than A cations, causing A cations to be in contact with each other, (4) anions are similar in size to A cations, causing contact between A and X, (5) B cations are much smaller than A cations and anions, causing anion-anion contact.

1.7 Aims and Objectives

Predictive models based on empirical evidence are powerful tools; however, no models have existed previously for perovskites with A-cation deficiencies, cation ordering, tetragonality, or trigonality. This work aims to fill this knowledge gap by providing composition-structure relationships that will be used for removing some guesswork for the development of new perovskites. The models developed in this work are based on experimental data from diffraction and refinements performed as part of this work coupled with reported experimental data from published scientific literature.

1.8 References:

[1] A. Chakhmouradian, P. Woodward, Celebrating 175 years of perovskite research: a tribute to Roger H. Mitchell, Physics and Chemistry of Minerals 41(6) (2014) 387-391.

[2] R.H. Mitchell, Perovskites: Modern and Ancient, Almaz Press, Ontario, Thunder Bay, 2002.

[3] G. Haertling, Ferroelectric ceramics: History and technology, Journal of the American Ceramic Society 82(4) (1999) 797-818.

[4] H. De Terra, Jay I. Kislak Reference Collection (Library of Congress), Humboldt; the life and times of Alexander von Humboldt, 1769-1859, 1st ed., Knopf, New York,, 1955.

[5] G. Rose, Certain new minerals discovered in the Ural Mountains: The perovskit, a new mineral, in: U.o. Berlin (Ed.) AG Schade, Berlin, 1839, pp. 3-5.

[6] B. Marello, Crystal of Perovskite Varenna Valley, in: $CaTiO_3$ (Ed.) mindat.org, Mineral Information and Data, Web Page, 2015, p. Public galleries.

[7] V.M. Goldschmidt, Titanium pigment and process of producing same, Google Patents, 1922.

[8] G.M. Victor, Pigment and method of its manufacture, Google Patents, 1920.

[9] H. Bowman, On the Structure of Perovskite from the Burgumer Alp, Pfitschthal, Tyrol, Mineralogical Magazine 15(69) (1908) 156-176.

[10] H. Kay, P. Bailey, Structure and Properties of $CaTiO_3$, Acta Crystallographica 10(3) (1957) 219-226.

[11] R. Mitchell, A. Chakhmouradian, P. Woodward, Crystal chemistry of perovskite-type compounds in the tausonite-loparite series, (Sr1-2xNaxLax)TiO3, Physics and Chemistry of Minerals 27(8) (2000) 583-589.

[12] R. Shannon, Revised Effective Ionic-Radii and Systematic Studies of Interatomic Distances in Halides and Chalcogenides, Acta Crystallographica Section a **32** 32 (SEP1) (1976) 751-767.

[13] F. Kassan-Ogly, V. Naish, The Immanent Chootization of Crystal-Structures and the Resulting Diffuse-Scattering .1. Mathematical Scheme and Physical Models, Acta Crystallographica Section B-Structural Science 42 (1986) 297-306.

[14] V.M. Goldschmidt, Geochemische Verteilungsgesetze VIII. Bau und Eigenschaften von Krystallen, 8 (1927) 1-156.

[15] H. Megaw, Crystal Structure of Barium Titanate, Nature 155(3938) (1945) 484-485.

[16] H. Megaw, Origin of Ferroelectricity in Barium Titanate and Other Perovskite-Type Crystals, Acta Crystallographica 5(6) (1952) 739-749.

[17] V. Goldschmidt, The laws of crystal chemistry, Naturwissenschaften **14** (1926) 477-485.

[18] I.D. Brown, Bond Valence Theory, in: D.I. Brown, R.K. Poeppelmeier (Eds.), Bond Valences, Springer Berlin Heidelberg, Berlin, Heidelberg, 2014, pp. 11-58.

[19] M. Kotelyanskii, I. Kotelyanskii, V. Kravchenko, New buffer sublayers for heteroepitaxial III-V nitride films on sapphire substrates, Technical Physics Letters 26(2) (2000) 163-164.

[20] K. Eisenbeiser, R. Emrick, R. Droopad, Z. Yu, J. Finder, S. Rockwell, J. Holmes, C. Overgaard, W. Ooms, GaAs MESFETs fabricated on Si substrates using a SrTiO3 buffer layer, Ieee Electron Device Letters 23(6) (2002) 300-302.

[21] A. Soukiassian, W. Tian, V. Vaithyanathan, J. Haeni, L. Chen, X. Xi, D. Schlom, D. Tenne, H. Sun, X. Pan, K. Choi, C. Eom, Y. Li, Q. Jia, C. Constantin, R. Feenstra, M. Bernhagen, P. Reiche, R. Uecker, Growth of nanoscale $BaTiO_3/SrTiO_3$ superlattices by molecular-beam epitaxy, Journal of Materials Research 23(5) (2008) 1417-1432.

[22] D. Tenne, X. Xi, Raman spectroscopy of ferroelectric thin films and superlattices, Journal of the American Ceramic Society 91(6) (2008) 1820-1834.

[23] D. Tenne, H. Lee, R. Katiyar, X. Xi, Ferroelectric phase transitions in three-component short-period superlattices studied by ultraviolet Raman spectroscopy, Journal of Applied Physics 105(5) (2009).

[24] J. Hlinka, V. Zelezny, S. Nakhmanson, A. Soukiassian, X. Xi, D. Schlom, Soft-mode spectroscopy of epitaxial BaTiO3/SrTiO3 superlattices, Physical Review B 82(22) (2010).

[25] C. Howard, H. Stokes, Group-theoretical analysis of octahedral tilting in perovskites, Acta Crystallographica Section B-Structural Science 54 (1998) 782-789.

[26] C. Howard, H. Stokes, Octahedral tilting in cation-ordered perovskites - a group-theoretical analysis, Acta Crystallographica Section B-Structural Science 60 (2004) 674-684.

[27] C. Howard, H. Stokes, Structures and phase transitions in perovskites - a group-theoretical approach, Acta Crystallographica Section a 61 (2005) 93-111.

[28] H. Stokes, E. Kisi, D. Hatch, C. Howard, Group-theoretical analysis of octahedral tilting in ferroelectric perovskites, Acta Crystallographica Section B-Structural Science 58 (2002) 934-938.

[29] P. Sundell, M. Bjorketun, G. Wahnstrom, Thermodynamics of doping and vacancy formation in BaZrO3 perovskite oxide from density functional calculations, Physical Review B 73(10) (2006).

[30] R. Pushpa, D. Daniel, D. Butt, Electronic properties of Ca doped LaFeO3: A first-principles study, Solid State Ionics 249 (2013) 184-190.

[31] H. Sreemoolanadhan, R. Ratheesh, M. Sebastian, P. Mohanan, Ba(Tb1/2Nb1/2)O3: A new ceramic microwave dielectric resonator, Materials Letters 33(3-4) (1997) 161-165.

[32] R. Cava, B. Batlogg, R. Vandover, D. Murphy, S. Sunshine, T. Siegrist, J. Remeika, E. Rietman, S. Zahurad, G. Espinosa, Bulk Superconductivity at 91-K in Single-Phast Oxygen-Deficient Perovskite $Ba_2YCu_3O_9$-Delta, Physical Review Letters 58(16) (1987) 1676-1679.

[33] S. Rao, K. Wang, N. Yen, Y. Chen, C. Tsai, S. Neeleshwar, M. Wu, J. Srivastava, M. Ling, H. Liu, D. Ling, Magnetic and superconducting properties of single crystals of Sr2HoRu1-xCuxO6 grown from high temperature solutions, Applied Physics Letters 89(23) (2006).

[34] C. Michel, L. Errakho, B. Raveau, The Oxygen Defect Perovskite $BaLa_4Cu_5O_{13.4}$, A Metallic Conductor, Materials Research Bulletin 20(6) (1985) 667-671.

[35] S. Kawashima, M. Nishida, I. Ueda, H. Ouchi, $Ba(Zn_{1/3}Ta_{2/3})O_3$ Ceramics with Low Dielectric Loss at Microwave-Frequencies, Journal of the American Ceramic Society 66(6) (1983) 421-423.

[36] D. Cox, B. Noheda, G. Shirane, Y. Uesu, K. Fujishiro, Y. Yamada, Universal phase diagram for high-piezoelectric perovskite systems, Applied Physics Letters 79(3) (2001) 400-402.

[37] K. Kobayashi, T. Kimura, H. Sawada, K. Terakura, Y. Tokura, Room-temperature magnetoresistance in an oxide material with an ordered double-perovskite structure, Nature 395(6703) (1998) 677-680.

[38] Y. Lee, R. Lago, J. Fierro, J. Gonzalez, Hydrogen peroxide decomposition over *Ln*(1-x)A(x)MnO(3) (*Ln* = La or Nd and A = K or Sr) perovskites, Applied Catalysis a-General 215(1-2) (2001) 245-256.

[39] C. Kim, G. Qi, K. Dahlberg, W. Li, Strontium-Doped Perovskites Rival Platinum Catalysts for Treating NOx in Simulated Diesel Exhaust, Science 327(5973) (2010) 1624-1627.

[40] B. Wul, Barium Titanate - A New Ferro-Electric, Nature 157(3998) (1946) 808-808.

[41] K. Ueda, H. Tabata, T. Kawai, Ferromagnetism in LaFeO3-LaCrO3 superlattices, Science 280(5366) (1998) 1064-1066.

[42] H. Iwahara, H. Uchida, S. Tanada, High-Temperature Type Proton Conductor Based on $SrCeO_3$ and its Application to Solid Electrolyte Fuel-Cells, Solid State Ionics 9-10(DEC) (1983) 1021-1025.

[43] M. Li, M. Pietrowski, R. De Souza, H. Zhang, I. Reaney, S. Cook, J. Kilner, D. Sinclair, A family of oxide ion conductors based on the ferroelectric perovskite Na0.5Bi0.5TiO3, Nature Materials 13(1) (2014) 31-35.

[44] A. Kojima, K. Teshima, Y. Shirai, T. Miyasaka, Organometal Halide Perovskites as Visible-Light Sensitizers for Photovoltaic Cells, Journal of the American Chemical Society 131(17) (2009) 6050-+.

[45] C. Roundy, R. Byer, Sensitive $LiTaO_3$ Pyroelectric Detector, Journal of Applied Physics 44(2) (1973) 929-931.

[46] G. Smolenskii, A. Agranovskaia, Dielectric Polarization and Losses of Some Complex Compounds, Soviet Physics-Technical Physics 3(7) (1958) 1380-1382.

[47] I. Reaney, E. Colla, N. Setter, Dielectric and Structural Characteristics of Ba-Based and Sr-Based Complex Perovskites as a Function of Tolerance Factor, Japanese Journal of Applied Physics Part 1-Regular Papers Short Notes & Review Papers 33(7A) (1994) 3984-3990.

[48] A.M. Glazer, The classification of tilted octahedra in perovskites, Acta Crystallographica Section B, 1972, pp. 3384-3392.

[49] P. Woodward, Octahedral tilting in perovskites .1. Geometrical considerations, Acta Crystallographica Section B-Structural Science 53 (1997) 32-43.

[50] P. Woodward, Octahedral tilting in perovskites .2. Structure stabilizing forces, Acta Crystallographica Section B-Structural Science 53 (1997) 44-66.

[51] I.D. Brown, K.R. Poeppelmeier, Bond Valences, Springer Berlin Heidelberg, Berlin, 2014.

[52] R. Pearson, The 2nd-order Jahn-Teller effect, Theochem-Journal of Molecular Structure 12(AUG) (1983) 25-34.

[53] M. Kunz, I. Brown, Out-of-center distortions around octahedrally coordinated d(0) transition-metals, Journal of Solid State Chemistry 115(2) (1995) 395-406.

[54] R. Shpanchenko, V. Chernaya, A. Tsirlin, P. Chizhov, D. Sklovsky, E. Antipov, E. Khlybov, V. Pomjakushin, A. Balagurov, J. Medvedeva, E. Kaul, C. Geibel, Synthesis, structure, and properties of new perovskite PbVO3, Chemistry of Materials 16(17) (2004) 3267-3273.

[55] R. Roth, Classification of Perovskite and Other ABO_3-Type Compounds, Journal of Research of the National Bureau of Standards 58(2) (1957) 75-88.

[56] D. Giaquinta, H. Zurloye, Structural Predictions in the ABO_3 Phase-Diagram, Chemistry of Materials 6(4) (1994) 365-372.

[57] F. Kassan-Ogly, V. Naish, The Immanent Chaotization of Crystal-Structures and the Resulting Diffuse-Scattering .2. Crystallochemical Conditions of Perovskite Chaotization, Acta Crystallographica Section B-Structural Science 42 (1986) 307-313.

[58] F. Kassan-Ogly, V. Naish, The Immanent Chaotization of Crystal-Structures and the Resulting Diffuse-Scattering .3. Diffuse-Scattering in Perovskites with One-Dimensional Movable Objects (Shifting), Acta Crystallographica Section B-Structural Science 42 (1986) 314-325.

[59] F. Kassanogly, V. Naish, The Immanent Chaotization of Crystal-Structures and the Resulting Diffuse-Scattering .4. Diffuse-Scattering in Perovskites with Two-Dimensional Movable Objects (Tilting), Acta Crystallographica Section B-Structural Science 42 (1986) 325-335.

[60] C. Li, K. Soh, P. Wu, Formability of ABO(3) perovskites, Journal of Alloys and Compounds 372(1-2) (2004) 40-48.

[61] H. Zhang, N. Li, K. Li, D. Xue, Structural stability and formability of ABO3-type perovskite compounds, Acta Crystallographica Section B 63(6) (2007) 812-818.

[62] S. Adams, O. Moretzki, E. Canadell, Global instability index optimizations for the localization of mobile protons, Solid State Ionics 168(3-4) (2004) 281-290.

[63] P. Woodward, POTATO - a program for generating perovskite structures distorted by tilting of rigid octahedra, Journal of Applied Crystallography 30(2) (1997) 206-207.

[64] M. Lufaso, P. Woodward, Prediction of the crystal structures of perovskites using the software program SPuDS, Acta Crystallographica Section B-Structural Science 57 (2001) 725-738.

[65] C. Ye, J. Yang, L. Yao, N. Chen, Regularities of formation and lattice distortion of perovskite-type compounds, Chinese Science Bulletin 47(6) (2002) 458-460.

[66] L. Jiang, J. Guo, H. Liu, M. Zhu, X. Zhou, P. Wu, C. Li, Prediction of lattice constant in cubic perovskites, Journal of Physics and Chemistry of Solids 67(7) (2006) 1531-1536.

[67] R. Ubic, Revised method for the prediction of lattice constants in cubic and pseudocubic perovskites, Journal of the American Ceramic Society **90** (10) (2007) 3326-3330.

[68] R. Ubic, G. Subodh, M.T. Sebastian, Effective size of vacancies in the $Sr_{1-3x/2}Ce_xTiO3$ superstructure, Ceramic Transactions 204 (2009) 177-185.

[69] R. Ubic, G. Subodh, The prediction of lattice constants in orthorhombic perovskites, Journal of Alloys and Compounds 488(1) (2009) 374-379.

[70] V. Miller, S. Tidrow, Perovskites: Temperature and Coordination Dependent Ionic Radii, Integrated Ferroelectrics 148(1) (2013) 1-16.

[71] S. Tidrow, Mapping Comparison of Goldschmidt's Tolerance Factor with Perovskite Structural Conditions, Ferroelectrics 470(1) (2014) 13-27.

CHAPTER TWO: THE STRUCTURAL EFFECT OF EXTRINSIC VACANCIES IN PEROVSKITES

2.1 Introduction

The perovskite $E2_1$ structure is central to many useful properties via defect engineering, for which precise understanding of composition–structure relationships are needed. Additionally, the design of cation-deficient perovskite materials is aided by an understanding of this relationship between chemical composition and crystal structure. Lattice-constant predictions are important on their own, particularly in heteroepitaxial designs; however, the exact nature (chemical and structural) of vacancies remains unknown.

Extrinsic stoichiometric vacancies, commonly introduced by doping, contribute profoundly to the structure and properties of perovskites. Donor doping is commonly used in perovskites to control the effect of metal-oxide volatilisation upon sintering and enhance the dielectric properties. [1] The potential loss of the metal oxide can cause vacancies. Oxygen vacancies are particularly damaging to the dielectric properties, as they are highly mobile and can result in ionic conduction and a large increase in dielectric loss. In commercial Pb-based perovskites like $PbTiO_3$ and $Pb(Zr_yTi_{1-y})O_3$ it is common to dope the A site with La^{+3} in order to allow the formation of intrinsic Pb vacancies, V_{Pb}, without necessitating the creation of charge-compensating oxygen vacancies, according to:

$$La_2O_3 \xrightarrow{PZT} 2La^{\bullet}_{Pb} + V^{''}_{Pb} + 3O^{x}_{O}$$

Furthermore, such doping is very important in industry because of its additional beneficial effects which include: increased mechanical compliance, maximal electromechanical coupling coefficients, increased dielectric constant, decreased coercive field, increased squareness of the hysteresis loop, and enhanced optical transparency, [2, 3] yet no attempt has been made to study the exact nature of vacancies in lanthanum-doped titanates.

Although previous stoichiometric models [4-6] have proven to be exceptionally useful in predicting cubic lattice constants (ABX_3 unit volume), they are limited to stoichiometric perovskites alone. To quantitatively study the effect of defects in non-stoichiometric perovskites, a model which involves the correct coordinations and effective ionic sizes was needed. In 2007 Ubic [7] published a revised method of calculating pseudocubic lattice constants, a_{pc}, of stoichiometric perovskites based on 132 compositions found in the literature. That model (equation (2.1)) used effective ionic radii assuming sixfold coordination for all ionic species because, even though that coordination is incorrect for A and X ions, those values resulted in the best fit for a_{pc} (average relative error = 0.60%). The average relative error is calculated by the quantity of the difference between the calculated and experimental values divided by the experimental and then averaged for all 132 compositions.

$$a_{pc} = 0.06741 + 0.49052\left(r_{\mathrm{A}(id)}^{VI} + r_{\mathrm{X}(id)}^{VI}\right) + 1.29212\left(r_{\mathrm{B}} + r_{\mathrm{X}}^{VI}\right) \tag{2.1}$$

where $r_{\mathrm{A}(id)}^{VI}$, r_{B}, and $r_{\mathrm{X}(id)}^{VI}$ are the effective ionic radii of A, B, and X ions in sixfold coordination.

Although this model has proven extremely accurate in predicting cubic/pseudocubic lattice constants (and hence ABX_3 unit volume) in stoichiometric perovskites, in order to quantitatively study the effect of defects on crystal structure, a model which involves the actual sizes of ions (in their correct coordinations) is required. Towards that end, the same linear regression method and revised lattice constants reported in that work can be used to derive a new equation in which A, B, and X ions are assumed in XII, VI, and II coordinations, respectively. As it happens, this new model (equation (2.2)) yields results only slightly less accurate than the original (average relative error = 0.77%):

$$a_{pc} = 0.01173 + 0.50977\left(r_{\mathrm{A}(id)} + r_{\mathrm{X}(id)}\right) + 1.26954\left(r_{\mathrm{B}} + r_{\mathrm{X}(id)}\right) \tag{2.2}$$

where $r_{\mathrm{A}(id)}$ and $r_{\mathrm{X}(id)}$ are the effective ionic radii of A and X ionic species in XII and II coordination, respectively.

Equation (2.2) can be solved for *t* according to equation (1.8):

$$t_1 = \frac{a_{pc} - 0.011730139}{0.7209203\left(r_{\mathrm{B}} + r_{\mathrm{X}(id)}\right)} - 1.760998 \tag{2.3}$$

Ideally $t_1 = t_*$. Equation (2.3) is similar to that reported previously [8, 9] but, as it was derived from corrected lattice-constant data, is slightly more accurate than the earlier version. Significantly, equation (2.3) removes the necessity of calculating effective or average A-site ionic radii for compositions for which this value is ambiguous to define (*e.g.*, compositions with mixed occupancies or A-site vacancies). The required a_{pc} value in this expression can either be calculated via equation (2.1) (in the case of stoichiometric perovskites) or experimentally measured.

It is important to consider four factors that directly influence ionic radii: 1. valence, 2. coordinaltion, 3. covalency, and 4. the cation-to-anion radius ratio. In the case where the A-site cation is too small, or absent, the anions will interact and the repulsion forces between anions will increase. This effect is the very reason why large concentrations of vacancies can exist and not collapse the perovskite structure.

2.2 $A_{1-3x}Ln_{2x}V_x\text{TiO}_3$ Perovskite Systems

Lanthanide-modified perovskites in the system $A_{1-3x}Ln_{2x}V_x\text{TiO}_3$, where V_X is the vacancy concentration on the A-cation site. This formulation is not expected to generate B-site vacancies; rather, charge compensation causes A-site vacancy formation exclusively as follows:

$$Ln_2O_3 \xrightarrow{A^{2+}B^{4+}O_3^{2-}} 2Ln_A^{\bullet} + V_A'' + 3O_O^{\times}$$

resulting in

$$A^{2+}_{XII\,(1-3x)}Ln^{3+}_{XII\,(2x)}V_xTi^{4+}_{VI}O^{2-}_{II\;\;3}$$

This formulation is convenient, as x is then directly equivalent to the A-site vacancy concentration, $x = [\text{V}]$.

2.2.1 $\text{Sr}_{1-3x}Ln_{2x}V_x\text{TiO}_3$

Studies of the $\text{Sr}_{1-3x}Ln_{2x}\text{TiO}_3$ (*Ln* = La, Nb, Bi) system by Tien and Hummel [10, 11] suggested that vacancies may order at higher x values. At compositions above $x = 0.23$ they noticed extra superlattice reflections, which they attributed to ordering. They found the same structural phenomenon in the La end member, $\text{La}_{2/3}\text{TiO}_3$. Later, Battle *et* *al*. [12] conducted X-ray and electron-diffraction studies in the system $Sr_{1-3x}La_{2x}TiO_3$ ($0.125 \leq x \leq 0.3$) and observed vacancy pairing at higher x values and long-range cation/vacancy ordering at $x = 0.25$ (*Pban*); however, not all reflections were accounted for in electron diffraction patterns. Howard *et al*. [13] conducted X-ray and neutron diffraction studies in the system $Sr_{1-3x}La_{2x}TiO_3$ ($0.0 \leq x \leq 0.33$) with stoichiometric vacancies and proposed a phase diagram. They reported that the structure of compositions corresponding to $0.0 \leq x \leq 0.11$ is cubic, $Pm\bar{3}m$; tetragonal, *I4/mcm*, for $0.11 < x \leq 0.26$; and orthorhombic, *Cmmm*, for $x > 0.26$. Ubic *et al*. [8, 14] studied $Sr_{1-3x}Ce_{2x}TiO_3$ ($0 < x < 0.2$) using electron and neutron diffraction and found antiphase octahedral tilting, $a^-a^-a^-$, consistent with $R\bar{3}c$ symmetry. Tilting of TiO_6 octahedra is virtually undetectable via X-ray diffraction, especially in very low-x concentrations where tilt angles are extremely small, which may explain why previous work [15-19] reported cubic structures in $Pm\bar{3}m$, for $0.0 \leq x \leq 0.1$ Additionally, Ubic *et al*. [8, 14] found that $C2/c$ provided better refinement results for $x = 0.2$ provided that a subtle, probably short-range doubling of the c axis was neglected.

2.2.2 $Ca_{1-3x}Ln_{2x}V_xTiO_3$

Compositions in the system $Ca_{1-3x}La_{2x}TiO_3$ have been reported by Vashook *et al*. [20, 21] and by Zhang *et al*. [22]. In 2006, Vashook *et al*. [20, 21] reported a room-temperature diagram for the $CaTiO_3 – La_{2/3}TiO_3$ system in which compositions corresponding to $0 \leq x \leq 0.133$ form in *Pbnm*, those in the range $0.133 \leq x \leq 0.233$ in *Imma*, those in the range $0.233 \leq x \leq 0.267$ in *I*4/*mcm*, and those in the range $0.267 \leq x \leq 0.333$ in *Cmmm*. Zhang *et al*. [22] used neutron and synchrotron data to study the system $Ca_{1-3x}La_{2x}TiO_3$ at room temperature and reported similar results to that of

Vashook's work, with structures in *Pbnm* for $0.0 \leq x \leq 0.167$, *Ibmm* for $0.167 \leq x \leq 0.233$, *I*4/*mcm* for $0.233 \leq x \leq 0.3$, and *Cmmm* for $x > 0.3$.

2.2.3 $Pb_{1-3x}Ln_{2x}V_xTiO_3$

Hennings and Rosenstein [23] showed that the La^{3+} ions and vacancies are found at the A sites in $Pb_{1-3x}La_{2x}TiO_3$. Hennings and Hardtl [24, 25] found that by controlling a PbO partial pressure with a sacrificial $PbZrO_3$ powder that it is possible to inhibit/induce B-site vacancies. Undoped $PbTiO_3$ reportedly [26, 27] forms in *P*4*mm*, but as lanthanum concentrations increase in the $Pb_{1-3x}La_{2x}TiO_3$ system the symmetry changes to cubic $Pm\overline{3}m$ at about $x = 0.14$.[29] Chen Jun *et al*. [28, 29] showed that the cation displacements decrease along the c-axis (*i.e.*, the spontaneous polarization direction) with increasing vacancy concentration.

2.2.4 $Ba_{1-3x}Ln_{2x}V_xTiO_3$

It has been previously reported [30] that at very low dopant concentrations ($x \leq 0.0025$) La^{3+} ions prefer to substitute at the A site in $Ba_{1-3x}Ln_{2x}V_xTiO_3$ with charge-compensation conferred by Ti^{4+} reduction; however, recently Ganguly *et al*. [31] showed A-site vacancy formation at higher dopant levels using a photoluminescence study. They found a tetragonal-to-cubic phase transition at about $x = 0.02$, where the cation displacements decrease along the c-axis (*i.e.*, the spontaneous polarization direction), and a gradual decrease in the Curie temperature with increasing vacancy concentration. In this work, doped $BaTiO_3$ compositions were formulated assuming compensation by A-site vacancies according to the stoichiometry $Ba_{1-3x}La_{2x}TiO_3$. If compensation is via either Ti reduction or Ti vacancy formation, then La^{3+} doping should leave an appreciable amount of unreacted TiO_2 secondary phase according to:

$$Ba_{1-3x}La_{2x}TiO_3 \rightarrow (1-x)\left[\left(Ba_{\frac{1-3x}{1-x}}La_{\frac{2x}{1-x}}\right)\left(Ti^{4+}_{\frac{1-3x}{1-x}}Ti^{3+}_{\frac{2x}{1-x}}\right)O_3\right] + xTiO_2$$

or

$$Ba_{1-3x}La_{2x}TiO_3 \rightarrow (1-x)\left[\left(Ba_{\frac{1-3x}{1-x}}La_{\frac{2x}{1-x}}\right)Ti^{4+}_{\frac{3-\frac{1}{1-x}}{2}}O_3\right] + \frac{3x}{2}TiO_2$$

At $x = 0.04$ these reactions would yield 2-3 vol% TiO_2, a quantity easily detectable via XRD especially given the intensity of the TiO_2 (110) peak. Similarly, if the $Ba_{6-3y}La_{8+2y}Ti_{18}O_{54}$ solid-solution phase were to form (*e.g.*, $BaLa_2Ti_4O_{12}$), it would also result in a multiphase microstructure according to either:

$$Ba_{1-3x}La_{2x}TiO_3 \rightarrow x(BaLa_2Ti_4O_{12}) + (1-4x)BaTiO_3$$

where $x \leq 0.25$, or, assuming that the perovskite phase would be Ti-deficient (*e.g.*, $Ba_{0.95}La_{0.05}Ti_{0.9875}O_3$):

$$Ba_{1-3x}La_{2x}TiO_3 \rightarrow \frac{12.3x-0.3}{11.1}(BaLa_2Ti_4O_{12}) + \frac{2-8x}{1.85}(Ba_{0.95}La_{0.05})Ti_{0.9875}O_3$$
$$+ (0.04053 - 0.1621x)TiO_2$$

where $0.02439 \leq x \leq 0.25$. In the former scenario, all of the La^{3+} is accommodated in the ternary phase; therefore, no change in lattice constants should be detectable in the perovskite phase. In the latter scenario, the La^{3+} dopant is assumed to cause Ti vacancies in the perovskite but simultaneously requires the presence of both the $Ba_{6-3y}La_{8+2y}Ti_{18}O_{54}$ phase and excess TiO_2; therefore, experimental results showing the absence of both $Ba_{6-3y}La_{8+2y}Ti_{18}O_{54}$ and TiO_2 as well as the perovskite lattice constants changing with x would verify that a small amount of La_2O_3 solubility in $BaTiO_3$ is possible without causing Ti reduction or vacancy formation on calcining in air. It is possible that, while the large size of Ba^{2+} (and consequently Ba^{2+} vacancies) energetically inhibits the formation/stabilization of these vacancies, it is still possible to engineer them into the structure extrinsically.

2.2.5 $La_{2/3}V_{1/3}TiO_3$, $La_{1/3}V_{2/3}NbO_3$, $Th_{1/4}V_{3/4}NbO_3$, and $VReO_3$

Some perovskite compositions can accommodate very high vacancy concentrations on the A site from 33% ($La_{2/3}TiO_3$) to 67% ($La_{1/3}NbO_3$), 75% ($Th_{1/4}NbO_3$), and even to 100% (ReO_3). One of the earliest recorded $x = ⅓$ end-member compounds was $La_{2/3}TiO_3$, reported by the Dubiler Condenser Company Ltd. in 1946 (US patent No. 574,577). [32] In 1955, Kestigian and Ward [33] predicted a pseudocubic lattice constant for $La_{2/3}TiO_3$ of about $a_{pc} = 3.8846$ Å. MacChesney and Sauer [34] provided the La_2O_3–TiO_2 phase diagram between 1300°C–1900°C. Later, Abe and Uchino [35] reported a very similar pseudocubic lattice constant, but slightly oxygen-deficient $La_{2/3}Ti^{4+}_{1-2\lambda}Ti^{3+}_{2\lambda}O_{3-\lambda}$ ($\lambda = 0.007$) structure in *Pbnm* with $a = 3.869$ Å, $b = 3.882$ Å, $c = 3.891$ Å (*i.e.*, $a_{pc} = 3.881$ Å), isostructural with $CaTiO_3$. Gönen *et al.*, [36] used a wet-chemical route in air to synthesize $La_{2/3}TiO_3$ ($a_{pc} = 3.9384$ Å) from either $HLa_2Ti_3O_9$ or $KLa_2La_3O_9$. Their structural model (ICSD collection code 240300) in space group *I4/mmm* consists of shifted $(La_2Ti_3O_{9.5})^{1-}$ slabs with 5% oxygen vacancies, yielding a $La_{2/3}TiO_3$ compound with a layered structure in which successive planes are either La- or vacancy-rich This model gave superior Rietveld fits to XRD data and is "consistent with expectations based on the K_2O elimination in the formation of $KLa_2Ti_3O_{9.5}$ and the fact that $La_2Ti_3O_9$ readily reacts with KNO_3 to re-form the $K_2La_2Ti_3O_{10}$ starting material." [36] As this model is the only one listed in the ICSD for a La-deficient titanate perovskite, it was the one used in this work.

Kennedy *et al*. [37] and Zhang *et al*. [38] showed other vacancy-rich rare-earth perovskites give analogous results in terms of the compounds' pseudocubic lattice constants. Kennedy *et al*. [37] reported an orthorhombic perovskite $La_{1/3}NbO_3$ at room temperature with lattice constants a = 7.8562 Å, b = 7.8361 Å, and c = 7.9298 Å (a_{pc} = 3.941 Å) with NbO_6 octahedra showing ~ 4.4° out-of-phase tilting about the a-axis, which they compared to the ~4.7° tilting reported in $La_{2/3}TiO_3$. Zhang *et al.*, [38] using high-resolution neutron powder-diffraction data reported an orthorhombic structure in space group *Cmmm* for both $Nd_{1/3}NbO_3$ (a_{pc} = 3.90212 Å) and $Pr_{1/3}NbO_3$ (a_{pc} = 3.90972 Å). Recently, Zhou *et al*. [39] studied the lanthanide series of high-vacancy tantalates, $Ln_{1/3}TaO_3$ (Table 2.1), which shows how the pseudocubic lattice constants compare. Jorgensen *et al*. [40] reported neutron powder-diffraction data for the extreme case of cubic ReO_6, in which the A site is completely vacant.

Table 2.1 Lattice parameters for the rare earth lanthanide series $Ln_{1/3}TaO_3$. [39]

Compound	Space Group	*Ln* (Å)	*a* (Å)	*b* (Å)	*c* (Å)	a_{pc} (Å)
$La_{1/3}TaO_3$	*P4/mmm*	1.36	3.91858	-	7.91320	3.93121
$Ce_{1/3}TaO_3$	*Cmmm*	1.34	7.83019	7.80769	7.87930	3.91950
$Pr_{1/3}TaO_3$	*Cmmm*	1.278	7.82781	7.78882	7.85469	3.91186
$Nd_{1/3}TaO_3$	*Cmmm*	1.27	7.81968	7.77320	7.83508	3.90464
$Sm_{1/3}TaO_3$	*Cmmm*	1.24	7.79301	7.74820	7.80662	3.89128
$Eu_{1/3}TaO_3$	*Cmmm*	1.258	7.77801	7.73869	7.79669	3.88555
$Gd_{1/3}TaO_3$	*Cmmm*	1.239	7.74592	7.73841	7.79172	3.87932
$Tb_{1/3}TaO_3$	*Pbmm*	1.259	5.47920	5.41150	7.79351	3.86577
$Dy_{1/3}TaO_3$	*Pbmm*	1.254	5.47790	5.38971	7.78390	3.85868
$Ho_{1/3}TaO_3$	$P2_1am$	1.218	5.47550	5.37044	7.77129	3.85143
$Er_{1/3}TaO_3$	$P2_1am$	1.234	5.47391	5.35349	7.76061	3.84524
$Tm_{1/3}TaO_3$	*P4/mmm*	1.224	3.83091	-	7.74370	3.84451

2.3 Methods

A total of 11 compositions in the system $Sr_{1-3x}Ln_{2x}TiO_3$ (Ln = La, Nd) corresponding to $0 < x \leq 0.25$ were prepared via the conventional mixed-oxide route as described by Ubic *et al.* [9] where La- and Nd-doped compositions, as-received La_2O_3 (99.9%, Alfa-Aesar, Ward Hill, MA) and Nd_2O_3 (99.9%, Meldform Rare Earths, Cambide, UK) powders were first hydroxylated by mixing with an excess of deionized water and drying overnight, forming $Ln(OH)_3$ compounds. For compositions corresponding to $x \leq 0.15$, these powders were then mixed with stoichiometric amounts of $SrCO_3$ (99.9%, Aldrich Chemical Co., Milwaukee, WI) and TiO_2 (99.9%, Aldrich Chemical Co., Milwaukee, WI) and ball-milled in deionized water for 4 hr, using YSZ media in a high-density nylon pot. Slurries were dried, ground, and calcined at 1300 °C for 4 hr. In the case of pure $SrTiO_3$, starting powders were milled for 6 hr prior to drying and calcining. This formulation is convenient in that x is equal to the concentration of A-site vacancies, [V]. In addition, 13 compositions in the system $Ca_{1-3x}Ln_{2x}TiO_3$ (Ln=La, Nd, Y), two compositions in the system $Pb_{1-3x}La_{2x}TiO_3$, four compositions in the system $Ba_{1-3x}La_{2x}TiO_3$, six compositions in the system $Pb_{1-3x}La_{2x}(Zr_{0.6}Ti_{0.4})O_3$ (PLZT), five compositions in the system $[(Ca_{0.252}Sr_{0.748})_{1-3x}La_{2x}]TiO_3$, and $Sr_{0.97}La_{0.02}(Mg_{⅓}Nb_{⅔})O_3$ were all produced in a similar manner. Raw materials included $SrCO_3$ (99.99%, Alfa-Aesar), $CaCO_3$ (99.5%, Fisher Scientific), PbO (99.9%, Fisher Scientific), $BaCO_3$ (99.95%, Alfa-Aesar), La_2O_3 (99.9%, Alfa-Aesar), Nd_2O_3 (99.9%, Meldform Rare Earths), TiO_2 (99.5%, Fisher Scientific), Y_2O_3 (99.9%, Alfa-Aesar), and ZrO_2 (99.5%, Alpha Aesar). A further 11 PLZT compositions ($0 \leq x \leq 0.03$) were processed via attrition milling according to the method previously described by Tolman *et al*. [41] where the lanthanum oxide was heated to 700 °C for 1hr and weighed after cooling. The oxides PbO (>99%, Liebau), ZrO_2 (>99%, SEPR), TiO_2 (>99%, Tronox), and La_2O_3 (>99%, Merck) were homogenized via attrition milling with 2 mm YSZ media in isopropanol with a polyamide crucible and rotors. After drying in a roto-evaporator the compounds were stored in an oven for several days, after which they were sieved (160 μm mesh) and calcined in an Al_2O_3 precontaminated crucible covered with a ground Al_2O_3 lid in air at 850 °C for 2 hr. After calcination, the materials were milled in a planetary ball mill (polyamide crucible, 10 mm YTZ media, 200 rpm, 6hr) in isopropanol to breakup any agglomerates. Final drying was conducted in an atmospheric oven at 80–100 °C and the powder was sieved once again (160 μm mesh). Smaller doping amounts resulted in coarser powders. After drying, the powders were pressed in to green compacts by cold isostatic pressing at about 600 MPa. The forming was done by low-pressure uniaxial pressing and subsequent isostatic pressing (500 MPa). Sintering was performed in an oxygen atmosphere at 1225 °C for 2 hr in a closed pre-contaminated Al_2O_3 crucible with $PbZrO_3$/8 wt% ZrO_2 powder bed.

Powder samples were prepared for x-ray diffraction from post-calcined batches or, in the case of the 11 attrition-milled PLZT samples, pulverized pellets. For $Sr_{1\text{-}3x}Ln_{2x}TiO_3$ samples, synchrotron x-ray data were (mail-in) acquired on the high-resolution beamline 11-BM at the Advanced Photon Source, Argonne National Laboratory. Le Bail fits to these data were conducted using the General Structure Analysis System (GSAS). [42] For all other compositions, diffraction was conducted using a Miniflex 600 (Rigaku, Woodlands, TX) in Bragg-Brentano theta-2 theta geometry (10^6 cps on Si standard (111) peak), and refinements conducted using DiffracPLUS TOPAS 4.2 (Bruker AXS Inc., Madison, WI). In addition to the cubic/pseudocubic lattice constants and average crystallite size, non-structural parameters, including background, peak shape, zero-point, and instrument line profile were also refined. The instrument line profile was characterized as the convolution of both equatorial and axial profiles. Equatorial divergence was refined using the receiving-slit width and the fixed-divergence slit angle parameters, while axial divergence was modeled using the Finger *et al.* [43] asymmetry correction. Background was fitted with a fourth-order Chebyshev polynomial and a $1/x$ function to fit the rise in the background at low angles caused by scatter from the direct beam.

Le Bail refinement is a diffraction pattern profile fitting technique developed by Armel Le Bail based on a least squares analysis. The Le Bail method uses a starting model consisting of the unit cell and space group. The algorithm involves refining unit-cell parameters, instrumental zero, peak width, and the peak intensities to match the observed diffraction pattern. The structure factor and other structural parameters are not considered in Le Bail refinements. Le Bail analysis is commonly a part of Rietveld analysis software, such as GSAS/EXPGUI, FullProf and TOPAS.

Refinements in the system $Sr_{1-3x}Ln_{2x}TiO_3$ were conducted in either $R\bar{3}c$ ($0 < x < 0.2$) or $C2/c$ ($0.2 \leq x \leq 0.25$), while refinements in the system $Ca_{1-3x}Ln_{2x}TiO_3$ ($x < 0.2$) were all conducted in space group *Pnma*. Analogues in the $Pb_{1-3x}La_{2x}TiO_3$ system were refined in either *P*4*mm* ($x < 0.15$) or $Pm\bar{3}m$ ($x = 0.15$). The $Pb_{1-3x}La_{2x}(Zr_{0.6}Ti_{0.4})O_3$ compositions were refined in *R*3*c* ($0 \leq x \leq 0.025$), *P*4*mm* (0.03 ≤

$x \leq 0.05$), or $Pm\bar{3}m$ ($0.06 \leq x \leq 0.1$). The system $Sr_{1-3x}La_{2x}(Mg_{⅓}Nb_{⅔})O_3$ was refined in space group $P\bar{3}m1$, whilst $(Na,K)_{(1-3x)/2}La_{(1+x)/2}(Mg_{½}W_{½})O_3$ was refined in $P2_1/m$.

Samples for transmission electron microscopy (TEM) were first pressed into cylindrical pellets and sintered in flowing oxygen at 1525 °C for four hours. TEM specimens were then prepared by thinning pellets to electron transparency using conventional ceramographic techniques followed by ion thinning (Model 600, Gatan, Pleasanton, CA) to electron transparency for observation in the TEM (JEM-2100HR, JEOL, Tokyo, Japan).

2.4 Results and Discussion

2.4.1 Perovskites Generally

In order to develop a workable model for the effect of A-site vacancies in perovskites, one must first start by assuming that r_B remains unaffected by A-site doping (a reasonable approximation), then the effective value of r_X can be calculated from a pseudocubic lattice constant (derived from refined *real* lattice constants) as:

$$r_O = \frac{a_{pc,exptl}}{2} - r_B \tag{2.4}$$

$$r_A = \frac{a_{pc,exptl}}{\sqrt{2}} - r_O = \left(\frac{\sqrt{2}-1}{2}\right) a_{pc} + r_B \tag{2.5}$$

The ratio of r_X (from equation 2.4) to $r_{X(id)}$ as well as the difference between this r_A (from equation 2.5) and $r_{A(id)}$ can be quantified using the same data set used by Ubic, [7] as shown graphically in Figure 1.

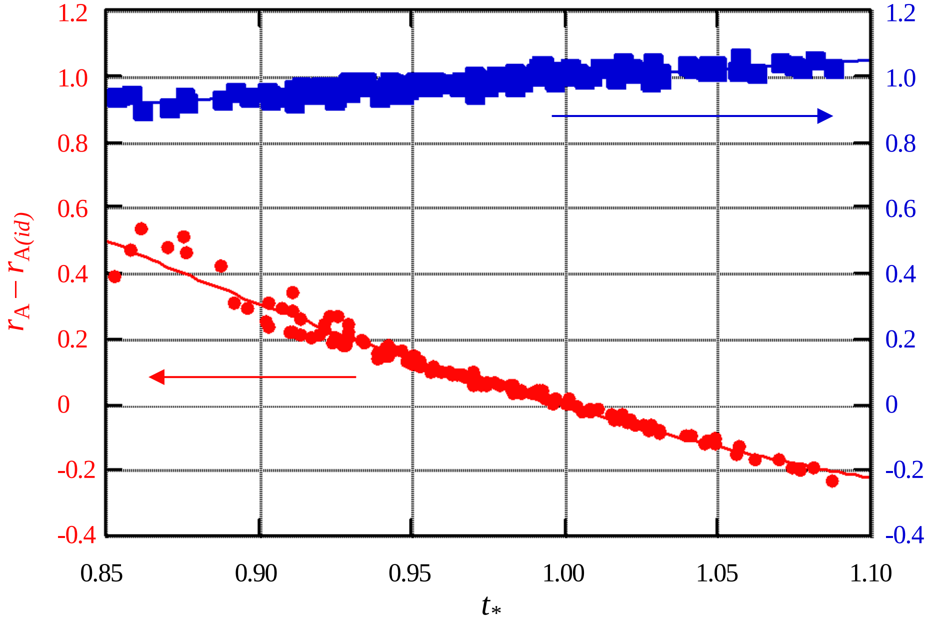

Figure 2.1 Non-ideality of the effective A- and X-site sizes calculated for the 132 compositions reported in reference [7].

The equations which describe this behavior are:

$$\frac{r_X}{r_{X(id)}} = 0.43269 + 0.56393 t_* \quad (R^2 = 0.80439) \tag{2.6}$$

$$r_A - r_{A(id)} = 7.4801 - 12.3139 t_* + 4.8257 t_*^2 \quad (R^2 = 0.97079) \tag{2.7}$$

The values of R^2 indicate the goodness of fit. As figure 2.2 and equation (2.6) show, the fit for $r_X/r_{X(id)}$ can be improved significantly by using t_1 (equaiton (2.3)) rather than t_* (equation (1.8)), but as t_1 requires a foreknowledge of a_{pc}, it cannot be used as an input for a predictive model.

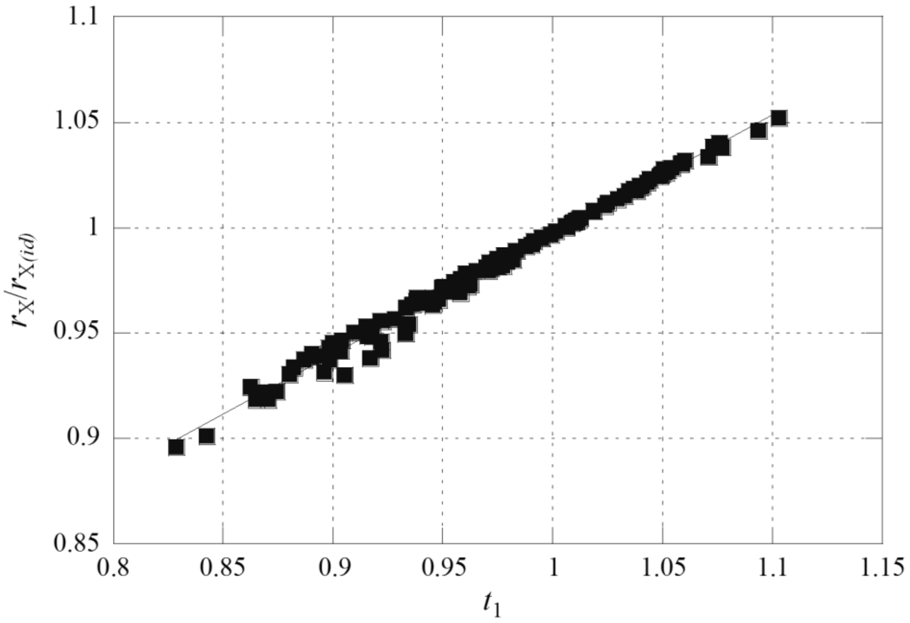

Figure 2.2 Non-ideality of the effective anion size as a function of t_1 (equation (2.3)) calculated for the 132 compositions reported in reference [7].

The equation which describes this behavior is:

$$\frac{r_X}{r_{X(id)}} = 0.42983 + 0.56696 t_1 \quad (R^2 = 0.99548) \tag{2.8}$$

For compositions without stoichiometric vacancies, $t_{BV} \sim t_1$, so it would be possible in theory to use bond-valence parameters instead of t_1 to refine r_X and ultimately a_{pc} in the cases where bond-valence parameters are known. Unfortunately, using this method as a predictive model is complicated by the fact that, in the cases where bond-valence parameters are known, multiple r_0 values have been reported, making predications ambiguous at best. Where such predictions are possible for the data points shown in Figs. 1 and 2, the average relative error is >1% - not as good as that achieved with equation (2.1).

In the unique case for which $t_* = 1$, $r_A = r_{A(id)}$ so the difference $r_A - r_{A(id)} = 0$; and $r_X = r_{X(id)}$ so the ratio $r_X/r_{X(id)} = 1$. In the cases where $t_* < 1$, A-X bonds are stretched whilst B-X bonds are compressed, resulting in underestimations in a'_{pc} (equation (1.3)) but overestimations in a''_{pc} (equation (1.4)). This effect can be interpreted, for the purposes of this model, as a large increase in r_A and a simultaneous smaller decrease in r_X. Conversely, when $t_* > 1$, it is A-X bonds which are compressed and B-X bonds which are stretched, an effect interpreted in this model as an increase in r_X and a simultaneous larger decrease in r_A (Fig. 2.1).

Because of this stretching/compressing, it is not strictly possible to use only ideal values for effective ionic radii to calculate a_{pc} in most real perovskites; however, because equation (2.3) is explicitly a function of a_{pc}, t_1 accounts for the effective ionic size variation as well as the effects of any non-stoichiometry, which is why it is more accurate than equation (1.8) at predicting structure.

It is now possible to revise equation (2.2) to account for the general non-ideal nature of both the A site and anion size. In fact, as a_{pc} is much more sensitive to the B-X bond length than to the A-X bond length, it is only necessary to combine equations (1.4) and (2.6) to yield a model with an average relative error of 0.74%:

$$a''_{pc} = 2\left[r_B + r_{X(id)}\left(0.43269 + 0.56393t_*\right)\right] \quad (R^2 = 0.99354) \qquad (2.9)$$

The results are shown in figure 3.

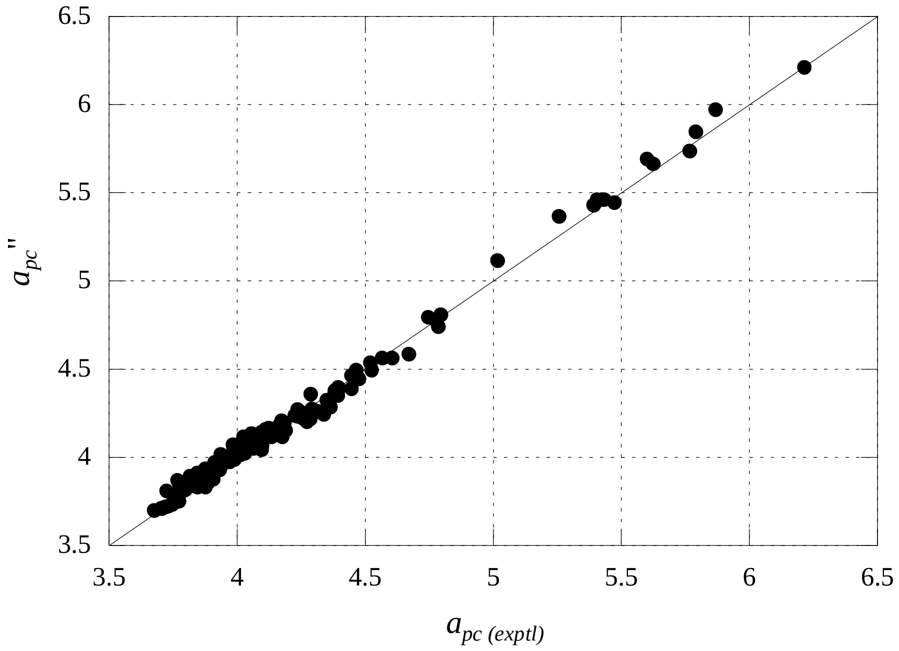

Figure 2.3 Calculated values of a''_{pc} (equation (2.9)) vs experimental values.

Equation (2.9) can also be re-arranged as:

$$t_2 = \frac{a''_{pc}/2 - r_{\mathrm{B}}}{0.56393 r_{\mathrm{X}(id)}} - 0.76728 \tag{2.10}$$

which yields results very similar to those of equation (2.3). Like t_1 (equation (2.3)), t_2 (equation (2.10)) is explicitly a function of a_{pc}, which accounts for both the effective ionic size variation (figure 2.1) as well as the effects of any non-stoichiometry; however, also like equation (2.3), it requires the foreknowledge of a_{pc} and so cannot be used in a predictive model.

2.4.2 Application to $A^{2+}_{1\text{-}3x}A^{3+}_{2x}B^{4+}X^{2-}_{3}$ Perovskites

All of the compositions processed were verified to be single-phase via x-ray diffraction. The results of Le Bail refinements of all the compositions produced in this work are shown in Tables 1 - 6 supplemented with additional data from open literature. In all cases involving non-cubic crystal systems, pseudocubic lattice constants were calculated using equation (1.6)

In agreement with previous work on $Sr_{1-3x}Ce_{2x}TiO_3$, [19] superlattice reflections consistent with an $a^-a^-a^-$ tilt system in $R\bar{3}c$ were observed here for $Sr_{1-3x}Nd_{2x}TiO_3$ (Fig. 4), and using the curve derived elsewhere, [8] the tilt angle about the pseudocubic [111] can be estimated at just 0.2° for $x = 0.01$, reaching 2.6° by $x = 0.2$.

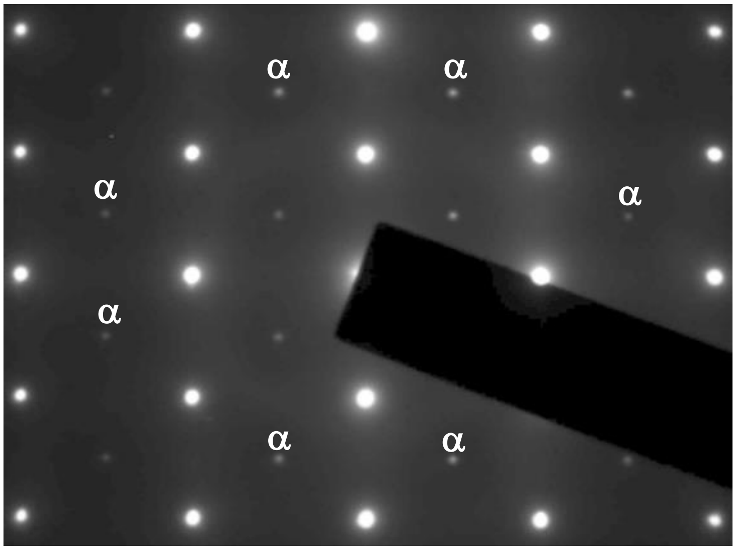

Figure 2.4 Selected-area electron-diffraction pattern of Sr0.97Nd0.02TiO3 parallel to the pseudocubic [110] showing α superlattice reflections consistent with an a-a-a- tilt system in space group $R\bar{3}c$**.**

Table 2.2 $Ca_{1-3x}Nd_{2x}TiO_3$ refinement results, where *Z* is the number of formula units per unit cell.

Composition	SG	*a* (Å)	*b* (Å)	*c* (Å)	Z	$a_{pc(exptl)}$ (Å)
$CaTiO_3$†	*Pnma*	5.4425	7.6410	5.3805	4	3.8245
$Ca_{0.97}La_{0.02}TiO_3$	*Pnma*	5.4447	7.6536	5.3911	4	3.8296
$Ca_{0.94}La_{0.04}TiO_3$	*Pnma*	5.4434	7.6500	5.3891	4	3.8282
$Ca_{0.91}La_{0.06}TiO_3$	*Pnma*	5.4454	7.6577	5.3960	4	3.8316
$Ca_{0.7}La_{0.2}TiO_3$	*Pnma*	5.4454	7.6784	5.4242	4	3.8417
$Ca_{0.55}La_{0.3}TiO_3$	*Pnma*	5.4462	7.6968	5.4449	4	3.8499
$Ca_{0.4}La_{0.4}TiO_3$	*Pnma*	5.4887	7.7279	5.4666	4	3.8702
$La_{2/3}TiO_3$‡	*I4/mmm*	3.8565	3.8565	24.645	6	3.9384
$Ca_{0.97}Nd_{0.02}TiO_3$	*Pnma*	5.4469	7.6529	5.3899	4	3.8297
$Ca_{0.94}Nd_{0.04}TiO_3$	*Pnma*	5.4459	7.6541	5.3908	4	3.8299
$Ca_{0.91}Nd_{0.06}TiO_3$	*Pnma*	5.4459	7.6548	5.3937	4	3.8307
$Ca_{0.85}Nd_{0.1}TiO_3$	*Pnma*	5.4510	7.6632	5.40145	4	3.8351
$Ca_{0.97}Y_{0.02}TiO_3$	*Pnma*	5.4422	7.6421	5.3814	4	3.8248
$Ca_{0.94}Y_{0.04}TiO_3$	*Pnma*	5.4466	7.6490	5.3859	4	3.8280
$Ca_{0.85}Y_{0.1}TiO_3$	*Pnma*	5.4457	7.6381	5.3734	4	3.8230

† = [44]
‡ = [36]

Table 2.3 $Sr_{1-3x}Ln_{2x}TiO_3$ refinement results, where Z is the number of formula units per unit cell.

Composition	SG	a (Å)	b (Å)	c (Å)	β	Z	$a_{pc(exptl)}$ (Å)
$SrTiO_3$†	$Pm\bar{3}m$	3.9050	3.9050	3.9050	90°	1	3.9050
$Sr_{0.97}La_{0.02}TiO_3$	$R\bar{3}c$	5.5255	5.5255	13.5388	90°	6	3.9075
$Sr_{0.85}La_{0.1}TiO_3$	$R\bar{3}c$	5.5201	5.5201	13.5248	90°	6	3.9036
$Sr_{0.7}La_{0.2}TiO_3$	$R\bar{3}c$	5.5124	5.5124	13.5085	90°	6	3.8984
$Sr_{0.55}La_{0.3}TiO_3$	$R\bar{3}c$	5.5078	5.5078	13.4886	90°	6	3.8943
$Sr_{0.5}La_{0.33}TiO_3$	$R\bar{3}c$	5.5062	5.5062	13.4834	90°	6	3.8931
$Sr_{0.4}La_{0.4}TiO_3$	$C2/c$	9.5340	5.5005	5.5007	125.26°	4	3.8905
$Sr_{0.33}La_{0.44}TiO_3$	$C2/c$	9.5261	5.4995	5.5036	125.29°	4	3.8894
$Sr_{0.25}La_{0.5}TiO_3$	$C2/c$	9.5214	5.4969	5.4993	125.28°	4	3.8872
$La_{2/3}TiO_3$‡	$I4/mmm$	3.8565	3.8565	24.645	90°	6	3.9384
$Sr_{0.97}Nd_{0.02}TiO_3$	$R\bar{3}c$	5.5247	5.5247	13.5340	90°	6	3.9067
$Sr_{0.94}Nd_{0.04}TiO_3$	$R\bar{3}c$	5.5202	5.5202	13.5218	90°	6	3.9034
$Sr_{0.91}Nd_{0.06}TiO_3$	$R\bar{3}c$	5.5196	5.5196	13.5192	90°	6	3.9028
$Sr_{0.8}Ce_{0.13}TiO_3$*	$R\bar{3}c$	5.5091	5.5091	13.5071	90°	6	3.8967
$Sr_{0.75}Ce_{0.17}TiO_3$*	$R\bar{3}c$	5.5062	5.5062	13.4989	90°	6	3.8946
$Sr_{0.63}Ce_{0.25}TiO_3$*	$R\bar{3}c$	5.5005	5.5005	13.4797	90°	6	3.8900
$Sr_{0.4}Ce_{0.4}TiO_3$**	$C2/c$	9.5228	5.4869	5.4818	125.22°	4	3.8819

† = [45]
‡ = [36]
* = [14]
** = [8]

Table 2.4 $Pb_{1-3x}La_{2x}TiO_3$ refinement results, where *Z* is the number of formula units per unit cell.

Composition	SG	*a* (Å)	*b* (Å)	*c* (Å)	Z	$a_{pc(exptl)}$ (Å)
$PbTiO_3^{\dagger}$	*P*4*mm*	3.9039	3.9039	4.1348	1	3.9794
$Pb_{0.93}La_{0.05}TiO_3^{*}$	*P*4*mm*	3.9099	3.9099	4.0712	1	3.9629
$Pb_{0.85}La_{0.1}TiO_3^{*}$	*P*4*mm*	3.9139	3.9139	4.0337	1	3.9534
$Pb_{0.82}La_{0.12}TiO_3$	*P*4*mm*	3.9174	3.9174	4.0194	1	3.9511
$Pb_{0.78}La_{0.15}TiO_3^{*}$	*P*4*mm*	3.9207	3.9207	4.0007	1	3.9472
$Pb_{0.7}La_{0.2}TiO_3^{*}$	*P*4*mm*	3.9185	3.9185	3.9647	1	3.9338
$Pb_{0.63}La_{0.25}TiO^{*}{}_{3}$	*P*4*mm*	3.9279	3.9279	3.947	1	3.9343
$Pb_{0.55}La_{0.3}TiO_3^{*}$	$Pm\bar{3}m$	3.9283	3.9283	3.9283	1	3.9283
$La_{2/3}TiO_3^{\ddagger}$	*I4/mmm*	3.8565	3.8565	24.645	6	3.9384

† = [46]
‡ = [36]
* = [23]

Table 2.5 $Ba_{1-3x}La_{2x}TiO_3$ refinement results, where *Z* is the number of formula units per unit cell.

Composition	SG	*a* (Å)	*b* (Å)	*c* (Å)	Z	$a_{pc(exptl)}$ (Å)
$BaTiO_3^{\dagger}$	*P*4*mm*	3.994	3.994	4.038	1	4.0086
$Ba_{0.97}La_{0.02}TiO_3$	*P*4*mm*	4.009781	4.009781	4.004798	1	4.0081
$Ba_{0.94}La_{0.04}TiO_3$	*P*4*mm*	4.004346	4.004346	4.012112	1	4.0069
$Ba_{0.91}La_{0.06}TiO_3$	*P*4*mm*	4.005401	4.005401	4.008477	1	4.0064
$Ba_{0.88}La_{0.08}TiO_3$	*P*4*mm*	4.002055	4.002055	3.999579	1	4.0012
$La_{2/3}TiO_3^{\ddagger}$	*I4/mmm*	3.8565	3.8565	24.645	6	3.9384

† = [47]
‡ = [36]

Table 2.6 $Pb_{1-3x}La_{2x}(Zr_{0.6}Ti_{0.4})O_3$ refinement results, where *Z* is the number of formula units per unit cell.

Composition[a]	SG	*a* (Å)	*b* (Å)	*c* (Å)	Z	$a_{pc(exptl)}$ (Å)
$PbZr_{0.6}Ti_{0.4}O_3$	$R3c$	5.7587	5.7587	14.2390	6	4.0848
$Pb_{0.997}La_{0.002}Zr_{0.6}Ti_{0.4}O_3$	$R3c$	5.7533	5.7533	14.2298	6	4.0814
$Pb_{0.9955}La_{0.003}Zr_{0.6}Ti_{0.4}O_3$	$R3c$	5.7539	5.7539	14.2225	6	4.0809
$Pb_{0.9925}La_{0.005}Zr_{0.6}Ti_{0.4}O_3$	$R3c$	5.7525	5.7525	14.2224	6	4.0803
$Pb_{0.9895}La_{0.007}Zr_{0.6}Ti_{0.4}O_3$	$R3c$	5.7525	5.7525	14.2244	6	4.0805
$Pb_{0.985}La_{0.01}Zr_{0.6}Ti_{0.4}O_3$	$R3c$	5.7531	5.7531	14.2184	6	4.0802
$Pb_{0.97}La_{0.02}Zr_{0.6}Ti_{0.4}O_3$	$R3c$	5.7514	5.7514	14.2021	6	4.0778
$Pb_{0.955}La_{0.03}Zr_{0.6}Ti_{0.4}O_3$	$R3c$	5.7504	5.7504	14.1890	6	4.0761
$Pb_{0.94}La_{0.04}Zr_{0.6}Ti_{0.4}O_3$	$R3c$	5.7514	5.7514	14.1807	6	4.0758
$Pb_{0.925}La_{0.05}Zr_{0.6}Ti_{0.4}O_3$	$R3c$	5.7757	5.7757	14.0706	6	4.0766
$Pb_{0.91}La_{0.06}Zr_{0.6}Ti_{0.4}O_3$	$P4mm$	4.0629	4.0629	4.0942	1	4.0733
$Pb_{0.88}La_{0.08}Zr_{0.6}Ti_{0.4}O_3$	$P4mm$	4.0594	4.0594	4.0943	1	4.0710
$Pb_{0.85}La_{0.1}Zr_{0.6}Ti_{0.4}O_3$	$P4mm$	4.0580	4.0580	4.0910	1	4.0689
$Pb_{0.82}La_{0.12}Zr_{0.6}Ti_{0.4}O_3$	$Pm\bar{3}m$	4.0677	4.0677	4.0677	1	4.0677
$Pb_{0.79}La_{0.14}Zr_{0.6}Ti_{0.4}O_3$	$Pm\bar{3}m$	4.0630	4.0630	4.0630	1	4.0630
$Pb_{0.76}La_{0.16}Zr_{0.6}Ti_{0.4}O_3$	$Pm\bar{3}m$	4.0641	4.0641	4.0641	1	4.0641
$Pb_{0.7}La_{0.2}Zr_{0.6}Ti_{0.4}O_3$	$Pm\bar{3}m$	4.0588	4.0588	4.0588	1	4.0588

a = Nominal compositions are shown. Compositions refined via wavelength-dispersive spectroscopy (WDS) are given in reference [41].

Table 2.7 Refinement results, where *Z* is the number of formula units per unit cell.

Composition	SG	*a* (Å)	*b* (Å)	*c* (Å)	β	Z	$a_{pc(exptl)}$ (Å)
$SrMg_{0.3333}Nb_{0.6667}O_3$†	$P\bar{3}m1$	5.66	5.66	6.98	90	3	4.0114
$Sr_{0.97}La_{0.02}Mg_{0.3333}Nb_{0.6667}O_3$	$P\bar{3}m1$	5.6467	5.6467	6.9344	90	3	3.9964
$Na_{0.5}La_{0.5}(Mg_{0.5}W_{0.5})O_3$‡	$P2_1/m$	5.529	5.532	7.91	90.11	4	3.9254
$Na_{0.3333}La_{0.5556}(Mg_{0.5}W_{0.5})O_3$‡	$P2_1/m$	5.539	5.535	7.912	90.08	4	3.9288
$Na_{0.1667}La_{0.6111}(Mg_{0.5}W_{0.5})O_3$‡	$P2_1/m$	5.533	5.532	7.906	90.05	4	3.9257
$K_{0.5}La_{0.5}(Mg_{0.5}W_{0.5})O_3$‡	$P2_1/m$	5.57	5.571	7.962	90.02	4	3.9529
$K_{0.3333}La_{0.5556}(Mg_{0.5}W_{0.5})O_3$‡	$P2_1/m$	5.565	5.562	7.955	89.99	4	3.9484
$K_{0.1667}La_{0.6111}(Mg_{0.5}W_{0.5})O_3$‡	$P2_1/m$	5.551	5.553	7.937	89.93	4	3.9400

† = [48]
‡ = [49]

In order to apply either equation (1.3) or equation (1.4) to perovskites of the form $A^{2+}_{1-3x}A^{3+}_{2x}B^{4+}X^{2-}_{3}$ which contain stoichiometric extrinsic vacancy concentrations, it is still necessary to first assume that r_B remains identical to the Shannon radius and then to determine appropriate values for r_A and r_X, neither of which will retain their ideal values. [9] In the case of r_A, the effective size contains four distinct components: the ideal (Shannon) size of the A-site cation(s), the bond deformation caused when $t \neq 1$, partial covalency, and the effective size of A-site vacancies. The bond deformation (*i.e.*, stretching/compression) and covalency effect can be calculated as a single parameter from equation (2.7); however, the effective size of vacancies requires additional data.

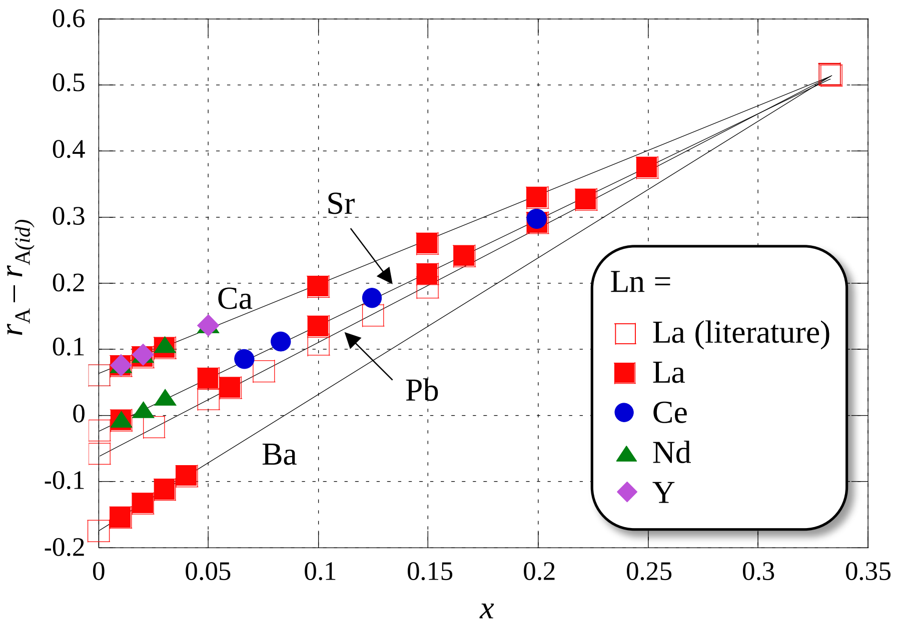

Figure 2.5 Divergence of effective A-site size from ideal (Ca, Sr, Ba, Pb)$_{1-3x}$Ln$_{2x}$TiO$_3$ (Ln = La, Ce, Nd, Y).

In figure 2.5, $r_A - r_{A(id)}$ represents the *sum* of bond deformation, covalency, and effective vacancy size. In all cases data for $La_{2/3}TiO_3$ and all of the $x = 0$ compositions were obtained from the open literature. [36, 44-47] The result is clearly linear for each system, and each line can be generally defined in terms of t_0 (the tolerance factor for that system corresponding to $x = 0$, calculated via equation (1.8)):

$$r_A - r_{A(id)} = (2.4866 - 8.8433t_0 + 7.8922t_0^2)x - 10.249 + 22.492t_0 - 12.223t_0^2$$

(2.11)

It should be noted here that, while a single parameter can conveniently capture both covalency and bond deformation, covalency alone cannot explain the trends observed in figure 2.6. According to Pauling's formula [50] and electronegativity values as revised by Allred, [51] the percent covalency of A-O bonds in $CaTiO_3$, $SrTiO_3$, $PbTiO_3$, and $BaTiO_3$ is 23%, 21%, 73%, and 20%, respectively – clearly inconsistent with the trend illustrated in figure 2.6.

It is also interesting to note that data points corresponding to different trivalent dopants fall on the same line in each system, suggesting that $r_A - r_{A(id)}$ is independent of dopant species; therefore, it is not necessary to normalize by $r_{A(id)}$ as was done in previous work. [9] It is also possible to define these linear trends by using equation (2.7) to define their intercepts (which correspond to the combined effect of bond deformation and covelency) and the common data point at $x = ⅓$ (which corresponds to the composition $La_{⅔}TiO_3$), in which case the following expression is obtained:

$$r_A - r_{A(id)} = (-20.8983 + 36.9417 t_0 - 14.4771 t_0^2)x + \left(7.4801 - 12.3139 t_0 + 4.8257 t_0^2\right) \tag{2.12}$$

The first term on the right-hand side of equation (2.12) corresponds to the vacancy-size effect whilst the second term is recognizable from equation (2.7) as the bond deformation/covalency component. The coefficient of x is the effective vacancy size, r_V, which can be written as:

$$r_V = -20.8796 + 36.9049\, t_0 - 14.4590\, t_0^2 \tag{2.13}$$

and illustrated in figure 2.7.

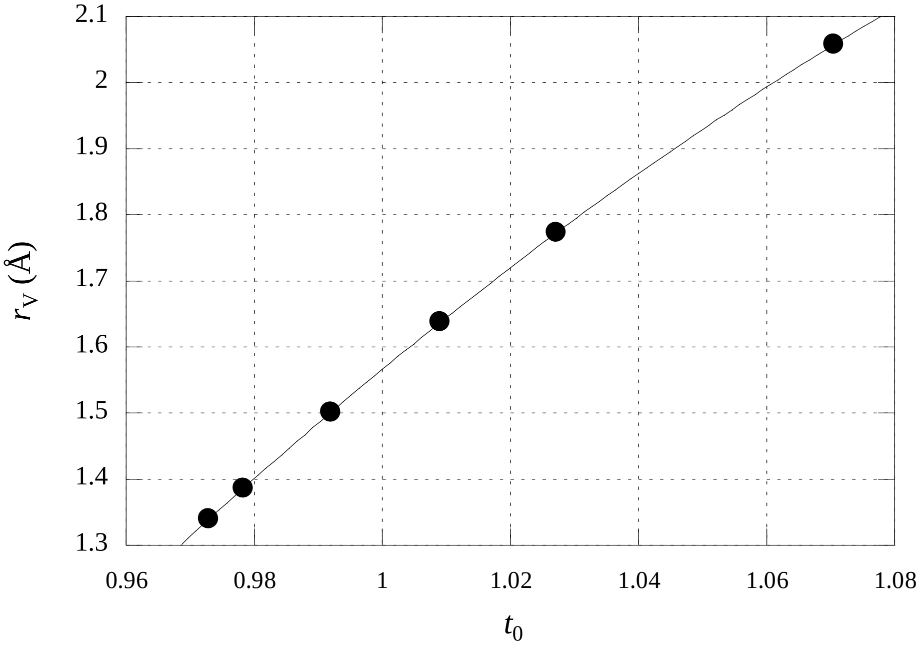

Figure 2.6 Effective vacancy size vs tolerance factor. Data includes $(A_{1-3x}Ln_{2x})TiO_3$. (A = Ca, Sr, Pb, Ba), $(Pb_{1-3x}La_{2x})(Zr_{0.6}Ti_{0.4})O_3$, and $(Sr_{1-3x}La_{2x})(Mg_{⅓}Nb_{⅔})O_3$.

In most cases studied here, $r_V > r_{A^{2+}}$. The exceptions include $CaTiO_3$, in which case $r_{A^{2+}} \sim r_V$, and $Sr(Mg_{⅓}Nb_{⅔})O_3$, in which r_V is slightly smaller than $r_{A^{2+}}$. Equation (2.13) uniquely defines r_V for any $A^{2+}_{1-3x}Ln^{3+}_{2x}BO_3$ perovskite, including complex perovskites.

As shown by equations (2.7) and (2.13), both the bond deformation/covalency and vacancy size for a given system are approximated as functions of t_0 only and do not vary with x in this model. A comparison of $r_{A(id)}$ and r_V in the various systems (A = Ca, Sr, Pb, Ba) is shown in figures 2.7a; and 2.7b shows the same effect but accounting for the bond deformation (BD). As can be seen, all curves in figure 8b tend towards convergence at [V] = 0 with a value of ~1.4 Å, which corresponds well with the ideal size of Sr^{2+} in this coordination (1.44 Å). [52] As $SrTiO_3$ has a tolerance factor extremely close to unity ($t_* = 1.0091$), it seems clear that the effect of bond deformation in undoped samples is to bring the effective tolerance factors as close to unity as possible.

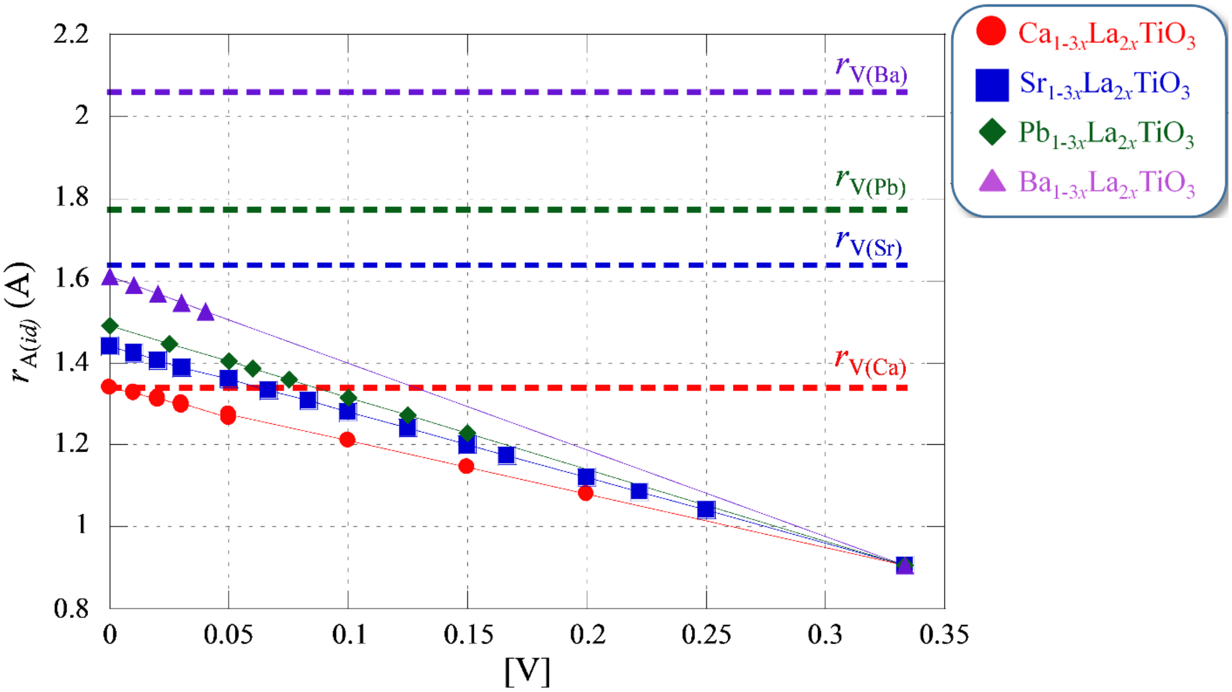

Figure 2.7a The effect of [V] on $r_{A(id)}$ with effective vacancy sizes overlaid.

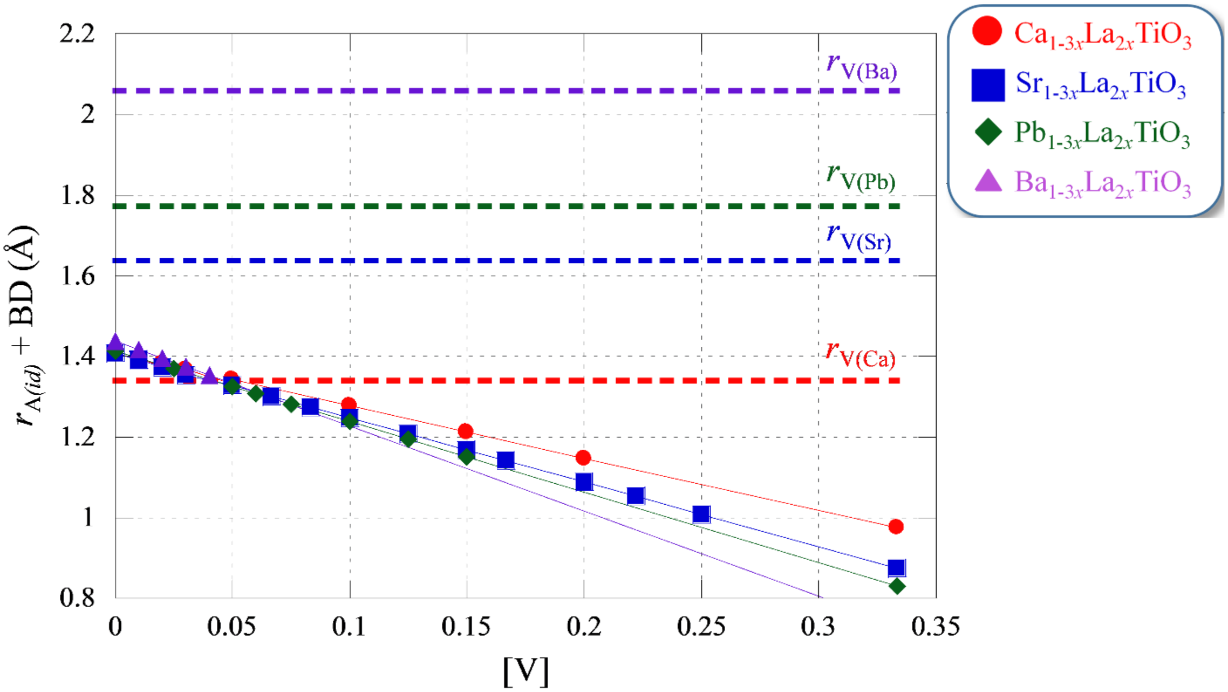

Figure 2.7b The effect of [V] on $r_{A(id)}$ accounting for bond deformation (BD) with effective vacancy sizes overlaid. The convergence at [V] = 0 is at ~1.4 Å, which corresponds well with the ideal size of Sr^{2+} and t_* ~ 1.

As figure 8b demonstrates, in the case of $(Ca_{1-3x}Ln_{2x})TiO_3$, the stretching of A-X bonds means that A-site vacancies allow a very slight pull on coordinating anions for $x \leq 0.05$, as can be demonstrated by their effective size (1.3396 Å) being not only slightly smaller than the Shannon effective ionic radius of Ca^{2+} (1.34 Å) but also smaller than the effective radius of Ca^{2+} including bond deformation/covalency effects (1.3971 Å in $CaTiO_3$). On the other hand, the A-X bonds in $(A_{1-3x}La_{2x})TiO_3$ (A = Sr, Pb, Ba) are rather compressed, resulting in A-site vacancies which always push against coordinating anions, as demonstrated by their effective size (1.6379 Å, 1.7729 Å, 2.0581 Å, respectively) being larger than either Shannon effective ionic radii (1.44 Å, 1.49 Å, 1.61 Å, respectively) or effective radii of A^{2+} ions including bond deformation/covalency effects (1.408 Å, 1.4130 Å, 1.4380 Å, respectively). The larger the $r_{\mathrm{A}^{2+}}$ the larger the push.

The effective size of r_A is now the sum of the three terms:

$$r_\mathrm{A} = r_{\mathrm{A}(id)} + \left(7.4801 - 12.3139\,t_0 + 4.8257\,t_0^2\right) - (20.8983 - 36.9417\,t_0 + 14.4771\,t_0^2)x \tag{2.14}$$

In order to calculate the appropriate values of r_X to use in equations (1.3) and (1.4) for defective perovskites, equation (2.6) can be used; however, it then becomes necessary to define an appropriate expression for t. Using t_* for defective perovskites results in large errors. As it happens, using either t_1 (Eq. (2.3)) or t_2 (Eq. (2.10)) works very well because both incorporate the effects of bond deformation/covalency and vacancies, but both also require pre-knowledge of a_{pc}. What is required, is a way to relate t_1 (or t_2) to t_*. Such a relationship can be defined as shown in figure 2.9.

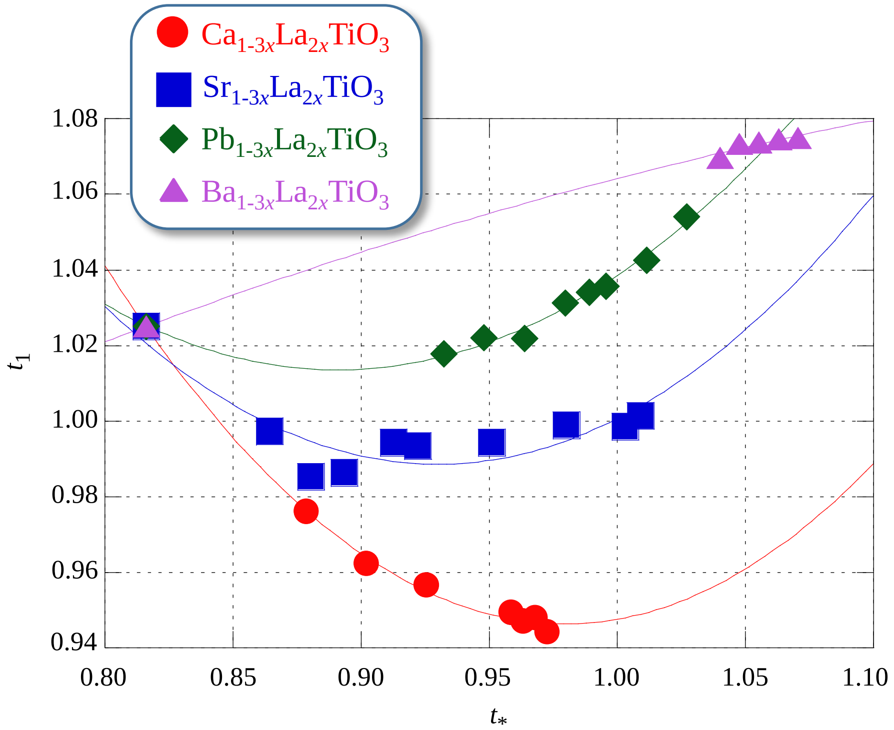

Figure 2.8 Relationship between t_1 (equation (2.3)) and t_* (equation (1.8)) in $A_{1-3x}La_{2x}TiO_3$. (A = Ca, Sr, Pb, Ba).

Each curve in figure 2.8 can be described as a quadratic equation of the form

$$t_1 = A + B\,t_* + C\,t_*^2 \tag{2.15}$$

The coefficients A, B, and C can be defined in terms of $r_{A(id)}$ for the $x = 0$ compositions $\left(r_{A(id)0}\right)$, as shown in figure 2.9.

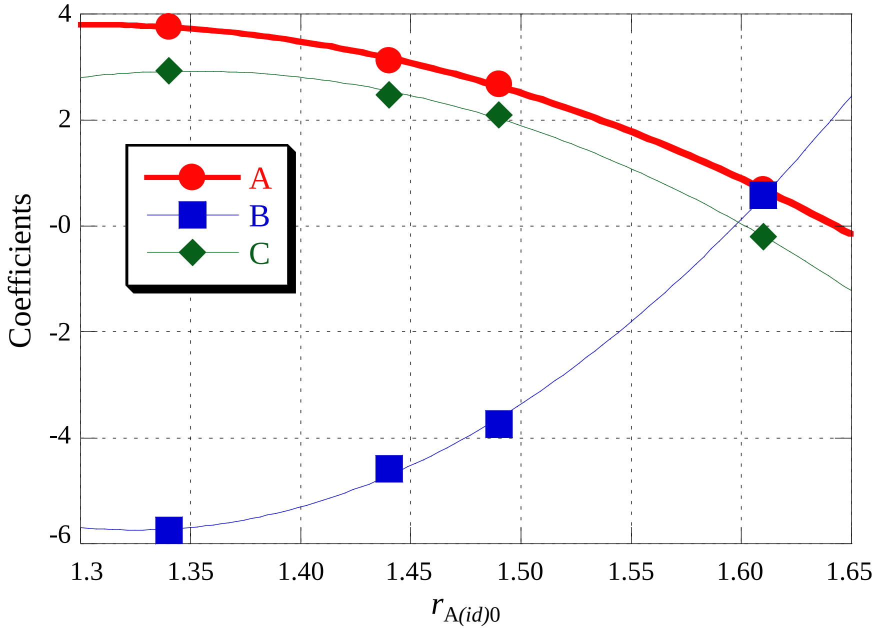

Figure 2.9 Coefficients of the formula $t_1 = A + Bt_* + Ct_*^2$. Data points on each curve correspond to (from left to right) A = Ca, Sr, Pb, and Ba.

The equations which describe these curves are:

$$A = -50.978 + 84.274 r_{A(id)0} - 32.411 r_{A(id)0}^2 \tag{2.16}$$

$$B = 130.35 - 205.44 r_{A(id)0} + 77.539 r_{A(id)0}^2 \tag{2.17}$$

$$C = -81.294 + 124.73 r_{A(id)0} - 46.185 r_{A(id)0}^2 \tag{2.18}$$

According to equation (2.13), when $t_0 = 1$, $r_V = 1.5663$ Å; and $r_V = 0$ only if $t_0 = 0.8465$ (or unrealistically 1.7059). As oxide perovskites with $t_0 <$ ~0.85 have only rarely, if ever, been reported, the value of $t_0 = 0.8465$ may represent the theoretical lower limit for their stability. Compounds with lower values of t_0 would presumably crystallize in the ilmenite system. It is noteworthy again that t_* is a less reliable indicator of structure than is t_1, as the case of geikielite ($MgTiO_3$) demonstrates.

Geikielite takes the ilmenite structure, [53] but using Shannon ionic radii data, including an extrapolation for the twelvefold radius of Mg^{2+} (~1.23 Å), the t_* for this compound would be 0.9341 – well within the tilted perovskite range. Solving equations (1.8), (2.5), and (2.7) simultaneously, a similar value (1.17 Å) can be derived, corresponding to $t_* = 0.9115$, again within the tilted perovskite range. Interestingly, using equations (2.3), (1.3), and (2.8), and the unit cell reported by Dobson and Jacobsen [54] for $MgSiO_3$ (the equations are not valid for the ilmenite structure of $MgTiO_3$), a more realistic ionic radius for Mg^{2+} in twelvefold coordination can be derived (1.12 Å). A very similar value (1.11 Å) can simply be calculated from equation (2.5) using the $MgTiO_3$ unit cell reported by Wechsler and von Dreele [53]. Using either of these values, $t^* = 0.8934$ for $MgTiO_3$, still corresponds to a tilted perovskite. Meanwhile, the t_1 value (equation (2.3)) of $MgTiO_3$ based on the model of Wechsler and von Dreele [53] is just 0.8673, better explaining its ilmenite structure.

With equaitons (2.16-2.18) the correct t_1 vs t_* curve can be calculated and appropriate values of t_1 inserted into equation (2.6), in order to calculate the effective anion size, can in-turn be used in equations (2.3), (1.3), and/or (1.4) to calculate a_{pc} values. For example, figure 10 illustrates the results when equation (2.15) is used to calculate a_{pc} for $A_{1-3x}Ln_{2x}TiO_3$ (A = Ca, Sr, Pb, Ba) and PLZT.

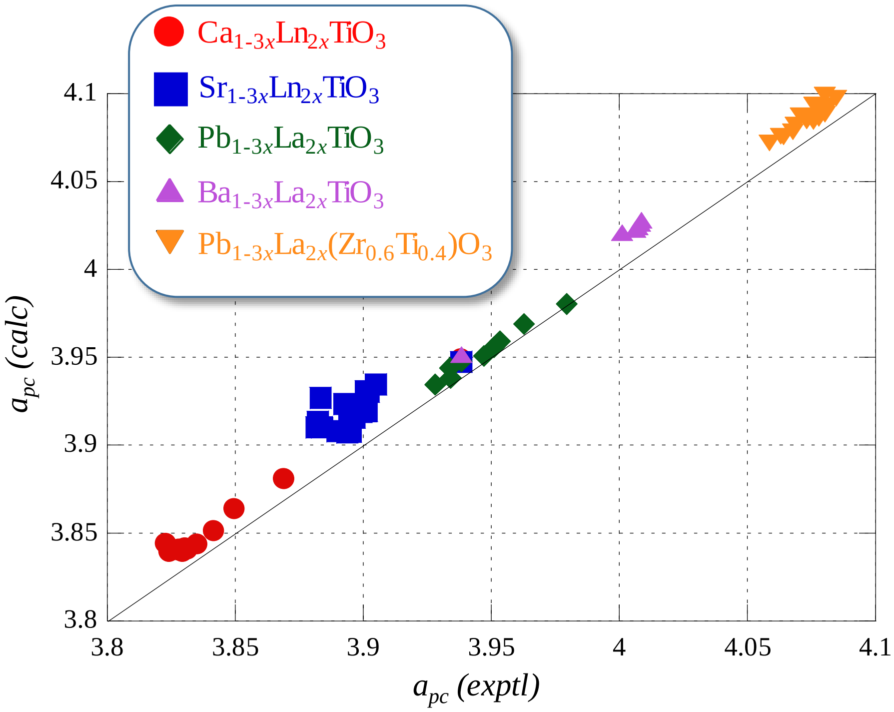

Figure 2.10 Comparison of a_{pc} calculated via equation (2.3) and experimental a_{pc} values. The average relative errors for each series are all < 0.59%.

Values of BD (equation (2.7)), which includes covalency effects, for $A_{1-3x}Ln_{2x}TiO_3$ (A = Ca, Sr, Pb, Ba) and PLZT are 0.0675 Å, -0.0320 Å, -0.0770 Å, and -0.17203 Å, and 0.0135 Å, respectively. Positive values signify A-X stretching while negative values signify A-X compression. The corresponding values of r_V (equation (2.13)) are 1.3396 Å, 1.6379 Å, 1.7729 Å, 2.0581 Å, and 1.5014 Å, respectively. The average relative errors in a_{pc} for each series are all < 0.59% despite the fact that the PLZT end member is not $La_{⅔}TiO_3$ and so equations (2.12-2.18) are not *exactly* applicable.

2.4.3 Second-Order Jahn Teller Distortions

These results seem very straightforward, and equation (2.2) seems adequate in all cases to calculate pseudocubic lattice constants. As Tables 2.8 – 2.10 show, for the

$A_{1-3x}Ln_{2x}TiO_3$ (A = Ca, Sr, Ba) cases, there is little to gain by invoking either equation (1.3) for a'_{pc} or (1.4) for a''_{pc}; however, in other cases the ability to calculate lattice constants as either a function of A-X bond length (a'_{pc},equation (1.3)) *or* B-X bond length $(a''_{pc}$, equation (1.4)) independently can yield further structural information.

Table 2.8 Model values for $Ca_{1-3x}Ln_{2x}TiO_3$

Composition	$a_{pc(exptl)}$ (Å)	r_O (Å)	a_{pc} (Å)	error	a_{pc}’ (Å)	error	a_{pc}” (Å)	error
$CaTiO_3$[†]	3.8245	1.3110	3.8393	0.39%	3.8444	0.52%	3.8320	0.20%
$Ca_{0.97}La_{0.02}TiO_3$	3.8296	1.3112	3.8396	0.26%	3.8453	0.41%	3.8323	0.07%
$Ca_{0.94}La_{0.04}TiO_3$	3.8282	1.3115	3.8402	0.31%	3.8462	0.47%	3.8329	0.12%
$Ca_{0.91}La_{0.06}TiO_3$	3.8316	1.3118	3.8409	0.24%	3.8474	0.41%	3.8337	0.05%
$Ca_{0.7}La_{0.2}TiO_3$	3.8417	1.3173	3.8510	0.24%	3.8590	0.45%	3.8446	0.07%
$Ca_{0.55}La_{0.3}TiO_3$	3.8499	1.3241	3.8636	0.36%	3.8715	0.56%	3.8583	0.22%
$Ca_{0.4}La_{0.4}TiO_3$	3.8702	1.3334	3.8808	0.28%	3.8874	0.45%	3.8769	0.17%
$La_{2/3}TiO_3$[‡]	3.9384	1.3702	3.9489	0.27%	3.9469	0.22%	3.9504	0.30%
$Ca_{0.97}Nd_{0.02}TiO_3$	3.8297	1.3112	3.8397	0.26%	3.8428	0.34%	3.8324	0.07%
$Ca_{0.94}Nd_{0.04}TiO_3$	3.8299	1.3116	3.8404	0.27%	3.8413	0.30%	3.8331	0.08%
$Ca_{0.91}Nd_{0.06}TiO_3$	3.8307	1.3120	3.8412	0.28%	3.8400	0.24%	3.8341	0.09%
$Ca_{0.85}Nd_{0.1}TiO_3$	3.8351	1.3134	3.8437	0.22%	3.8379	0.07%	3.8368	0.04%
$Ca_{0.97}Y_{0.02}TiO_3$	3.8248	1.3112	3.8397	0.39%	3.8423	0.46%	3.8324	0.20%
$Ca_{0.94}Y_{0.04}TiO_3$	3.8280	1.3116	3.8404	0.32%	3.8403	0.32%	3.8332	0.13%
$Ca_{0.85}Y_{0.1}TiO_3$	3.8230	1.3135	3.8439	0.55%	3.8354	0.32%	3.8370	0.36%
AVERAGE RELATIVE ABSOLUTE ERROR				0.31%		0.37%		0.15%

† = [44]
‡ = [36]

Table 2.9 Model values for $Sr_{1-3x}Ln_{2x}TiO_3$

Composition	$a_{pc(exptl)}$ (Å)	r_O (Å)	a_{pc} (Å)	error	a_{pc}' (Å)	error	a_{pc}" (Å)	error
$SrTiO_3$†	3.9050	1.3623	3.9344	0.75%	3.9179	0.33%	3.9347	0.75%
$Sr_{0.97}La_{0.02}TiO_3$	3.9075	1.3604	3.9309	0.60%	3.9157	0.21%	3.9309	0.60%
$Sr_{0.85}La_{0.1}TiO_3$	3.9036	1.3542	3.9193	0.40%	3.9090	0.14%	3.9184	0.38%
$Sr_{0.7}La_{0.2}TiO_3$	3.8984	1.3493	3.9102	0.30%	3.9048	0.16%	3.9086	0.26%
$Sr_{0.55}La_{0.3}TiO_3$	3.8943	1.3476	3.9071	0.33%	3.9051	0.28%	3.9053	0.28%
$Sr_{0.5}La_{0.33}TiO_3$	3.8931	1.3478	3.9075	0.37%	3.9063	0.34%	3.9056	0.32%
$Sr_{0.4}La_{0.4}TiO_3$	3.8905	1.3492	3.9101	0.50%	3.9101	0.50%	3.9085	0.46%
$Sr_{0.33}La_{0.44}TiO_3$	3.8894	1.3510	3.9133	0.62%	3.9137	0.63%	3.9120	0.58%
$Sr_{0.25}La_{0.5}TiO_3$	3.8872	1.3541	3.9191	0.82%	3.9196	0.83%	3.9181	0.80%
$La_{2/3}TiO_3$‡	3.9384	1.3694	3.9474	0.23%	3.9457	0.18%	3.9487	0.26%
$Sr_{0.97}Nd_{0.02}TiO_3$	3.9067	1.3602	3.9305	0.61%	3.9129	0.16%	3.9305	0.61%
$Sr_{0.94}Nd_{0.04}TiO_3$	3.9034	1.3583	3.9269	0.60%	3.9082	0.12%	3.9266	0.59%
$Sr_{0.91}Nd_{0.06}TiO_3$	3.9028	1.3565	3.9236	0.53%	3.9036	0.02%	3.9231	0.52%
$Sr_{0.8}Ce_{0.13}TiO_3$	3.8967	1.3522	3.9156	0.48%	3.9071	0.27%	3.9144	0.45%
$Sr_{0.75}Ce_{0.17}TiO_3$	3.8946	1.3506	3.9126	0.46%	3.9057	0.28%	3.9111	0.42%
$Sr_{0.63}Ce_{0.25}TiO_3$	3.8900	1.3481	3.9079	0.46%	3.9044	0.37%	3.9061	0.41%
$Sr_{0.4}Ce_{0.4}TiO_3$	3.8819	1.3492	3.9101	0.73%	3.9101	0.73%	3.9085	0.68%
AVERAGE RELATIVE ABSOLUTE ERROR				0.52%		0.33%		0.49%

† = [45]
‡ = [36]

Table 2.10 Model values for $Ba_{1-3x}La_{2x}TiO_3$

Composition	$a_{pc(exptl)}$ (Å)	r_O (Å)	a_{pc} (Å)	error	a_{pc}' (Å)	error	a_{pc}'' (Å)	error
$BaTiO_3^*$	4.0086	1.4130	4.0281	0.49%	4.0318	0.58%	4.0359	0.68%
$Ba_{0.97}La_{0.02}TiO_3$	4.0081	1.4120	4.0263	0.45%	4.0297	0.54%	4.0340	0.65%
$Ba_{0.94}La_{0.04}TiO_3$	4.0069	1.4110	4.0245	0.44%	4.0276	0.52%	4.0320	0.63%
$Ba_{0.91}La_{0.06}TiO_3$	4.0064	1.4100	4.0227	0.41%	4.0255	0.48%	4.0301	0.59%
$Ba_{0.88}La_{0.08}TiO_3$	4.0012	1.4090	4.0208	0.49%	4.0233	0.55%	4.0280	0.67%
$La_{2/3}TiO_3^*$	3.9384	1.3717	3.9518	0.34%	3.9491	0.27%	3.9535	0.38%
AVERAGE RELATIVE ABSOLUTE ERROR				0.44%		0.49%		0.60%

† = [47]
‡ = [36]

Table 10 shows the results of Eqs. (2.2 – 1.4) in the $Pb_{1-3x}La_{2x}TiO_3$ system. The absolute relative errors in both $a_{pc}^{'}$ and $a_{pc}^{''}$ are both very low, but while the errors in $a_{pc}^{''}$ are all positive, like those in a_{pc}, those in $a_{pc}^{'}$ are almost all negative. As this anomaly occurs only in $a_{pc}^{'}$, the discrepancy is likely due to an underestimation of r_A rather than r_O or r_B The calculated values of r_A include components from $r_{A(id)}$, bond deformation/covalency, and vacancies. As the last two terms are functions of t_*, all three terms are clearly affected by the value of $r_{\mathrm{Pb}^{2+}_{(id)}}$. An antiferrodistortive instability is unlikely to be the cause of the discrepancy, as it would give rise to octahedral tilting which is forbidden in the *P*4*mm* form of bulk $PbTiO_3$ and which is vanishingly weak in the *R*3*c* form of $Pb(Zr_{0.6}Ti_{0.4})O_3$. In any event, such tilting is present in most of the examples in Tables 2.8 – 2.10 and does not cause anomalies in lattice-constant errors. On the other hand, the ferroelectric distortion in $PbTiO_3$ is much stronger than in, for example, $BaTiO_3$. In $BaTiO_3$, the stretching of octahedra caused by the large size of Ba^{2+} stabilizes the second-order Jahn-Teller (SOJT) distortion of Ti^{4+} (due to its d^0 electronic configuration and octahedral coordination) resulting in a fairly small (~0.06 Å) antiparallel <001> displacement of the cations with respect to the O^{2-} sublattice; however, such ferroelectric displacements do not seem to affect the accuracy of the model or give rise to any anomalies in the errors. In $PbTiO_3$, Pb^{2+} also has a SOJT instability which turns its $6s^2$ valence electrons into a stereoactive lone pair, distorting the ion and consequently the unit cell such that the net displacement of Pb^{2+} and Ti^{4+} with respect to the O^{2-} sublattice is ~0.47 Å and ~0.35 Å, respectively. The larger distortion is observable in the fact that the tetragonality of $PbTiO_3$ ($c/a = 1.0592$) is larger than that of $BaTiO_3$ ($c/a = 1.0046$); however, as the ionic displacements do not seem to adversely affect a_{pc} or a''_{pc} in either case, it is the distortion of the Pb^{2+} ion itself which may explain the negative errors observed in a'_{pc}.

With equation (1.3) it is possible to semiquantify the distortion effect for various structures/ions. In the case of $Pb_{1-3x}La_{2x}TiO_3$, an increase of 0.34% in the radius of Pb^{2+} (~0.0051 Å) in <110> directions (r_{110}) combined with a simultaneous 0.34% decrease in the isotropic radius (r_{iso}) of Pb^{2+} is sufficient to significantly improve the errors on a_{pc}, a'_{pc}, and a''_{pc}, as shown in Table 2.12, with just over half of the errors in a'_{pc} remaining negative. A similar phenomenon can be observed for $Pb_{1-3x}La_{2x}(Zr_{0.6}Ti_{0.4})O_3$ in Table 2.13. In this case BD = 0.0135 Å and $r_V = 1.5014$ Å. While the absolute relative errors in both a_{pc} and a''_{pc} are *all* positive, those in a'_{pc} are *all* negative. Whereas a symmetrical increase in r_A alone results in improvements in a'_{pc}, it also significantly increases errors in both a_{pc} and a''_{pc} (> 0.8%); however, a 1.21% increase in r_{110} (~0.018 Å) combined with a simultaneous 1.28% decrease in r_{iso} is sufficient to significantly improve the errors on a_{pc}, a'_{pc}, and a''_{pc}, as shown in Table 2.14, with fewer than half of the errors in a'_{pc} remaining negative.

The coordinations of Pb^{2+} ions in both $PbTiO_3$ and $Pb(Zr_{0.6}Ti_{0.4})O_3$ are essentially the same (CN = 12), but their site symmetries are quite different. Whereas Pb^{2+} in $PbTiO_3$ has 4*mm* point symmetry at the 1*a* position in space group *P*4*mm*, [22] in $Pb(Zr_{0.6}Ti_{0.4})O_3$ it has point symmetry 3, residing in the 6*a* position of space group *R*3*c*; [28] therefore, it is likely that the difference in point symmetry contributes to the different SOJT distortions of Pb^{2+} in these two cases. The chemistry of the B site also probably plays a part, as both $Pb_{1-3x}La_{2x}TiO_3$ and $Pb_{1-3x}La_{2x}(Zr_{0.6}Ti_{0.4})O_3$ share the same tetragonal or cubic structures for parts of their compositional ranges. While equation (1.3) cannot be used to *predict* this distortion, it can potentially be used to identify and even semiquantify it; and the effect is small enough not to result in large errors anyway, as Tables 2.11 and 2.13 demonstrate.

Table 2.11 Model values for $Pb1_{-3x}La_{2x}TiO_3$

Composition	$a_{pc(exptl)}$ (Å)	r_O (Å)	a_{pc} (Å)	error	a_{pc}' (Å)	error	a_{pc}'' (Å)	error
$PbTiO_3$*	3.9794	1.3871	3.9803	0.02%	3.9601	-0.49%	3.9843	0.12%
$Pb_{0.93}La_{0.05}TiO_3$	3.9629	1.3811	3.9691	0.15%	3.9523	-0.27%	3.9722	0.23%
$Pb_{0.85}La_{0.1}TiO_3$	3.9534	1.3758	3.9593	0.15%	3.9456	-0.20%	3.9616	0.21%
$Pb_{0.82}La_{0.12}TiO_3$	3.9511	1.3739	3.9557	0.12%	3.9432	-0.20%	3.9578	0.17%
$Pb_{0.78}La_{0.15}TiO_3$	3.9472	1.3713	3.9509	0.09%	3.9400	-0.18%	3.9525	0.14%
$Pb_{0.7}La_{0.2}TiO_3$	3.9338	1.3675	3.9439	0.26%	3.9355	0.04%	3.9450	0.28%
$Pb_{0.63}La_{0.25}TiO_3$	3.9343	1.3645	3.9384	0.11%	3.9321	-0.05%	3.9390	0.12%
$Pb_{0.55}La_{0.3}TiO_3$	3.9283	1.3623	3.9343	0.15%	3.9298	0.04%	3.9346	0.16%
$La_{⅔}TiO_3$*	3.9384	1.3696	3.9477	0.24%	3.9460	0.19%	3.9491	0.27%
AVERAGE RELATIVE ABSOLUTE ERROR				0.14%		0.18%		0.19%

* = [46]
** = [36]

Table 2.12 Model values for $Pb_{1-3x}La_{2x}TiO_3$ including SOJT distortion

Composition	$a_{pc(exptl)}$ (Å)	r_O (Å)	a_{pc} (Å)	error	a_{pc}’ (Å)	error	a_{pc}” (Å)	error
$PbTiO_3^*$	3.9794	1.3856	3.9774	-0.05%	3.9651	-0.36%	3.9812	0.04%
$Pb_{0.93}La_{0.05}TiO_3$	3.9629	1.3795	3.9661	0.08%	3.9573	-0.14%	3.9690	0.15%
$Pb_{0.85}La_{0.1}TiO_3$	3.9534	1.3742	3.9563	0.07%	3.9506	-0.07%	3.9584	0.13%
$Pb_{0.82}La_{0.12}TiO_3$	3.9511	1.3723	3.9528	0.04%	3.9482	-0.07%	3.9546	0.09%
$Pb_{0.78}La_{0.15}TiO_3$	3.9472	1.3697	3.9480	0.02%	3.9450	-0.06%	3.9494	0.05%
$Pb_{0.7}La_{0.2}TiO_3$	3.9338	1.3660	3.9411	0.18%	3.9405	0.17%	3.9419	0.21%
$Pb_{0.63}La_{0.25}TiO_3$	3.9343	1.3630	3.9357	0.04%	3.9372	0.08%	3.9361	0.05%
$Pb_{0.55}La_{0.3}TiO_3$	3.9283	1.3609	3.9317	0.09%	3.9350	0.17%	3.9318	0.09%
$La_{2/3}TiO_3^*$	3.9384	1.3695	3.9477	0.23%	3.9531	0.37%	3.9490	0.27%
AVERAGE RELATIVE ABSOLUTE ERROR				0.09%		0.17%		0.12%

* = [46]
** = [36]

Table 2.13 Model values for $Pba_{1-3x}La_{2x}(Zr_{0.6}Ti_{0.4})O_3$

Composition	$a_{pc(exptl)}$ (Å)	r_O (Å)	a_{pc} (Å)	error	a_{pc}' (Å)	error	a_{pc}'' (Å)	error
$PbZr_{0.6}Ti_{0.4}O_3$	4.0848	1.3747	4.0973	0.31%	4.0704	-0.35%	4.0982	0.33%
$Pb_{0.997}La_{0.002}Zr_{0.6}Ti_{0.4}O_3$	4.0814	1.3748	4.0932	0.29%	4.0695	-0.29%	4.0942	0.31%
$Pb_{0.9955}La_{0.003}Zr_{0.6}Ti_{0.4}O_3$	4.0809	1.3749	4.0918	0.27%	4.0710	-0.24%	4.0928	0.29%
$Pb_{0.9925}La_{0.005}Zr_{0.6}Ti_{0.4}O_3$	4.0803	1.3742	4.0993	0.47%	4.0716	-0.21%	4.1002	0.49%
$Pb_{0.9895}La_{0.007}Zr_{0.6}Ti_{0.4}O_3$	4.0805	1.3746	4.0909	0.26%	4.0699	-0.26%	4.0918	0.28%
$Pb_{0.985}La_{0.01}Zr_{0.6}Ti_{0.4}O_3$	4.0802	1.3745	4.0883	0.20%	4.0697	-0.26%	4.0893	0.22%
$Pb_{0.97}La_{0.02}Zr_{0.6}Ti_{0.4}O_3$	4.0778	1.3734	4.0860	0.20%	4.0636	-0.35%	4.0869	0.22%
$Pb_{0.955}La_{0.03}Zr_{0.6}Ti_{0.4}O_3$	4.0761	1.3723	4.0934	0.43%	4.0650	-0.27%	4.0941	0.44%
$Pb_{0.94}La_{0.04}Zr_{0.6}Ti_{0.4}O_3$	4.0758	1.3717	4.0843	0.21%	4.0581	-0.43%	4.0850	0.23%
$Pb_{0.925}La_{0.05}Zr_{0.6}Ti_{0.4}O_3$	4.0766	1.3710	4.0867	0.25%	4.0604	-0.40%	4.0873	0.26%
$Pb_{0.91}La_{0.06}Zr_{0.6}Ti_{0.4}O_3$	4.0733	1.3701	4.0844	0.27%	4.0552	-0.45%	4.0849	0.28%
$Pb_{0.88}La_{0.08}Zr_{0.6}Ti_{0.4}O_3$	4.0710	1.3685	4.0874	0.40%	4.0539	-0.42%	4.0877	0.41%
$Pb_{0.85}La_{0.1}Zr_{0.6}Ti_{0.4}O_3$	4.0689	1.3673	4.0822	0.33%	4.0477	-0.52%	4.0825	0.33%
$Pb_{0.82}La_{0.12}Zr_{0.6}Ti_{0.4}O_3$	4.0677	1.3664	4.0786	0.27%	4.0471	-0.51%	4.0788	0.27%

$Pb_{0.79}La_{0.14}Zr_{0.6}Ti_{0.4}O_3$	4.0630	1.3642	4.0758	0.31%	4.0159	-1.16%	4.0758	0.31%
$Pb_{0.76}La_{0.16}Zr_{0.6}Ti_{0.4}O_3$	4.0641	1.3644	4.0754	0.28%	4.0420	-0.55%	4.0755	0.28%
$Pb_{0.7}La_{0.2}Zr_{0.6}Ti_{0.4}O_3$	4.0588	1.3629	4.0721	0.33%	4.0420	-0.41%	4.0720	0.33%
AVERAGE RELATIVE ABSOLUTE ERROR				0.30%		0.42%		0.31%

Table 2.14 Model values for $Pba1_{-3x}La_{2x}(Zr_{0.6}Ti_{0.4})O_3$ including SOJT distortion

Composition	$a_{pc(exptl)}$ (Å)	r_O (Å)	a_{pc} (Å)	error	a_{pc}’ (Å)	error	a_{pc}” (Å)	error
$PbZr_{0.6}Ti_{0.4}O_3$	4.0848	1.3684	4.0853	0.01%	4.0871	0.06%	4.0857	0.02%
$Pb_{0.997}La_{0.002}Zr_{0.6}Ti_{0.4}O_3$	4.0814	1.3685	4.0813	0.00%	4.0861	0.12%	4.0817	0.01%
$Pb_{0.9955}La_{0.003}Zr_{0.6}Ti_{0.4}O_3$	4.0809	1.3687	4.0798	-0.03%	4.0876	0.16%	4.0803	-0.02%
$Pb_{0.9925}La_{0.005}Zr_{0.6}Ti_{0.4}O_3$	4.0803	1.3680	4.0873	0.17%	4.0882	0.19%	4.0877	0.18%
$Pb_{0.9895}La_{0.007}Zr_{0.6}Ti_{0.4}O_3$	4.0805	1.3683	4.0789	-0.04%	4.0865	0.15%	4.0793	-0.03%
$Pb_{0.985}La_{0.01}Zr_{0.6}Ti_{0.4}O_3$	4.0802	1.3683	4.0764	-0.09%	4.0864	0.15%	4.0768	-0.08%
$Pb_{0.97}La_{0.02}Zr_{0.6}Ti_{0.4}O_3$	4.0778	1.3672	4.0741	-0.09%	4.0802	0.06%	4.0744	-0.08%
$Pb_{0.955}La_{0.03}Zr_{0.6}Ti_{0.4}O_3$	4.0761	1.3660	4.0815	0.13%	4.0816	0.14%	4.0817	0.14%
$Pb_{0.94}La_{0.04}Zr_{0.6}Ti_{0.4}O_3$	4.0758	1.3655	4.0724	-0.08%	4.0748	-0.03%	4.0726	-0.08%
$Pb_{0.925}La_{0.05}Zr_{0.6}Ti_{0.4}O_3$	4.0766	1.3648	4.0748	-0.04%	4.0772	0.01%	4.0749	-0.04%
$Pb_{0.91}La_{0.06}Zr_{0.6}Ti_{0.4}O_3$	4.0733	1.3639	4.0726	-0.02%	4.0719	-0.03%	4.0726	-0.02%
$Pb_{0.88}La_{0.08}Zr_{0.6}Ti_{0.4}O_3$	4.0710	1.3625	4.0757	0.12%	4.0708	0.00%	4.0756	0.11%
$Pb_{0.85}La_{0.1}Zr_{0.6}Ti_{0.4}O_3$	4.0689	1.3613	4.0707	0.04%	4.0647	-0.10%	4.0705	0.04%
$Pb_{0.82}La_{0.12}Zr_{0.6}Ti_{0.4}O_3$	4.0677	1.3604	4.0673	-0.01%	4.0642	-0.09%	4.0670	-0.02%

$Pb_{0.79}La_{0.14}Zr_{0.6}Ti_{0.4}O_3$	4.0630	1.3585	4.0649	0.05%	4.0333	-0.73%	4.0644	0.03%
$Pb_{0.76}La_{0.16}Zr_{0.6}Ti_{0.4}O_3$	4.0641	1.3586	4.0645	0.01%	4.0593	-0.12%	4.0641	0.00%
$Pb_{0.7}La_{0.2}Zr_{0.6}Ti_{0.4}O_3$	4.0588	1.3574	4.0616	0.07%	4.0597	0.02%	4.0610	0.06%
AVERAGE RELATIVE ABSOLUTE ERROR				0.06%		0.13%		0.06%

2.4.4 Effect of B-Site Ordering

This model depends on randomness both in the distribution of vacancies as well as cations. Any kind of chemical ordering (*e.g.*, of vacancies on the A site or cations on the B site) will affect the effective size of the relevant site and so require a new parameter in the model. The effect of chemical ordering on the B-site can be inferred from differences in a'_{pc} and a''_{pc} as well as large errors in a_{pc}. Table 2.15 shows the results for three sets of order double perovskites. In all cases, large positive errors in a''_{pc} are indicative of an overestimation of r_B, causing a consequent overestimation of r_O and hence a''_{pc}. It is well known that ordered structures pack more efficiently than disordered ones, so it follows that an ordered arrangement of cations on the B-site should result in an overall shrinkage which, in terms of this model, is translated into reduced ionic radii for these cations. In the case of $(Sr_{1-3x}La_{2x})(Mg_{⅓}Nb_{⅔})O_3$ (BD = 0.0521 Å, r_V = 1.3858 Å), simply using the weighted average of the size of B-site cations (0.6667 Å) for r_B results in an average errors of 0.92%, 0.46%, 0.90% for a_{pc}, a'_{pc}, and a''_{pc}, as shown in Table 2.15; however, by reducing the value of r_B by just 3.5% to 0.6432 Å, the average errors drop to just 0.15%, 0.58%, and 0.15% for a_{pc}, a'_{pc}, and a''_{pc}, respectively. The effective r_O values simultaneously increase slightly. This 3.5% decrease in the effective r_B value is a measure of the ordering on the B site. Assuming this value corresponds to a fully ordered structure, smaller percent reductions would correspond to smaller degrees of order. This effect could theoretically be calibrated and quantified as an easy means of estimating cation order from lattice constants alone.

A similar analysis is possible in the $(Na,K)_{(1-3x)/2}La_{(1+x)/2}(Mg_{½}W_{½})O_3$ systems reported by Arillo *et al*. [49] Without accounting for r_B shrinkage average errors are quite large for both Na and K analogues, as shown in Table 2.15. By shrinking r_B by 4.6% (to 0.6295 Å) in the case of $Na_{(1-3x)/2}La_{(1+x)/2}(Mg_{½}W_{½})O_3$ (BD = 0.1103 Å, r_V = 1.2112 Å) and 13.7% (to 0.5694 Å) in the case of $K_{(1-3x)/2}La_{(1+x)/2}(Mg_{½}W_{½})O_3$ (BD = -0.0150 Å, rV = 1.5871 Å), average errors are drastically reduced, as shown in Table 2.16. It is unclear why different amounts of shrinkage are required in these two analogous systems with the same B-site composition unless they are indeed ordered to different degrees, which seems unlikely given the size and charge differences involved. A potential complicating factor in these cases is that $Na_{½}La_{½}(Mg_{½}W_{½})O_3$ is typically reported [55, 56] with cation ordering on *both* A and B sublattices. It is unclear how the effect of A-site order influences the model, but it may have the same shrinkage effects as B-site ordering. Because of the dependence of both a'_{pc} and a''_{pc} on r_O, which itself is a function of t_1 and so ultimately both $r_{A(id)}$ and r_B, it is not possible to independently solve for the effects of order on both sublattices simultaneously. Although the model proposed can be used in this way to explain and even semiquantify B-site ordering, it cannot yet be used to predict the effect of such ordering on a_{pc} or structure.

Table 2.15 Model values

Composition	$a_{pc(exptl)}$ (Å)	r_O (Å)	a_{pc} (Å)	error	a_{pc}' (Å)	error	a_{pc}'' (Å)	error
$SrMg_{0.3333}Nb_{0.6667}O_3$	4.0114	1.3538	4.0418	0.76%	4.0246	0.33%	4.0409	0.74%
$Sr_{0.97}La_{0.02}Mg_{0.3333}Nb_{0.6667}O_3$	3.9964	1.3526	4.0396	1.08%	4.0199	0.59%	4.0385	1.06%
AVERAGE RELATIVE ABSOLUTE ERROR				0.92%		0.46%		0.90%
$Na_{0.5}La_{0.5}(Mg_{0.5}W_{0.5})O_3$*	3.9254	1.3320	3.9871	1.57%	3.9843	1.50%	3.9841	1.50%
$Na_{0.3333}La_{0.5556}(Mg_{0.5}W_{0.5})O_3$*	3.9288	1.3361	3.9948	1.68%	3.9596	0.78%	3.9922	1.61%
$Na_{0.1667}La_{0.6111}(Mg_{0.5}W_{0.5})O_3$*	3.9257	1.3532	4.0274	2.59%	3.9533	0.70%	4.0265	2.57%
AVERAGE RELATIVE ABSOLUTE ERROR				1.95%		1.00%		1.89%
$K_{0.5}La_{0.5}(Mg_{0.5}W_{0.5})O_3$*	3.9529	1.4065	4.1288	4.45%	4.0892	3.45%	4.1330	4.56%
$K_{0.3333}La_{0.5556}(Mg_{0.5}W_{0.5})O_3$*	3.9484	1.3998	4.1160	4.24%	4.0494	2.56%	4.1196	4.33%
$K_{0.1667}La_{0.6111}(Mg_{0.5}W_{0.5})O_3$*	3.9400	1.3860	4.0898	3.80%	3.9996	1.51%	4.0920	3.86%
AVERAGE RELATIVE ABSOLUTE ERROR				4.16%		2.50%		4.25%

* = [49]

Table 2.16 Model values accounting for the effect of B-site ordering

Composition	$a_{pc(exptl)}$ (Å)	r_O (Å)	a_{pc} (Å)	error	a_{pc}’ (Å)	error	a_{pc}” (Å)	error
$SrMg_{0.3333}Nb_{0.6667}O_3$	4.0114	1.3565	3.9999	-0.29%	3.9825	-0.72%	3.9993	-0.30%
$Sr_{0.97}La_{0.02}Mg_{0.3333}Nb_{0.6667}O_3$	3.9964	1.3551	3.9972	0.02%	3.9788	-0.44%	3.9964	0.00%
AVERAGE RELATIVE ABSOLUTE ERROR				0.15%		0.58%		0.15%
$Na_{0.5}La_{0.5}(Mg_{0.5}W_{0.5})O_3$*	3.9254	1.3332	3.9289	0.09%	3.9234	-0.05%	3.9254	0.00%
$Na_{0.3333}La_{0.5556}(Mg_{0.5}W_{0.5})O_3$*	3.9288	1.3338	3.9301	0.03%	3.9147	-0.36%	3.9267	-0.05%
$Na_{0.1667}La_{0.6111}(Mg_{0.5}W_{0.5})O_3$*	3.9257	1.3480	3.9566	0.79%	3.9251	-0.02%	3.9549	0.75%
AVERAGE RELATIVE ABSOLUTE ERROR				0.30%		0.14%		0.27%
$K_{0.5}La_{0.5}(Mg_{0.5}W_{0.5})O_3$*	3.9529	1.4071	3.9442	-0.22%	3.9287	-0.61%	3.9529	0.00%
$K_{0.3333}La_{0.5556}(Mg_{0.5}W_{0.5})O_3$*	3.9484	1.4049	3.9402	-0.21%	3.9490	0.02%	3.9485	0.00%
$K_{0.1667}La_{0.6111}(Mg_{0.5}W_{0.5})O_3$*	3.9400	1.3949	3.9222	-0.45%	3.9584	0.47%	3.9287	-0.29%
AVERAGE RELATIVE ABSOLUTE ERROR				0.29%		0.36%		0.10%

* = [49]

2.4.5 Anomalies

This same model can be used successfully to analyze the vacancy behavior of other systems previously reported in the literature as well. For example, Ruiz *et al.* [57] reported that the cell volume of $Na_{(1-3x)/2}La_{(1+x)/2}TiO_3$ (Table 2.17) seemed to *increase* slightly as the number of vacancies increased from 5.3% to 17.3% whilst the degree of tilt simultaneously *decreased* (see Chapter 3). Equation (2.13) shows that in either case r_V = 1.6379 Å, which is larger than either the weighted average of Shannon radii or the effective radius including bond distortion/covalency, suggesting that vacancies push against anions. The bond deformation (equation (2.7)) in this system is -0.0320 Å. The unit-cell expansion was previously explained [8, 9] by an increased effective r_V; however, it can now be understood more completely as an increase in xr_V (*i.e.*, the contribution of vacancies to r_A). With a constant r_V = 1.6379 Å, xr_V increases from 0.0868 Å (x = 0.053) to 0.2834 (x = 0.173). It was also previously reported [8, 9] that $\bar{r}_O$ simultaneously decreased slightly; however, it can now be shown that $\bar{r}_O$ actually *increases* slightly from 1.3348 Å to 1.3446 Å, further contributing to the increase in lattice constant The effective increase in r_A also explains why the tolerance factor (t_1) is higher for x = 0.173 (t_1 = 0.9800) than for x = 0.053 (t_1 = 0.9784), thus further explaining why the degree of tilt was seen to decrease with increasing vacancy concentration. Pseudocubic lattice constants calculated with this model are accurate to an average absolute relative error of 0.24% (a_{pc}) and 0.14% (a_{pc}”).

Table 2.17 Model values for $Na_{(1-3x)/2}La_{(1+x)/2}TiO_3$

Composition	$a_{pc(exptl)}$ (Å)	r_O (Å)	a_{pc} (Å)	error %	a_{pc}' (Å)	error %	a_{pc}'' (Å)	error %
$Na_{0.5}La_{0.5}TiO_3$*	3.8742	1.3348	3.8835	0.24	3.8670	-0.19	3.8663	-0.20
$Na_{0.42}La_{0.5267}TiO_3$**	3.8727	1.3320	3.8783	0.14	3.8677	-0.13	3.8626	-0.26
$Na_{0.24}La_{0.5867}TiO_3$**	3.8754	1.3374	3.8882	0.34	3.8860	0.28	3.8782	0.07
$Na_{0.1625}La_{0.6125}TiO_3$**	3.8753	1.3446	3.9016	0.68	3.9011	0.66	3.8950	0.51
AVERAGE RELATIVE ABSOLUTE ERROR				0.24		0.32		0.26

* = [58]
** = [57]

What can also be seen in Table 2.17 are fairly large relative errors in a'_{pc} which are not only all negative but which decrease (*i.e.*, become less negative) as x increases. A large error in a'_{pc} without a correspondingly large error in a''_{pc} might be attributable to an underestimation of r_A, but the cause of such an underestimation is unclear and is investigated/discussed further in Chapter 3. The effective r_A of $(Na,K)_{(1-3x)/2}La_{(1+x)/2}(Mg_{½}W_{½})O_3$ was calculated from Shannon data and used with accuracy in Table 2.16, so the difference in the case of $La_{(1+x)/2}Na_{(1-3x)/2}TiO_3$ presumably lies in a structural difference between these two systems rather than a purely chemical one. Ordering is the natural hypothesis, especially given that the errors in a'_{pc} decrease (become less negative) as the stoichiometry moves away from the 1:1 ratio of La:Na, where the order would be expected to break down; however, that explanation requires a volume *increase* upon ordering, which does not agree with conventional wisdom. Nevertheless, by increasing the total r_A by 0.0498 Å (~3.6%) at x = 0, a minimum in the absolute error occurs with the relative error just -0.30%. Smaller increases in r_A of

0.0494 Å , 0.0207 Å , and 0.0002 Å as x increases to 0.0533, 0.1733, and 0.225, respectively, are required to yield errors of 0.00%. The physical explanation for these seemingly anomalous observations is still unclear.

2.4.6 Crystal Chemistry of Vacancies

It might be noted that the compound $La_{2/3}TiO_3$ appears in Tables 2.8-2.11 but with slightly different values of a_{pc}, a'_{pc}, and a''_{pc}. This compound corresponds to the end member $x = 1/3$ so can be attributed to *any* $(Ca, Sr, Pb, Ba)_{1-3x}La_{2x}TiO_3$ system, each with its own effective bond deformations and r_V values. All such compositional families converge here. As there *are no* divalent species in this unique case, it no longer makes sense to interpret bond deformation values as A^{2+}-O bond deformation or covalency, as there *is no* A^{2+} present; and r_V values become notional.

For all $ATiO_3$ (A=Ca, Sr, Pb, Ba) perovskites, the effective vacancy size scales not only with A cation size but also with A cation bond valence sum (2.08, 2.11, 2.12, 2.74 for A = Ca, Sr, Pb, Ba, respectively). Vacancies obviously decrease the bond valence of coordinating anions, so the push can help restore their bond valence sum (BV) by reducing the other bond lengths. These results are somewhat counterintuitive, as the difference in cationic sizes would mean that coordinating anions in $CaTiO_3$ would be much closer to the A site than those in $BaTiO_3$. As a consequence, A-site vacancies might be expected to push anions away in $CaTiO_3$ due to Coloumbic repulsion ($r_V > r_A$) but allow overbonded anions to relax towards the vacant site ($r_V < r_A$) in $BaTiO_3$. Instead, it seems that vacancies in $SrTiO_3$, $PbTiO_3$, and $BaTiO_3$ *push* anions while vacancies in $CaTiO_3$ ($x \leq 0.05$), $Pb(Zr_{0.6}Ti_{0.4})O_3$, and $Sr(Mg_{1/3}Nb_{2/3})O_3$ *pull* on them.

A more useful way of demonstrating the effect of vacancies on structure might be to examine the effect of vacancy concentration on $r_{\mathrm{A}} - r_{\mathrm{A}(id)}$, which includes contributions from bond deformation, covalency, and vacancies. It is convenient to artificially incorporate *all* of these contributions into a single virtual size parameter, S, such that:

$$S = \frac{\left(r_A - r_{\mathrm{A}(id)}\right)}{x} \qquad (2.19)$$

When S is normalized by $r_{\mathrm{A}(id)}$, the effect of vacancies on bond valence can be demonstrated (figure 2.8). In this case, all values above unity should represent cases where the effective A-site size is greater than the ideal A-site size (*i.e.*, that derived from Shannon radii alone). Such compositions would correspond to underbonding of the A-site species, whereas values below unity would correspond to overbonding. This prediction is borne out in the cases of $\mathrm{A}_{1\text{-}3x}Ln_{2x}\mathrm{TiO}_3$ (A = Sr, Pb, Ba). For example, based on published [59] Rietveld refinements of $\mathrm{Sr}_{1\text{-}3x}\mathrm{Ce}_{2x}\mathrm{TiO}_3$, the A site is slightly overbonded for $x = 0.0833$ (BV = 2.0118, $S/r_{\mathrm{A(id)}} = 0.9598$) but underbonded for $x = 0.125$ (BV = 1.9745, $S/r_{\mathrm{A(id)}} = 1.1146$). Similarly, according to published structural data [23] the A site in $\mathrm{Pb}_{1\text{-}3x}\mathrm{La}_{2x}\mathrm{TiO}_3$ is overbonded at $x = 0.125$ (BV = 2.0778, $S/r_{\mathrm{A(id)}} = 0.9103$) but underbonded at $x = 0.15$ (BV = 1.9836, $S/r_{\mathrm{A(id)}} = 1.0263$). Insufficient structural data exist to make a definitive argument either way in the case of $\mathrm{Ba}_{1\text{-}3x}Ln_{2x}\mathrm{TiO}_3$; however, published data [36, 47] do show for the end members that Ba^{2+} is overbonded in BaTiO_3 (BV = 2.74) whilst La^{3+} is underbonded in $\mathrm{La}_{2/3}\mathrm{TiO}_3$ (BV = 2.6723). The case of $\mathrm{Ca}_{1\text{-}3x}Ln_{2x}\mathrm{TiO}_3$ is different in that, according to published structural data, [20, 22] the Ca^{2+} in $CaTiO_3$ is slightly overbonded (BV = 2.08) despite having an $S/r_{A(id)}$ ratio >> 1. This apparent anomaly might be explained by octahedral tilting.

The octahedra in $CaTiO_3$ are tilted both in-phase and anti-phase. [20, 36] Using the *average* Ca-O nearest-neighbor bond length, the bond valence sum for Ca would be 1.5446, showing Ca^{2+} to be severely underbonded, in agreement with the prediction above; however, the effect of the tilts is to slightly lengthen four of the Ca-O nearest-neighbor bonds but shorten the remaining eight such that the overall bond valence sum increases to the point that Ca^{2+} becomes slightly overbonded.

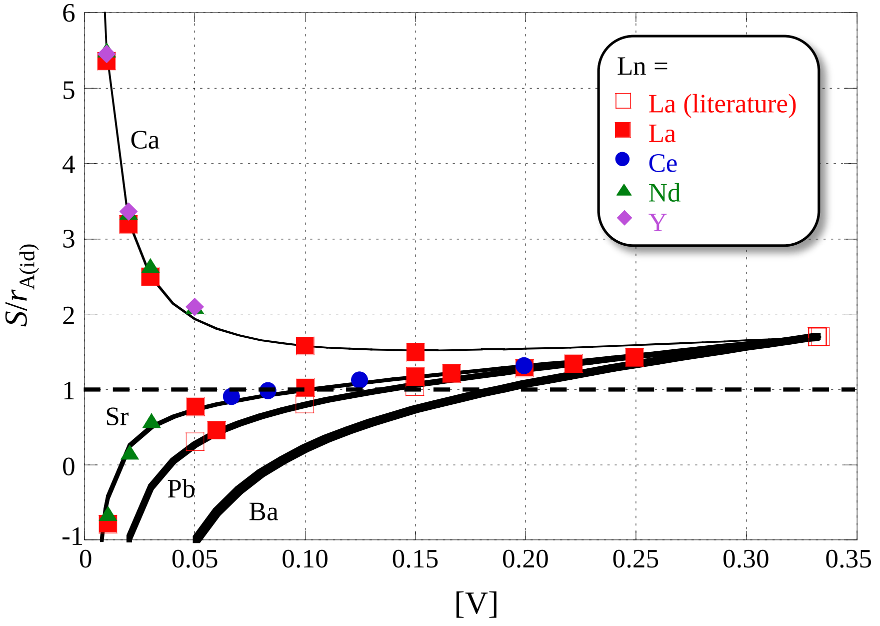

Figure 2.11 The effect of vacancies on A-site bond valence in $A_{1-3x}Ln_{2x}TiO_3$ (A = Ca, Sr, Pb, Ba; B = La, Ce, Nd, Y).

In the case of $SrTiO_3$, the cubic structure allows no tilting or distortion of octahedra; but antiphase tilting is triggered for x values at least as low as 0.01 (figure 2.4), in which case some Sr-O bond lengths begin to lengthen until eventually Sr^{2+} becomes underbonded ($0.0833 < x < 0.125$). In the cases of tetragonal ($P4mm$) $BaTiO_3$

and $PbTiO_3$, the single degree of freedom in each oxygen position allows only octahedral distortion, not tilting. The extent of that distortion is significant in $PbTiO_3$ (≤ 0.5536 Å) and Pb-O bond lengths are such that Pb^{2+} is overbonded. As x increases in $(Pb_{1-3x}La_{2x})TiO_3$, the Pb-O bond lengths gradually increase (the degree of distortion decreases) until, at $x = 0.15$, the structure becomes cubic and Pb^{2+} becomes slightly underbonded.

Although insufficient structural data exists for $Ba_{1-3x}Ln_{2x}TiO_3$ to be sure, a similar phenomenon would probably be active in that system. The octahedral distortion in $BaTiO_3$ is already extremely small (< 0.0643 Å) and Ba^{2+} very overbonded (BV = 2.74), so as x increases ($0 \leq x \leq \sim 0.2$) that distortion would likely increase in order to reduce the BV.

The system $Pb_{1-3x}La_{2x}(Zr_{0.6}Ti_{0.4})O_3$ also seems to obey this trend. Its curve (not shown in figure 11) is similar to that for $Ca_{1-3x}Ln_{2x}TiO_3$, which can be explained by the fact that, unlike in $PbTiO_3$, the Pb in $Pb(Zr_{0.6}Ti_{0.4})O_3$ is actually underbonded (BV = 1.55).

It is interesting to note the apparent effect vacancies have on the effective size of oxygen ions. From Tables 2.8-2.15 it is apparent that vacancies increase the effective $r_{O^{2-}}$ for small A-site cations including Ca^{2+} and Sr^{2+} ($x \leq 0.15$) but decrease $r_{O^{2-}}$ in systems with larger A-site species including Sr^{2+} ($x > 0.15$), Pb^{2+}, and Ba^{2+}.

Using the Shannon radii data it is possible to define a composition for which $t^* = t_0 = 1$, as in $[(Ca_{0.252}Sr_{0.748})_{1-3x}La_{2x}]TiO_3$. The results are shown in Table 2.18 and agree very well with the model. In this case BD is very small (-0.0081 Å). Ideally there should be no bond distortion/covalency component (*i.e.*, the effects of both bond distortion and covalency exactly cancel out) so the difference between the weighted average of Shannon radii (1.4148 Å) and the effective radius including bond distortion/covalency (1.4109 Å) should be ~0, *i.e.*, $r_A - r_A(\text{id}) \sim 0$. The effective vacancy size (1.5663 Å) in this system is larger than either value, again indicating a push against coordinating anions. Although the model works well for even the extreme case of $x \leq ⅓$ in $Sr_{1-3x}La_{2x}TiO_3$, in this system it begins to break down slightly at $x = 0.3$ ($Sr_{0.0726}Ca_{0.0274}La_{0.6}TiO_3$), in which case t_1 would have to be ~0.98, which is below the minimum possible here given equations (2.15) – (2.17). The model instead yields $t_1 = 1.020554$ and a_{pc}, a_{pc}', and a_{pc}" values with errors of 1.26%, 1.25% and 1.27%, respectively.

Table 2.18 Model values for $[(Ca_{0.252}Sr_{0.748})_{1-3x}La_{2x}]TiO_3$, where t_0 = 1.

Composition	a_{pc} (Å)	r_O (Å)	a_{pc} (Å)	error	a_{pc}’ (Å)	error	a_{pc}” (Å)	error
$Sr_{0.748}Ca_{0.252}TiO_3$	3.8914	1.3489	3.9096	0.47%	3.8970	0.14%	3.9079	0.42%
$Sr_{0.7042}Ca_{0.2658}La_{0.02}TiO_3$	3.8927	1.3473	3.9066	0.35%	3.8923	-0.01%	3.9046	0.31%
$Sr_{0.5082}Ca_{0.1918}La_{0.2}TiO_3$	3.8918	1.3403	3.8936	0.05%	3.8886	-0.08%	3.8907	-0.03%
$Sr_{0.2904}Ca_{0.1096}La_{0.4}TiO_3$	3.9020	1.3444	3.9012	-0.02%	3.9013	-0.02%	3.8989	-0.08%
$Sr_{0.0726}Ca_{0.0274}La_{0.6}TiO_3$	3.8830	1.3611	3.9320	1.26%	3.9317	1.25%	3.9322	1.27%
AVERAGE RELATIVE ABSOLUTE ERROR				0.43%		0.30%		0.42%

2.5 Conclusions

A predictive model for the pseudocubic lattice constant of $A_{1-3x}Ln_{2x}BX_3$ perovskites, based solely on published ionic radii data, has been developed and applied with great accuracy to many such perovskite systems. Using this model it is also possible to calculate the effective size of anions and A-site cation vacancies as well as to semiquantify the effects of both B-site cation ordering and second-order Jahn Teller distortions. A lower limit for the tolerance factor of oxide perovskites is proposed (t = 0.8465).

2.6 References

[1] F. Kahoul, L. Hamzioui, N. Abdessalem, A. Boutarfaia, Synthesis and Piezoelectric Properties of $Pb_{0.98}Sm_{0.02}[(Zr_y,Ti_{1-y})_{0.98}(Fe_{1/2},Nb_{1/2})_{0.02}]O_3$ Ceramics, Materials Sciences and Applications Vol.03No.01 (2012) 9.

[2] R.C. Buchanan, Ceramic materials for electronics, Marcel Dekker, New York, 2004.

[3] M.T. Sebastian, Dielectric materials for wireless communication, Elsevier, Amsterdam; Boston, 2008.

[4] L. Jiang, J. Guo, H. Liu, M. Zhu, X. Zhou, P. Wu, C. Li, Prediction of lattice constant in cubic perovskites, Journal of Physics and Chemistry of Solids 67(7) (2006) 1531-1536.

[5] R. Moreira, A. Dias, Comment on "Prediction of lattice constant in cubic perovskites", Journal of Physics and Chemistry of Solids 68(8) (2007) 1617-1622.

[6] M. Lufaso, P. Woodward, Prediction of the crystal structures of perovskites using the software program SPuDS, Acta Crystallographica Section B-Structural Science 57 (2001) 725-738.

[7] R. Ubic, Revised method for the prediction of lattice constants in cubic and pseudocubic perovskites, Journal of the American Ceramic Society **90** (10) (2007) 3326-3330.

[8] R. Ubic, G. Subodh, M.T. Sebastian, Effective size of vacancies in the $Sr_{1-3x/2}Ce_xTiO3$ superstructure, Ceramic Transactions 204 (2009) 177-185.

[9] R. Ubic, K. Tolman, K. Chan, N. Lundy, S. Letourneau, W. Kriven, Effective size of vacancies in aliovalently doped $SrTiO_3$ perovskites, Journal of Alloys and Compounds **575** (2013) 239-245.

[10] T. Tien, F. Hummel, Solid Solutions in System $SrTiO_3$-La_2O_3-$_3TiO_2$, Transactions of the British Ceramic Society 66(5) (1967) 233-&.

[11] T. Tien, C. Moratis, Dielectric Properites of Strontium Titanate Solid Solutions Containing Niobia, Journal of the American Ceramic Society 50(8) (1967) 392-&.

[12] P. Battle, J. Bennett, J. Sloan, R. Tilley, J. Vente, A-site cation-vacancy ordering in Sr1-3x/2LaxTiO3: A study by HRTEM, Journal of Solid State Chemistry 149(2) (2000) 360-369.

[13] C. Howard, G. Lumpkin, R. Smith, Z. Zhang, Crystal structures and phase transition in the system $SrTiO_3$-$La_{2/3}TiO_3$, Journal of Solid State Chemistry 177(8) (2004) 2726-2732.

[14] R. Ubic, G. Subodh, M. Sebastian, D. Gout, T. Proffen, Structure of compounds in the $Sr_{1-3x/2}Ce_xTiO_3$ homologous series, Chemistry of Materials **20** (9) (2008) 3127-3133.

[15] Q. Ma, F. Tietz, D. Stover, Nonstoichiometric Y-substituted SrTiO3 materials as anodes for solid oxide fuel cells, Solid State Ionics 192(1) (2011) 535-539.

[16] L. Fang, W. Dong, F. Zheng, M. Shen, Effects of Gd substitution on microstructures and low temperature dielectric relaxation behaviors of SrTiO3 ceramics, Journal of Applied Physics 112(3) (2012).

[17] A. Kovalevsky, A. Yaremchenko, S. Populoh, A. Weidenkaff, J. Frade, Enhancement of thermoelectric performance in strontium titanate by praseodymium substitution, Journal of Applied Physics 113(5) (2013).

[18] M. Sotomayor, A. Varez, W. Bucheli, R. Jimenez, J. Sanz, Structural characterisation and Li conductivity of Li1/2-x,Sr2xLa1/2-xTiO3 (0 < x < 0.5) perovskites, Ceramics International 39(8) (2013) 9619-9626.

[19] W. Luo, Z. Shen, Y. Li, Z. Wang, R. Liao, X. Gu, Structural characterizations, dielectric properties and impedance spectroscopy analysis of Nd (x) Sr1-1.5x TiO3 ceramics, Journal of Electroceramics 31(1-2) (2013) 117-123.

[20] V. Vashook, L. Vasylechko, M. Knapp, H. Ullmann, U. Guth, Lanthanum doped calcium titanates: synthesis, crystal structure, thermal expansion and transport properties, Journal of Alloys and Compounds 354(1-2) (2003) 13-23.

[21] V. Vashook, L. Vasylechko, N. Trofimenko, M. Kuznecov, P. Otchik, J. Zosel, U. Guth, A-site deficient perovskite-type compounds in the ternary CaTiO3-LaCrO3-La2/3TiO3 system, Journal of Alloys and Compounds 419(1-2) (2006) 271-280.

[22] Z. Zhang, G. Lumpkin, C. Howard, K. Knight, K. Whittle, K. Osaka, Structures and phase diagram for the system CaTiO3-La2/3TiO3, Journal of Solid State Chemistry 180(3) (2007) 1083-1092.

[23] D. Hennings, G. Rosenstein, X-Ray Structure Investigation of Lanthanum Modified Lead Titanate with A-Site and B-Site Vacancies, Materials Research Bulletin 7(12) (1972) 1505-1513.

[24] D. Hennings, K. Hardtl, The Distribution of Vacancies in Lanthana-Doped Lead Titanate, Physica Status Solidi a-Applications and Materials Science 3(2) (1970) 465-474.

[25] K. Hardtl, D. Hennings, Distribution of A-Site and B-Site Vacancites in (Pb,La)(Ti,Zr)O3 Ceramics, Journal of the American Ceramic Society 55(5) (1972) 230-&.

[26] V. Chaudhari, G. Bichile, Study of Phase Transitions and Response of Dielectric Behavior of Pb1-1.5xLaxTiO3 Ceramics, Integrated Ferroelectrics 150(1) (2014) 1-13.

[27] A. Glazer, S. Mabud, Powder Profile Refinement of Lead Zirconate Titanate at Several Temperatures .II. Pure $PbTiO_3$, Acta Crystallographica Section B-Structural Science 34(APR) (1978) 1065-1070.

[28] C. Jun, X. Xianran, Y. Ranbo, L. Guirong, W. Li, C.X. Long, Structural investigations on ferroelectric $Pb_{1-3x/2}La_xTiO_3$ using the X-ray Rietveld method, Journal of Materials Research 19(12) (2004) 3614-3619.

[29] J. Chen, X. Xing, R. Yu, G. Liu, L. Wu, X. Chen, Structural investigations on ferroelectric Pb1-3/2xLaTiO3 using the x-ray Rietveld method, Journal of Materials Research 19(12) (2004) 3614-3619.

[30] M. Buscaglia, V. Buscaglia, M. Viviani, P. Nanni, M. Hanuskova, Influence of foreign ions on the crystal structure of BaTiO3, Journal of the European Ceramic Society 20(12) (2000) 1997-2007.

[31] M. Ganguly, S. Rout, T. Sinha, S. Sharma, H. Park, C. Ahn, I. Kim, Characterization and Rietveld Refinement of A-site deficient Lanthanum doped Barium Titanate, Journal of Alloys and Compounds 579 (2013) 473-484.

[32] D.C.C. Ltd., Improvements in or relating to Ceramic Compositions, in: L.P. Office (Ed.) US Patents, Great Britain, 1946.

[33] M. Kestigian, R. Ward, The Lanthanum-Titanium-Oxygen System, Journal of the American Chemical Society 77(23) (1955) 6199-6200.

[34] J. MacChesney, H. Sauer, The System La_2O_3-TiO_2 - Phase Equilibria and Electrical Properties, Journal of the American Ceramic Society 45(9) (1962) 416-422.

[35] M. Abe, K. Uchino, X-ray Study of Deficient Perovskite $La_{2/3}TiO_3$, Materials Research Bulletin 9(2) (1974) 147-155.

[36] Z. Gönen, D. Paluchowski, P. Zavalij, B. Eichhorn, J. Gopalakrishnan, Reversible cation/anion extraction from $K_2La_2Ti_3O_{10}$: Formation of new layered titanates, $KLa_2Ti_3O_{9.5}$ and $La_2Ti_3O_9$, Inorganic Chemistry **45** (21) (2006) 8736-8742.

[37] B. Kennedy, C. Howard, Y. Kubota, K. Kato, Phase transition behaviour in the A-site deficient perovskite oxide La1/3NbO3, Journal of Solid State Chemistry 177(12) (2004) 4552-4556.

[38] Z. Zhang, C. Howard, B. Kennedy, K. Knight, Q. Zhou, Crystal structure of *Ln*(1/3)NbO(3) (*Ln* = Nd, Pr) and phase transition in Nd1/3NbO3, Journal of Solid State Chemistry 180(6) (2007) 1846-1851.

[39] Q. Zhou, P. Saines, N. Sharma, J. Ting, B. Kennedy, Z. Zhang, R. Withers, K. Wallwork, Crystal Structures and Phase Transitions in A-Site Deficient Perovskites *Ln*(1/3)TaO(3), Chemistry of Materials 20(21) (2008) 6666-6676.

[40] J. Jorgensen, J. Jorgensen, B. Batlogg, J. Reneika, J. Axe, Order Parameter and Critical Exponent for the Pressure-Induced Phase-Transitions in ReO_3, Physical Review B 33(7) (1986) 4793-4798.

[41] K. Tolman, R. Ubic, M. Papac, K. Seymour, S. McCormack, W. Kriven, H. Kungl, Structural effect of aliovalent doping in lead perovskites, Journal of Solid State Chemistry **225** (2015) 359-367.

[42] B. Toby, EXPGUI, a graphical user interface for GSAS, Journal of Applied Crystallography 34 (2001) 210-213.

[43] L. Finger, D. Cox, A. Jephcoat, A Correction for Powder Diffraction Peak Asymmetry Due to Axial Divergence, Journal of Applied Crystallography **27** (1994) 892-900.

[44] H. Kay, P. Bailey, Structure and Properties of $CaTiO_3$, Acta Crystallographica 10(3) (1957) 219-226.

[45] H. Megaw, Crystal Structure of Double Oxices of the Perovskite Type, Proceedings of the Physical Society of London 58(326) (1946) 133-&.

[46] J. Joseph, T. Vimala, V. Sivasubramanian, V. Murthy, Structural investigations on Pb(ZrxT1-x)O-3 solid solutions using the X-ray Rietveld method, Journal of Materials Science 35(6) (2000) 1571-1575.

[47] H. Megaw, Refinement of Structure of $BaTiO_3$ and Other Ferroelectrics, Acta Crystallographica 15(OCT) (1962) 972-&.

[48] F. Galasso, J. Pyle, Preparation and Study of Ordering in A $B'_{0.33}Nb_{0.67}O_3$ Perovskite-Type Compounds, Journal of Physical Chemistry 67(7) (1963) 1561-&.

[49] M. Arillo, J. Gomez, M. Lopez, C. Pico, M. Veiga, Structural and electrical characterization of new materials with perovskite structure, Solid State Ionics **95** (3-4) (1997) 241-248.

[50] L. Pauling, The nature of the chemical bond IV The energy of single bonds and the relative electronegativity of atoms, Journal of the American Chemical Society 54 (1932) 3570-3582.

[51] A. Allred, Electronegativity Values from Thermochemical Data, Journal of Inorganic & Nuclear Chemistry 17(3-4) (1961) 215-221.

[52] R. Shannon, Revised Effective Ionic-Radii and Systematic Studies of Interatomic Distances in Halides and Chalcogenides, Acta Crystallographica Section a **32** (SEP1) (1976) 751-767.

[53] B. Wechsler, R. VonDreele, Structure Refinements of Mg2TiO4, MgTiO3 and MgTi2O5 by Time-of-Flight Neutron Powder Diffraction, Acta Crystallographica Section B-Structural Science 45 (1989) 542-549.

[54] D. Dobson, S. Jacobsen, The flux growth of magnesium silicate perovskite single crystals, American Mineralogist 89(5-6) (2004) 807-811.

[55] M. Knapp, P. Woodward, A-site cation ordering in $AA'BB'O_6$ perovskites, Journal of Solid State Chemistry **179** (4) (2006) 1076-1085.

[56] S. Li, Q. Gao, J. Li, X. He, Q. Zhang, C. Li, Y. Shen, L. Gu, Y. Yao, Y. Wang, R. Yu, X. Duan, Y. Ikuhara, Revealing Antiphase Boundaries and Defects at

Atomic Resolution in NaLaMgWO6 Double Perovskites, Materials Express 2(1) (2012) 51-56.

[57] A. Ruiz, M. Lopez, C. Pico, M. Veiga, New $La_{2/3}TiO_3$ derivatives: Structure and impedance spectroscopy, Journal of Solid State Chemistry **163** (2) (2002) 472-478.

[58] Y. Li, S. Qin, F. Seifert, Phase transitions in A-site substituted perovskite compounds: The $(Ca_{1-2x}Na_xLa_x)$TiO3 (0 <= x <= 0.5) solid solution, Journal of Solid State Chemistry **180** (3) (2007) 824-833.

[59] R. Ubic, G. Subodh, M. Sebastian, D. Gout, T. Proffen, Structure of compounds in the Sr1-3x/2CexTiO3 homologous series, Chemistry of Materials 20(9) (2008) 3127-3133.

CHAPTER THREE: Cation Ordering in Perovskites

3.1 Introduction

Predicting perovskite structures is a subject of continuous and significant interest. Perovskites arguably exhibit a wider variety of useful phenomena (*e.g.*, ferroelectricity, piezoelectricity, superconductivity, colossal magnetoresistance, *etc.*) than any other structure type.[1] Predicting structures – and, by extension, properties – based on chemical compositions, without the need for expensive trial and error or time-consuming computation, is the primary key to fully exploiting these highly useful materials.

The compound $Na_{0.5}La_{0.5}TiO_3$ is the $x = 0$ end-member of the $Na_{(1-3x)/2}La_{(1+x)/2}TiO_3$ (NLT) solid solution and belongs to the loparite family of minerals found in foidolites and aegirine-albite metasomatic rocks. It is particularly remarkable because it exhibits quantum paraelectricity at low temperatures (<50 K).[2] Furthermore, it is thought that the paraelectric phase at these low temperatures is stabilized by “zero point quantum fluctuations” which prevent the freezing of its ferroelectric soft mode.[3] The perovskite SrTiO3 displays the same behavior below ~4 K.

Evidence of short-range A-site cation and vacancy ordering domains is difficult to establish via X-ray diffraction (XRD); however, electron diffraction is generally more sensitive to such structural effects. The existence of diffuse pseudocubic ½{*even,even,odd*} superlattice reflections (so-called β superlattice reflections) can be evidence of either short-range 1:1 A-site cation ordering or antiparallel A-site cation displacements.

All previous reported models of $Na_{0.5}La_{0.5}TiO_3$ have included a disordered long-range distribution of the A-site cations (*i.e.*, random distributions of Na^+ and La^{3+} cations). The first such studies[5-7] reported that the structure of $Na_{0.5}La_{0.5}TiO_3$ was cubic, space group $Pm\bar{3}m$. Others later proposed an orthorhombic structure in space group *Pnma*.[8-10] Most recently, several groups[11-17] have used synchrotron- and neutron-diffraction data to establish either tetragonal (*I4/mcm*) or trigonal $(R\bar{3}c)$ structural models, with a phase transition to an orthorhombic form in the region $0 < x < 0.05$. Knapp & Woodward[14] suggested that the A-site ordering observed in the analogous perovskite $(Na_{0.5}La_{0.5})(Mg_{0.5}W_{0.5})O_3$ would imply that $Na_{0.5}La_{0.5}TiO_3$ should also have A-site cation ordering; however, they observed no such long-range ordering. Garcia-Martin *et al.*[18] used electron diffraction to observe diffuse ½{*even,even,odd*} β superlattice reflections in $Na_{0.5}La_{0.5}TiO_3$, which they attributed to ordered nanodomains (*i.e.*, short-range order).

Ruiz *et al.*[9] initially studied the structures of $Na_{0.42}La_{0.5267}TiO_3$ ($x = 0.053$) and $Na_{0.24}La_{0.5867}TiO_3$ ($x = 0.173$) by electron and neutron diffraction as a means to determine the structures of solid solutions intermediate between the two end members, $Na_{0.5}La_{0.5}TiO_3$ ($x = 0$) and $La_{2/3}TiO_3$ ($x = ⅓$). They found that more than one type of superlattice reflection existed for these compositions and proposed orthorhombic (*Ibmm*) structures for both, each containing small octahedral tilt angles. Ruiz *et al.*[10] later studied these compositions again plus $Na_{0.165}La_{0.6117}TiO_3$ ($x = 0.223$) via electron and neutron diffraction to re-address the origin of the superlattice reflections, and they claimed that the ½{*even,even,odd*} reflections were formed by three sets of micro-domains; however, their Rietveld refinement fit for x = 0.173 was improved by using ordered *Pbmm* rather than disordered *Ibmm*. They reported[9, 10] an orthorhombic cell in space group *Pbmm* for $x = 0.053$, *Ibmm* for $x = 0.173$, and an ordered doubled orthorhombic cell in *Cmmm* for $x = 0.225$. In 2003, Howard and Zhang[19] proposed the *Cmmm* structure for $La_{2/3}TiO_3$ ($x = ⅓$); however, Gönen *et al.*[20] found that $La_{2/3}TiO_3$ is isomorphous with the $Nd_{2/3}TiO_3$ model in *I4/mmm* reported by Richard *et al.*,[21] consisting of shifted $La_2Ti_3O_9$ slabs, yielding a $La_{2/3}TiO_3$ compound with a layered structure in which vacancies cluster on every third {001} plane.

While A-site ordering in perovskites is most commonly reported on pseudocubic {001} (layered), 1:1 A-site ordering can potentially occur in two other geometries: {110} (columnar) and {111} (rock-salt) (Figure 3.1). For example, $(NaLa)(MgW)O_6$ forms in tetragonal *P4/mmm* and orders with a layered geometry[22] while $(CaFe)Ti_2O_6$ forms in tetragonal $P4_2/nmc$ and orders with a columnar geometry[23]; and $(NaBa)(LiNi)F_6$ forms in cubic $Fm\bar{3}m$, ordering with a rock-salt geometry.[24] Other geometries are possible for different stoichiometries. For example, the 1:3 ordered $CaCu_3Ti_4O_{12}$ compound orders in a more complicated way in cubic space group $Im\bar{3}$ [25, 26]

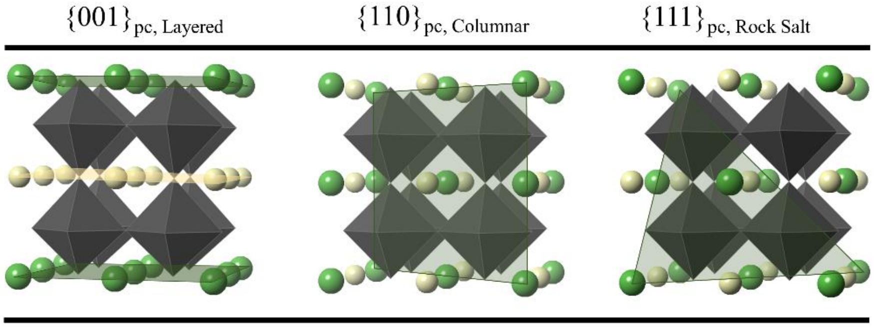

Figure 3.1. Pseudocubic view of $Na_{(1-3x)/2}La_{(1+x)/2}TiO_3$ for the three types of 1:1 geometries in which A-site ordering can occur: {001} (layered), {110} (columnar) and {111} (rock-salt).

Inaguma *et al.*[15] refined the structure of $Na_{0.5}La_{0.5}TiO_3$ in both *I*4*/mcm* and $R\bar{3}c$ because the anti-phase octahedral tilting was difficult to quantify; however, they also assumed a fully disordered structure. The octahedral tilting in *I*4*/mcm* is about a single pseudocubic axis parallel to the tetragonal *c* axis (*i.e.*, $a^0a^0c^-$ in Glazer's notation [27]), whereas in $R\bar{3}c$ the degree of tilting is equal along all three pseudocubic <100> axes ($a^-a^-a^-$), which is equivalent to a tilt about the pseudocubic [111] or hexagonal *c* axis.

Using a combination of synchrotron and neutron powder-diffraction data, Garg *et al.*[13] showed that $R\bar{3}c$ was a better description of the structure of $Na_{0.5}La_{0.5}TiO_3$ than was *I*4*/mcm*. The octahedral tilting about the hexagonal [001] was quantified at about 8°. Again, no evidence of ordering was found; however, their synchrotron data did not extend below 5° (2θ) and they used a wavelength of 0.5 Å, which means that the largest possible *d* spacing observable would have been 5.7 Å – far too small to detect a ½{001} superlattice peak at ~7.75 Å should one have existed. Similarly, they used a wavelength of 1.548 Å for their neutron-diffraction data, which did not extend below 20°; therefore, the maximum *d* spacing observable would have been just 4.5 Å. As a consequence, while higher-order superlattice reflections indicative of A-site order might have been detectable in these experiments, the stronger fundamental ½{001} peak could not have been detected even if present.

Superlattice ½{*even*,*even*,*odd*} β reflections observed by Garcia-Martin *et al.*[18] in electron-diffraction studies suggested cation ordering in both $Na_{0.5}La_{0.5}TiO_3$ and $Na_{0.5}La_{0.5}ZrO_3$; however, the superlattice reflections of the former composition were much more diffuse. They hypothesized that short-range A-site ordering may form nanodomains in which the ordered planes are mutually perpendicular, as they would be on various pseudocubic {001}.

Recently, Ubic *et al.* [28-30] studied $Sr_{1-3x}Ln_{2x}TiO_3$ (*Ln* = La, Nd, Ce) and developed [31] a general empirical model for the effective sizes of A-site species (including vacancies) and anions in perovskites which can thus be used to predict pseudocubic lattice constants. By analyzing the systematic errors between the NLT experimental pseudocubic lattice constants $a_{\mathrm{pc,(Exptl.)}}$ (equation 3.1) and the predicted pseudocubic lattice constants (equations. 3.2 – 3.3) based on the empirical model, they suggested [31] the existence of A-site ordering in NLT, the degree of which decreased with increasing *x*; but they were unable to reconcile this conclusion with the reported structures of $Na_{0.5}La_{0.5}TiO_3$ or the counterintuitive apparent volume increase which the model predicted upon ordering in this system.

$$a_{pc(Exptl.)} = \left(\frac{V}{Z}\right)^{1/3} \tag{3.1}$$

$$a'_{pc} = \sqrt{2}(r_A + r_X) \tag{3.2}$$

$$a''_{pc} = 2(r_B + r_X) \tag{3.3}$$

In equations 3.1 – 3.3, V, Z, r_A, r_B, and r_X are the cell volume, number of ABX_3 units per unit cell, and the effective ionic radii of A, B, and X ions, respectively.[32]

The conventional tolerance factor [33] can be calculated as the ratio of a'_{pc}/a''_{pc}:

$$t_* = \frac{a'_{pc}}{a''_{pc}} = \frac{r_A + r_X}{\sqrt{2}(r_B + r_X)} \tag{3.4}$$

In 2007 Ubic *et al.* [34] published a method of calculating pseudocubic lattice constants and later [30-35] revised it in order to accommodate extrinsic defects, deriving from the revised formula a new model for tolerance factor:

$$t_1 = \frac{a_{pc} - 0.011730139}{0.7209203(r_B + r_X)} - 0.760998 \tag{3.5}$$

where r_B and r_X correspond to the published [32] ionic radii of B and X ions, respectively. Ideally $t_1 = t$; [29, 30] however, t_1 predicts tilt structures of perovskites better and does not require knowledge of r_A (but does require foreknowledge of a_{pc}). Equation 3.5 can also be solved for a_{pc} in terms of t_1, r_B, and r_X:

$$a_{pc} = 0.7209203(t_1 + 1.760998)(r_B + r_X) + 0.011730139 \tag{3.6}$$

Neither equations 3.5 nor 3.6 requires explicit knowledge of the A-site size, which is a non-trivial problem especially when vacancies are involved. According to the model of Ubic *et al.*,[31] it is the sum of three separate terms: the ideal (Shannon) size, a bond-deformation (*BD*) term (equation 2.7), and the effective size of vacancies, r_V (equation 2.13). The effective anion size is reportedly[31] a function of t_1 (equation 2.6).

Finally, the empirical relation between t_1 and the conventional t developed [31] (see Chapter 2) allows the prediction of effective values for r_X without experimental a_{pc} data, thus the model can accurately predict a_{pc} values of A-deficient perovskites from published ionic radii data alone.

The present work provides both validation of this empirical model as well as confirmation of the true structure of several members of the $Na_{(1-3x)/2}La_{(1+x)/2}TiO_3$ solid solution. A total of four compositions (x = 0, 0.0533, 0.1733 and 0.225) were synthesized and studied to investigate the sensitivity of this empirical model regarding short- and long-range A-site ordering.

In all compositions tested, the A site maintains a 2+ formal charge, which is conveniently formulated as:

$$\left[Na_{\left(\frac{1-3x}{2}\right)}La_{\left(\frac{1+x}{2}\right)}\right]^{2+} V_x Ti^{4+} O_3^{2-}$$

where V corresponds to vacancies. The defect chemistry can be formulated as:

$$La_2O_3 \xrightarrow{Na_{1/2}La_{1/2}TiO_3} 2La_{Na}^{\bullet\bullet} + 4V_{Na}' + 3O_O^x$$

There are three A-site components (*i.e.*, increasing [La], decreasing [Na], and increasing [V]) that must be considered with this defect chemistry, and all are accounted for in this formulation.

The model as developed in Chapter 2 starts with the assumption of an “average” cation size which, in this case, would be $((1 - 3x)r_{\mathrm{Na}} + (1 + x)r_{\mathrm{La}})/4$, and the stoichiometry is purposely formulated so that x represents the degree of vacancy "doping" on this site (*i.e.*, x = [V]). Alternately, this system can be thought of as doping the “average” cation site with La^{3+} according to:

$$(Na_{½}La_{½})^{2+}_{1-3x}La^{3+}_{2x}Ti^{4+}O^{2-}_{3}$$

In this way the model used here is exactly analogous to $A^{2+}_{(1-3x)}Ln^{3+}_{(2x)}BO_3$ systems already studied,[31] in which x = [V].

3.2 Methods

Four compositions in the system $Na_{(1-3x)/2}La_{(1+x)/2}TiO_3$ (x = 0, 0.0533, 0.1733 and 0.225) (NLT) and a series of samples from $Ba(Mg_{1/3}Ta_{2/3})O_3$ (BMT) were synthesized via the solid-state mixed-oxide route. No excess sodium was added to the NLT compositions, but a sacrificial powder bed was used to induce a sodium-rich closed environment. Additionally, the calcination and sintering were conducted in a pre-contaminated crucible to inhibit sodium-loss into the crucible walls. As-received La_2O_3 (99.9%, Alfa-Aesar, Ward Hill, MA) powder was first hydroxylated by mixing with an excess of deionized water and drying overnight, forming $La(OH)_3$. Stoichiometric amounts of Na_2CO_3 (99.5%, Thermo Fisher Scientific Inc., Pittsburgh, PA), TiO_2 (99.9%, Aldrich Chemical Co., Milwaukee, WI), and $La(OH)_3$ were then ball milled with yttria-stabilized ZrO_2 (YSZ) media using deionized water in a high-density nylon pot for ~24 hours. Powders were then dried overnight in an atmospheric drying oven at 95-100°C until the water was evaporated. Calcination was conducted at 1000°C for three hours in a box furnace (1807FL, CM Furnaces Inc., Bloomfield, NJ) with a sacrificial powder in an inverted pre-contaminated Al_2O_3 crucible placed on an Y_2O_3 plate. After calcination the powders were crushed using a mortar and pestle. Calcined powders were then sieved to under 250 μm and mixed in water with 2 wt% polyethylene glycol (PEG 10,000, Alfa-Aesar, Heysham, UK) and powder which was dissolved in water prior to mixing. The mixture was then dried overnight in an atmospheric drying oven at 95-100°C until the water was evaporated. Cylindrical green compacts 8-10 mm in height and 10 mm in diameter were then formed by applying a uniaxial pressure of 63 MPa. Compacts were sintered for three hours at 1350°C with a sacrificial sodium-rich powder and the same pre-contaminated plate / inverted crucible apparatus previously described. Stoichiometric amounts of $BaCO_3$ (99.95%, Alfa-Aesar, Thermo Fisher Scientific, Tewksbury, MA), $4MgCO_3.Mg(OH)_2 \bullet 4H_2O$ (43.5%, Alfa-Aesar, Thermo Fisher Scientific, Tewksbury, MA), and Ta_2O_5 (99.95%, Alfa-Aesar, Thermo Fisher Scientific, Tewksbury, MA) were then ball milled with yttria-stabilized ZrO_2 (YSZ) media using deionized water in a high-density nylon pot for ~24 hours. Powders were then dried overnight in an atmospheric drying oven at 95-100°C until the water was evaporated. Calcination was conducted at 1200°C for 12 hours in a box furnace (1807FL, CM Furnaces Inc., Bloomfield, NJ) in an alumina crucible. Calcined powders were then sieved to under 250 μm and mixed in water with 2 wt% polyethylene glycol (PEG 10,000, Alfa-Aesar, Heysham, UK) and powder which was dissolved in water prior to mixing. The mixture was then dried overnight in an atmospheric drying oven at 95-100°C until the water was evaporated. Cylindrical green compacts 8-10 mm in height and 10 mm in diameter were then formed by applying a uniaxial pressure of 63 MPa. A compact and powder were annealed for 5, 10, 15, 20, 30 and 40 hours at 1500°C.

Powder XRD measurements were performed in a diffractometer (Miniflex-600, Rigaku, Woodlands, TX) operating with convergent-beam geometry and Cu Kα radiation. Le Bail fits of the XRD data were analyzed using DiffracPLUS TOPAS 4.2 (Bruker AXS Inc., Madison, WI). The background was fitted with a fourth-order Chebyshev polynomial, and asymmetry was corrected using the Finger *et al*. model.[36]

Neutron time of flight measurements for $Na_{(1-3x)/2}La_{(1+x)/2}TiO_3$ were performed at the Spallation Neutron Source POWGEN beamline BL-11A at Oak Ridge National Laboratory using bank 2 (60 Hz) with a *d*-space range of ~0.4 – 4 Å, diffractometer constant (DIFC) of 22575.22 μsec/Å, and neutron diffraction absorption correction (DIFA) of 8.06; and bank 4 (60 Hz) with a *d*-space range of ~2 – 10 Å, DIFC of 22562.90 μsec/Å, and DIFA of 6.49. The source-to-sample distance was 60 m and the sample-to-detector distance was between 2.5 – 4.5 m. The resolution was $0.001 < \Delta d/d < 0.016$.

Rietveld refinement is a method that uses statistical modeling by regression between a theoretical profile (calculated) and an observed profile (experimental) for estimating its solution (best least-squares fit). The Rietveld refinement method [37] was developed by Hugo M. Rietveld [38-41] and is used to refine a crystal structure from diffraction data.

Diffraction is a wave-interference phenomenon that relates an observed pattern (*i.e.*, constructive versus destructive intensity contrast) to a material's structure factor (Equation 1). For example, Bragg's law ($n\lambda=2d\sin\theta$) relates wavelength (λ), interatomic planar spacing (*d*), and the Bragg angle (θ). There were three main sources used in this study: X-ray, electron, and neutron.

The structure factor, $F_{K,}$ for the j^{th} atom is

$$F_K = \sum_j N_j f_j exp\left[2\pi i\left(hx_j + ky_j + lz_j\right)\right] exp\left[-M_j\right] \tag{1}$$

where N_j is the site occupancy, f_j is the atomic scattering factor, *hkl* are the Miller indices of the diffracting plane, *xyz* are average atomic positions, and M_j is the temperature factor. It is noteworthy to mention that there is a significant difference between the refinement of X-ray and neutron data due to the atomic scattering factor, *fj*, which directly influences the intensities (Equation 2).

The calculated intensity is

$$y_{ci} = s \sum_K L_K |F_K|^2 \varphi(2\theta_i - 2\theta_K) P_K A + y_{bi} \tag{2}$$

where *s* is the scale factor, *K* represents Miller indices *hkl*, L_K contains the Lorentz polarization and multiplicity factors, F_K is the structure factor, φ is the reflection profile function, θ is the Bragg angle, P_K is the preferred orientation function, *A* is the effective absorption factor, and y_{bi} is the background intensity. The instrument diffractometer geometry is accounted for with the absorption factor, *A*.

The reflection full-width-at-half-maximum (FWHM) profile, H, is

$$H = \sqrt{Utan^2\theta + Vtan\theta + W} \tag{3}$$

where U, V, and W are profile peak-shape parameters in units of $(°2\theta)^2$.

There are three commonly used symmetric analytical profile functions: Gaussian (G, Equation 4), Lorentzian (L, Equation 5), and pseudo-Voigt (pV, Equation 6).[38-44]

$$\frac{C_0^{\frac{1}{2}}}{H_K\pi^{\frac{1}{2}}} exp[-C_0(2\theta_i 2\theta_K)^2/H_K^2] \qquad (4)$$

$$\left(\frac{4^{1/2}}{\pi H_K}\right)\frac{1}{\left[1+4\frac{(2\theta_i 2\theta_K)^2}{H_K^2}\right]} \qquad (5)$$

$$\eta L + (1-\eta)G \qquad (6)$$

where H_K is the FWHM, and $C_0 = 4\ln 2$. Underlying peak shapes are typically Gaussian, but the actual peak shape can often result from multiple contributions such as diffraction optics. Finger *et al*. [45] developed a peak shape asymmetry formulation to correct for axial divergence.

The temperature factor M_j of the j^{th} atom

$$M_j = 8\pi^2\bar{u}_s^2\frac{sin^2\theta}{\lambda^2} \qquad (7)$$

where $\bar{u}_s^2$ is the root mean squared thermal displacement.

The FULLPROF suite [46, 47] is a set of programs used for Rietveld refinements of X-ray- and neutron-diffraction data. FullProf was built in Fortran 95 but was transformed in the Crystallographic Fortran 95 Modules and works with allocatable arrays for direct control of the dimensions by the user. [48]

To conduct refinements in FullProf the user must first know the diffraction source, instrument parameters, a diffraction data file, and a starting model (*i.e.*, information about the assumed crystal structure). The starting model can be based on a hypothesis derived from literature. In cases where a good starting model is not available it is recommended that a Le Bail refinement is conducted to determine the correct profile function, background, and cell parameters. Once these are determined then a full Rietveld refinement can be implemented.

It is unadvisable to start a refinement by refining all of the structural parameters at the same time. It may easily cause divergence or the refinement can get "stuck" in a false minimum. Some parameters should weakly affect the residuals and shouldn't be refined until after those parameters that strongly affect the residuals. A good strategy can save time and disappointment. A typical refinement may progress through the refinement systematically. First, choose the scale factor and run the FullProf program; Second, select the instrument zero point and the profile background; Third, refine the atomic positions (*e.g.*, may try each non-ideal atomic position one at a time); Fourth, refine the peak shape and asymmetry parameters; Fifth, refine the site occupancies. Refinement procedures and/or complexity will vary.

Other considerations will include the background profile and goodness-of-fit. The background profile should be a smooth function. Too many variables or an incorrect background profile can lead to misleading results. Chi-square is used as a measure between the calculated and observed weighted intensity squared

$$\chi^2 = \sum_{i=1}^{n} w_i \{y_i - y_{c,i}(\alpha)\}^2 \tag{8}$$

where $w_i = \frac{1}{\sigma_i^2}$, σ_i^2 is the variance of the observed intensity y_i, y_{ci} is the calculated intensity, and α is the parameter vector. The "Goodness-of-Fit" (Equation 12) is calculated from profile factors (Equations 9-11) that numerically describe the agreement between the calculated and observed intensities.

Profile factor R_p

$$R_p = 100\left[\frac{\sum_{i=1}\left|y_i - y_{c,i}\right|}{\sum_{i=1} y_i}\right] \tag{9}$$

Weighted profile factor R_wp

$$R_{wp} = 100\left[\frac{\sum_{i=1} w_i\left|y_i - y_{c,i}\right|^2}{\sum_{i=1} w_i {y_i}^2}\right]^{1/2} \tag{10}$$

Expected weighted profile factor R_{exp}

$$R_{wp} = 100\left[\frac{n-p}{\sum_{i=1} w_i {y_i}^2}\right]^{1/2} \tag{11}$$

where n - p is the number of degrees of freedom, n is the total number of points, and p is the number of refined parameters.

Goodness of fit R_p /R_exp

$$S = \frac{R_{wp}}{R_{exp}} \tag{12}$$

Scanning electron microscopy (SEM) (S-3400N-II, Hitachi High Technology, USA) and quantitative energy dispersive X-ray spectroscopy (EDS) (Energy+, Oxford Instruments, UK) were performed on each of the samples to verify composition and homogeneity, as conventional processing can result in compositional fluctuations due to the volatility of sodium oxide. Quantitative EDS for each sample was performed using the same conditions (*i.e.*, accelerating voltage, beam current, and working distance).

Amelia albite, lanthanum phosphate, and ilmenite standards were used to quantify Na, La, and Ti, respectively.

Specimens for transmission electron microscopy (TEM) (JEM-2100 HR, JEOL, Japan) were prepared from sintered pellets by mechanically cutting them with a diamond wafering blade then polishing the faces via conventional ceramographic techniques, finishing with a precision ion polisher (Model 691 PIPS, Gatan, USA) at low ion-beam angles to achieve electron transparency (*i.e.*, thickness ~100nm). Amorphous material caused by ion damage was removed using a plasma cleaner (Model 1400, E. A. Fischione Instruments Inc., USA) prior to observation in the TEM, which was operated at 200 kV.

The Vienna Ab-initio Software Package (VASP)[49] was used to conduct structural and energetic calculations according to density functional theory (DFT). The spin-polarized generalized gradient approximation (GGA) was used within the Perdew Burke Ernzerhoff formalism (PBE).[50] Plane-wave basis sets were expanded using projector-augmented wave (PAW)[51, 52] pseudopotentials to a cutoff energy of 500 eV. The Brillouin zone integration was performed on a 10x10x10 gamma-centered mesh for tetragonal and a 10x10x5 gamma-centered mesh for trigonal settings. To account for Fermi surface broadening, a Gaussian smearing value of 0.05 eV was applied. All relaxations of the lattice parameters and atomic positions were performed until residual forces were reduced to 0.01 eV/Å.

The $(Na,Li)_{(1-3x)/2}La_{(1+x)/2}TiO_3$ order parameter was calculated by the absolute quantity of the difference between the species occupancy in site one and its occupancy in site two. For example, in $Na_{0.24}La_{0.5867}TiO_3$ the Na order parameter would be solved by |[Na]2e-[Na]2f| = |0.72-0.48| = 0.48 and/or for vacancy order parameter it would then be |[V]2e-[V]2f| = |0.6-0.1| = 0.5.

3.3 Results and Discussion

No secondary phases were detected in $Na_{(1-3x)/2}La_{(1+x)/2}TiO_3$ samples via XRD (Figure 3.2) or EDS (Table 3.1); however, no ordering superlattice reflections were observed via XRD in $Na_{0.5}La_{0.5}TiO_3$ either. The lack of superlattice reflections was expected, as the ordering reportedly exists [18] as nanodomains within a disordered matrix. No long-range order exists. The XRD patterns have been indexed in the following space groups: x = 0 in $I4/mcm$, x = 0.0533 in $Ibmm$, x = 0.1733 in $Pmma$, and x = 0.225 in $Cmmm$ (Figure 3.2).

Table 3.1. $Na_{(1-3x)/2}La_{(1+x)/2}TiO_3$ energy dispersive X-ray spectroscopy (EDS) results. Both ideal and experimentally determined stoichiometries are shown.

nominal composition	x (ideal)	Na	La	x (Exptl.)
$Na_{0.5}La_{0.5}TiO_3$	0	0.4957(27)	0.5015(14)	0.0000(29)
$Na_{0.42}La_{0.5267}TiO_3$	0.0533	0.4187(33)	0.5271(11)	0.0542(33)
$Na_{0.24}La_{0.5867}TiO_3$	0.1733	0.2389(54)	0.5871(20)	0.1741(98)
$Na_{0.1625}La_{0.6125}TiO_3$	0.2250	0.1607(62)	0.6131(21)	0.2262(42)

Table 3.2.1 $Na_{(1-3x)/2}La_{(1+x)/2}TiO_3$ Rietveld refinement for sodium lanthanum titanate. Data from Oak Ridge neutron source (POWGEN)

$Na_{0.5}La_{0.5}TiO_3$	x	a (Å)	b (Å)	c (Å)	α	β	γ
	0	5.4841	5.4841	13.4198	90	90	120
R-3c H	Wyckoff	x	y	z	Uiso	Occ	
Na	6a	0	0	0.25	0.0176	0.5	
La	6a	0	0	0.25	0.0061	0.5	

Ti	6b	0	0	0	0.0073	1
O	18e	0.5403	0	0.25	0.0107	1
χ^2	Rp					
4.399	0.06					

Table 3.2.2 $Na_{(1-3x)/2}La_{(1+x)/2}TiO_3$ Rietveld refinement for sodium lanthanum titanate. Data from Oak Ridge neutron source (POWGEN)

$Na_{0.42}La_{0.545}TiO_3$	x	a (Å)	b (Å)	c (Å)	α	β	γ
Ibmm	0.0542	5.4878	5.4811	7.7559	90	90	90
	Wyckoff	x	y	z	Uiso	Occ	
Na	4e	0.0029	0	0.25	0.0109	0.5271	
La	4e	0.0029	0	0.25	0.001	0.4187	
Ti	4b	0	0.5	0	0.0075	1	
O1	4e	0.0413	0.5	0.25	0.0083	1	
O2	8g	0.75	0.25	0.0248	0.0127	1	
χ^2	Rp						
5.554	0.05						

Table 3.2.3 $Na_{(1-3x)/2}La_{(1+x)/2}TiO_3$ Rietveld refinement for sodium lanthanum titanate. Data from Oak Ridge neutron source (POWGEN)

$Na_{0.24}La_{0.5867}TiO_3$	x	a (Å)	b (Å)	c (Å)	α	β	γ
Pbmm	0.173	5.4871	5.4834	7.7578	90	90	90
	Wyckoff	x	y	z	Uiso	Occ	
La	2e	0.7541	0.25	0	0.0095	0.827	
Na	2e	0.7541	0.25	0	0.0291	0.0964	
La	2f	0.7464	0.25	0.5	0.0019	0.3522	
Na	2f	0.7464	0.25	0.5	0.0043	0.3791	
Ti	4k	0.2541	0.25	0.252	0.0082		
O	2e	0.222	0.25	0	0.005		
O	2f	0.2666	0.25	0.5	0.0116		
O	4g	0	0	0.7314	0.0209		
O	4h	0.5	0	0.7793	0.013		
χ^2	Rp						
7.455	0.09						

Table 3.2.4 $Na_{(1-3x)/2}La_{(1+x)/2}TiO_3$ Rietveld refinement for sodium lanthanum titanate. Data from Oak Ridge neutron source (POWGEN)

$Na_{0.1625}La_{0.6125}TiO_3$	x	a (Å)	b (Å)	c (Å)	α	β	γ
Cmmm	0.173	7.7367	7.7591	7.7796	90	90	90
	Wyckoff	x	y	z	Uiso	Occ	
La	4i	0	0.25495	0	0.00267	0.9448	
Na	4i	0	0.25495	0	0.00883	0.0097	
La	4j	0	0.26182	0.5	0.00782	0.2814	
Na	4j	0	0.26182	0.5	0.00075	0.3117	
Ti	8o	0.24758	0	0.26021	0.00605		
O	4g	0.27316	0	0	0.00785		
O	4h	0.22411	0	0.5	0.01417		
O	4k	0	0	0.21414	0.006		
O	4l	0	0.5	0.26554	0.01089		
O	8m	0.25	0.75	0.23728	0.01262		
χ^2	Rp						
6.373	0.06						

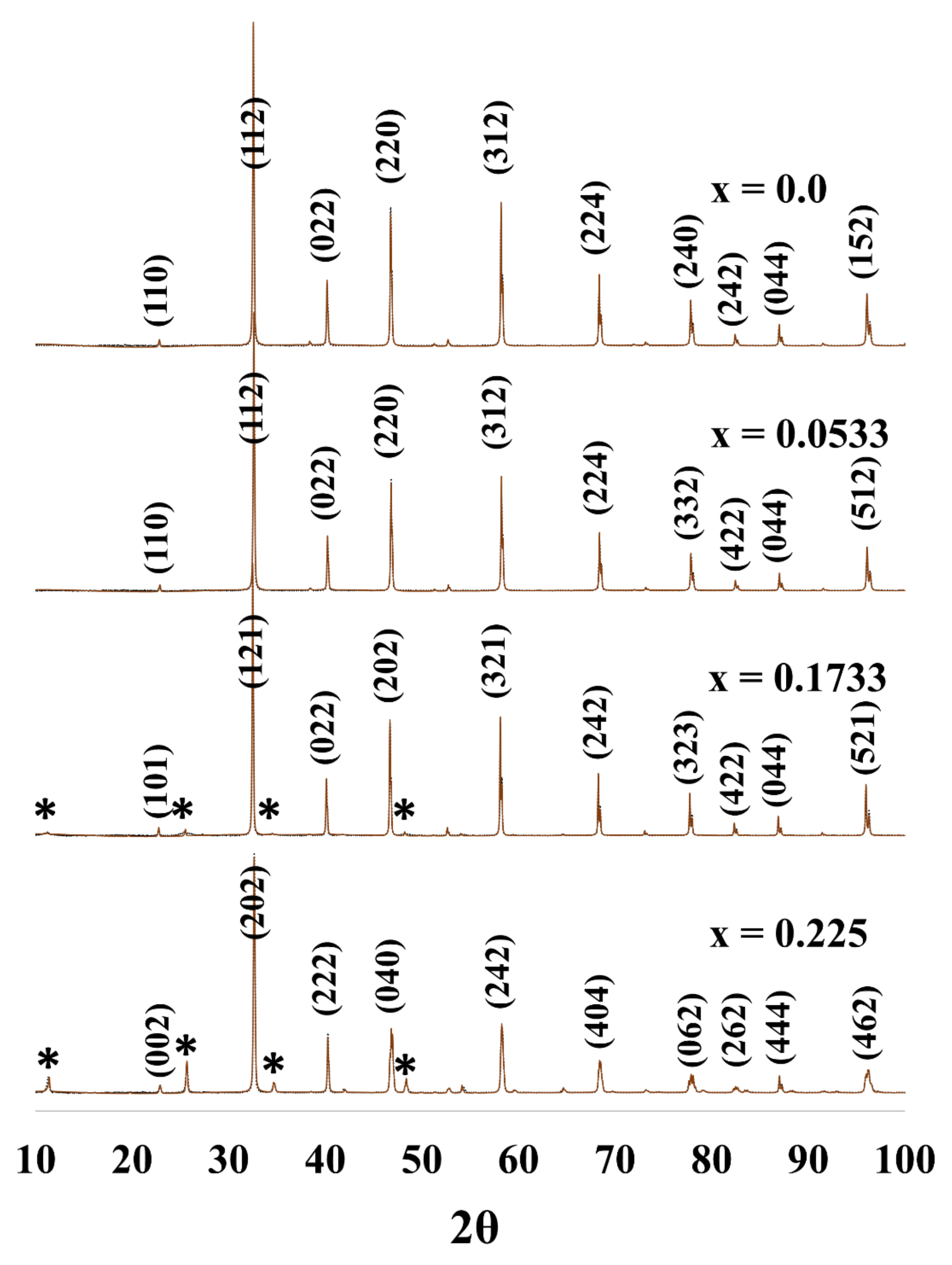

Figure 3.2. **$Na_{(1-3x)/2}La_{(1+x)/2}TiO_3$ X-ray diffraction $x = 0.0 – 0.225$. Peaks marked with * result from long-range A-site cation ordering.**

Figure 3.3 shows a comparison of calculated XRD patterns for the $x = 0.1733$ composition in space group *Pmma*. In this setting the A-site Wyckoff positions are 2e $\left(\frac{1}{4}, 0, z\right)$ and 2f $\left(\frac{1}{4}, \frac{1}{2}, z\right)$, each with a single degree of freedom. When $z = 0.75$ on both

2e and 2f, the result is non-characteristic orbits in which the atomic positions are identical to those in an ideal perovskite. These *z* values were adjusted in model calculations to analyze their effects on XRD patterns. Four different combinations of *z* values were compared in both ordered and disordered variations of this composition. Figure 3.3 has been indexed according to the pseudocubic unit cell, which is related to the orthorhombic one in *Pmma* by the following matrix transformation:

$$[a_o b_o c_o] = \begin{bmatrix} 1 & 0 & -1 \\ 0 & 2 & 0 \\ 1 & 0 & 1 \end{bmatrix} \begin{bmatrix} a_{pc} \\ b_{pc} \\ c_{pc} \end{bmatrix}$$

Clearly, alterations in *z* correspond to A-site cation displacements along $[101]_{pc}$. The simulations show that the peaks at 11.39° and 25.69°, corresponding to β superlattice reflections ½(010) and ½(012), respectively, are due to cation ordering alone; whereas the peaks corresponding to A-site cation displacements were dependent on the nature of those displacements. Unequal 2e and 2f *z* parameters give rise to the ½(111) peak at 19.82° and contribute weakly to the ½(101) and ½ (121) peaks at 16.17° and 28.16°, respectively. Equal 2e and 2f parameters yield strong ½(101) and ½(121) peaks but also contribute weakly to the ½(111) peak.

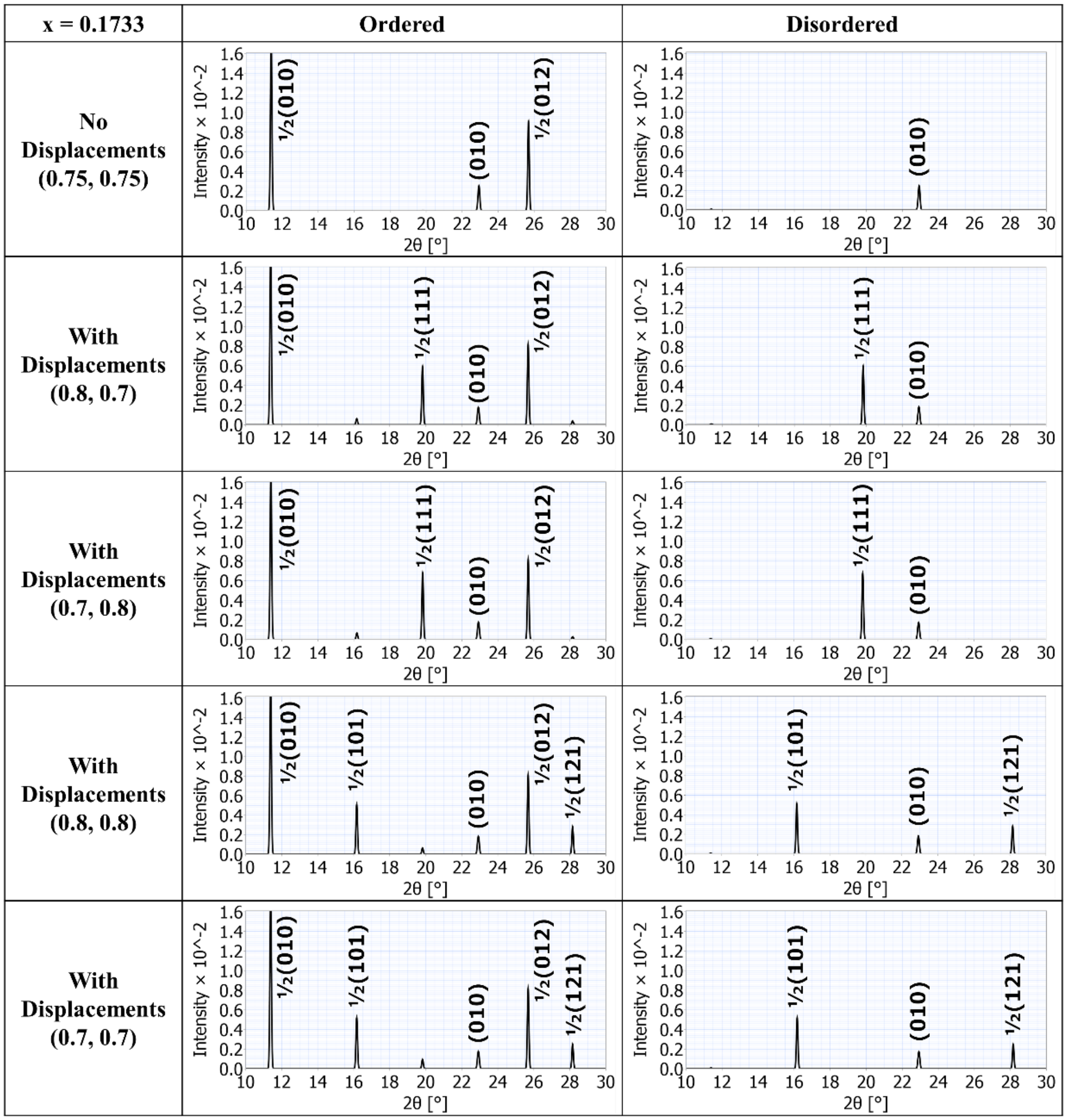

Figure 3.3. Simulated XRD traces for $Na_{(1-3x)/2}La_{(1+x)/2}TiO_3$ $x = 0.1733$ in *Pmma*, varying both the ordering state and A-site atomic positional displacements. The peaks have been indexed according to the pseudocubic unit cell.

EDS results are shown in Table 3.1 and demonstrate that there were no impurities detected and that the overall compositions were close (*i.e.*, within resolution error) to the nominal compositions. Moreover, the small amount of sodium loss resulted in a compositional average absolute relative error of less than 0.68 at%.

It is well known that ordered structures generally pack more efficiently than disordered ones,[53] which is the basis for the decrease in specific volume generally observed upon crystallization, so ordering in complex perovskites is typically expected to result in a decrease in unit volume. Zhang *et al.*[54] reported pyrochlore-to-defect-fluorite results for $Y_2Sn_{2-x}Zr_xO_7$ that support the conventional view of lattice contraction upon ordering. In that work, the lattice constant was found to decrease as Zr^{4+} (0.72 Å) was replaced by Sn^{+4} (0.69 Å). Part of the contraction is no doubt due to the size difference between these two species; however, the degree of order also reportedly increased (from defect-fluorite to pyrochlore) as the Sn^{4+} content (and so lattice constant) decreased. On the other hand, Karthik *et al.*[55] reported a decrease in cation order in lanthanide pyrohafnates as lattice constant decreased across the lanthanide series, a phenomenon that was easily explainable due to the large size reduction in the lanthanide species from La^{3+} to Lu^{3+}. In the case of B-site ordered $Ba(Mg_{1/3}Ta_{2/3})O_3$, Mani *et al.*[56] reported a unit cell with $a_{pc} = 4.0868$ Å. In this case, the modeling technique described above results in unexpectedly large positive errors in both a'_{pc} (0.952%) and a''_{pc} (1.595%), suggesting an overestimation of r_B caused by the volume shrinkage induced by ordering. Other examples are listed in Tables 3.2–3.3. Table 3.2 shows the results using the weighted average of B-site cation sizes[32] while r_B values in Table 3.3 [57-62] have been reduced, effectively decreasing the absolute errors in both a'_{pc} (0.000%) and a''_{pc} (0.000%). In order to confirm the assumption of volume shrinkage upon B-site ordering and thereby validate this method, the effect of B-site ordering was also calculated via DFT for $La(Zn_{0.5}Ti_{0.5})O_3$, reported [57] to form with B-site ordering in space group $P2_1/n$. These calculations show that the unit volume does, in fact, decrease upon ordering. The disordered form had a calculated unit volume at 0 K of 253.27 Å^3 compared to the ordered variant which had a unit volume of 252.24 Å^3., which had relative energies of 0.0952 eV and -0.2131 eV respectively; where these relative energies are measures of stability relative to each other (*i.e.*, centered around their respective average).

Table 3.3. B-site ordered compounds using ideal B cation sizes

Composition	$a_{pc(exptl)}$ (Å) Eqn. 1	a_{pc} (Å) Eqn. 6	Error (%)	a'_{pc} (Å) Eqn. 2	Error (%)	a''_{pc} (Å) Eqn. 3	Error (%)
[a]$Ba(Mg_{1/3}Ta_{2/3})O_3$	4.0868	4.1467	1.47	4.1257	0.95	4.1519	1.59
[b]$La(Zn_{1/2}Ti_{1/2})O_3$	3.9503	3.9903	1.01	3.9966	1.17	3.9868	0.92
[c]$Ca(Mg_{1/2}W_{1/2})O_3$	3.8707	3.9515	2.09	3.9628	2.38	3.9468	1.97
[d]$Sr(Mg_{1/2}W_{1/2})O_6$	3.9530	4.0298	1.94	4.0129	1.52	4.0295	1.94
[e]$Ba(Mg_{1/2}W_{1/2})O_3$	4.0542	4.1339	1.97	4.1152	1.51	4.1395	2.10
[f]$Pb(Mg_{1/2}W_{1/2})O_3$	4.0085	4.0724	1.60	4.0469	0.96	4.0746	1.65

[a] [56]
[b] [57]
[c] [58]
[d] [59]
[e] [60]
[f] [61]

Table 3.4. B-site ordered compounds accounting for the effect of B-site ordering

Composition	$r_{\text{B Corr.}}$ (Å)	a_{pc} (Å) Eqn. 6	Error (%)	a'_{pc} (Å) Eqn. 2	Error (%)	a''_{pc} (Å) Eqn. 3	Error (%)
$^{a}Ba_3MgTa_2O_9$	-0.02835	4.0806	-0.15	4.0868	0.00	4.0868	0.00
$^{b}La_2ZnTiO_6$	-0.02721	3.9536	0.08	3.9504	0.00	3.9503	0.00
$^{c}Ca_2MgWO_6$	-0.05385	3.8750	0.11	3.8707	0.00	3.8707	0.00
$^{d}Sr_2MgWO_6$	-0.10547	3.9395	-0.34	3.9530	0.00	3.9530	0.00
$^{e}Ba_2MgWO_6$	-0.04239	4.0464	-0.19	4.0542	0.00	4.0542	0.00
$^{f}Pb_2MgWO_6$	-0.07126	3.9982	-0.26	4.0085	0.00	4.0085	0.00

[a] [56]
[b] [57]
[c] [58]
[d] [59]
[e] [60]
[f] [61]

$Ba(Mg_{1/3}Ta_{2/3})O_3$ (BMT) results are shown in tables 3.4-3.17. This compound, which is known to fully order only after long periods at high temperature, was used to unambiguously support the prediction that B-site ordering is the cause of the volume shrinkage. Figure 3.4 demonstrates that as the order parameter increases the volume of the unit cell shrinks. The results showed that there was larger scatter/error in the data around the 10hrs domain; thus, additional samples were annealed for 10 hours in the box and tube furnaces to improve the statistical precision. Most samples were annealed for longer durations ($15 \leq \text{hrs} \leq 40$) in the tube furnace. The order parameter was calculated by the difference of the occupancies of the two B site species between the two Wyckoff positions $|[Mg]_{Mg(1b)} - [Mg]_{Ta(2d)}|$, or $|[Ta]_{Ta(2d)} - [Ta]_{Mg(1b)}|$.

Table 3.5.1 1st $Ba_2(MgTa_2)O_9$ Unannealed, X-ray Powder Rietveld Refinement Results

a (Å)	**b (Å)**	**c (Å)**	**α (°)**	**β (°)**	**γ (°)**	**S.G.**	**Vol(Å^3)**	**Order**
5.7823	5.7823	7.0748	90	90	120	*P*-3*m*1	204.855	0.248
	Species	**Valence**	**Wyckoff**	**x**	**y**	**z**	**U**	**SOF**
	Ba	+2	1a	0	0	0	0.0005	
	Ba	+2	2d	0.3333	0.6667	0.6619	0.0045	
	Mg	+2	1b	0	0	0.5	0.0016	0.4991
	Ta	+5	1b	0	0	0.5	0.0016	0.5220
	Ta	+5	2d	0.3333	0.6667	0.1675	0.0041	0.7404
	Mg	+2	2d	0.3333	0.6667	0.1675	0.0041	0.2512
	O	-2	3e	0.5	0	0	0.0071	
	O	-2	6i	0.1589	-0.1589	0.3429	0.0051	

Table 3.5.2 1st $Ba_2(MgTa_2)O_9$ Annealed 5-hours, X-ray Powder Rietveld Refinement Results

a (Å)	**b (Å)**	**c (Å)**	**α (°)**	**β (°)**	**γ (°)**	**S.G.**	**Vol(Å^3)**	**Order**
5.7783	5.7783	7.0805	90	90	120	*P*-3*m*1	204.737	0.275
	Species	**Valence**	**Wyckoff**	**x**	**y**	**z**	**U**	**SOF**
	Ba	+2	1a	0	0	0	0.0061	
	Ba	+2	2d	0.3333	0.6667	0.6647	0.0035	
	Mg	+2	1b	0	0	0.5	0.0005	0.5164
	Ta	+5	1b	0	0	0.5	0.0005	0.4888
	Ta	+5	2d	0.3333	0.6667	0.1696	0.0044	0.7560
	Mg	+2	2d	0.3333	0.6667	0.1696	0.0044	0.2418
	O	-2	3e	0.5	0	0	0.0101	
	O	-2	6i	0.1710	-0.171	0.3437	0.0047	

Table 3.5.3 2nd $Ba_2(MgTa_2)O_9$ Annealed 5-hours, X-ray Powder Rietveld Refinement Results

a (Å)	**b (Å)**	**c (Å)**	**α (°)**	**β (°)**	**γ (°)**	**S.G.**	**Vol(Å^3)**	**Order**
5.7767	5.7767	7.0816	90	90	120	*P*-3*m*1	204.656	0.454
	Species	**Valence**	**Wyckoff**	**x**	**y**	**z**	**U**	**SOF**
	Ba	+2	1a	0	0	0	0.0029	
	Ba	+2	2d	0.3333	0.6667	0.6646	0.0029	
	Mg	+2	1b	0	0	0.5	0.0017	0.6335
	Ta	+5	1b	0	0	0.5	0.0017	0.3707
	Ta	+5	2d	0.3333	0.6667	0.1724	0.0021	0.8184
	Mg	+2	2d	0.3333	0.6667	0.1724	0.0021	0.1792
	O	-2	3e	0.5	0	0	0.0101	
	O	-2	6i	0.1700	-0.1700	0.3432	0.0020	

Table 3.5.4 1st $Ba_2(MgTa_2)O_9$ Annealed 10-hours (box), X-ray Powder Rietveld Refinement Results

a (Å)	**b (Å)**	**c (Å)**	**α (°)**	**β (°)**	**γ (°)**	**S.G.**	**Vol(Å^3)**	**Order**
5.7771	5.7771	7.0797	90	90	120	*P*-3*m*1	204.623	0.326
	Species	**Valence**	**Wyckoff**	**x**	**y**	**z**	**U**	**SOF**
	Ba	+2	1a	0	0	0	0.0043	
	Ba	+2	2d	0.3333	0.6667	0.6649	0.0027	
	Mg	+2	1b	0	0	0.5	0.0009	0.5503
	Ta	+5	1b	0	0	0.5	0.0009	0.4499
	Ta	+5	2d	0.3333	0.6667	0.1706	0.0031	0.7721
	Mg	+2	2d	0.3333	0.6667	0.1706	0.0031	0.2244
	O	-2	3e	0.5	0	0	0.0124	
	O	-2	6i	0.1703	-0.1703	0.3439	0.0030	

Table 3.5.5 1st $Ba_2(MgTa_2)O_9$ Annealed 10-hours, X-ray Powder Rietveld Refinement Results

a (Å)	b (Å)	c (Å)	α (°)	β (°)	γ (°)	S.G.	Vol(Å^3)	Order
5.7768	5.7768	7.0823	90	90	120	*P*-3*m*1	204.683	0.491
	Species	**Valence**	**Wyckoff**	**x**	**y**	**z**	**U**	**SOF**
	Ba	+2	1a	0	0	0	0.0039	
	Ba	+2	2d	0.3333	0.6667	0.6645	0.0026	
	Mg	+2	1b	0	0	0.5	0.0007	0.6612
	Ta	+5	1b	0	0	0.5	0.0007	0.3431
	Ta	+5	2d	0.3333	0.6667	0.1737	0.0031	0.8267
	Mg	+2	2d	0.3333	0.6667	0.1737	0.0031	0.1702
	O	-2	3e	0.5	0	0	0.0266	
	O	-2	6i	0.1696	-0.1696	0.3462	0.0009	

Table 3.5.6 2nd $Ba_2(MgTa_2)O_9$ Annealed 10-hours, X-ray Powder Rietveld Refinement Results

a (Å)	b (Å)	c (Å)	α (°)	β (°)	γ (°)	S.G.	Vol(Å^3)	Order
5.7728	5.7728	7.0839	90	90	120	*P*-3*m*1	204.442	0.677
	Species	**Valence**	**Wyckoff**	**x**	**y**	**z**	**U**	**SOF**
	Ba	+2	1a	0	0	0	0.0022	
	Ba	+2	2d	0.3333	0.6667	0.6645	0.0010	
	Mg	+2	1b	0	0	0.5	0.0009	0.7851
	Ta	+5	1b	0	0	0.5	0.0009	0.2176
	Ta	+5	2d	0.3333	0.6667	0.1765	0.0017	0.8901
	Mg	+2	2d	0.3333	0.6667	0.1765	0.0017	0.1084
	O	-2	3e	0.5	0	0	0.0339	
	O	-2	6i	0.1698	-0.1698	0.3443	0.0023	

Table 3.5.7 1st $Ba_2(MgTa_2)O_9$ Annealed 15-hours, X-ray Powder Rietveld Refinement Results

a (Å)	**b (Å)**	**c (Å)**	**α (°)**	**β (°)**	**γ (°)**	**S.G.**	**Vol(Å^3)**	**Order**
5.7712	5.7712	7.0822	90	90	120	*P*-3*m*1	204.289	0.661
	Species	**Valence**	**Wyckoff**	**x**	**y**	**z**	**U**	**SOF**
	Ba	+2	1a	0	0	0	0.0030	
	Ba	+2	2d	0.3333	0.6667	0.6651	0.0032	
	Mg	+2	1b	0	0	0.5	0.0074	0.7737
	Ta	+5	1b	0	0	0.5	0.0074	0.2148
	Ta	+5	2d	0.3333	0.6667	0.1769	0.0018	0.8886
	Mg	+2	2d	0.3333	0.6667	0.1769	0.0018	0.1127
	O	-2	3e	0.5	0	0	0.0288	
	O	-2	6i	0.1751	-0.1751	0.3398	0.0010	

Table 3.5.8 2nd $Ba_2(MgTa_2)O_9$ Annealed 15-hours, X-ray Powder Rietveld Refinement Results

a (Å)	**b (Å)**	**c (Å)**	**α (°)**	**β (°)**	**γ (°)**	**S.G.**	**Vol(Å^3)**	**Order**
5.7726	5.7726	7.0898	90	90	120	*P*-3*m*1	204.602	0.725
	Species	**Valence**	**Wyckoff**	**x**	**y**	**z**	**U**	**SOF**
	Ba	+2	1a	0	0	0	0.0020	
	Ba	+2	2d	0.3333	0.6667	0.6656	0.0053	
	Mg	+2	1b	0	0	0.5	0.0195	0.8153
	Ta	+5	1b	0	0	0.5	0.0195	0.1579
	Ta	+5	2d	0.3333	0.6667	0.1803	0.0006	0.9118
	Mg	+2	2d	0.3333	0.6667	0.1803	0.0006	0.0908
	O	-2	3e	0.5	0	0	0.0298	
	O	-2	6i	0.1743	-0.1743	0.3348	0.0001	

Table 3.5.9 1st $Ba_2(MgTa_2)O_9$ Annealed 20-hours, X-ray Powder Rietveld Refinement Results

a (Å)	**b (Å)**	**c (Å)**	**α (°)**	**β (°)**	**γ (°)**	**S.G.**	**Vol(Å^3)**	**Order**
5.7731	5.7731	7.0857	90	90	120	*P*-3*m*1	204.518	0.763
	Species	**Valence**	**Wyckoff**	**x**	**y**	**z**	**U**	**SOF**
	Ba	+2	1a	0	0	0	0.0039	
	Ba	+2	2d	0.3333	0.6667	0.6640	0.0026	
	Mg	+2	1b	0	0	0.5	0.0024	0.8416
	Ta	+5	1b	0	0	0.5	0.0024	0.1603
	Ta	+5	2d	0.3333	0.6667	0.1770	0.0023	0.9186
	Mg	+2	2d	0.3333	0.6667	0.1770	0.0023	0.0786
	O	-2	3e	0.5	0	0	0.0406	
	O	-2	6i	0.1693	-0.1693	0.3459	0.0033	

Table 3.5.10 2nd $Ba_2(MgTa_2)O_9$ Annealed 20-hours, X-ray Powder Rietveld Refinement Results

a (Å)	**b (Å)**	**c (Å)**	**α (°)**	**β (°)**	**γ (°)**	**S.G.**	**Vol(Å^3)**	**Order**
5.7726	5.7726	7.0883	90	90	120	*P*-3*m*1	204.559	0.860
	Species	**Valence**	**Wyckoff**	**x**	**y**	**z**	**U**	**SOF**
	Ba	+2	1a	0	0	0	0.0036	
	Ba	+2	2d	0.3333	0.6667	0.6639	0.0026	
	Mg	+2	1b	0	0	0.5	0.0007	0.9076
	Ta	+5	1b	0	0	0.5	0.0007	0.1024
	Ta	+5	2d	0.3333	0.6667	0.1783	0.0025	0.9495
	Mg	+2	2d	0.3333	0.6667	0.1783	0.0025	0.0476
	O	-2	3e	0.5	0	0	0.0423	
	O	-2	6i	0.1672	-0.1672	0.3467	0.0033	

Table 3.5.11 1st $Ba_2(MgTa_2)O_9$ Annealed 30-hours, X-ray Powder Rietveld Refinement Results

a (Å)	**b (Å)**	**c (Å)**	**α (°)**	**β (°)**	**γ (°)**	**S.G.**	**Vol(Å^3)**	**Order**
5.7716	5.7716	7.0906	90	90	120	*P*-3*m*1	204.554	0.928
	Species	**Valence**	**Wyckoff**	**x**	**y**	**z**	**U**	**SOF**
	Ba	+2	1a	0	0	0	0.0035	
	Ba	+2	2d	0.3333	0.6667	0.6637	0.0029	
	Mg	+2	1b	0	0	0.5	0.0017	0.9524
	Ta	+5	1b	0	0	0.5	0.0017	0.0565
	Ta	+5	2d	0.3333	0.6667	0.1795	0.0022	0.9720
	Mg	+2	2d	0.3333	0.6667	0.1795	0.0022	0.0245
	O	-2	3e	0.5	0	0	0.0455	
	O	-2	6i	0.1661	-0.1661	0.3455	0.0034	

Table 3.5.12 2nd $Ba_2(MgTa_2)O_9$ Annealed 30-hours, X-ray Powder Rietveld Refinement Results

a (Å)	**b (Å)**	**c (Å)**	**α (°)**	**β (°)**	**γ (°)**	**S.G.**	**Vol(Å^3)**	**Order**
5.7722	5.7722	7.0914	90	90	120	*P*-3*m*1	204.617	0.939
	Species	**Valence**	**Wyckoff**	**x**	**y**	**z**	**U**	**SOF**
	Ba	+2	1a	0	0	0	0.0038	
	Ba	+2	2d	0.3333	0.6667	0.6633	0.0026	
	Mg	+2	1b	0	0	0.5	0.0019	0.9600
	Ta	+5	1b	0	0	0.5	0.0019	0.0502
	Ta	+5	2d	0.3333	0.6667	0.1793	0.0024	0.9756
	Mg	+2	2d	0.3333	0.6667	0.1793	0.0024	0.0208
	O	-2	3e	0.5	0	0	0.0560	
	O	-2	6i	0.1656	-0.1656	0.3458	0.0033	

Table 3.5.13 1st $Ba_2(MgTa_2)O_9$ Annealed 40-hours, X-ray Powder Rietveld Refinement Results

a (Å)	**b (Å)**	**c (Å)**	**α (°)**	**β (°)**	**γ (°)**	**S.G.**	**Vol(Å^3)**	**Order**
5.7700	5.7700	7.0888	90	90	120	*P*-3*m*1	204.383	0.941
	Species	**Valence**	**Wyckoff**	**x**	**y**	**z**	**U**	**SOF**
	Ba	+2	1a	0	0	0	0.0036	
	Ba	+2	2d	0.3333	0.6667	0.6634	0.0028	
	Mg	+2	1b	0	0	0.5	0.0044	0.9604
	Ta	+5	1b	0	0	0.5	0.0044	0.0462
	Ta	+5	2d	0.3333	0.6667	0.1795	0.0020	0.9760
	Mg	+2	2d	0.3333	0.6667	0.1795	0.0020	0.0198
	O	-2	3e	0.5	0	0	0.0607	
	O	-2	6i	0.1654	-0.1654	0.3494	0.0046	

Table 3.5.14 2nd $Ba_2(MgTa_2)O_9$ Annealed 40-hours, X-ray Powder Rietveld Refinement Results

a (Å)	**b (Å)**	**c (Å)**	**α (°)**	**β (°)**	**γ (°)**	**S.G.**	**Vol(Å^3)**	**Order**
5.7709	5.7709	7.0899	90	90	120	*P*-3*m*1	204.483	0.945
	Species	**Valence**	**Wyckoff**	**x**	**y**	**z**	**U**	**SOF**
	Ba	+2	1a	0	0	0	0.0038	
	Ba	+2	2d	0.3333	0.6667	0.6635	0.0027	
	Mg	+2	1b	0	0	0.5	0.0039	0.9635
	Ta	+5	1b	0	0	0.5	0.0039	0.0457
	Ta	+5	2d	0.3333	0.6667	0.1792	0.0022	0.9776
	Mg	+2	2d	0.3333	0.6667	0.1792	0.0022	0.0190
	O	-2	3e	0.5	0	0	0.0561	
	O	-2	6i	0.1668	-0.1668	0.3461	0.0033	

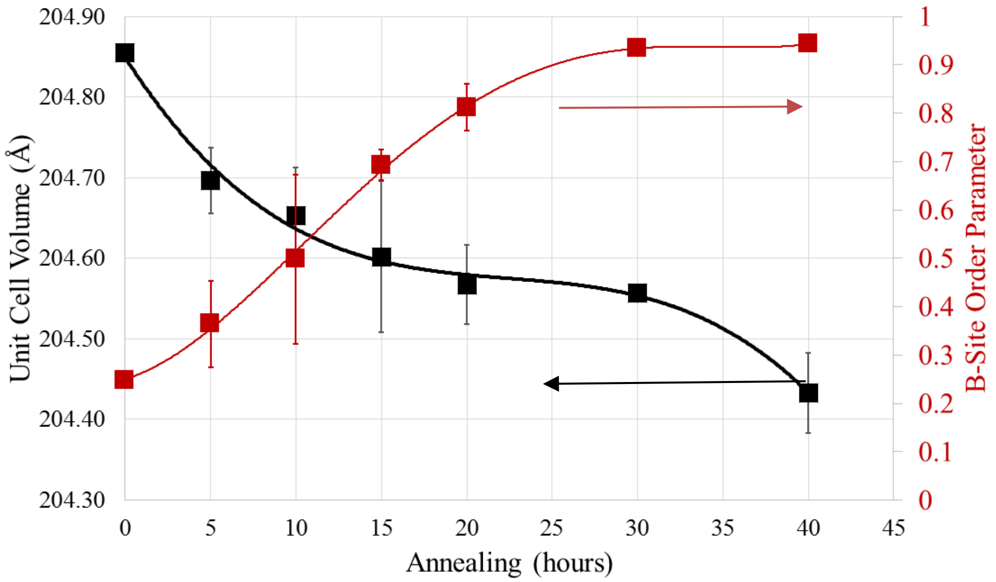

Figure 3.4 $Ba_2(MgTa_2)O_9$ unit-cell volume (black curve) and order parameter (red curve) as a function of annealing time.

$$Vol = 204.85 - 0.0332h + 0.0014h^2 - 2\times10^{-5}h^3 (R^2 = 0.9917) \qquad (3.7)$$

$$\eta_{BMT}[t] = \frac{a}{1+Exp\left[\frac{b-t}{c}\right]} \quad (R^2 = 0.9989) \qquad (3.8)$$

where the order parameter (as a function of time) constants are: a = 0.973062, b = 8.72456, and c = 7.37166.

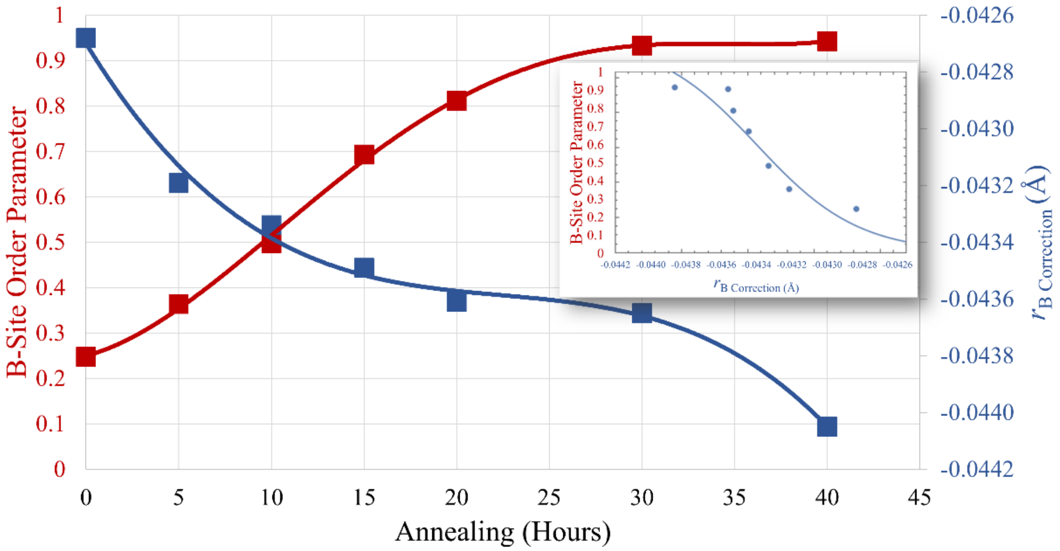

Figure 3.5 $Ba_2(MgTa_2)O_9$ order parameter (red curve) and B-site size adjustment (blue curve) as a function of annealing time. The inset shows the order parameter as a function of $r_{B\ \mathrm{correction}}$ and can be thought of as an empirical model for ordering (0 = disorder, 1 = fully ordered).

$$r_{B(Corr.)} = -0.0427 - 0.0001h + 5\times10^{-6}h^2 - 7\times10^{-8}h^3 (R^2 = 0.9925) \tag{3.9}$$

where the $r_{B(\mathrm{corr.})}$ is a function of annealing hours, hrs.

$$\eta_{BMT}[\delta_{rB}] = \frac{a}{1 + Exp\left[\frac{b + \delta_{rB}}{c}\right]} + d \tag{3.10}$$

where the order parameter (as a function of $r_{B(\mathrm{corr.})}$) constants are: a = 0.722859, b = 0.0434335, and c = 1.26873x10^{-4}, and d = 0.251083.

The same volume shrinkage observed upon B-site ordering might be assumed for the case of A-site ordering as well; however, it seems that the volume actually *increases* for A-site ordering (Tables 3.4–3.8). First-principles DFT calculations for $Na_{0.5}La_{0.5}TiO_3$ in a tetragonal setting (*I4/mcm*) show that the unit volume increases upon A-site layered or columnar type ordering compared to the disordered structure (Table 3.6), which is both counterintuitive and opposite to the shrinkage observed upon B-site ordering. The relative-energy results suggest that the type of A-site ordering in NLT would likely be layered, as expected from the observed frequency of the occurrence of this type of ordering with respect to the other types. These calculations included only a few unit cells and so the results are consistent with the existence of ordered nanodomains found experimentally via electron diffraction and do not necessarily imply the existence of long-range order.

Table 3.6. DFT (500 eV) Tetragonal $Na_{0.5}La_{0.5}TiO_3$ A-site ordered nanodomain structures

Tetragonal	*a* (Å)	*b* (Å)	*c* (Å)	V (Å^3)	Rel. E (eV)
Columnar	5.4901	5.4901	7.8880	237.75	0.0570
Layered	5.4744	5.4744	7.9358	237.83	-0.1915
Rocksalt	5.4660	5.4660	7.8901	235.74	0.1344
Disordered	5.5187	5.5187	7.7838	237.06	-0.0664

The same DFT calculations for $Na_{0.5}La_{0.5}TiO_3$ in a trigonal setting show that the unit volume increases upon any type of A-site ordering (Table 3.7); however, once again the layered-type ordering is the most energetically favorable geometry. Table 3.8 shows the calculated errors corresponding to the empirical model described in chapter 2. This model shows a small but negative error in a'_{pc} for the $x = 0$ composition which suggests that the calculated a'_{pc} (which is a function of the A – O bond length, equation 3.2), which assumes cation disorder, is smaller than the $a_{pc\ (Exptl.)}$. The difference can be explained if the A-site ordered form, suggested to exist in nanodomains, has a larger unit volume than does the disordered form. Errors generally increase as x increases

(Table 3.8), suggesting that the degree of cation ordering simultaneously decreases. The $(Na,Li)_{(1-3x)/2}La_{(1+x)/2}TiO_3$ order parameter was calculated by the absolute quantity of the difference between the species occupancy in site one and its occupancy in site two. For example, in $Na_{0.24}La_{0.5867}TiO_3$ the Na order parameter would be solved by |[Na]2e-[Na]2f| = |0.72-0.48| = 0.48 and/or for vacancy order parameter it would then be |[V]2e-[V]2f| = |0.6-0.1| = 0.5. Structural models for $0 < x \leq ⅓$ [10, 20] show that the degree of cation ordering indeed decreases with x whilst the degree of vacancy ordering generally increases, and the $x = ⅓$ end member ($La_{2/3}TiO_3$) has a layered structure in which slabs of $La_2Ti_3O_9$ are separated and sheared by interlayers without cations[20] (*i.e.*, full vacancy ordering). The empirical model, which just produces a 0.21% error for $La_{2/3}TiO_3$, is apparently sensitive to cation ordering (which affects bond lengths) but not vacancy ordering (which does not). It should be further noted that at $x = 0$, where the strongest evidence of an ordering phenomenon exists, there can be no contribution from vacancy ordering, as no stoichiometric vacancies exist in this composition. Increasing the effective r_A value has the effect of both increasing a'_{pc} and, because of its effect on tolerance factor and hence r_O, a''_{pc}. Table 3.9 shows the results after increasing r_A in order to simultaneously minimize the absolute relative errors in both a'_{pc} and a''_{pc} in $0 \leq x \leq 0.055$ compositions.

Table 3.7 DFT (500 eV) Trigonal $Na_{0.5}La_{0.5}TiO_3$ A-site ordered nanodomain structures

Hexagonal	a (Å)	b (Å)	c (Å)	V (Å^3)	Rel. E (eV)
Columnar	5.5356	5.5356	13.5601	359.82	-0.0012
Layered	5.5304	5.5304	13.5573	359.70	-0.0176
Rocksalt	5.5274	5.5274	13.5256	357.87	0.0188
Disordered	5.5185	5.5185	13.5080	356.31	-0.0204

Table 3.8 $Na_{(1-3x)/2}La_{(1+x)/2}TiO_3$ calculated pseudocubic lattice constants a'_{pc} and a''_{pc}

Composition	a (Å)	b (Å)	c (Å)	a_{pc}	a'_{pc}	Error%	a''_{pc}	Error%
[a] x = 0.0	5.4769	5.4769	7.7539	3.8742	3.8670	-0.19	3.8663	-0.20
[b] x = 0.0533	5.4798	5.4753	7.7432	3.8727	3.8677	-0.13	3.8626	-0.26
[b] x = 0.1733	5.4763	7.7624	5.4766	3.8754	3.8860	0.28	3.8782	0.07
[b] x = 0.2233	7.7234	7.7485	7.7803	3.8753	3.9011	0.66	3.8950	0.51
[c] x = 0.3333	3.8565	3.8565	24.645	3.9384	3.9467	0.21	3.9501	0.30

[a] [10]
[b] [9]
[c] [19]

Table 3.9 $Na_{(1-3x)/2}La_{(1+x)/2}TiO_3$ accounting for the cation effective sizes

Composition	$r_{A\ Corr.}$ (Å)	%	a_{pc}	Error%	a'_{pc}	Error%	a''_{pc}	Error%
[a] x = 0.0	0.0251	1.183	3.8969	0.588	3.8706	-0.090	3.8776	0.090
[b] x = 0.0533	0.0236	1.182	3.8873	0.377	3.8726	-0.001	3.8732	0.013
[b] x = 0.1733	0.0052	0.460	3.8908	0.399	3.8754	0.001	3.8754	0.001
[b] x = 0.2233	0.0005	0.047	3.9015	0.675	3.8881	0.330	3.8753	0.000
[c] x = 0.3333	0.0000	0.000	3.9457	0.185	3.9449	0.165	3.9384	0.000

[a] [10]
[b] [9]
[c] [19]

If increasing r_A reduces the absolute error in a'_{pc}, then the initial underestimation in r_A could indicate A-site cation ordering (*i.e.*, such ordering manifests itself in this empirical model as an increased effective A-site size). Furthermore, the degree of this ordering can be calibrated from published models (*i.e.*, Figure 3.4) and the model used to interpolate/extrapolate it for other compositions by comparing the error in a'_{pc} to that in either a''_{pc} or a_{pc}. In this case, the smaller correction needed at $x = 0.053$ than at $x = 0$ is indicative of the lower degree of order which one would anyway expect further from the 1:1 stoichiometry (even though that order is only short-range at $x = 0$).

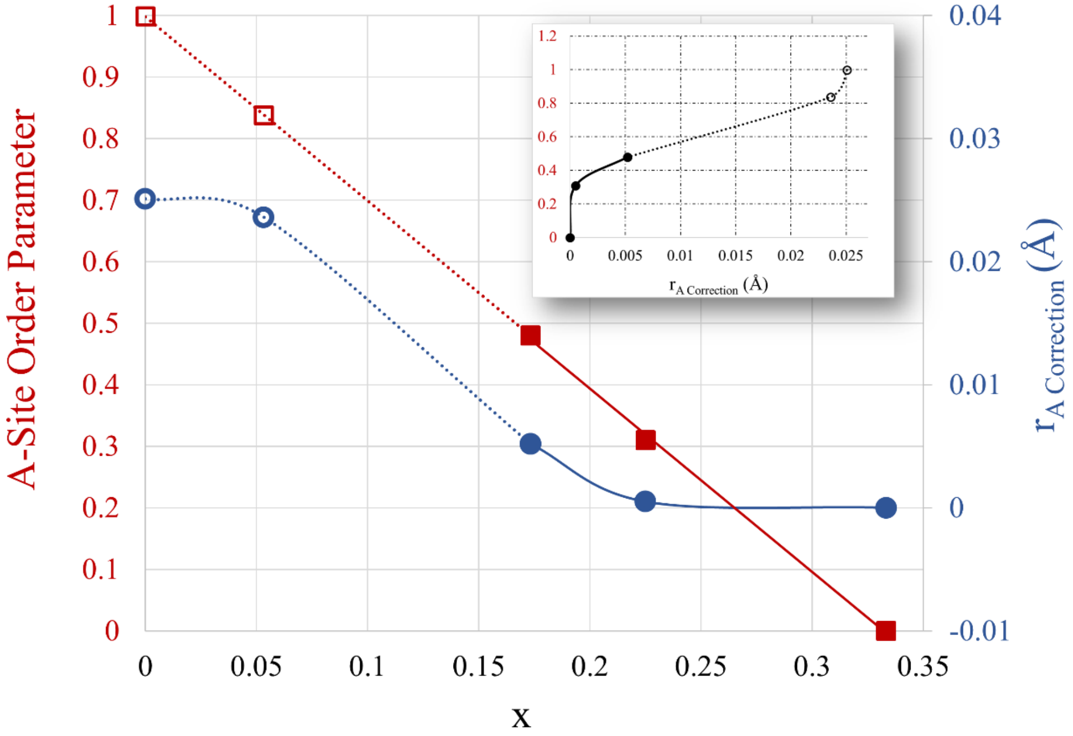

Figure 3.6. $Na_{(1-3x)/2}La_{(1+x)/2}TiO_3$ ordering from reported [9] site occupancies where the open data points are extrapolated according to the empirical model and correspond to compositions in which the order is short-range only. The inset shows the order parameter as a function of $r_{A\ correction}$ and can be thought of as an empirical model for ordering (0 = disorder, 1 = fully ordered).

$$\delta r_{A(NLT)} = \frac{a}{1 + Exp\left[\frac{x-b}{c}\right]} \tag{3.11}$$

where the NLT $r_{A(Corr.)}$ (as a function of vacancy concentration) constants are: *a* = 0.0262713, *b* = 0.123861, and *c* = 0.0352378.

$$\eta_{NLT-Short-Range-Order} = a - b\left[Log\left(\frac{c}{r_{B(Corr.)}} - 1\right)\right] \tag{3.12}$$

where the NLT short-range-order parameter (as a function of $r_{\mathrm{A(Corr.)}}$) constants are: $a = 0.62$, $b = 0.088$, and $c = 0.0254$.

Figure 3.7 shows selected-area electron-diffraction patterns (SADPs) of $\mathrm{Na_{(1-3x)/2}La_{(1+x)/2}TiO_3}$ indexed according to the pseudocubic unit cell; whereas Figure 3.8 shows the same SADPs calculated by inputting the crystallographic data into SingleCrystal$^{\mathrm{TM}}$ Software (CrystalMaker Software Limited, Oxfordshire, UK). TEM results show two sets of superlattice reflections (*i.e.*, β reflections from A-site ordering and γ reflections from in-phase octahedral tilting) in the $[100]_{\mathrm{pc}}$ zone axis for $x \geq 0.0533$, but a single diffuse β set at $x = 0$ corresponding only to short-range ordering. The β reflections observed in the $x = 0$ composition are not only diffuse, indicative of short-range order, but also slightly curved (Fig. 3.6 inset), suggestive of the existence of ordered nanodomains for which the Bragg condition is relaxed. Diffraction from such nanodomains occurs at a wider angular range than would otherwise be expected, in an analogous way to peak broadening observed in XRD patterns and explained via the Scherrer formula, but the spacing of crystalline planes within the domains remains constant; thus diffraction arcs are observed in SADPs. Two sets of superlattice reflections also appeared in the $[110]_{\mathrm{pc}}$ zone-axis patterns (Figure 3.7) due to A-site ordering (β) and anti-phase octahedral tilting (α); but while the latter are always discrete spots, the ordering reflections are again diffuse for $x = 0$ and only discrete for $x \geq 0.0533$. In figure 3.5, the symbols α, β, and γ correspond to ½{*odd, odd, odd*}, ½{*even, even, odd*}, and ½{*odd, odd, even*}, respectively.

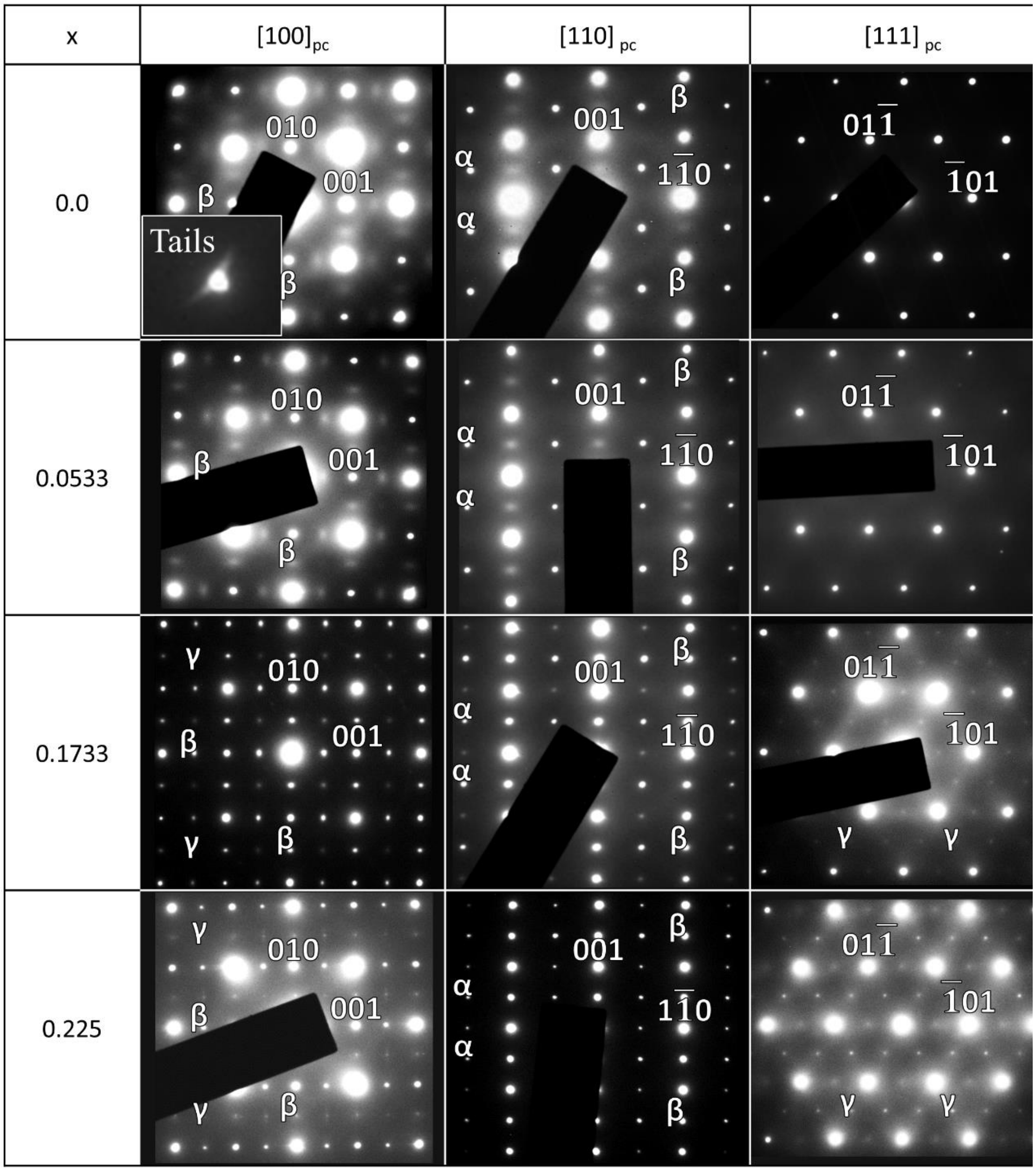

Figure 3.7. $Na_{(1-3x)/2}La_{(1+x)/2}TiO_3$ selected area electron diffraction patterns of $x = 0.0 – 0.225$ with the associated pseudocubic indexing. Some of the α, β, and γ superlattice reflections are indicated for each pattern.

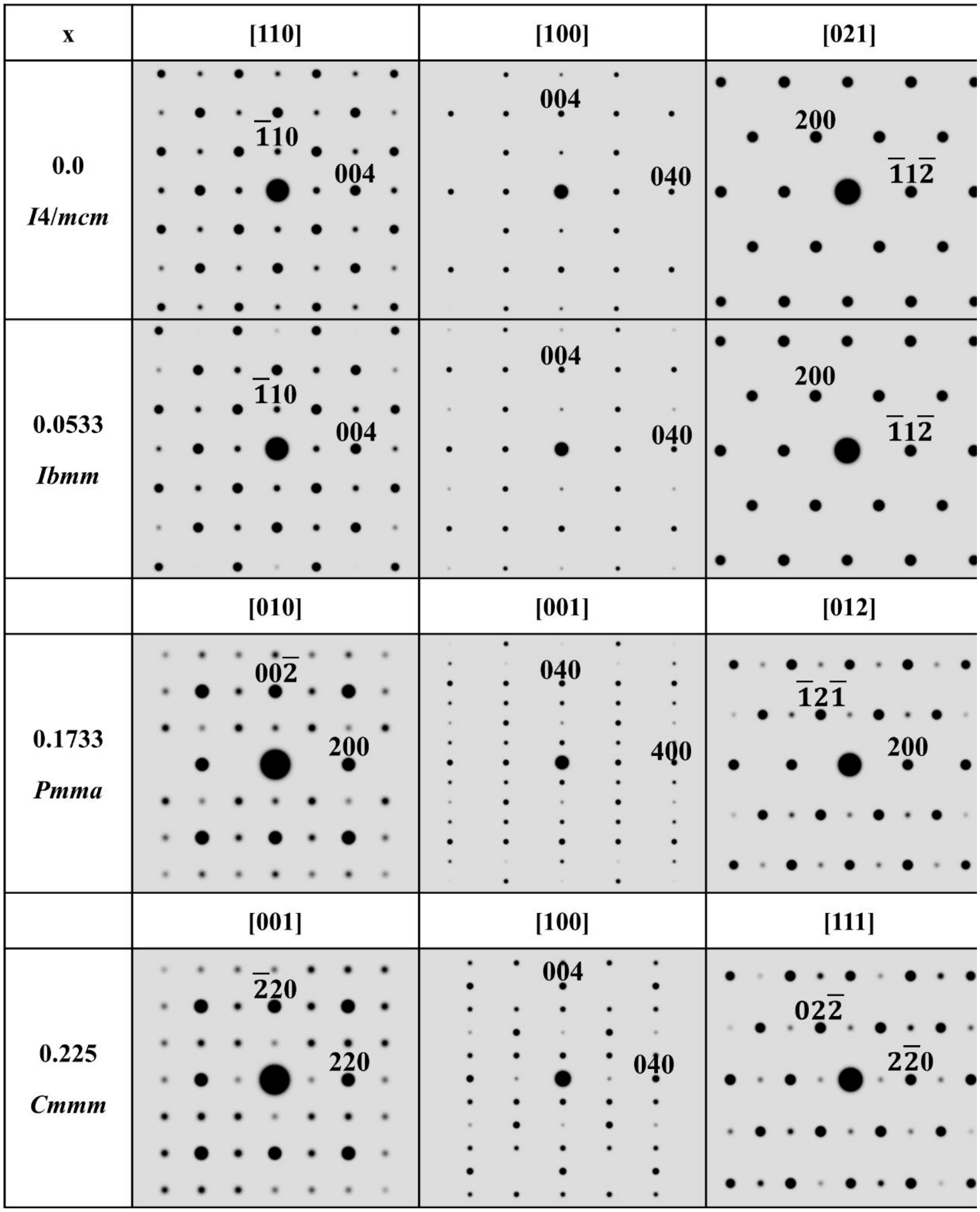

Figure 3.8. $Na_{(1-3x)/2}La_{(1+x)/2}TiO_3$ selected area electron diffraction patterns of $x = 0.0 – 0.225$ with the appropriate space group indexing

While reflections of the type ½{*even*, *even*, *odd*} (β) have typically been ascribed to antiparallel cation displacements, the superlattice peaks observed in Figure 3.2 correspond to those in the top left-hand side pattern of Figure 3.3 (*i.e.*, ordering, not cation displacement). Furthermore, ordering is the only explanation for the observed ½(010) peak at 11.39° in Figure 3.3 or, by extension, the ½{010} diffuse spots in Figure 3.7. Antiparallel cation displacements can be discounted due to the lack of a strong ½(111) reflection, and parallel displacement can similarly be ruled out due to the lack of a strong ½(101) reflection. Diffuse scattering such as that observed in Figure 3.7 is commonly attributed to short-range ordering effects but can also arise due to spinodal decomposition or premartensitic reactions,[62] neither of which is expected in this system. Indeed, such diffuse scattering is normally attributed to short-range ordering phenomena in both pyrochlores[43] and NaCl-structured transition-metal carbides/nitrides [63] as well as other systems.[64]

In Figure 3.7 it is noteworthy that the $[111]_{pc}$ patterns for $x = 0.1733$ and $x = 0.225$ both contain three sets of weak γ superlattice reflections, whereas the corresponding calculated patterns in Figure 3.8 contain just a single set each. The extra two sets of reflections could be explained by overlapping twin variants;[45] however, as care was taken to avoid this potential complication and every $<111>_{pc}$ pattern observed in both compositions contained similar reflections, it seems more likely that the models in *Pmma* [10] or *Cmmm* (reported for $x = 0.2233$) [10] cannot fully explain these structures.

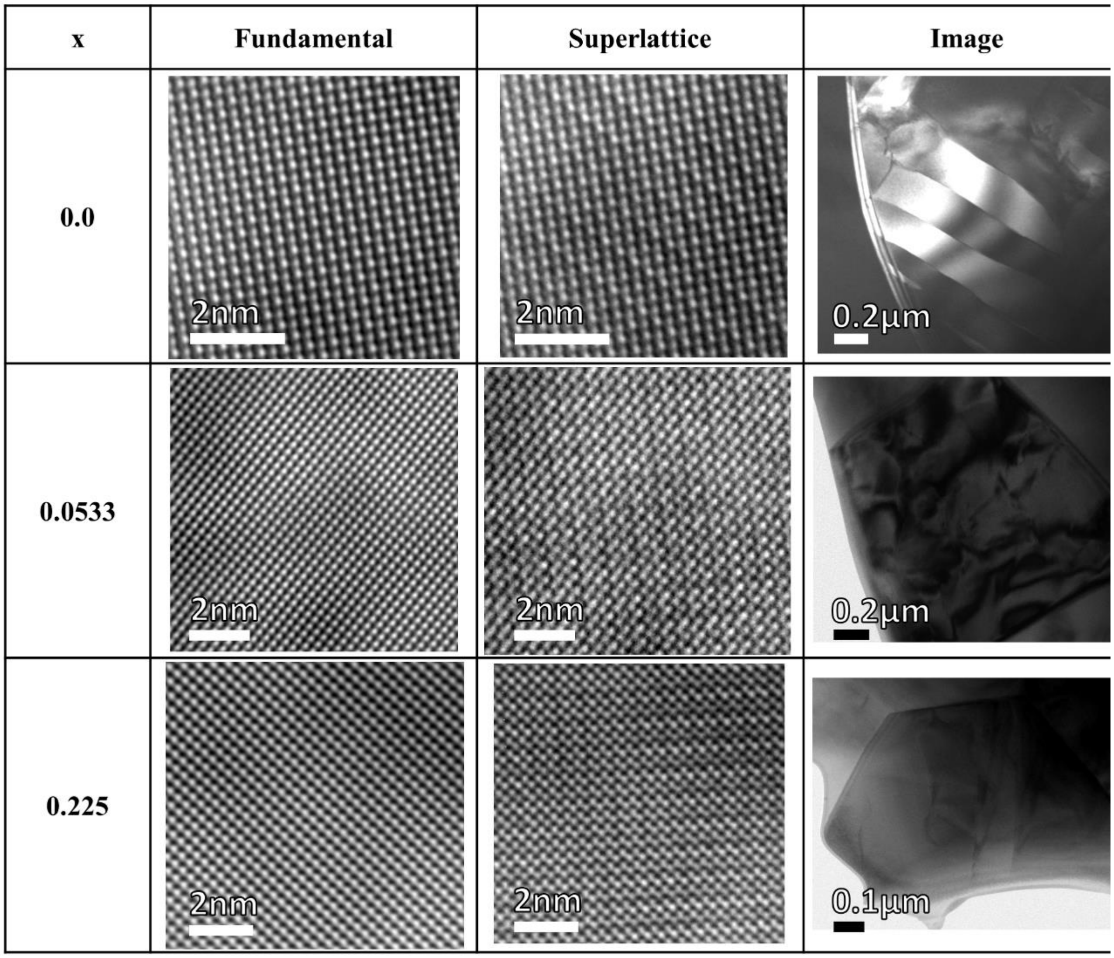

Figure 3.9. $Na_{(1-3x)/2}La_{(1+x)/2}TiO_3$ selected TEM images using a reflections mask and inverse-FFT to show the difference between the fundamental and superlattice reflections

A fast Fourier transform (FFT) mask was applied to high-resolution (HR-TEM) images in the $[100]_{pc}$ zone axis (Figure 3.9) to show the difference between the fundamental structure and the superstructure. Twinning is also apparent in Figure 3.9 at $x = 0$.

As an additional example of A-site ordering, the well-studied ion-conductor $(Li_{0.5}La_{0.5})TiO_3$ was considered. Because its ideal A-site size is so small, $r_A = 1.3059$ Å, this composition falls outside the existing range of the empirical model (1.34 Å $\leq r_A \leq$ 1.61 Å) described in Chapter 2; however, the negative errors for a'_{pc} also suggest cation ordering on the A site causing a volume expansion, or to be more precise, a stretching of the average A-O bond length (Figure 3.10). In this case the $Li_{(1-3x)/2}La_{(1+x)/2}TiO_3$ (LLT) $x = 0$ composition has been reported with long-range A-site order. Increasing the r_A for $x = 0$ by just 0.072 Å is sufficient to reduce the error in a'_{pc} to 0.00%. As is the case for NLT, the degree of cation order in LLT decreases with increasing x even as the degree of vacancy ordering increases [4, 65-79] (Figure 3.10). Table 3.10 shows data which verify via DFT calculations that the unit volume of $Li_{0.5}La_{0.5}TiO_3$ increases upon layered A-site ordering.

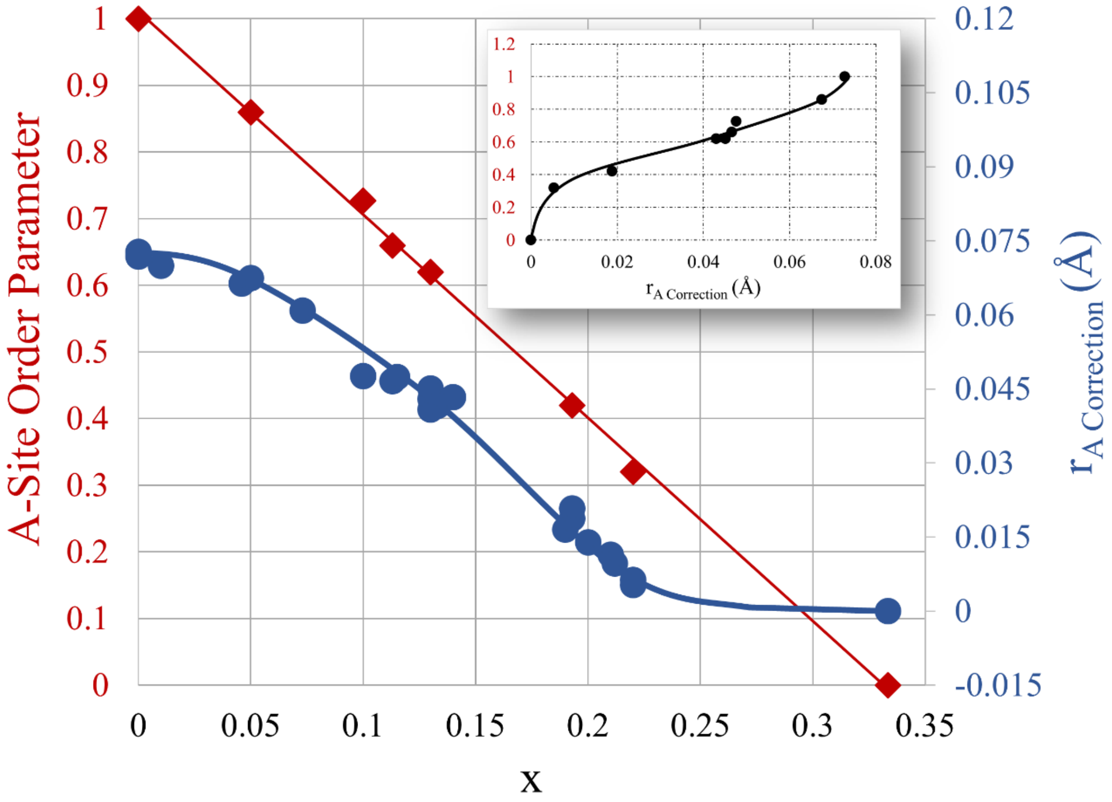

Figure 3.10. $Li_{(1-3x)/2}La_{(1+x)/2}TiO_3$ order parameter (calculated from reported site-occupancy numbers.[4, 54-67]) and $r_{A\ correction}$ where both are functions of x. The inset shows the order parameter as a function of $r_{A\ correction}$ and can be thought of as an empirical model for ordering (0 = disorder, 1 = fully ordered).

The equation which describes this behavior is:

$$\delta r_{A(LLT)} = \frac{a}{1+Exp\left[\dfrac{x-b}{c}\right]} \tag{3.13}$$

where the LLT $r_{\mathrm{A(Corr.)}}$ (as a function of vacancy concentration) constants are: *a* = 0.0740887, *b* = 0.141918, and *c* = 0.0399016.

$$\eta_{LLT-Long-Range-Order} = a - b\left[Log\left(\frac{c}{r_{B(Corr.)}} - 1\right)\right] \tag{3.14}$$

where the LLT order parameter (as a function of r_B correction) constants are: *a* = 0.6, *b* = 0.118, and *c* = 0.0753.

Table 3.10. DFT(500eV) Trigonal $Li_{0.5}La_{0.5}TiO_3$ A-site ordered nanodomain structures.

Hexagonal	a (Å)	b (Å)	c (Å)	V (Å^3)	Rel. E (eV)
Columnar	5.5221	5.5221	13.5280	357.33	-0.0105
Layered	5.5160	5.5160	13.5264	357.18	-0.0264
Rocksalt	5.5118	5.5118	13.5029	355.26	0.0047
Disordered	5.5018	5.5018	13.5219	352.38	-0.0284

As yet another example, the superconductor $(Na_{0.5}La_{0.5})(Mg_{0.5}W_{0.5})O_3$ (NLMW) is an oxide perovskite that has the same A-site species as NLT; however, NLMW has been reported [79] with long-range cation ordering on both the A and B sites. As reported previously,[31] the model suggests that the B site contracts upon ordering while the A site expands. Initially, NLMW calculations show a'_{pc} = 3.9762Å and a''_{pc} = 3.9727Å, resulting in errors of 1.29484% and 1.20427%, respectively. Using an iterative process to determine the A- and B-site sizes which minimize both errors, it was found that r_B decreases by 0.026793 Å (to r_B = 0.63321 Å) while r_A simultaneously increases in size by 0.005849 Å (to r_A = 1.38085 Å). The final error in both a'_{pc} and a''_{pc} is 0.0000%. For the composition $(Na_{0.3333}La_{0.5556})(Mg_{0.5}W_{0.5})O_3$, the model predicts an A-site size increase of about 0.01336 Å (to r_A = 1.23225 Å) – a lower value than for NLMW, indicative of the lower degree of cation ordering expected further from the 1:1 stoichiometry. In the case of $(K_{0.5}La_{0.5})(Mg_{0.5}W_{0.5})O_3$ (KLMW), which has the same B-site species as NLMW, both the A-site and B-site cations are also ordered.[79] The model also shows that the B site contracts and the A site grows upon ordering. Initially, KLMW calculations show a'_{pc} = 4.0533 Å and a''_{pc} = 4.0822 Å, resulting in errors of 2.53874% and 3.27163%, respectively. Again using an iterative process to determine the correct A- and B-site sizes, it was found that the B-site size decreases by 0.104757 Å (to r_B = 0.55524 Å) and the A-site size increases by 0.073501 Å (to r_A = 1.5735Å), which results in errors of 0.0000% for both a'_{pc} and a''_{pc}. In addition, the model shows that for $(K_{0.3333}La_{0.5556})(Mg_{0.5}W_{0.5})O_3$ the A-site size increase is only 0.052644 Å – again less than that for KLMW, indicative of the lower degree of cation order as x increases. These results are summarized in Table 3.11.

Table 3.11. $Na_{(1-3x)/2}La_{(1+x)/2}(Mg_{½}W_{½})O_3$ and $K_{(1-3x)/2}La_{(1+x)/2}(Mg_{½}W_{½})O_3$ summary results.

Comp.	r_A (Å)	$r_{A\ (cor.)}$ (Å)	r_B (Å)	$r_{B\ (cor.)}$ (Å)	a' (Å)	$a'_{(Error)}$ (%)	a'' (Å)	$a''_{(Error)}$ (%)
[a] NLMW								
x=0	1.375	0.0058	0.660	-0.0268	3.9254	0.000	3.9254	0.000
x=0.1111	1.219	0.0133	0.660	-0.0266	3.9288	0.000	3.9288	0.000
x=0.2222	1.063	0.0041	0.660	-0.0417	3.9257	0.000	3.9257	0.000
[a] KLMW								
x=0	1.500	0.0735	0.660	-0.1048	3.9529	0.000	3.9529	0.00
x=0.1111	1.302	0.0552	0.660	-0.0821	3.9484	0.000	3.9484	0.000
x=0.2222	1.104	0.0257	0.660	-0.0698	3.940	0.000	3.940	0.000

[a] [79]

3.4 Conclusions

Four samples in the $Na_{(1-3x)/2}La_{(1+x)/2}TiO_3$ system (x = 0, 0.0533, 0.1733 and 0.225) and $Ba(Mg_{1/3}Ta_{2/3})O_3$ were synthesized using a conventional solid-state mixed-oxide method. $Ba(Mg_{1/3}Ta_{2/3})O_3$ showed a decreasing unit cell volume with annealing due to increasing B-site ordering. The short-range ordered structure of $Na_{0.5}La_{0.5}TiO_3$ was observed via electron diffraction and predicted via an empirical model, which also suggests a volume increase upon ordering. First-principles calculations using density functional theory support these conclusions. Even though thermodynamics dictates that a finite concentration of vacancies exists even at $x = 0$, there can be no 1:1 long-range vacancy ordering at this or other low-x compositions where the presence of vacancies is nonstoichiometric. Perovskites in the $Na_{(1-3x)/2}La_{(1+x)/2}TiO_3$ system have an A-site ordered layered structure, and the degree of cation order decreases as x increases.

Similar A-site ordering and volume expansion has been inferred from previously reported models of $Li_{(1-3x)/2}La_{(1+x)/2}TiO_3$ and both $(Na_{0.5}La_{0.5})(Mg_{0.5}W_{0.5})O_3$ and $(K_{0.5}La_{0.5})(Mg_{0.5}W_{0.5})O_3$. The implication of this empirical modeling method is that it may be possible to predict the degree of cation ordering in complex perovskite systems from Shannon data and experimentally-derived pseudocubic lattice constants alone. It may also be possible to predict the degree of volume expansion/contraction, which has implications for functional properties, especially ionic conduction.

3.5 References

[1] V. Miller, S. Tidrow, Perovskites: Temperature and Coordination Dependent Ionic Radii, Integrated Ferroelectrics **148** (1) (2013) 1-16.

[2] P. Sun, T. Nakamura, Y. Shan, Y. Inaguma, M. Itoh, High temperature quantum paraelectricity in perovskite-type titanates $Ln_{(1/2)}Na_{(1/2)}TiO_{(3)}$ (*Ln* = La, Pr, Nd, Sm, Eu, Gd and Tb), Ferroelectrics **200** (1-4) (1997) 93-107.

[3] K. Muller, H. Burkard, $SrTiO_3$ - Intrinsic Quantum Para-Electric Below 4-K, Physical Review B **19** (7) (1979) 3593-3602.

[4] M. Sommariva, M. Catti, Neutron diffraction study of quenched $Li_{0.3}La_{0.567}TiO_3$ lithium ion conducting perovskite, Chemistry of Materials **18** (9) (2006) 2411-2417.

[5] J. Brous, I. Fankuchen, E. Banks, Rare Earth Titianates with a Perovskite Structure, Acta Crystallographica **6** (1) (1953) 67-70.

[6] A. Agranovskaya, Physical-chemical investigation of the formation of complex ferroelectrics with perovskite structure, Izvestiya Akademii Nauk SSR, Seriya Fizicheskaya **24** (1960).

[7] J. Miao, L. Li, H. Liu, D. Xu, Z. Lu, Y. Song, W. Su, Y. Zheng, Structure characteristics and valence state study for $La_{1-x}Na_xTiO_3$ synthesized under high-pressure and high-temperature conditions, Materials Letters **42** (1-2) (2000) 1-6.

[8] R. Mitchell, A. Chakhmouradian, A structural study of the perovskite series $Na_{1/2+x}La_{1/2-3x}Th_{2x}TiO_3$, Journal of Solid State Chemistry **138** (2) (1998) 307-312.

[9] A. Ruiz, M. Lopez, C. Pico, M. Veiga, New $La_{2/3}TiO_3$ derivatives: Structure and impedance spectroscopy, Journal of Solid State Chemistry **163** (2) (2002) 472-478.

[10] A. Ruiz, M. Lopez, C. Pico, M. Veiga, Structural modifications induced by composition in the $La_{1.33-x}Na_{3x}Ti_2O_6$ perovskites: A neutron diffraction study, Chemistry of Materials **17** (6) (2005) 1391-1397.

[11] Y. Li, S. Qin, F. Seifert, Phase transitions in A-site substituted perovskite compounds: The $(Ca_{1-2x}Na_xLa_x)TiO3$ $(0 <= x <= 0.5)$ solid solution, Journal of Solid State Chemistry **180** (3) (2007) 824-833.

[12] R. Ranjan, A. Senyshyn, H. Boysen, C. Baehtz, F. Frey, Crystal structures of $Na_{(1/2)}Ln_{(1/2)}TiO_{(3)}$ (*Ln* : La, Eu, Tb), Journal of Solid State Chemistry **180** (3) (2007) 995-1001.

[13] R. Garg, A. Senyshyn, H. Boysen, R. Ranjan, Structure and phase transition of $Na_{(0.5)}La_{(0.5)}TiO_{(3)}$, Journal of Physics-Condensed Matter **20** (50) (2008).

[14] M. Knapp, P. Woodward, A-site cation ordering in $AA'BB'O_6$ perovskites, Journal of Solid State Chemistry **179** (4) (2006) 1076-1085.

[15] Y. Inaguma, T. Tsuchiya, T. Katsumata, Systematic study of photoluminescence upon band gap excitation in perovskite-type titanates $R_{1/2}Na_{1/2}TiO_3$: Pr (R = La, Gd, Lu, and Y), Journal of Solid State Chemistry **180** (5) (2007) 1678-1685.

[16] R. Jimenez, A. Rivera, A. Varez, J. Sanz, Li mobility in $Li_{0.5-x}Na_xLa_{0.5}TiO_3$ perovskites $(0 <= x <= 0.5)$ Influence of structural and compositional parameters, Solid State Ionics **180** (26-27) (2009) 1362-1371.

[17] M. Harunsani, D. Woodward, M. Peel, S. Ashbrook, R. Walton, Investigation of the hydrothermal crystallisation of the perovskite solid solution $NaCe_{1-x}La_xTi_2O_6$ and its defect chemistry, Journal of Solid State Chemistry **207** (2013) 117-125.

[18] S. García-Martína, E. Urones-Garrote, M.C. Knapp, G. King, P.M. Woodward, Structural complexity in AA′MM′O_6 Perovskites. A Transmission Electron Microscopy Study, Materials Research Society Symposium Proceedings **1148** (2009).

[19] C. Howard, Z. Zhang, Structures and phase transition in the layered perovskite $La_{0.6}Sr_{0.1}TiO_3$: a new orthorhombic structure solved from high-resolution diffraction in combination with group theoretical analysis, Journal of Physics-Condensed Matter **15** (26) (2003) 4543-4553.

[20] Z. Gönen, D. Paluchowski, P. Zavalij, B. Eichhorn, J. Gopalakrishnan, Reversible cation/anion extraction from $K_2La_2Ti_3O_{10}$: Formation of new layered titanates, $KLa_2Ti_3O_{9.5}$ and $La_2Ti_3O_9$Reversible cation/anion extraction from K2La2Ti3O10: Formation of new layered titanates, KLa2Ti3O9.5 and La2Ti3O9, Inorganic Chemistry **45** 45 (21) (2006) 8736-8742.

[21] M. Richard, L. Brohan, M. Tournoux, Synthesis, Characterization, and Acid Exchange of the Layered Perovskites - $A_2Nd_2Ti_3O_{10}$ (A=NA, K), Journal of Solid State Chemistry **112** (2) (1994) 345-354.

[22] T. Sekiya, T. Yamamoto, Y. Torii, Cation Ordering in (NaLa)(MgW)O_6 with the Perovskite Structure, Bulletin of the Chemical Society of Japan **57** (7) (1984) 1859-1862.

[23] K. Leinenweber, J. Parise, High-Pressure Synthesis and Crystal-Structure of $CaFeTi_2O_6$, a New Perovskite Structure Type, Journal of Solid State Chemistry **114** (1) (1995) 277-281.

[24] M. Ducau, K. Suh, J. Senegas, J. Darriet, Crystal-Structure and NMR-Studies of a Cubic Perovskite - The Fluoride $NaBaLiNiF_6$, Materials Research Bulletin **27** (9) (1992) 1115-1123.

[25] A. Deschanvres, B. Raveau, F. Tollemer, Substitution of Copper for a Bivalent Metal in Titanates of Perovskite Type, Bulletin De La Societe Chimique De France **11** (1967) 4077-4078.

[26] V. Propach, Kristallstruktur von $Ca_{0.5}Cu_{1.5}Ti_2O_6$, $Cu_{1.5}TaTiO_6$ und $CuTa_2O_6$. Das spektroskopische Verhalten von Cu^{2+}-Ionen in kuboktaedrischer Umgebung, Zeitschrift für anorganische und allgemeine Chemie, 1977, pp. 161-171.

[27] A.M. Glazer, The classification of tilted octahedra in perovskites, Acta Crystallographica Section B, 1972, pp. 3384-3392.

[28] R. Ubic, G. Subodh, M. Sebastian, D. Gout, T. Proffen, Structure of compounds in the $Sr_{1-3x/2}Ce_xTiO_3$ homologous series, Chemistry of Materials **20** (9) (2008) 3127-3133.

[29] R. Ubic, G. Subodh, D. Gout, M. Sebastian, T. Proffen, Crystal Structure of $Sr_{0.4}Ce_{0.4}TiO_3$ Ceramics, Chemistry of Materials **21** (19) (2009) 4706-4710.

[30] R. Ubic, K. Tolman, K. Chan, N. Lundy, S. Letourneau, W. Kriven, Effective size of vacancies in aliovalently doped $SrTiO_3$ perovskitesEffective size of vacancies in aliovalently doped SrTiO3 perovskites, Journal of Alloys and Compounds **575** 575 (2013) 239-245.

[31] R. Ubic, K. Tolman, K. Talley, B. Joshi, J. Schmidt, E. Faulkner, J. Owens, M. Papac, A. Garland, C. Rumrill, K. Chan, N. Lundy, H. Kungl, Lattice-constant prediction and effect of vacancies in aliovalently doped perovskites, Journal of Alloys and Compounds **644** (2015) 982-995.

[32] R. Shannon, Revised Effective Ionic-Radii and Systematic Studies of Interatomic Distances in Halides and Chalcogenides, Acta Crystallographica Section a **32** 32 (SEP1) (1976) 751-767.

[33] V. Goldschmidt, The laws of crystal chemistry, Naturwissenschaften **14** 14 (1926) 477-485.

[34] R. Ubic, Revised method for the prediction of lattice constants in cubic and pseudocubic perovskites, Journal of the American Ceramic Society **90** (10) (2007) 3326-3330.

[35] K. Tolman, R. Ubic, M. Papac, K. Seymour, S. McCormack, W. Kriven, H. Kungl, Structural effect of aliovalent doping in lead perovskites, Journal of Solid State Chemistry **225** 225 (2015) 359-367.

[36] L. Finger, D. Cox, A. Jephcoat, A Correction for Powder Diffraction Peak Asymmetry Due to Axial Divergence, Journal of Applied Crystallography **27** 27 (1994) 892-900.

[37] R.A. Young, The Rietveld method, International Union of Crystallograhy ; Oxford University Press, [Chester, England]; Oxford; New York, 1995.

[38] H. Rietveld, Line Profiles of Neutron Powder-Diffraction Peaks for Structure Refinement, Acta Crystallographica 22 (1967) 151.

[39] H. Rietveld, Line Profiles of Neutron Powder-Diffraction Peaks for Structure Refinement, Acta Crystallographica 22 (1967) 151.

[40] H. Rietveld, A Profile Refinement Method for Nuclear and Magnetic Structures, Journal of Applied Crystallography 2 (1969) 65.

[41] H.M. Rietveld, The Rietveld method, Phys Scr Physica Scripta 89(9) (2014).

[42] C. International Union of, T. Commission on International, International tables for crystallography, (2006).

[43] C. Howard, H. Stokes, Group-theoretical analysis of octahedral tilting in perovskites, Acta Crystallographica Section B-Structural Science 54 (1998) 782-789.

[44] R. Young, D. Wiles, Profile Shape Functions in Rietveld Refinements, Journal of Applied Crystallography 15(AUG) (1982) 430-438.

[45] L. Finger, D. Cox, A. Jephcoat, A Correction for Powder Diffraction Peak Asymmetry Due to Axial Divergence, Journal of Applied Crystallography **27** (1994) 892-900.

[46] J. Rodriguez-Carvajal, Recent Advances in Magnetic-Structure Determination by Neutron Powder Diffraction, Physica B 192(1-2) (1993) 55-69.

[47] R.-C. J, An Introduction to the Program FULLPROF, in: L.L.B. (CEA-CNRS) (Ed.) Physica B, France, 2000.

[48] D. Wiles, R. Young, A New Computer-Program for Rietveld Analysis of X-Ray-Powder Diffraction Patterns, Journal of Applied Crystallography 14(APR) (1981) 149-151.

[49] G. Kresse, J. Furthmuller, Efficient iterative schemes for ab initio total-energy calculations using a plane-wave basis set, Physical Review B **54** (16) (1996) 11169-11186.

[50] J. Perdew, K. Burke, M. Ernzerhof, Generalized gradient approximation made simple, Physical Review Letters **77** (18) (1996) 3865-3868.

[51] P. Blöchl, Projector Augmented-Wave Method, Physical Review B **50** (24) (1994) 17953-17979.

[52] G. Kresse, D. Joubert, From ultrasoft pseudopotentials to the projector augmented-wave method, Physical Review B **59** (3) (1999) 1758-1775.

[53] D.R. Askeland, The science and engineering of materials, PWS-Kent Pub. Co., Boston, 1989.

[54] Z. Zhang, S.C. Middleburgh, M. De Los Reyes, G.R. Lumpkin, B.J. Kennedy, P.E.R. Blanchard, E. Reynolds, L.Y. Jang, Gradual structural evolution from pyrochlore to defect-fluorite in $Y_2Sn_{2-x}Zr_xO_7$: Average vs local structure, J. Phys. Chem. C Journal of Physical Chemistry C 117(50) (2013) 26740-26749.

[55] C. Karthik, T. Anderson, D. Gout, R. Ubic, Transmission electron microscopic study of pyrochlore to defect-fluorite transition in rare-earth pyrohafnates, Journal of Solid State Chemistry 194 (2012) 168-172.

[56] R. Mani, N. Bhuvanesh, K. Ramanujachary, W. Green, S. Lofland, J. Gopalakrishnan, A novel one-pot metathesis route for the synthesis of double perovskites, $Ba_3MM'_2O_9$ (M = Mg, Ni, Zn; M ' = Nb, Ta) with 1:2 ordering of M and M ' atoms, Journal of Materials Chemistry **17** (16) (2007) 1589-1592.

[57] R. Ubic, Y. Hu, I. Abrahams, Neutron and electron diffraction studies of $La(Zn_{1/2}Ti_{1/2})O_3$ perovskite, Acta Crystallographica Section B-Structural Science **62** (2006) 521-529.

[58] J. Yang, W. Choo, C. Lee, Ca_2MgWO_6 from neutron and X-ray powder data, Acta Crystallographica Section C-Crystal Structure Communications **59** (2003) I86-I88.

[59] A. Mishra, H. Poswal, S. Acharya, A. Tyagi, S. Sharma, Structural evolution of double perovskite $Sr_{(2)}MgWO_{(6)}$ under high pressure, Physica Status Solidi B-Basic Solid State Physics **247** (7) (2010) 1773-1777.

[60] B. Day, N. Bley, H. Jones, R. McCullough, H. Eng, S. Porter, P. Woodward, P. Barnes, Structures of ordered tungsten- or molybdenum-containing quaternary perovskite oxides, Journal of Solid State Chemistry **185** (2012) 107-116.

[61] G. Baldinozzi, P. Sciau, M. Pinot, D. Grebille, Crystal-Structure of the Antiferroelectric Perovskite Pb_2MgWO_6, Acta Crystallographica Section B-Structural Science **51** (1995) 668-673.

[62] M.H. Loretto, Electron beam analysis of materials, Chapman and Hall, London; New York, 1984.

[63] M. Sauvage, E. Parthé, Vacancy short-range order in substoichiometric transition metal carbides and nitrides with the NaCl structure. II. Numerical calculation of vacancy arrangement, AYA Acta Crystallographica Section A 28(6) (1972) 607-616.

[64] D.B. Williams, C.B. Carter, Transmission electron microscopy : a textbook for materials science, Springer, New York, 2009.

[65] J.A. Alonso, J. Ibarra, M.A. Paris, J. Sanz, J. Santamaria, C. LeÓn, A. Vdrez, M.T. Fermandez, Relationship Between Crystal Structure and Li+-Conductivity in $La_{0.5}Li_{0.5}TiO_3$ Perovskite, Materials Research Society Symposia Proceedings **575** (2000) 337-342.

[66] J. Ibarra, A. Varez, C. Leon, J. Santamaria, L. Torres-Martinez, J. Sanz, Influence of composition on the structure and conductivity of the fast ionic conductors $La_{2/3-x}Li_{3x}TiO_3$ (0.03 <= x <= 0.167), Solid State Ionics **134** (3-4) (2000) 219-228.

[67] J. Alonso, J. Sanz, J. Santamaria, C. Leon, A. Varez, M. Fernandez-Diaz, On the location of Li^+ cations in the fast Li cation conductor La0.5Li0.5TiO3 perovskite, Angewandte Chemie-International Edition **39** (3) (2000) 619-+.

[68] E.-T. Kang, Y.-J. Kwon, The structure determination of $La_{2/3-x}Li_{3x}\square_{1/3-2x}TiO_3$ by the powder neutron and X-ray diffraction, Journal of the Korean Ceramic Society **40** (6) (2003) 513-518.

[69] A. Ruiz, M. Lopez, M. Veiga, C. Pico, Electrical properties of $La_{1.33-x}Li_{3x}Ti_2O_6$ $(0.1 < x < 0.3)$, Solid State Ionics **112** (3-4) (1998) 291-297.

[70] Y. Inaguma, T. Katsumata, M. Itoh, Y. Morii, T. Tsurui, Structural investigations of migration pathways in lithium ion-conducting $La_{2/3-x}Li_{3x}TiO_3$ perovskites, Solid State Ionics **177** (35-36) (2006) 3037-3044.

[71] J. Fourquet, H. Duroy, M. CrosnierLopez, Structural and microstructural studies of the series $La_{2/3-x}Li_{3x}\ V_{1/3-2x}TiO_3$, Journal of Solid State Chemistry **127** (2) (1996) 283-294.

[72] Y. Cheng, Z. Bi, A. Huq, M. Feygenson, C. Bridges, M. Paranthaman, B. Sumpter, An integrated approach for structural characterization of complex solid state electrolytes: the case of lithium lanthanum titanate, Journal of Materials Chemistry a **2** (7) (2014) 2418-2426.

[73] A. Ruiz, M. Lopez, M. Veiga, C. Pico, Structural refinement by neutron diffraction of $La_{1.12}Li_{0.62}Ti_2O_6$, Journal of Solid State Chemistry **148** (2) (1999) 329-332.

[74] K. Kishida, M. Miyata, N. Wada, N. Okamoto, K. Tanaka, H. Inui, H. Koyama, T. Hattori, Y. Iriyama, Z. Ogumi, Crystal and defect structures of $La_{2/3-x}Li_{3x}TiO_3$ (x similar to 0.1) produced by a melt process, Journal of Electron Microscopy **56** (6) (2007) 225-234.

[75] N. Bhuvanesh, O. Bohnke, H. Duroy, M. Crosnier-Lopez, J. Emery, J. Fourquet, Topotactic H^+/Li^+ ion exchange on $La_{2/3-x}Li_{3x}TiO_3$: New metastable perovskite phases $La_{2/3-x}TiO_{3-3x}(OH)_{(3x)}$ and $La_{2/3-x}TiO_{3-3x/2}$ obtained by further dehydration, Materials Research Bulletin **33** (11) (1998) 1681-1691.

[76] J. Sanz, A. Varez, J. Alonso, M. Fernandez, Structural changes produced during heating of the fast ion conductor $Li_{0.18}La_{0.61}TiO_3$. A neutron diffraction study, Journal of Solid State Chemistry **177** (4-5) (2004) 1157-1164.

[77] Y. Inaguma, T. Katsumata, M. Itoh, Y. Morii, Crystal structure of a lithium ion-conducting perovskite $La_{2/3-x}Li_{3x}TiO_3$ (x=0.05), Journal of Solid State Chemistry **166** (1) (2002) 67-72.

[78] M. Yashima, D. Ishimura, K. Ohoyama, Temperature dependence of lattice parameters and anisotropic thermal expansion of bismuth oxide, Journal of the American Ceramic Society **88** (8) (2005) 2332-2335.

[79] M. Arillo, J. Gomez, M. Lopez, C. Pico, M. Veiga, Structural and electrical characterization of new materials with perovskite structure, Solid State Ionics **95** (3-4) (1997) 241-248.

CHAPTER FOUR: TETRAGONAL DISTORTIONS IN PEROVSKITES

4.1 Introduction

Fundamentally, the science of materials is based on processing-structure-property relationships, with composition being a key processing parameter. For example, there is a direct link between the degree of tetragonality and the resultant polarization in tetragonally distorted perovskites.[1] As such, predicting and controlling perovskite tetragonality would be useful for the design of materials with specific properties for a whole range of applications including high-K (*i.e.*, dielectric K = ε_r) capacitors (*e.g.*, $BaTiO_3$), ferroelectrics (*e.g.*, $BaTiO_3$), pyroelectrics (*e.g.*, $LiTaO_3$), piezoelectrics (*e.g.*, $Pb_{1-3x}La_{2x}Zr_yTi_{1-y}O_3$), ferroelectrics (*e.g.*, $Ba_{1-x}Sr_xTiO_3$), high-temperature superconductors (*e.g.*, $YBa_2(Cu_{1-x}Ga_x)_3O_{7-\delta}$[*])[2-5] Unfortunately, no empirical model which can predict the tetragonality of perovskites yet exists.

In 2001, Lufaso and Woodward[6] developed a perovskite structural prediction program (SPuDS) based on the earlier global-instability-index concept of Salinas-Sanchez *et al.*;[7] however, as powerful as SPuDS is, it does not consider *P*4*mm* structures nor any stoichiometry with extrinsic vacancy concentrations or complex compositions. Others have derived methods for predicting the structural stability of cubic perovskites.[8, 9] Later, methods for predicting lattice constants for orthorhombic perovskites emerged.[10, 11]

---

[*] A perovskite *derivative*

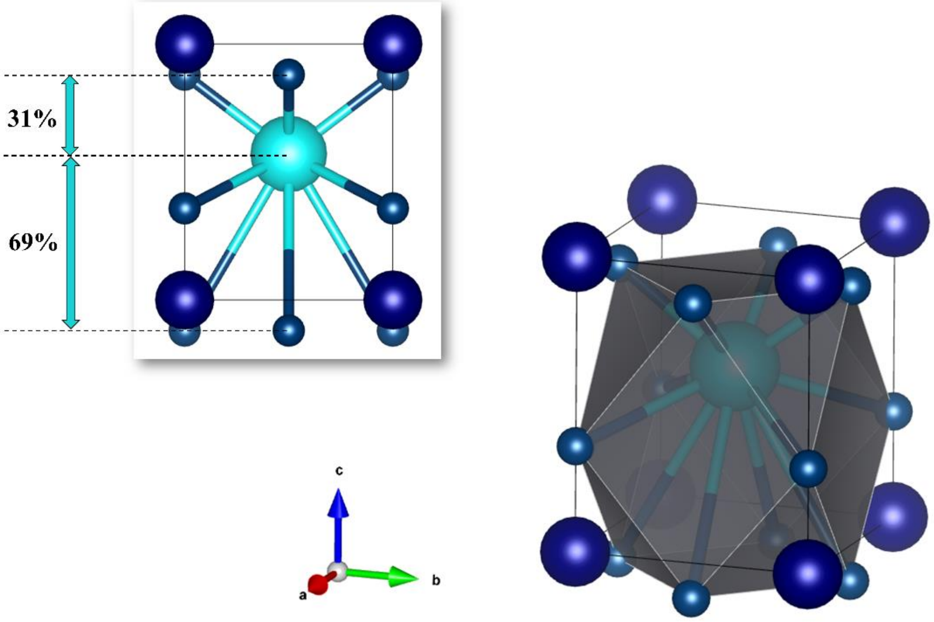

Figure 4.1. Tetragonal $PbTiO_3$ showing the result of SOJT distortions which exist in *P*4*mm* perovskite compounds; unlike *P*4/*mmm* compounds which maintain the ionic coordinates of the aristotype. Pb^{2+} is shown at the origin.

For space group *P*4*/mmm*, the anions retain their ideal positions at 0.5, 0.5, 0 and 0.5, 0, 0.5 and B cations remain at 0.5, 0.5, 0.5, resulting in no dipole moment; however, in the case of *P*4*mm* second-order Jahn-Teller (SOJT) distortions arise (Figure 4.1) and yield measurable dipole moments. First-order Jahn-Teller (FOJT) distortions are due to incompletely filled electron shells, which are doubly or triply degenerate molecular orbitals. The nature of the FOJT effect is such that distortions are inevitably so weak as to be negligible. On the other hand, SOJT distortions occur when shells are full, but where there is only a small energy difference between the highest filled orbital and the lowest empty one. These distortions can result in detectible antiparallel (therefore polar) ionic displacements of cation and anion sublattices and typically yield piezoelectric or ferroelectric behavior. They occur when the HOMO-LUMO gap is small and there is a symmetry-allowed distortion which gives rise to mixing between the two. This distortion is favored because it stabilizes the HOMO while destabilizing the LUMO. SOJT distortions are typically observed for two classes of cations: octahedrally coordinated high-valent d^0 cations (*e.g.*, Ti^{4+}, V^{4+}) and cations containing filled valence s shells (*e.g.*, Pb^{2+}).[12, 13] In the case of $SrTiO_3$, Ti^{4+} is driven off-center within the octahedron as strontium is increasingly replaced with lead. In the extreme case of $PbVO_3$, the d^0 V^{4+} adopts a five-fold coordination whilst the Pb^{2+} cuboctahedral geometry distorts off-center by 19% (Figure 4.1).[14, 15]

In 2010, Qi *et al*.[16] used density-functional theory calculations to investigate the tetragonality of 25 ferroelectric perovskites. They found a consistent trend with respect to B-site cation displacements, showing that tetragonality is empirically predictable. In 2011, Kumar and Bhardwaj[17] found a trend in tetragonality using a log-log scale of lattice constants versus average radii[18] for several compositions; however, they did not explicitly state which compositions were modeled.

In general, the vertex-sharing nature of perovskite octahedra necessitates either bond stretching or compression to maintain stability. Chapter 1 showed that the tolerance factor, *t*, is a relative measure of the perovskite stability and was first introduced by Goldschmidt[19] in 1926 (Equation 4.1), where r_A, r_B, and r_X are the published ionic radii of A, B, and X ions, respectively.[18]

$$t_* = \frac{r_A + r_X}{\sqrt{2}(r_B + r_X)} \tag{1.8}$$

This formulation cannot account for the effect of extrinsic vacancies on effective ionic sizes. Chapter 2 showed that Ubic *et al*.[20-22] derived a tolerance factor (Equation 2.3), based on the pseudocubic cell volume rather than r_A, which can account for the effect of extrinsic A-site vacancies:

$$t_1 = \frac{a_{pc} - 0.011730139}{0.7209203(r_B + r_X)} - 0.760998 \tag{2.3}$$

Equation 2.3 is a better predictor of octahedral distortions in perovskites than is Equation 1.8; however, it requires the foreknowledge of a_{pc}. As part of this model[20], an empirical relationship between t_* and t_1 for defective perovskites was derived (Equation 4.3)

$$t_1 = A + Bt_* + Ct_*^2 \tag{2.15}$$

where the coefficients A, B, and C are in terms of the ideal (*i.e.*, weighted average of Shannon radii) A-site size without extrinsic vacancies, and

$$\begin{aligned} A &= -50.978 + 84.274 r_{A(id)0} - 32.411 r_{A(id)0}^2 \\ B &= 130.35 - 205.44 r_{A(id)0} + 77.539 r_{A(id)0}^2 \\ C &= -81.294 + 124.73 r_{A(id)0} - 46.185 r_{A(id)0}^2 \end{aligned}$$

In the present work, the $[(Pb_yBa_{1-y})_{(1-3x)}La_{(2x)}]TiO_3$ ($0 \le x \le 0.05$, $0 \le y \le 1.0$) system was investigated in order to develop empirical models for tetragonality. With this formulation, the value of x is equal to the concentration of extrinsic A-site vacancies, [V].

4.2 Methods

A total of 21 compositions in the system $[(Pb_yBa_{1-y})_{(1-3x)}La_{(2x)}]TiO_3$ ($y = 0.0$, 0.25, 0.5, 0.667, 0.75 and 1.0) ($x = 0.0$, 0.01, 0.02, 0.03, 0.04 and 0.05) were synthesized via the solid-state mixed-oxide route. Stoichiometric amounts of PbO (99.9%, Thermo Fisher Scientific Inc., Pittsburgh, PA), $BaCO_3$ (99.9%, Alfa-Aesar, Ward Hill, MA), TiO_2 (99.9%, Aldrich Chemical Co., Milwaukee, WI), and La_2O_3 (99.95%, Alfa-Aesar, Ward Hill, MA) were ball milled with yttria-stabilized ZrO_2 (YSZ) media in deionized water for ~24 hours in a high-density nylon pot. Powders were then dried overnight in an atmospheric drying oven at 80-100°C until the water was evaporated. Calcination was conducted at 1000°C for three hours in a box furnace (1807FL, CM Furnaces Inc., Bloomfield, NJ). No excess PbO was added to account for volatility; however, Pb-containing compositions ($y > 0$) were calcined adjacent to a sacrificial powder bed of the same composition on a pre-contaminated Al_2O_3 lid muffled by an inverted Al_2O_3 crucible (also pre-contaminated) to inhibit both volatility and lead-loss into the crucible walls. After calcination the powders were pulverized by hand using a mortar and pestle.

Powder X-ray diffraction (XRD) measurements were performed in a diffractometer (Miniflex-600, Rigaku, Woodlands, TX) operating with convergent-beam geometry and Cu Kα radiation (λ=1.540593 Å). Le Bail fits to the XRD data were analyzed using DiffracPLUS TOPAS 4.2 (Bruker AXS Inc., Madison, WI). The background was fitted with a fourth-order Chebyshev polynomial, and asymmetry was corrected using the Finger *et al*. model.[23]

4.3 Results and Discussion

Figure 4.2 demonstrates that the 21 synthesized compositions appeared via XRD to be single-phase tetragonal perovskites. Figure 4.3 shows how the tetragonality changes as a function of t_1 (Equation 4.2). Each line in this figure corresponds to a family of compositions, all in space group *P*4*mm*, with a single Pb/Ba ratio (*i.e.*, *y* value). The different data points on each line correspond to various values of *x* (*i.e.*, vacancy concentrations). These linear relationships are described by Equations 4.4–4.9., which all seem to (notionally) converge at $t_1 \sim 0.9640$, corresponding to a (notional) tetragonality of 0.9057.

Table 4.1. The weighted average B-site size and tetragaonality of Pb perovskites

Composition	c/a	t_1	$r_{\mathrm{B\ Avg.}}$ (Å)	ICSD #
$PbTiO_3$	1.064524	1.056747	0.605	183213
$PbTiO_3$	1.061888	1.055354	0.605	165498
$PbTiO_3$	1.059146	1.05415	0.605	90693
$Pb(Zr_{0.1}Ti_{0.9})O_3$	1.052124	1.048186	0.6165	90694
$Pb(Zr_{0.2}Ti_{0.8})O_3$	1.045019	1.044535	0.628	90695
$Pb(Zr_{0.3}Ti_{0.7})O_3$	1.036852	1.043805	0.6395	90696
$Pb(Zr_{0.3}Ti_{0.7})O_3$	1.042718	1.047756	0.6395	183587
$Pb_{0.96}Ce_{0.04}(Zr_{0.3}Ti_{0.7})O_3$	1.040693	1.04360	0.6395	153294
$Pb_{0.96}Nd_{0.04}(Zr_{0.3}Ti_{0.7})O_3$	1.03006	1.041733	0.6395	153295
$Pb(Zr_{0.35}Ti_{0.65})O_3$	1.039471	1.046321	0.64525	247782
$Pb(Zr_{0.4}Ti_{0.6})O_3$	1.031436	1.038146	0.651	90697
$Pb(Zr_{0.4}Ti_{0.6})O_3$	1.035439	1.038967	0.651	187471
$Pb(Zr_{0.45}Ti_{0.55})O_3$	1.024367	1.036188	0.65675	55700
$Pb(Zr_{0.5}Ti_{0.5})O_3$	1.021153	1.036373	0.6625	155328
$Pb(Zr_{0.52}Ti_{0.48})O_3$	1.021989	1.034568	0.6648	191123

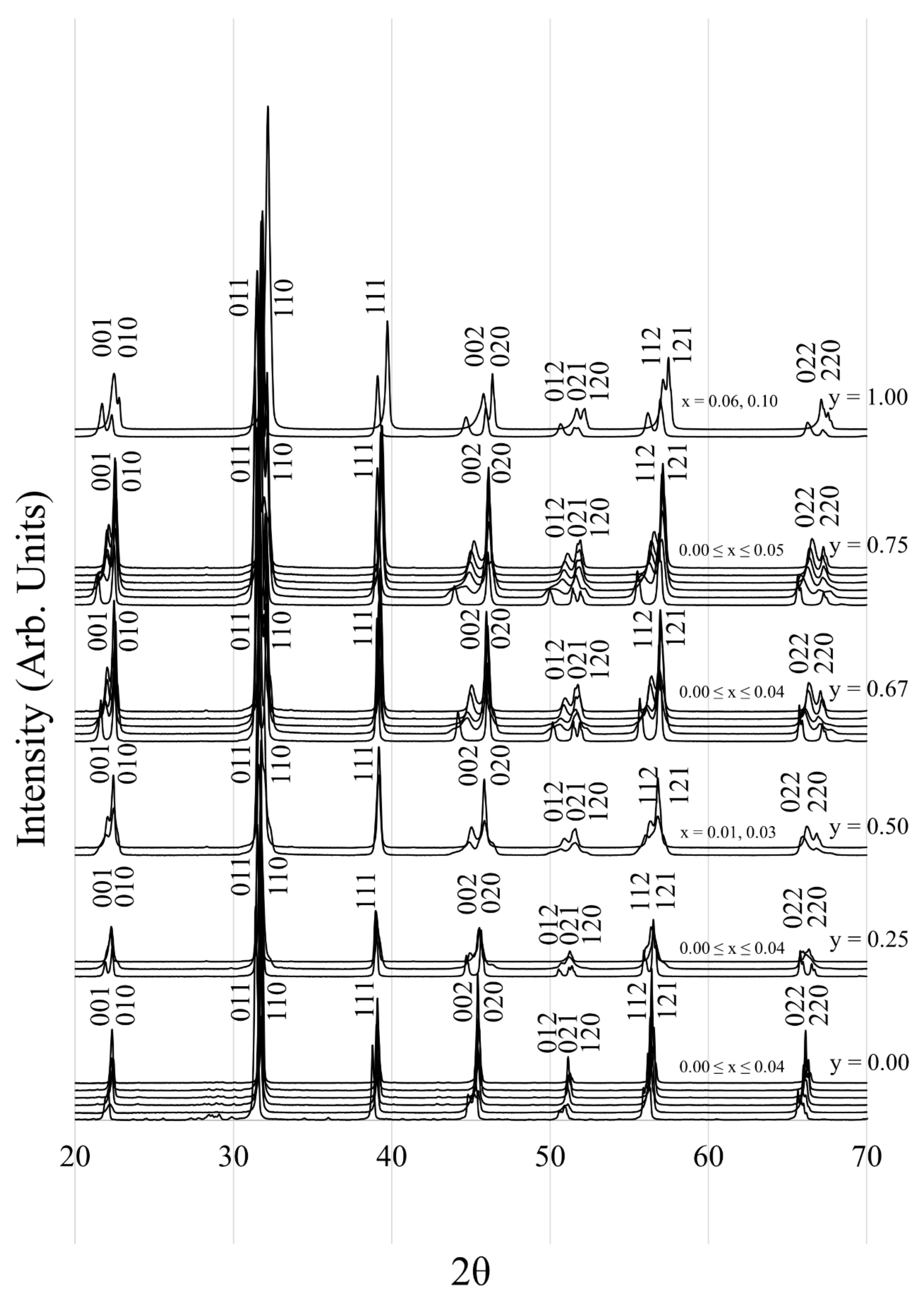

Figure 4.2. X-ray diffraction patterns of 24 synthesized compositions in the system $[(Pb_yBa_{1-y})_{(1-3x)}La_{(2x)}]TiO_3$ (y = 0.0, 0.25, 0.5, 0.667, 0.75 and 1.0) (x = 0.0, 0.01,

0.02, 0.03, 0.04 and 0.05). The patterns are in ascending order with $x = 0$ and $y = 0$ at the bottom.

$$({}^{c}/{}_{a})_{y=0} = 0.9348(t_1) + 0.0045 \tag{4.4}$$

$$({}^{c}/{}_{a})_{y=0.25} = 1.0325(t_1) - 0.0894 \tag{4.5}$$

$$({}^{c}/{}_{a})_{y=0.5} = 1.2352(t_1) - 0.2850 \tag{4.6}$$

$$({}^{c}/{}_{a})_{y=0.667} = 1.3867(t_1) - 0.4312 \tag{4.7}$$

$$({}^{c}/{}_{a})_{y=0.75} = 1.4755(t_1) - 0.5169 \tag{4.8}$$

$$({}^{c}/{}_{a})_{y=1} = 1.7130(t_1) - 0.7457 \tag{4.9}$$

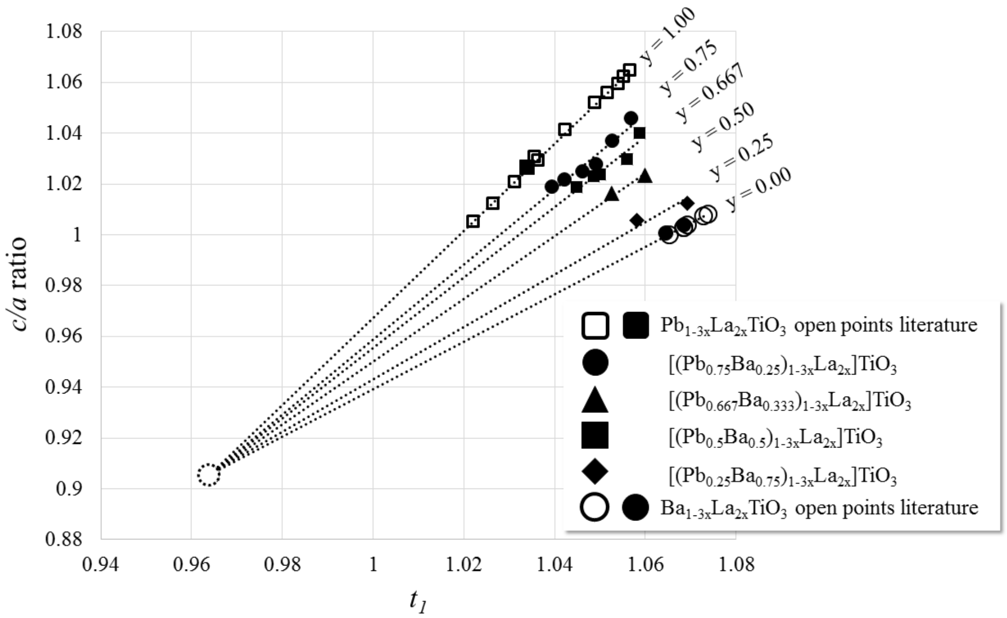

Figure 4.3. Tetragonal titanates in the system $[(Pb_yBa_{1-y})_{(1-3x)}La_{(2x)}]TiO_3$. The open data points are from literature.[3, 27-31] Data points for $0 \le x \le 0.5$ are shown as: $y = 0.0$ circles, $y = 0.25$ diamonds, $y = 0.50$ triangles, $y = 0.667$ squares, $y = 0.75$ circles and $y = 1.0$ squares; $Pb_{1-x}Bi_{2x}TiO_3$ ($x = 0.025$ and 0.05 squares) and $Ba_{1-3x}Sm_{2x}TiO_3$ ($x = 0.0333$ circle). The notional point of convergence is (0.964038, 0.905694).

Figure 4.4 illustrates that the slopes of these linear relationships, *m*, can be calculated (Equation 4.10) as a function of the tolerance factor, *t*, corresponding to $x = 0$ in each case, t_0 (Equation 4.1 at $x = 0$). Equation 4.11 can then be used to estimate the tetragonality of a specific composition using the point of convergence, t_1 and a slope defined by Equation 4.10. Figure 4.5 demonstrates the fit achieved with this method, which has an average relative absolute error of 0.29%; however, this fit only accounts for the 58 specific cases of *P*4*mm* titanate perovskites, *i.e.*, A(TiO_3). Furthermore, it is possible to predict r_A at the tetragonal-to-cubic phase transition using c/a ratio at unity because both r_B and r_O are constant when back-solving with the conventional tolerance factor.

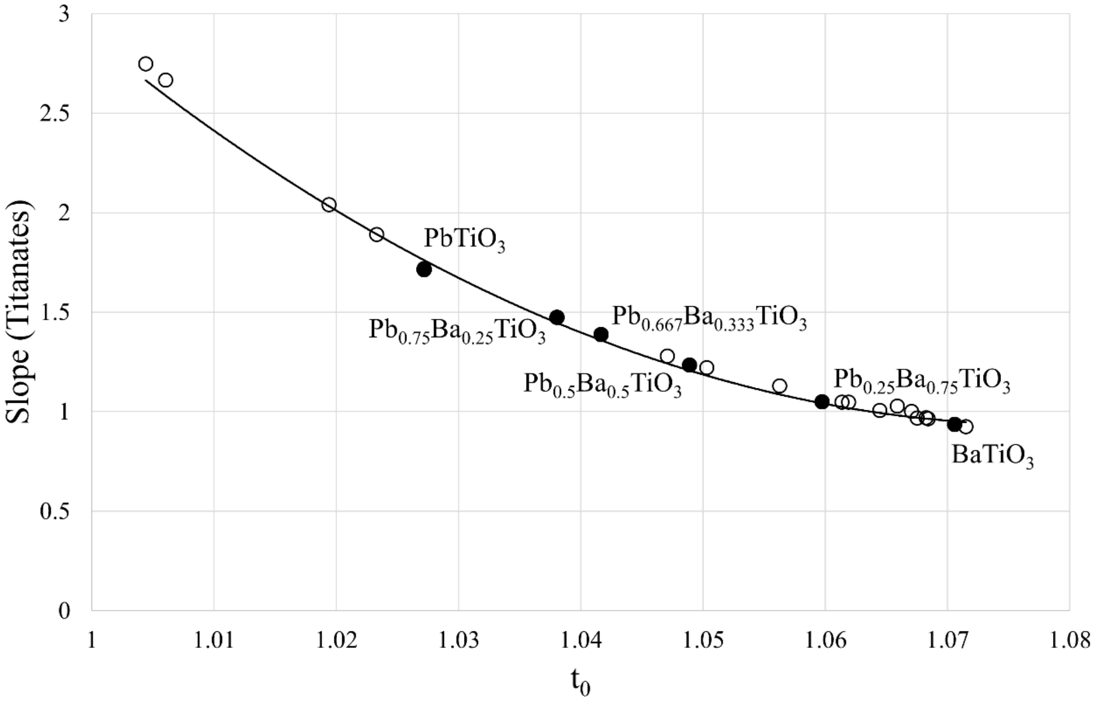

Figure 4.4. Slopes of *c*/*a* vs t_0 curves for $(Pb_{1-y}Ba_y)TiO_3$ $0 \leq y \leq 1$, including all 54 titanates in Table 4.2. The black curve is the fit described by Equation 4.10.

$$m = 317.07(t_0)^2 - 683.79(t_0) + 369.6 \quad (4.10)$$

$$c/a = m(t_1 - 0.964038) + 0.905694 \quad (4.11)$$

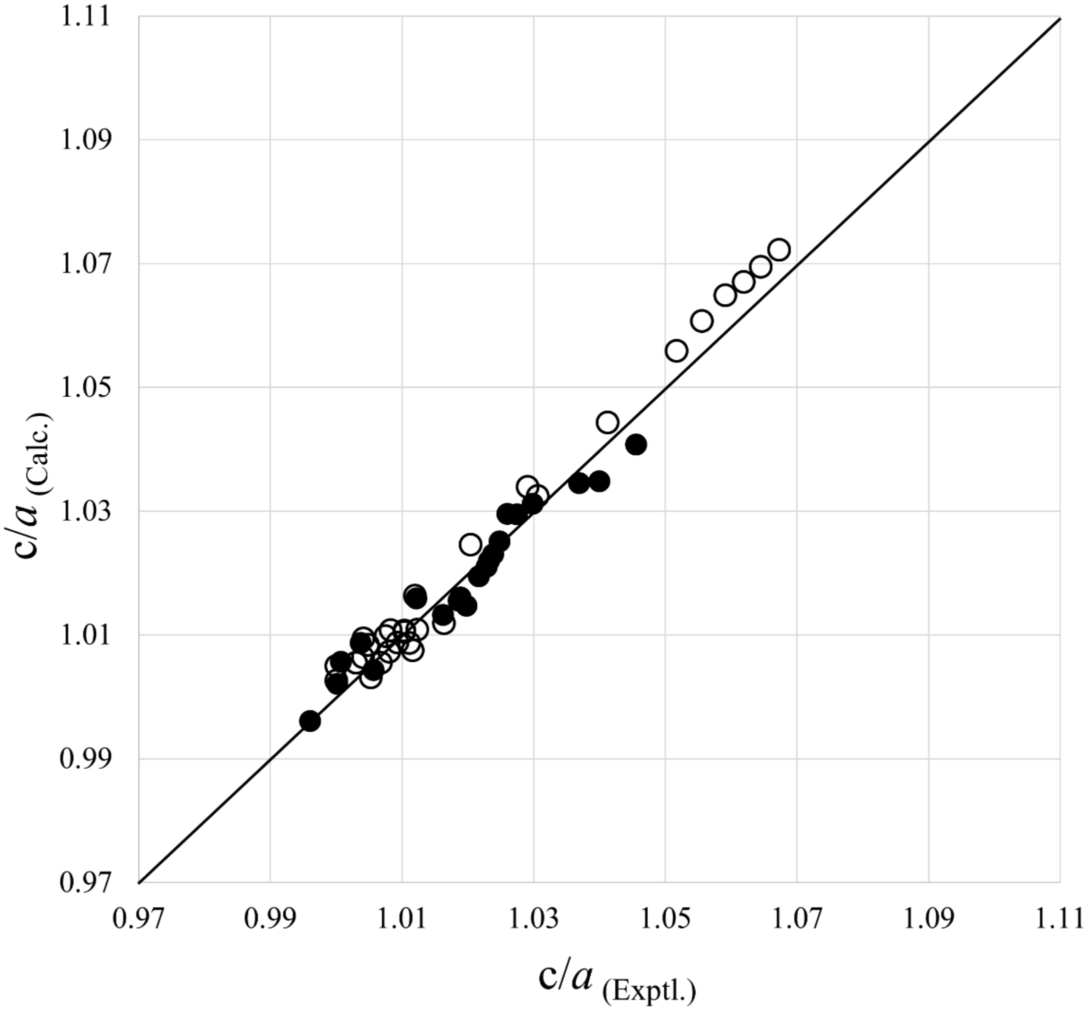

Figure 4.5. **Calculated tetragonalities of 54 titanate perovskites. The 21 filled data points are from this work and the open data points are from literature.[3, 27-34] These 54 titanates, *i.e.*, A(TiO_3), are listed in Table 4.2 (the remaining 79 of the 133 compositions listed in Table 4.2 are not purely titanates).**

Table 4.2. The 133 tetragonal compositions used for the generalized tetragonality relationship (Figure 4.8). 58 of these 133 are titanates, *i.e.*, A(TiO_3).

ICSD #	S.G.	Composition	t_0	slope	t_1	c/a_{exptl}	c/a_{calc}	|Error%|	$a_{\text{pc calc.}}$	|Error%|
28621	*P4mm*	$(Pb_{0.2}\ Ba_{0.8})\ (Ti\ O_3)$	1.0619	0.9819	1.0677	1.0163	1.0075	0.87	3.9904	0.20
54150	*P4mm*	$(Ba_{0.67}\ Sr_{0.33})\ (Ti\ O_3)$	1.0503	1.1601	1.0487	0.9995	1.0039	0.44	3.9740	0.06
55629	*P4/mmm*	$Ce\ (Ga\ O_3)$	0.7071	2.7066	1.0015	1.0018	1.0071	0.53	3.8765	0.03
55700	*P4mm*	$Pb\ ((Zr_{0.45}\ Ti_{0.55})\ O_3)$	1.0007	1.7397	1.0362	1.0244	1.0312	0.67	4.0071	1.26
80800	*P4/mmm*	$(Sr_{0.9}\ Bi_{0.1})\ (Fe\ O_3)$	0.7071	0.9126	1.0638	0.9971	0.9968	0.03	3.8542	0.69
88534	*P4/mmm*	$(Ba_{0.272}\ Sr_{0.728})\ (Zr_{0.403}\ Ti_{0.597})\ O_3$	1.0021	1.9132	1.0137	0.9975	1.0007	0.32	3.9983	0.42
90693	*P4mm*	$Pb\ (Ti\ O_3)$	1.0272	1.7483	1.0541	1.0591	1.0632	0.39	3.9414	0.95
90694	*P4mm*	$Pb\ (Zr_{0.1}\ Ti_{0.9})\ O_3$	1.0212	1.9040	1.0482	1.0521	1.0659	1.31	3.9560	0.96
90695	*P4mm*	$Pb\ (Zr_{0.2}\ Ti_{0.8})\ O_3$	1.0153	1.9857	1.0445	1.0450	1.0655	1.96	3.9706	1.04
90696	*P4mm*	$Pb\ (Zr_{0.3}\ Ti_{0.7})\ O_3$	1.0094	1.9781	1.0438	1.0369	1.0635	2.57	3.9852	1.22
90697	*P4mm*	$Pb\ (Zr_{0.4}\ Ti_{0.6})\ O_3$	1.0036	1.8580	1.0381	1.0314	1.0434	1.16	3.9998	1.23
97116	*P4/mmm*	$(Pr_{0.6}\ Ba_{0.4})\ Co\ O_3$	0.7071	0.7127	1.0623	0.9807	0.9757	0.51	3.8249	1.13
97117	*P4/mmm*	$(Pr_{0.5}\ Ba_{0.5})\ Co\ O_3$	0.7071	0.6352	1.0675	0.9764	0.9714	0.51	3.8418	0.88
97834	*P4mm*	$(Pb_{0.58}\ Ca_{0.42})\ (Ti\ O_3)$	1.0044	2.6688	1.0001	1.0180	1.0019	1.59	3.9093	0.16
97836	*P4mm*	$(Pb_{0.61}\ Ca_{0.39})\ (Ti\ O_3)$	1.0060	2.5927	1.0047	1.0232	1.0112	1.17	3.9116	0.05
98057	*P4mm*	$K_{0.5}\ Bi_{0.5}\ (Ti\ O_3)$	1.0471	1.2222	1.0307	1.0057	0.9871	1.85	3.9695	0.59
150085	*P4mm*	$(Pb_{0.925}\ La_{0.05})\ (Ti\ O_3)$ x=0.025	1.0272	1.7483	1.0425	1.0413	1.0428	0.15	3.9191	1.11
150086	*P4mm*	$(Pb_{0.85}\ La_{0.1})\ (Ti\ O_3)$ x=0.05	1.0272	1.7483	1.0357	1.0306	1.0310	0.04	3.8968	1.43
150087	*P4mm*	$(Pb_{0.775}\ La_{0.15})\ (Ti\ O_3)$ 0.075	1.0272	1.7483	1.0313	1.0204	1.0233	0.28	3.8745	1.84
150088	*P4mm*	$(Pb_{0.7}\ La_{0.2})\ (Ti\ O_3)$ x=0.1	1.0272	1.7483	1.0266	1.0120	1.0151	0.31	3.8522	2.24
150089	*P4mm*	$(Pb_{0.625}\ La_{0.25})\ (Ti\ O_3)$ x=0.125	1.0272	1.7483	1.0221	1.0049	1.0072	0.24	3.8299	2.65
152277	*P4mm*	$Pb\ (V\ O_3)$	0.7071	1.6612	1.1594	1.2295	1.2302	0.06	3.9351	3.44
153294	*P4mm*	$(Pb_{0.96}\ Ce_{0.04})\ (Zr_{0.3}\ Ti_{0.7})\ O_3$	1.0094	1.9781	1.0436	1.0407	1.0631	2.15	3.9822	1.29

153295	*P4mm*	$(Pb_{0.96} Nd_{0.04}) (Zr_{0.3} Ti_{0.7}) O_3$	1.0094	1.9781	1.0417	1.0301	1.0594	2.85	3.9807	1.26
154107	*P4/mmm*	$Nd Ba Co_2 O_6$	0.7071	0.6409	1.0608	0.9782	0.9677	1.07	3.8398	0.70
155328	*P4mm*	$Pb ((Zr_{0.5} Ti_{0.5}) O_3)$	0.9979	1.5580	1.0364	1.0212	1.0184	0.27	4.0144	1.37
155329	*P4mm*	$Pb ((Zr_{0.5} Ti_{0.5}) O_3)$	0.9979	1.5580	1.0364	1.0156	1.0184	0.28	4.0144	1.37
156987	*P4mm*	$(Pb_{0.97} Cd_{0.03}) (Ti O_3)$	1.0233	1.8820	1.0518	1.0673	1.0708	0.33	3.9359	1.01
156988	*P4mm*	$(Pb_{0.94} Cd_{0.06}) (Ti O_3)$	1.0194	2.0258	1.0539	1.0681	1.0878	1.85	3.9304	1.22
157807	*P4mm*	$(Pb_{0.333} Ba_{0.667}) (Ti O_3)$	1.0563	1.0601	1.0546	1.0284	1.0017	2.60	3.9824	0.06
158886	*P4/mmm*	$Pr Ba (Mn_2 O_6)$	0.7071	1.6327	1.0253	0.9972	1.0057	0.85	3.8837	0.12
158890	*P4/mmm*	$Nd Ba (Mn_2 O_6)$	0.7071	1.6814	1.0201	0.9939	1.0000	0.62	3.8817	0.01
161317	*P4mm*	$(Ba_{0.985} Na_{0.015}) ((Ti_{0.985} Nb_{0.015}) O_3)$	1.0688	0.9047	1.0746	1.0044	1.0057	0.14	4.0023	0.20
161710	*P4mm*	$(Pb_{0.95} Bi_{0.05}) (Ti O_3)$	1.0272	1.7483	1.0518	1.0556	1.0591	0.33	3.9404	0.90
161711	*P4mm*	$(Pb_{0.9} Bi_{0.1}) (Ti O_3)$	1.0272	1.7483	1.0490	1.0517	1.0543	0.25	3.9394	0.83
164352	*P4mm*	$(Pb_{0.85} La_{0.1}) (Ti O_3)$ x=0.05	1.0272	1.7483	1.0366	1.0291	1.0325	0.33	3.8968	1.46
164977	*P4mm*	$(Ba_{0.996} Y_{0.004}) (Ti O_3)$	1.0706	0.8883	1.0737	1.0104	1.0031	0.72	4.0018	0.13
165130	*P4mm*	$Pb ((Fe_{0.012} Ti_{0.988}) O_3)$	0.7071	1.6611	1.0615	1.0530	1.0676	1.39	3.9411	1.21
165131	*P4mm*	$(Pb_{0.7} Sr_{0.3}) ((Fe_{0.012} Ti_{0.988}) O_3)$	0.7071	1.7336	1.0222	1.0031	1.0065	0.34	3.9211	0.32
165498	*P4mm*	$Pb (Ti O_3)$	1.0272	1.7483	1.0554	1.0619	1.0653	0.33	3.9414	1.00
166283	*P4/mmm*	$Ce (Al O_3)$	0.7071	2.3952	1.0073	1.0049	1.0094	0.45	3.8078	0.90
169562	*P4/mmm*	$Nd Ba (Co_{1.5} Fe_{0.5}) O_6$	0.7071	0.6627	1.0687	0.9809	0.9750	0.60	3.8414	1.00
169563	*P4/mmm*	$Nd Ba (Co Fe) O_6$	0.7071	0.6876	1.0755	0.9847	0.9823	0.24	3.8429	1.26
169568	*P4/mmm*	$Gd Ba (Co Fe) O_6$	0.7071	0.7353	1.0636	0.9791	0.9789	0.02	3.8350	1.05
169588	*P4mm*	$(Bi_{0.69} Pb_{0.31}) ((Fe_{0.69} Ti_{0.31}) O_3)$	0.7071	1.5167	1.1514	1.1874	1.1899	0.21	3.8969	3.47
169589	*P4mm*	$(Bi_{0.6} Pb_{0.4}) ((Fe_{0.6} Ti_{0.4}) O_3)$	0.7071	1.3073	1.1370	1.1624	1.1318	2.64	3.8911	3.38
169590	*P4mm*	$(Bi_{0.5} Pb_{0.5}) ((Fe_{0.5} Ti_{0.5}) O_3)$	0.7071	1.3550	1.1212	1.1352	1.1187	1.45	3.8970	2.98
169591	*P4mm*	$(Bi_{0.4} Pb_{0.6}) ((Fe_{0.4} Ti_{0.6}) O_3)$	0.7071	1.4508	1.1064	1.1167	1.1123	0.40	3.9053	2.55
169592	*P4mm*	$(Bi_{0.3} Pb_{0.7}) ((Fe_{0.3} Ti_{0.7}) O_3)$	0.7071	1.5477	1.0926	1.0963	1.1047	0.77	3.9144	2.13

169593	*P4mm*	$(Bi_{0.2} Pb_{0.8}) ((Fe_{0.2} Ti_{0.8}) O_3)$	0.7071	1.5406	1.0795	1.0821	1.0835	0.13	3.9234	1.73
169594	*P4mm*	$(Bi_{0.1} Pb_{0.9}) ((Fe_{0.1} Ti_{0.9}) O_3)$	0.7071	1.6976	1.0669	1.0709	1.0804	0.88	3.9324	1.35
169595	*P4mm*	$(Bi_{0.7} Pb_{0.3}) ((Fe_{0.7} Ti_{0.3}) O_3)$	0.7071	1.5210	1.1521	1.1875	1.1917	0.35	3.8967	3.47
169597	*P4mm*	$(Bi_{0.71} Pb_{0.29}) ((Fe_{0.71} Ti_{0.29}) O_3)$	0.7071	1.4963	1.1529	1.1876	1.1882	0.06	3.8952	3.50
169599	*P4mm*	$(Bi_{0.72} Pb_{0.28}) ((Fe_{0.72} Ti_{0.28}) O_3)$	0.7071	1.5005	1.1537	1.1876	1.1903	0.22	3.8950	3.50
181726	*P4mm*	$(Bi_{0.85} Nd_{0.15}) (Fe O_3)$	0.7071	0.8187	1.0919	1.0118	1.0104	0.14	3.8374	2.09
183213	*P4mm*	$Pb (Ti O_3)$	1.0272	1.7483	1.0567	1.0645	1.0678	0.31	3.9414	1.05
183587	*P4mm*	$Pb (Zr_{0.3} Ti_{0.7}) O_3$	1.0094	1.9781	1.0478	1.0427	1.0713	2.74	3.9852	1.36
184861	*P4/mmm*	$Sr (Fe O_3)$	0.7071	1.1543	1.0477	1.0039	1.0023	0.16	3.8626	0.09
186228	*P4mm*	$Ba_{0.9} K_{0.05} Bi_{0.05} (Ti O_3)$	1.0683	0.9108	1.0720	1.0103	1.0040	0.62	3.9993	0.13
186229	*P4mm*	$(Ba_{0.85} K_{0.075} Bi_{0.075}) (Ti O_3)$	1.0671	0.9227	1.0693	1.0111	1.0028	0.82	3.9976	0.08
186230	*P4mm*	$(Ba_{0.8} K_{0.1} Bi_{0.1}) (Ti O_3)$	1.0659	0.9353	1.0671	1.0116	1.0021	0.93	3.9960	0.04
186683	*P4/mmm*	$(Ba_{0.5} Sr_{0.5}) (Ti_{0.946} Fe_{0.046}) O_3$	0.7071	1.3078	1.0457	0.9987	1.0125	1.39	3.9520	0.10
186684	*P4/mmm*	$(Ba_{0.5} Sr_{0.5}) (Ti_{0.876} Fe_{0.081}) O_3$	0.7071	0.9177	1.0798	0.9995	1.0119	1.25	3.9212	0.95
186685	*P4/mmm*	$(Ba_{0.5} Sr_{0.5}) (Ti_{0.849} Fe_{0.139}) O_3$	0.7071	1.0005	1.0577	0.9994	0.9994	0.00	3.9275	0.83
186686	*P4/mmm*	$(Ba_{0.5} Sr_{0.5}) (Ti_{0.806} Fe_{0.183}) O_3$	0.7071	0.7059	1.0946	0.9992	0.9979	0.14	3.9021	1.49
186687	*P4/mmm*	$(Ba_{0.5} Sr_{0.5}) (Ti_{0.624} Fe_{0.402}) O_3$	0.7071	1.3185	1.0376	0.9995	1.0026	0.32	3.9529	0.47
187081	*P4mm*	$(Ba_{0.91} Ca_{0.11}) (Ti O_3)$	1.0715	0.8802	1.0729	1.0041	1.0015	0.26	4.0039	0.05
187471	*P4mm*	$Pb (Zr_{0.4} Ti_{0.6}) O_3$	1.0036	1.8580	1.0390	1.0354	1.0449	0.92	3.9998	1.26
187472	*P4mm*	$(Pb_{0.9} Ba_{0.1}) ((Zr_{0.40} Ti_{0.60}) O_3)$	1.0078	1.6752	1.0393	1.0291	1.0318	0.26	4.0059	1.12
187472	*P4mm*	$(Pb_{0.9} Ba_{0.1}) ((Zr_{0.40} Ti_{0.60}) O_3)$	1.0078	1.6752	1.0393	1.0291	1.0318	0.26	4.0059	1.12
187473	*P4mm*	$(Pb_{0.8} Ba_{0.2}) ((Zr_{0.40} Ti_{0.60}) O_3)$	1.0121	1.5102	1.0457	1.0224	1.0290	0.64	4.0121	1.19
187473	*P4mm*	$(Pb_{0.8} Ba_{0.2}) ((Zr_{0.40} Ti_{0.60}) O_3)$	1.0121	1.5102	1.0457	1.0224	1.0290	0.64	4.0121	1.19
187474	*P4mm*	$(Pb_{0.7} Ba_{0.3}) ((Zr_{0.40} Ti_{0.60}) O_3)$	1.0163	1.3632	1.0453	1.0157	1.0165	0.07	4.0182	1.03
187474	*P4mm*	$(Pb_{0.7} Ba_{0.3}) ((Zr_{0.40} Ti_{0.60}) O_3)$	1.0163	1.3632	1.0453	1.0157	1.0165	0.07	4.0182	1.03
187475	*P4mm*	$(Pb_{0.6} Ba_{0.4}) ((Zr_{0.40} Ti_{0.60}) O_3)$	1.0206	1.2340	1.0468	1.0095	1.0078	0.17	4.0243	0.93

187475	*P4mm*	$(Pb_{0.6} Ba_{0.4}) ((Zr_{0.40} Ti_{0.60}) O_3)$	1.0206	1.2340	1.0468	1.0095	1.0078	0.17	4.0243	0.93
187635	*P4mm*	$Pb (V O_3)$	0.7071	1.6612	1.1566	1.2210	1.2256	0.38	3.9351	3.34
188645	*P4mm*	$(Ba_{0.9} Sm_{0.067}) (Ti O_3)$	1.0706	0.8883	1.0692	1.0040	0.9991	0.49	3.9629	0.94
188784	*P4mm*	$(Ba_{0.95} Sr_{0.05}) (Ti O_3)$	1.0675	0.9181	1.0697	1.0093	1.0027	0.65	3.9983	0.08
188785	*P4mm*	$(Ba_{0.9} Sr_{0.1}) (Ti O_3)$	1.0645	0.9514	1.0657	1.0080	1.0024	0.56	3.9939	0.04
188786	*P4mm*	$(Ba_{0.85} Sr_{0.15}) (Ti O_3)$	1.0614	0.9887	1.0609	1.0068	1.0015	0.52	3.9896	0.02
188985	*P4mm*	$(Bi_{0.6} Sr_{0.4}) (Mn O_3)$	0.7071	0.8842	1.0495	0.9747	0.9813	0.68	3.8568	0.64
188986	*P4mm*	$(Bi_{0.55} Sr_{0.45}) (Mn O_3)$	0.7071	0.8869	1.0413	0.9693	0.9742	0.50	3.8565	0.36
188987	*P4mm*	$(Bi_{0.5} Sr_{0.5}) (Mn O_3)$	0.7071	0.8897	1.0360	0.9706	0.9697	0.09	3.8563	0.18
188988	*P4mm*	$(Bi_{0.45} Sr_{0.55}) (Mn O_3)$	0.7071	0.8925	1.0343	0.9737	0.9684	0.54	3.8560	0.12
189052	*P4/mmm*	$Pr Ba Co_2 O_6$	0.7071	0.6352	1.0611	0.9847	0.9673	1.76	3.8418	0.65
189232	*P4/mmm*	$Sm Ba (Co_{1.2} Fe_{0.8}) O_6$	0.7071	0.7198	1.0641	0.9766	0.9777	0.11	3.8347	1.05
189382	*P4mm*	$(Ba_{0.96} La_{0.027}) (Ti O_3)$ x=0.0135	1.0706	0.8883	1.0683	1.0030	0.9983	0.47	3.9885	0.27
191123	*P4mm*	$Pb ((Zr_{0.52} Ti_{0.48}) O_3)$	0.9967	1.4562	1.0346	1.0220	1.0084	1.33	4.0173	1.35
191126	*P4mm*	$Pb ((Zr_{0.52} Ti_{0.48}) O_3)$	0.9967	1.4562	1.0382	1.0083	1.0136	0.53	4.0173	1.48
192240	*P4mm*	$(Bi_{0.6} Ca_{0.4}) (Fe O_3)$	0.7071	1.2788	1.0404	0.9991	1.0033	0.42	3.8732	1.18
192241	*P4mm*	$(Bi_{0.5} Ca_{0.5}) (Fe O_3)$	0.7071	1.4048	1.0298	0.9971	0.9981	0.10	3.8676	0.95
192848	*P4mm*	$(Bi_{0.6} Pb_{0.4}) ((Fe_{0.6} Ti_{0.4}) O_3)$	0.7071	1.3073	1.1524	1.1552	1.1520	0.28	3.8911	3.89
192849	*P4mm*	$(Bi_{0.57} La_{0.03} Pb_{0.4}) ((Fe_{0.6} Ti_{0.4}) O_3)$	0.7071	1.3323	1.1255	1.1308	1.1208	0.89	3.8897	3.03
193390	*P4mm*	$(Bi_{0.465} Na_{0.465} Ba_{0.07}) (Ti O_3)$	1.0067	2.5627	1.0001	1.0006	0.9982	0.24	3.9125	0.24
237599	*P4mm*	$(Bi_{0.9} Sm_{0.1}) (Fe_{0.5} Co_{0.5}) O_3$	0.7071	1.5245	1.1868	1.2611	1.2453	1.25	3.8659	4.41
240256	*P4mm*	$Pb V O_3$	0.7071	1.6612	1.1560	1.2290	1.2247	0.35	3.9351	3.33
245945	*P4mm*	$Ba (Ti O_3)$	1.0706	0.8883	1.0738	1.0082	1.0032	0.50	4.0026	0.11
247691	*P4mm*	$(Bi_{0.8} La_{0.2}) (Fe_{0.9} Ti_{0.1}) O_3$	0.7071	0.7767	1.1012	1.0101	1.0123	0.21	3.8420	2.58
247692	*P4mm*	$(Bi_{0.8} La_{0.2}) (Fe_{0.85} Ti_{0.15}) O_3$	0.7071	0.7487	1.0942	1.0031	1.0031	0.00	3.8408	2.51
247747	*P4mm*	$(La_{0.21} Pb_{0.79}) (Fe_{0.18} Ti_{0.82}) O_3$	0.7071	1.4590	1.0466	1.0157	1.0262	1.03	3.9289	0.50

247748	*P4mm*	$(La_{0.12} Pb_{0.88}) (Fe_{0.10} Ti_{0.90}) O_3$	0.7071	1.6519	1.0503	1.0399	1.0482	0.80	3.9344	0.72
247782	*P4mm*	$Pb (Zr_{0.35} Ti_{0.65}) O_3$	1.0065	1.9344	1.0463	1.0395	1.0649	2.44	3.9925	1.41
248396	*P4mm*	$(Ba_{0.96} Nd_{0.04}) Ti O_3$ x=0.02	1.0706	0.8883	1.0658	1.0052	0.9961	0.91	3.9957	0.00
249001	*P4/mmm*	$(Ce_{0.016} Sr_{0.984}) (Fe O_3)$	0.7071	1.1211	1.0492	0.9975	1.0011	0.37	3.8647	0.10
290401	*P4mm*	$(Bi_{0.65} Pb_{0.35}) (Fe_{0.65} Ti_{0.35}) O_3$	0.7071	0.8991	1.1197	1.0391	1.0457	0.63	3.8710	3.17
290951	*P4mm*	$(Bi_{0.8} Ba_{0.2}) (Fe_{0.97} Co_{0.03}) O_3$	0.7071	0.6507	1.1459	1.0176	1.0241	0.63	3.8673	3.15
291165	*P4mm*	$(Pb_{0.05} Ba_{0.95}) (Ti O_3)$	1.0684	0.9090	1.0725	1.0123	1.0043	0.79	3.9995	0.14
Ganguly[3]	*Pm-3m*	$(Ba_{0.9} La_{0.066667}) (Ti O_3)$ x=0.033333	1.0706	0.8883	1.0652	1.0000	0.9956	0.44	3.9667	0.71
Ganguly[3]	*P4mm*	$(Ba_{0.94} La_{0.04}) (Ti O_3)$ x=0.02	1.0706	0.8883	1.0677	1.0000	0.9978	0.22	3.9811	0.44
Ganguly[3]	*P4mm*	$(Ba_{0.96} La_{0.0267}) (Ti O_3)$ x=0.013333	1.0706	0.8883	1.0683	1.0030	0.9983	0.47	3.9883	0.28
This Work	*P4mm*	$Ba (Ti O_3)$ x=0	1.0706	0.8883	1.0727	1.0075	1.0023	0.52	4.0026	0.08
This Work	*P4mm*	$(Ba_{0.88} La_{0.08}) (Ti O_3)$ x=0.04	1.0706	0.8883	1.0647	1.0002	0.9951	0.51	3.9596	0.87
This Work	*P4mm*	$(Ba_{0.91} La_{0.06}) (Ti O_3)$ x=0.03	1.0706	0.8883	1.0584	0.9961	0.9895	0.66	3.9703	0.38
This Work	*P4mm*	$(Ba_{0.94} La_{0.04}) (Ti O_3)$ x=0.02	1.0706	0.8883	1.0684	1.0008	0.9984	0.23	3.9811	0.46
This Work	*P4mm*	$(Ba_{0.97} La_{0.02}) (Ti O_3)$ x=0.01	1.0706	0.8883	1.0716	1.0038	1.0012	0.25	3.9918	0.30
This Work	*P4mm*	$(Pb_{0.22} Ba_{0.66} La_{0.08}) (Ti O_3)$ x=0.04	1.0598	1.0102	1.0581	1.0057	1.0007	0.50	3.9461	0.97
This Work	*P4mm*	$(Pb_{0.235} Ba_{0.705} La_{0.04}) (Ti O_3)$ x=0.02	1.0598	1.0102	1.0692	1.0122	1.0119	0.03	3.9667	0.85
This Work	*P4mm*	$(Pb_{0.25} Ba_{0.75}) (Ti O_3)$ x=0	1.0598	1.0102	1.0680	1.0198	1.0107	0.89	3.9873	0.29
This Work	*P4mm*	$(Pb_{0.455} Ba_{0.455} La_{0.06}) (Ti O_3)$ x=0.03	1.0489	1.1866	1.0527	1.0162	1.0108	0.53	3.9217	1.40
This Work	*P4mm*	$(Pb_{0.485} Ba_{0.485} La_{0.02}) (Ti O_3)$ x=0.01	1.0489	1.1866	1.0599	1.0232	1.0194	0.37	3.9552	0.81
This Work	*P4mm*	$(Pb_{0.5867} Ba_{0.2933} La_{0.08}) (Ti O_3)$ x=0.04	1.0417	1.3406	1.0448	1.0189	1.0140	0.48	3.9237	1.07
This Work	*P4mm*	$(Pb_{0.6067} Ba_{0.3033} La_{0.06}) (Ti O_3)$ x=0.03	1.0417	1.3406	1.0485	1.0229	1.0190	0.38	3.9332	0.96
This Work	*P4mm*	$(Pb_{0.6267} Ba_{0.3133} La_{0.04}) (Ti O_3)$ x=0.02	1.0417	1.3406	1.0500	1.0239	1.0210	0.29	3.9428	0.78
This Work	*P4mm*	$(Pb_{0.6375} Ba_{0.2125} La_{0.1}) (Ti O_3)$ x=0.05	1.0381	1.4296	1.0396	1.0186	1.0137	0.48	3.9098	1.24
This Work	*P4mm*	$(Pb_{0.6467} Ba_{0.3233} La_{0.02}) (Ti O_3)$ x=0.01	1.0417	1.3406	1.0560	1.0299	1.0290	0.09	3.9523	0.75
This Work	*P4mm*	$(Pb_{0.66} Ba_{0.22} La_{0.08}) (Ti O_3)$ x=0.04	1.0381	1.4296	1.0423	1.0217	1.0176	0.40	3.9192	1.10

This Work	*P*4*mm*	$(Pb_{0.667}\ Ba_{0.333})\ (Ti\ O_3)$ x=0	1.0417	1.3406	1.0587	1.0400	1.0325	0.72	3.9618	0.60
This Work	*P*4*mm*	$(Pb_{0.6825}\ Ba_{0.2275}\ La_{0.06})\ (Ti\ O_3)$ x=0.03	1.0381	1.4296	1.0462	1.0249	1.0232	0.16	3.9286	1.00
This Work	*P*4*mm*	$(Pb_{0.705}\ Ba_{0.235}\ La_{0.04})\ (Ti\ O_3)$ x=0.02	1.0381	1.4296	1.0492	1.0275	1.0274	0.01	3.9380	0.87
This Work	*P*4*mm*	$(Pb_{0.7275}\ Ba_{0.2425}\ La_{0.02})\ (Ti\ O_3)$ x=0.01	1.0381	1.4296	1.0527	1.0370	1.0325	0.44	3.9473	0.75
This Work	*P*4*mm*	$(Pb_{0.75}\ Ba_{0.25})\ (Ti\ O_3)$ x=0	1.0381	1.4296	1.0570	1.0456	1.0386	0.66	3.9567	0.67
This Work	*P*4*mm*	$(Pb_{0.82}\ La_{0.12})\ (Ti\ O_3)$ x=0.06	1.0272	1.7483	1.0341	1.0260	1.0281	0.20	3.8879	1.60
		Mean Relative Errors %						0.64		1.13

The question then becomes whether or not this method can be extended to other tetragonal compounds. Perhaps the point of convergence (Figure 4.3) can be used to relate other tetragonal compositional systems. One may naturally shift attention to the effects of changing the B-site cation (Table 4.1) in an attempt to extend this method and further the understandings of tetragonality. Replacing Ti^{4+} (r_{Ti}^{VI} = 0.605 Å) with Zr^{4+} (r_{Zr}^{VI} = 0.72 Å) increases the average B-site cation size and so reduces the tolerance factor, which simultaneously decreases the tetragonality (Figure 4.6). The inset of Figure 4.6 shows 15 $Pb(Zr_{1-z}Ti_z)O_3$ data points in context with Figure 4.3.

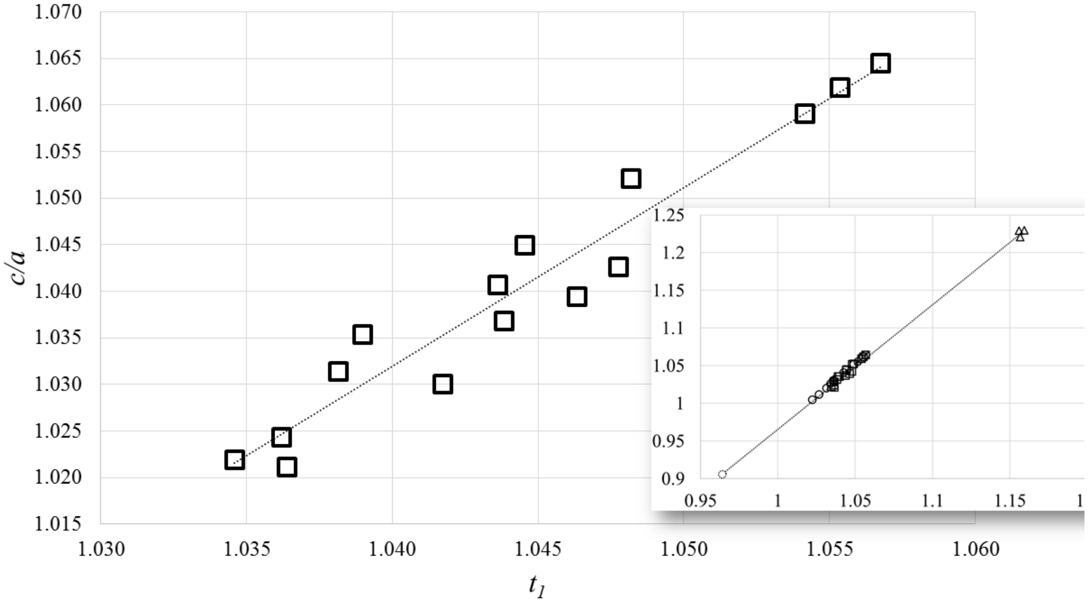

Figure 4.6. Effect of tolerance factor on tetragonality for $Pb(Zr_{1-z}Ti_z)O_3$ in P4mm, with the concentration of Ti^{4+} (*z*) increasing from left to right, simultaneously increasing both tetragonality and tolerance factor. These seven compositions were selected from Table 4.1. The inset shows these data points in context with Figure 4.3.

Assuming that this method may be used for any tetragonal compositional family which shares the same point of convergence, a combined total of 133 various tetragonal compounds in either *P*4*mm* or *P4/mmm* (Table 4.2) were used in conjunction with this point of convergence to calculate the slopes of their respective c/a vs t_1 curves (Figure 4.7) and to generalize Equation 4.10:

$$m = m_1 - (m_1 - m_2)\left(\frac{2}{\sqrt{\pi}}\right)\int_0^C e^{-n^2}\,dn \qquad (4.12)$$

Where

$$m_1 = -97.6891 + 337.225 r_B - 279.582 r_B^2,$$

$$m_2 = -9.33831 + 33.2458 r_B - 27.5444 r_B^2,$$

and

$$C = \frac{t_0 - (0.573697 + 1.34272 r_B - 1.11274 r_B^2)}{2\sqrt{-0.0839725 + 0.282206 r_B - 0.233808 r_B^2}}$$

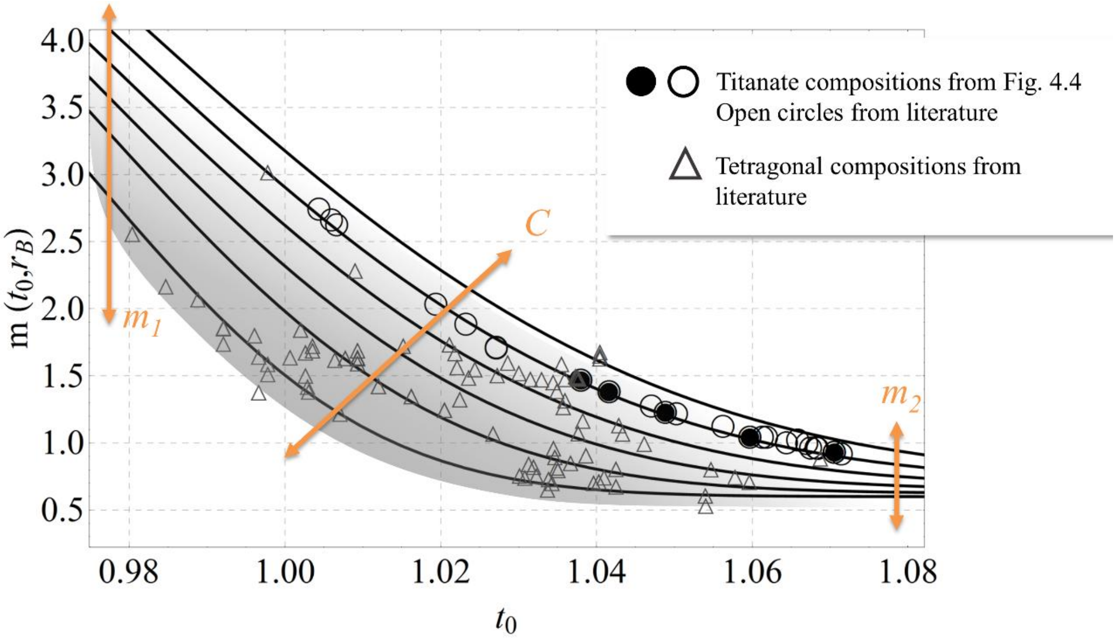

Figure 4.7. Slopes of the c/a vs t_1 curves in terms of tolerance factor at $x = 0$ (t_0) derived from the 133 perovskite oxides in Table 4.2.

As a proof of concept, Figure 4.8 shows the results of this method of estimating c/a using Equations 4.11–4.12, and Table 4.2 shows the results of this approach for each of the 133 compositions shown in Figure 4.8. It is noteworthy that Figure 4.8 includes the otherwise anomalous $PbVO_3$ outlier compound ($c/a = 1.229$)[15] and three compositions in space group $P4/mmm$ (*i.e.*, $SrFeO_3$, $Sr_{0.9}Bi_{0.1}FeO_3$ and $CeAlO_3$) [24-26] and still demonstrates a goodness of fit with an overall average absolute relative error of just 0.64%. The tetragonal lattice constants can then be derived (assuming the absence of any cation ordering - see Chapter 3) with Equations 4.12 and 4.13. Equation 4.13 shows the mathematical relationship between c/a and a_{pc} (assuming one ABX_3 formula unit, which is appropriate for perovskites in either $P4mm$ or $P4/mmm$). Table 4.3 shows experimental and calculated tetragonal lattice constants using Equations 4.3, 4.11, 4.12 and 4.13; where the calculated c/a (Equation 4.11) depends on m (Equation 4.12) and the calculated t_1 (Equation 4.3).

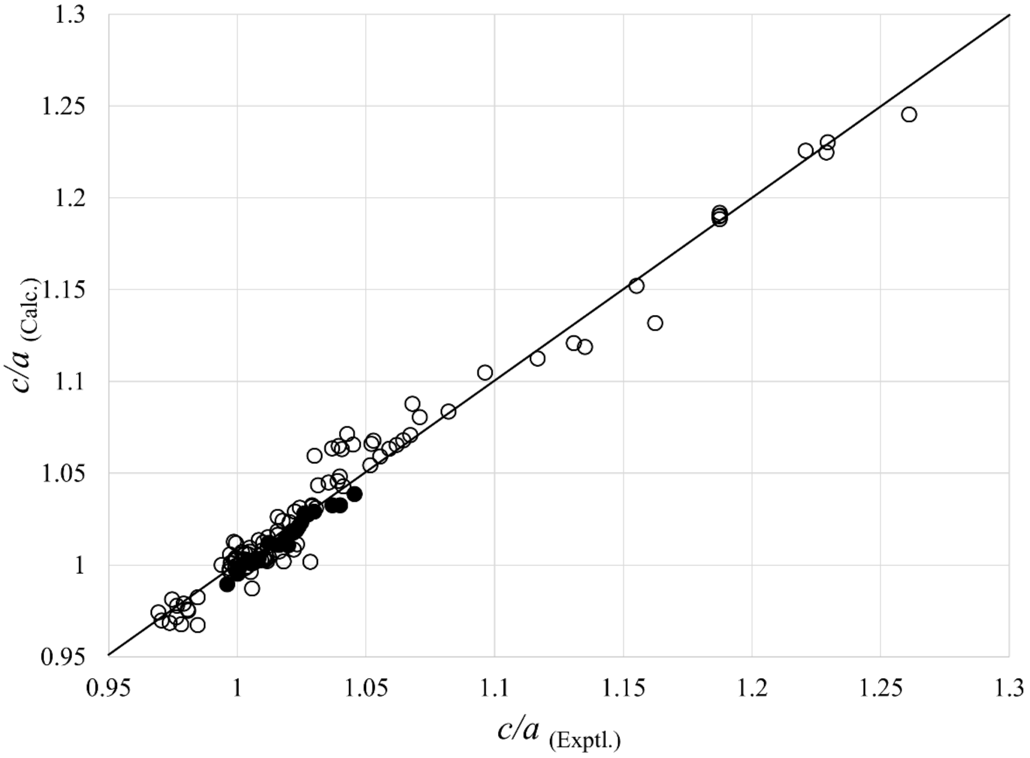

Figure 4.8. Calculated tetragonalities of the 133 perovskite oxides listed in Table 2. Open data points are from literature and filled data points are from this work.

$$\frac{c}{a} = \left(\frac{a_{pc}}{a}\right)^3 \tag{4.13}$$

Table 4.3. **Various experimental and calculated tetragonal lattice constants from Equations 4.3, 4.11, 4.12 and 4.13.**

ICSD#	Compound	$a_{\text{(Exptl.)}}$ (Å)	$a_{\text{(Calc.)}}$ (Å)	|Error%|	$c_{\text{(Exptl.)}}$ (Å)	$c_{\text{(Calc.)}}$ (Å)	|Error%|
28621	$(Pb_{0.2}Ba_{0.8})(TiO_3)$	3.9770	4.0198	1.08	4.0420	4.0500	0.20
54150	$(Ba_{0.67}Sr_{0.33})(TiO_3)$	3.9724	4.0165	1.11	3.9703	4.0322	1.56
55629	$Ce(GaO_3)$	3.8730	3.8594	0.35	3.8800	3.8869	0.18
55700	$Pb((Zr_{0.45}Ti_{0.55})O_3)$	4.0260	4.0254	0.01	4.1241	4.1511	0.65
80800	$(Sr_{0.9}Bi_{0.1})(FeO_3)$	3.8848	3.8595	0.65	3.8735	3.8469	0.69
88534	$(Ba_{0.272}Sr_{0.728})(Zr_{0.403}Ti_{0.597})O_3$	4.0184	4.0536	0.88	4.0084	4.0563	1.20
90693	$Pb(TiO_3)$	3.9039	3.8998	0.11	4.1348	4.1464	0.28
90694	$Pb(Zr_{0.1}Ti_{0.9})O_3$	3.9272	3.9150	0.31	4.1319	4.1730	1.00
90695	$Pb(Zr_{0.2}Ti_{0.8})O_3$	3.9539	3.9341	0.50	4.1319	4.1920	1.45
90696	$Pb(Zr_{0.3}Ti_{0.7})O_3$	3.9862	3.9556	0.77	4.1331	4.2067	1.78
90697	$Pb(Zr_{0.4}Ti_{0.6})O_3$	4.0081	4.0000	0.20	4.1341	4.1736	0.95
97116	$(Pr_{0.6}Ba_{0.4})CoO_3$	3.8939	3.8358	1.49	3.8189	3.7426	2.00
97117	$(Pr_{0.5}Ba_{0.5})CoO_3$	3.9069	3.8785	0.73	3.8145	3.7676	1.23
97834	$(Pb_{0.58}Ca_{0.42})(TiO_3)$	3.8800	3.9191	1.01	3.9500	3.9265	0.59
97836	$(Pb_{0.61}Ca_{0.39})(TiO_3)$	3.8800	3.9114	0.81	3.9700	3.9554	0.37
98057	$K_{0.5}Bi_{0.5}(TiO_3)$	3.9388	4.0351	2.45	3.9613	3.9832	0.55

150085	$(Pb_{0.925}La_{0.05})(TiO_3)$ x=0.025	3.9099	3.9140	0.10	4.0712	4.0816	0.26
150086	$(Pb_{0.85}La_{0.1})(TiO_3)$ x=0.05	3.9139	3.9191	0.13	4.0337	4.0407	0.17
150087	$(Pb_{0.775}La_{0.15})(TiO_3)$0.075	3.9207	3.9207	0.00	4.0007	4.0120	0.28
150088	$(Pb_{0.7}La_{0.2})(TiO_3)$ x=0.1	3.9250	3.9243	0.02	3.9720	3.9836	0.29
150089	$(Pb_{0.625}La_{0.25})(TiO_3)$ x=0.125	3.9279	3.9289	0.03	3.9470	3.9574	0.26
152277	$Pb(VO_3)$	3.8039	3.7071	2.55	4.6768	4.5604	2.49
153294	$(Pb_{0.96}Ce_{0.04})(Zr_{0.3}Ti_{0.7})O_3$	3.9810	3.9512	0.75	4.1430	4.2004	1.39
153295	$(Pb_{0.96}Nd_{0.04})(Zr_{0.3}Ti_{0.7})O_3$	3.9920	3.9534	0.97	4.1120	4.1882	1.85
154107	$NdBaCo_2O_6$	3.8952	3.8791	0.41	3.8104	3.7539	1.48
155328	$Pb((Zr_{0.5}Ti_{0.5})O_3)$	4.0420	4.0521	0.25	4.1275	4.1266	0.02
155329	$Pb((Zr_{0.5}Ti_{0.5})O_3)$	4.0494	4.0520	0.06	4.1125	4.1266	0.34
156987	$(Pb_{0.97}Cd_{0.03})(TiO_3)$	3.8907	3.8815	0.24	4.1524	4.1564	0.10
156988	$(Pb_{0.94}Cd_{0.06})(TiO_3)$	3.8927	3.8518	1.05	4.1576	4.1899	0.78
157807	$(Pb_{0.333}Ba_{0.667})(TiO_3)$	3.9430	4.0250	2.08	4.0550	4.0317	0.57
158886	$PrBa(Mn_2O_6)$	3.8921	3.8863	0.15	3.8813	3.9084	0.70
158890	$NdBa(Mn_2O_6)$	3.8893	3.8896	0.01	3.8655	3.8897	0.63
161317	$(Ba_{0.985}Na_{0.015})((Ti_{0.985}Nb_{0.015})O_3)$	4.0047	4.0233	0.46	4.0221	4.0462	0.60
161710	$(Pb_{0.95}Bi_{0.05})(TiO_3)$	3.9050	3.9043	0.02	4.1220	4.1349	0.31

161711	$(Pb_{0.9}Bi_{0.1})(TiO_3)$	3.9060	3.9097	0.09	4.1080	4.1220	0.34
164352	$(Pb_{0.85}La_{0.1})(TiO_3)$ x=0.05	3.9170	3.9172	0.01	4.0310	4.0446	0.34
164977	$(Ba_{0.996}Y_{0.004})(TiO_3)$	3.9932	4.0242	0.78	4.0346	4.0368	0.05
165130	$Pb((Fe_{0.012}Ti_{0.988})O_3)$	3.9212	3.8941	0.69	4.1289	4.1572	0.69
165131	$(Pb_{0.7}Sr_{0.3})((Fe_{0.012}Ti_{0.988})O_3)$	3.9298	3.9425	0.32	3.9420	3.9681	0.66
165498	$Pb(TiO_3)$	3.9022	3.8972	0.13	4.1437	4.1518	0.20
166283	$Ce(AlO_3)$	3.7676	3.7404	0.72	3.7860	3.7756	0.28
169562	$NdBa(Co_{1.5}Fe_{0.5})O_6$	3.9050	3.8713	0.86	3.8305	3.7747	1.46
169563	$NdBa(CoFe)O_6$	3.9120	3.8637	1.23	3.8520	3.7954	1.47
169568	$GdBa(CoFe)O_6$	3.9030	3.8512	1.33	3.8215	3.7699	1.35
169588	$(Bi_{0.69}Pb_{0.31})((Fe_{0.69}Ti_{0.31})O_3)$	3.8122	3.6961	3.05	4.5266	4.3981	2.84
169589	$(Bi_{0.6}Pb_{0.4})((Fe_{0.6}Ti_{0.4})O_3)$	3.8301	3.7524	2.03	4.4523	4.2469	4.61
169590	$(Bi_{0.5}Pb_{0.5})((Fe_{0.5}Ti_{0.5})O_3)$	3.8506	3.7752	1.96	4.3711	4.2233	3.38
169591	$(Bi_{0.4}Pb_{0.6})((Fe_{0.4}Ti_{0.6})O_3)$	3.8628	3.7937	1.79	4.3137	4.2198	2.18
169592	$(Bi_{0.3}Pb_{0.7})((Fe_{0.3}Ti_{0.7})O_3)$	3.8789	3.8144	1.66	4.2526	4.2139	0.91
169593	$(Bi_{0.2}Pb_{0.8})((Fe_{0.2}Ti_{0.8})O_3)$	3.8889	3.8512	0.97	4.2082	4.1729	0.84
169594	$(Bi_{0.1}Pb_{0.9})((Fe_{0.1}Ti_{0.9})O_3)$	3.8962	3.8670	0.75	4.1726	4.1778	0.13
169595	$(Bi_{0.7}Pb_{0.3})((Fe_{0.7}Ti_{0.3})O_3)$	3.8118	3.6939	3.09	4.5266	4.4020	2.75

169597	$(Bi_{0.71}Pb_{0.29})((Fe_{0.71}Ti_{0.29})O_3)$	3.8117	3.6956	3.05	4.5267	4.3913	2.99
169599	$(Bi_{0.72}Pb_{0.28})((Fe_{0.72}Ti_{0.28})O_3)$	3.8116	3.6932	3.11	4.5268	4.3958	2.89
181726	$(Bi_{0.85}Nd_{0.15})(FeO_3)$	3.9042	3.8131	2.33	3.9503	3.8527	2.47
183213	$Pb(TiO_3)$	3.9009	3.8942	0.17	4.1526	4.1582	0.13
183587	$Pb(Zr_{0.3}Ti_{0.7})O_3$	3.9843	3.9459	0.96	4.1545	4.2273	1.75
184861	$Sr(FeO_3)$	3.8540	3.8624	0.22	3.8690	3.8713	0.06
186228	$Ba_{0.9}K_{0.05}Bi_{0.05}(TiO_3)$	3.9909	4.0239	0.83	4.0321	4.0401	0.20
186229	$(Ba_{0.85}K_{0.075}Bi_{0.075})(TiO_3)$	3.9861	4.0259	1.00	4.0303	4.0373	0.17
186230	$(Ba_{0.8}K_{0.1}Bi_{0.1})(TiO_3)$	3.9824	4.0271	1.12	4.0285	4.0356	0.18
186683	$(Ba_{0.5}Sr_{0.5})(Ti_{0.946}Fe_{0.046})O_3$	3.9576	3.9803	0.57	3.9524	4.0302	1.97
186684	$(Ba_{0.5}Sr_{0.5})(Ti_{0.876}Fe_{0.081})O_3$	3.9596	3.9418	0.45	3.9575	3.9887	0.79
186685	$(Ba_{0.5}Sr_{0.5})(Ti_{0.849}Fe_{0.139})O_3$	3.9610	3.9663	0.13	3.9586	3.9638	0.13
186686	$(Ba_{0.5}Sr_{0.5})(Ti_{0.806}Fe_{0.183})O_3$	3.9620	3.9361	0.65	3.9590	3.9277	0.79
186687	$(Ba_{0.5}Sr_{0.5})(Ti_{0.624}Fe_{0.402})O_3$	3.9722	3.9947	0.56	3.9701	4.0051	0.88
187081	$(Ba_{0.91}Ca_{0.11})(TiO_3)$	4.0003	4.0254	0.63	4.0169	4.0315	0.36
187471	$Pb(Zr_{0.4}Ti_{0.6})O_3$	4.0041	3.9981	0.15	4.1460	4.1776	0.76
187472	$(Pb_{0.9}Ba_{0.1})((Zr_{0.40}Ti_{0.60})O_3)$	4.0128	4.0244	0.29	4.1297	4.1526	0.55
187472	$(Pb_{0.9}Ba_{0.1})((Zr_{0.40}Ti_{0.60})O_3)$	4.0128	4.0244	0.29	4.1297	4.1526	0.55

187473	$(Pb_{0.8}Ba_{0.2})((Zr_{0.40}Ti_{0.60})O_3)$	4.0306	4.0372	0.16	4.1210	4.1541	0.80
187473	$(Pb_{0.8}Ba_{0.2})((Zr_{0.40}Ti_{0.60})O_3)$	4.0306	4.0372	0.16	4.1210	4.1541	0.80
187474	$(Pb_{0.7}Ba_{0.3})((Zr_{0.40}Ti_{0.60})O_3)$	4.0389	4.0622	0.58	4.1025	4.1290	0.65
187474	$(Pb_{0.7}Ba_{0.3})((Zr_{0.40}Ti_{0.60})O_3)$	4.0389	4.0622	0.58	4.1025	4.1290	0.65
187475	$(Pb_{0.6}Ba_{0.4})((Zr_{0.40}Ti_{0.60})O_3)$	4.0493	4.0815	0.80	4.0879	4.1134	0.62
187475	$(Pb_{0.6}Ba_{0.4})((Zr_{0.40}Ti_{0.60})O_3)$	4.0493	4.0815	0.80	4.0879	4.1134	0.62
187635	$Pb(VO_3)$	3.8091	3.7117	2.56	4.6508	4.5490	2.19
188645	$(Ba_{0.9}Sm_{0.067})(TiO_3)$	3.9953	4.0119	0.42	4.0114	4.0085	0.07
188784	$(Ba_{0.95}Sr_{0.05})(TiO_3)$	3.9890	4.0259	0.93	4.0260	4.0368	0.27
188785	$(Ba_{0.9}Sr_{0.1})(TiO_3)$	3.9850	4.0269	1.05	4.0170	4.0365	0.49
188786	$(Ba_{0.85}Sr_{0.15})(TiO_3)$	3.9800	4.0277	1.20	4.0070	4.0338	0.67
188985	$(Bi_{0.6}Sr_{0.4})(MnO_3)$	3.9151	3.8849	0.77	3.8158	3.8122	0.10
188986	$(Bi_{0.55}Sr_{0.45})(MnO_3)$	3.9107	3.8938	0.43	3.7908	3.7933	0.06
188987	$(Bi_{0.5}Sr_{0.5})(MnO_3)$	3.9017	3.8993	0.06	3.7869	3.7811	0.15
188988	$(Bi_{0.45}Sr_{0.55})(MnO_3)$	3.8952	3.9004	0.13	3.7928	3.7773	0.41
189052	$PrBaCo_2O_6$	3.8870	3.8839	0.08	3.8275	3.7570	1.84
189232	$SmBa(Co_{1.2}Fe_{0.8})O_6$	3.9060	3.8525	1.37	3.8145	3.7666	1.26
189382	$(Ba_{0.96}La_{0.027})(TiO_3)$ x=0.0135	3.9953	4.0317	0.91	4.0073	4.0249	0.44

191123	$Pb((Zr_{0.52}Ti_{0.48})O_3)$	4.0429	4.0693	0.65	4.1318	4.1035	0.68
191126	$Pb((Zr_{0.52}Ti_{0.48})O_3)$	4.0663	4.0623	0.10	4.1001	4.1177	0.43
192240	$(Bi_{0.6}Ca_{0.4})(FeO_3)$	3.9207	3.8618	1.50	3.9173	3.8745	1.09
192241	$(Bi_{0.5}Ca_{0.5})(FeO_3)$	3.9086	3.8571	1.32	3.8973	3.8497	1.22
192848	$(Bi_{0.6}Pb_{0.4})((Fe_{0.6}Ti_{0.4})O_3)$	3.8585	3.7304	3.32	4.4573	4.2972	3.59
192849	$(Bi_{0.57}La_{0.03}Pb_{0.4})((Fe_{0.6}Ti_{0.4})O_3)$	3.8502	3.7622	2.29	4.3538	4.2165	3.15
193390	$(Bi_{0.465}Na_{0.465}Ba_{0.07})(TiO_3)$	3.9025	3.9302	0.71	3.9048	3.9231	0.47
237599	$(Bi_{0.9}Sm_{0.1})(Fe_{0.5}Co_{0.5})O_3$	3.7432	3.5926	4.02	4.7207	4.4739	5.23
240256	$PbVO_3$	3.8001	3.7127	2.30	4.6703	4.5467	2.65
245945	$Ba(TiO_3)$	3.9961	4.0238	0.69	4.0290	4.0366	0.19
247691	$(Bi_{0.8}La_{0.2})(Fe_{0.9}Ti_{0.1})O_3$	3.9304	3.8206	2.79	3.9702	3.8674	2.59
247692	$(Bi_{0.8}La_{0.2})(Fe_{0.85}Ti_{0.15})O_3$	3.9355	3.8306	2.67	3.9477	3.8425	2.66
247747	$(La_{0.21}Pb_{0.79})(Fe_{0.18}Ti_{0.82})O_3$	3.9283	3.9302	0.05	3.9899	4.0330	1.08
247748	$(La_{0.12}Pb_{0.88})(Fe_{0.10}Ti_{0.90})O_3$	3.9115	3.9095	0.05	4.0675	4.0979	0.75
247782	$Pb(Zr_{0.35}Ti_{0.65})O_3$	3.9979	3.9634	0.86	4.1557	4.2204	1.56
248396	$(Ba_{0.96}Nd_{0.04})TiO_3$ x=0.02	3.9889	4.0352	1.16	4.0098	4.0195	0.24
249001	$(Ce_{0.016}Sr_{0.984})(FeO_3)$	3.8642	3.8681	0.10	3.8544	3.8724	0.47
290401	$(Bi_{0.65}Pb_{0.35})(Fe_{0.65}Ti_{0.35})O_3$	3.9468	3.8275	3.02	4.1011	4.0023	2.41

290951	$(Bi_{0.8}Ba_{0.2})(Fe_{0.97}Co_{0.03})O_3$	3.9700	3.8551	2.89	4.0400	3.9479	2.28
291165	$(Pb_{0.05}Ba_{0.95})(TiO_3)$	3.9890	4.0218	0.82	4.0380	4.0390	0.03
Ganguly[3]	$(Ba_{0.9}La_{0.066667})(TiO_3)$ x=0.033333	3.9950	4.0280	0.83	3.9950	4.0102	0.38
Ganguly[3]	$(Ba_{0.94}La_{0.04})(TiO_3)$ x=0.02	3.9986	4.0274	0.72	3.9986	4.0186	0.50
Ganguly[3]	$(Ba_{0.96}La_{0.0267})(TiO_3)$ x=0.013333	3.9953	4.0280	0.82	4.0073	4.0211	0.34
This Work	$Ba(TiO_3)$ x=0	3.9957	4.0250	0.73	4.0256	4.0342	0.21
This Work	$(Ba_{0.88}La_{0.08})(TiO_3)$ x=0.04	3.9940	4.0274	0.84	3.9947	4.0076	0.32
This Work	$(Ba_{0.91}La_{0.06})(TiO_3)$ x=0.03	3.9906	4.0368	1.16	3.9750	3.9945	0.49
This Work	$(Ba_{0.94}La_{0.04})(TiO_3)$ x=0.02	3.9985	4.0266	0.70	4.0016	4.0203	0.47
This Work	$(Ba_{0.97}La_{0.02})(TiO_3)$ x=0.01	3.9990	4.0246	0.64	4.0140	4.0296	0.39
This Work	$(Pb_{0.22}Ba_{0.66}La_{0.08})(TiO_3)$ x=0.04	3.9774	4.0145	0.93	4.0001	4.0173	0.43
This Work	$(Pb_{0.235}Ba_{0.705}La_{0.04})(TiO_3)$ x=0.02	3.9844	4.0063	0.55	4.0332	4.0541	0.52
This Work	$(Pb_{0.25}Ba_{0.75})(TiO_3)$ x=0	3.9729	4.0148	1.06	4.0516	4.0579	0.16
This Work	$(Pb_{0.455}Ba_{0.455}La_{0.06})(TiO_3)$ x=0.03	3.9560	3.9842	0.71	4.0202	4.0274	0.18
This Work	$(Pb_{0.485}Ba_{0.485}La_{0.02})(TiO_3)$ x=0.01	3.9571	3.9868	0.75	4.0489	4.0642	0.38
This Work	$(Pb_{0.5867}Ba_{0.2933}La_{0.08})(TiO_3)$ x=0.04	3.9416	3.9729	0.79	4.0161	4.0286	0.31
This Work	$(Pb_{0.6067}Ba_{0.3033}La_{0.06})(TiO_3)$ x=0.03	3.9416	3.9707	0.74	4.0319	4.0460	0.35
This Work	$(Pb_{0.6267}Ba_{0.3133}La_{0.04})(TiO_3)$ x=0.02	3.9424	3.9725	0.76	4.0366	4.0558	0.47

This Work	$(Pb_{0.6375}Ba_{0.2125}La_{0.1})(TiO_3)$ x=0.05	3.9346	3.9628	0.72	4.0078	4.0171	0.23
This Work	$(Pb_{0.6467}Ba_{0.3233}La_{0.02})(TiO_3)$ x=0.01	3.9431	3.9668	0.60	4.0609	4.0817	0.51
This Work	$(Pb_{0.66}Ba_{0.22}La_{0.08})(TiO_3)$ x=0.04	3.9344	3.9618	0.69	4.0199	4.0316	0.29
This Work	$(Pb_{0.667}Ba_{0.333})(TiO_3)$ x=0	3.9340	3.9669	0.84	4.0914	4.0960	0.11
This Work	$(Pb_{0.6825}Ba_{0.2275}La_{0.06})(TiO_3)$ x=0.03	3.9359	3.9588	0.58	4.0337	4.0506	0.42
This Work	$(Pb_{0.705}Ba_{0.235}La_{0.04})(TiO_3)$ x=0.02	3.9367	3.9577	0.54	4.0449	4.0663	0.53
This Work	$(Pb_{0.7275}Ba_{0.2425}La_{0.02})(TiO_3)$ x=0.01	3.9295	3.9559	0.67	4.0748	4.0843	0.23
This Work	$(Pb_{0.75}Ba_{0.25})(TiO_3)$ x=0	3.9247	3.9529	0.72	4.1035	4.1055	0.05
This Work	$(Pb_{0.82}La_{0.12})(TiO_3)$ x=0.06	3.9174	3.9193	0.05	4.0194	4.0296	0.25
	Mean Relative Errors %			0.92			0.92

This tetragonal model showed the predicted values for the *c/a* ratio based on average ionic sizes. Assuming $a = b$ and $\alpha = \beta = \gamma = 90$, then the phase transition for tetragonal ($c/a \neq 1$) to cubic ($c/a = 1$) can be predicted. For PZT, this tetragonal model showed that the tetragonal phase transition to cubic would be around $PbZr_{0.5}Ti_{0.5}O_3$ with an average B-site size of about 0.66 Å, and lattice constant around 4.01 Å; however, the metamorphic phase boundary (MPB) interrupts this pathway. The phase diagram shows that changing B-site composition from the tetragonal side ([Ti] > [Zr]) as the Zr concentration increases the average B-site size increases (from $r_{Ti} = 0.605$ Å). The experimental results (from ICSD), on the approach toward the MPB, showed a decreasing *c/a* ratio towards unity, and a conventional tolerance factor decreasing towards unity. Figure 4.9 shows the combinations of *x* and *y* (*i.e.*, [Zr]) which yield $c/a = 1$ and hence summarizes the effect of composition on the MPB.

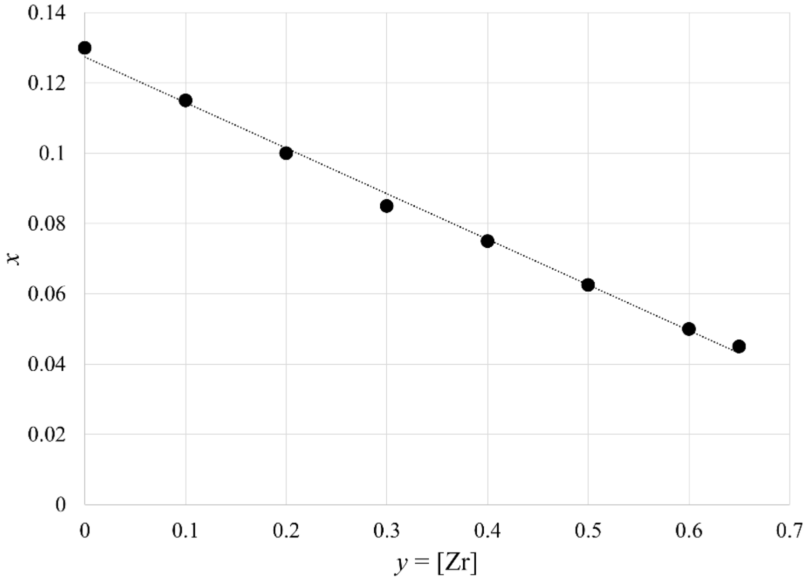

Figure 4.9 The combinations of *x* and *y* (*i.e.*, [Zr]) which yield $c/a = 1$ in $Pb_{1-3x}La_{2x}(Zr_yTi_{1-y})O_3$.

The trend in $Pb_{1-3x}La_{2x}(Zr_yTi_{1-y})O_3$ is linear and the equation that describes it is:

$$x = 0.1297y+0.1274 \ (R^2 = 0.9961) \quad (4.14)$$

For the $Pb_{1-3x}La_{2x}TiO_3$ predicted phase change is at t_1 = 1.018 which would correspond to [La] = 0.3098 (which agrees with ChenJun *et al.* [27]). For the $Ba_{1-3x}La_{2x}TiO_3$ the predicted phase change is at t_1 = 1.070 which would correspond to [La] = 0.0322 (which agrees with Ganguly *et al.* [3]).

It is also of significant interest in the field of electroceramics to relate tetragonality to polarization, which determines the intrinsic component of relative permittivity - a property at the heart of capacitance, pyroelectricity, piezoelectricity, and ferroelectricity. The dipole moment of a compound is a function of ionic charge and the relative separation between the two oppositely charged sublattice centroids.

The general Landau expansion for the thermodynamic-potential density (*i.e.*, Gibbs free energy per unit volume), which is valid for temperatures near T_C, is:

$$g = g_0 + \alpha\eta + \frac{a}{2}\eta^2 + \beta\eta^3 + \frac{b}{4}\eta^4 + ... \quad (4.15)$$

where η is the order parameter and α, a, β, b, *etc*. are functions of temperature and various functionals. In piezoelectric crystals (including ferroelectric ones), the order parameter is the polarization, *P*. For such materials, the Landau expansion can be re-written as:

$$g = g_0 + \frac{a}{2}P^2 + \frac{b}{4}P^4 + \frac{c}{6}P^6 + ... \quad (4.16)$$

Only even-power terms have been retained because $g(P) = g(-P)$ (*i.e.*, the reversal of *P* does not affect *g*). In this case, a polynomial curve describing *g* vs *P* need only include even-power terms. Figure 4.9 shows the fit for *P* vs *c*/*a* rather than *g* vs *P*. On the other hand, a dielectric subjected to a homogeneous field ***E*** carries a net dipole moment per unit volume ***P*** such that

$$\boldsymbol{P} = \varepsilon_o(\varepsilon_r - 1)\boldsymbol{E} \quad (4.17)$$

This net dipole moment per unit volume, ***P***, is called the *polarisation*. It is proportional to the field strength E as long as ε_r is independent of E, which it is for normal dielectrics below the breakdown field (which is not the case for ferroelectrics). This equation provides a link between the macroscopic and atomic theory of dielectrics.

The assumption of a linear relationship between ***P*** and ***E*** is valid only if the field strengths encountered in practice (typically < 10^6 V/m) are small compared to those that bind electrons in atoms (about 10^{11} V/m). However, the linear response is an approximation and the real response is non-linear and is of the form:

$$P = \varepsilon_o(\chi_1 E + \chi_2 E^2 + \cdots) \tag{4.18}$$

or

$$n = n^o + \alpha E_o + \beta E_o^2 + \cdots \tag{4.19}$$

where n is the refractive index (related to ε_r), n^o is the value measured under zero bias field, α and β are constants, and the χ factors are the electric *susceptibilities* ($\chi_1 = \varepsilon_r - 1$). In general, χ values are second-rank tensors; however, if ***P*** and ***E*** are parallel, then χ is just a scalar. Typically, the linear coefficients (α and χ_1) are much greater than the coefficients of higher order terms. The dependence of n on E_o is the *electro-optic effect*. The quadratic term and higher-order terms are called the *hyperpolarisability* and are the basis of *non-linear optics*.

If a material has a centre of symmetry or is amorphous, reversal of E_o will have no effect on n; therefore, $\alpha = 0$ and there is only a quadratic dependence of n on E_o and possibly a smaller dependence on higher even powers. The same argument can be made for the dependence of ε_r on E. This quadratic dependence is known as the *Kerr effect*. Single-crystal cubic $BaTiO_3$ shows this behaviour. If the crystal is non-centrosymmetric, reversal of E_o (or E) will have an effect on n (or P) and the linear term must be retained and higher-order terms are negligible. The linear effect is termed the *Pockels effect*. Single-crystal tetragonal $BaTiO_3$ behaves in this manner. In this case, a polynomial curve describing ε_r vs E is essentially linear and includes the first-order term.

Space group *P4/mmm* is centrosymmetric, which means that the two sublattice centroids coincide and there is no net dipole moment; however, perovskites in space group *P*4*mm* are non-centrosymmetric and have non-zero dipole moments. All such perovskites are piezoelectric, and many are also pyroelectric and ferroelectric. Table 4.4 shows the dipole moments, which arise as a direct result of tetragonal distortions, derived from experimental positional data of 43 various *P*4*mm* tetragonal $A^{2+}B^{4+}O_3$ perovskites. Figure 4.10 shows the relationship between tetragonality and polarization for these compounds. The inset shows the goodness of fit to experimental data, and the trend can be described by Equation 4.15.

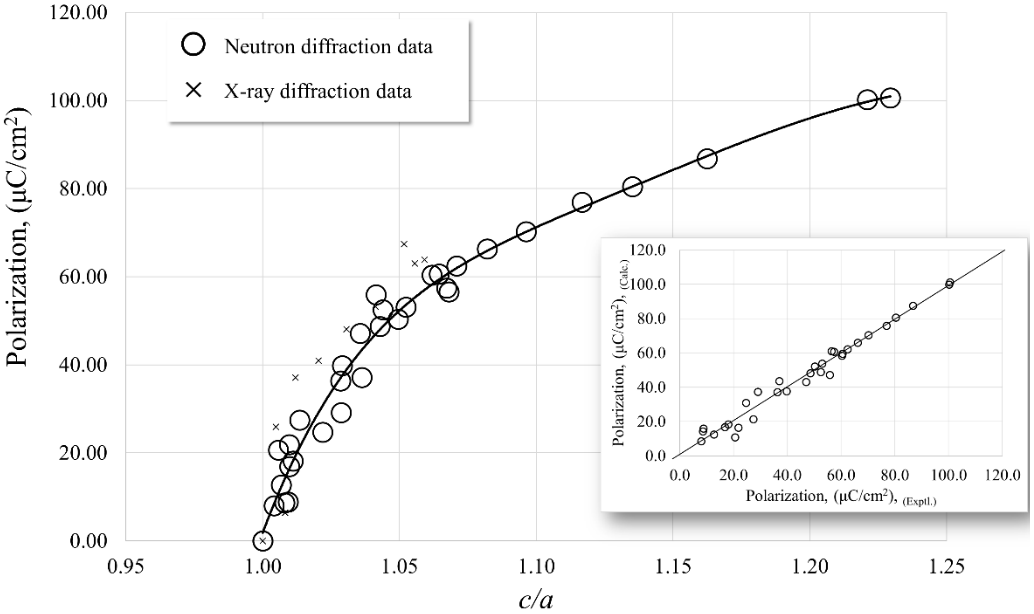

Figure 4.10. Polarization of 43 of $A^{2+}B^{4+}O_3$ perovskites as a function of *c/a* (Table 4.4) form literature. Circle data points indicate neutron diffraction data, and *x* data points indicate X-ray diffraction data. Equation 4.13 is illustrated by the solid curve. [28-34]

Table 4.4. Tetragonalities and polarizations of 43 *P4mm* tetragonal perovskites.

ICSD#	Data Type	Compound	$c/a_{\text{Exptl.}}$	$c/a_{\text{Calc.}}$	|*Error%*|	Polarizaiton, $\mu C/cm^2_{\text{Exptl.}}$	Polarizaiton, $\mu C/cm^2_{\text{Calc.}}$	|*Error%*|
183213	Neutron	$PbTiO_3$	1.0645	1.0692	0.44	60.6395	59.3921	2.06
164352	Neutron	$Pb_{0.85}La_{0.1}TiO_3$	1.0291	1.0337	0.44	39.8023	37.5841	5.57
165498	Neutron	$PbTiO_3$	1.0619	1.0668	0.46	60.3676	58.2479	3.51
73644	Neutron	$BaTiO_3$	1.0111	1.0095	0.15	18.1446	18.1824	0.21
185407	Neutron	$Ba(TiO_3)$	1.0098	1.0099	0.00	16.8794	16.5401	2.01
71368	Neutron	$(Ba_{0.88}Ca_{0.12})(TiO_3)$	1.0097	1.0060	0.37	21.9164	16.3317	25.48
280137	Neutron	$Pb((Hf_{0.4}Ti_{0.6})O_3)$	1.0219	1.0984	7.48	24.6827	30.7691	24.66
90472	Neutron	$Pb(Zr_{0.2}Ti_{0.8})O_3$	1.0496	1.0892	3.78	50.3498	52.0693	3.41
90473	Neutron	$Pb(Zr_{0.3}Ti_{0.7})O_3$	1.0429	1.0997	5.45	48.6938	48.0465	1.33
90474	Neutron	$Pb(Zr_{0.4}Ti_{0.6})O_3$	1.0363	1.1109	7.20	37.1466	43.4206	16.89
90475	Neutron	$Pb(Zr_{0.5}Ti_{0.5})O_3$	1.0284	1.1174	8.66	36.3525	36.9834	1.74
90478	Neutron	$Pb(Zr_{0.52}Ti_{0.48})O_3$	1.0135	1.1223	10.74	27.4355	21.2328	22.61
93451	Neutron	$Pb(Hf_{0.2}Ti_{0.8})O_3$	1.0414	0.9752	6.36	55.9190	47.0687	15.83
98057	Neutron	$K_{0.5}Bi_{0.5}(TiO_3)$	1.0057	0.9886	1.70	20.6315	10.7519	47.89
152424	Neutron	$Pb(Hf_{0.1}Ti_{0.9})O_3$	1.0524	1.0717	1.83	53.0715	53.6450	1.08

152426	Neutron	$Pb(Hf_{0.2}Ti_{0.8})O_3$	1.0440	1.0786	3.32	52.5066	48.7158	7.22
152428	Neutron	$Pb(Hf_{0.3}Ti_{0.7})O_3$	1.0357	1.0860	4.86	47.1210	42.9511	8.85
152430	Neutron	$Pb(Hf_{0.4}Ti_{0.6})O_3$	1.0287	1.0946	6.41	29.1294	37.2108	27.74
156987	Neutron	$(Pb_{0.97}Cd_{0.03})(TiO_3)$	1.0673	1.0720	0.44	57.4231	60.5267	5.40
156988	Neutron	$(Pb_{0.94}Cd_{0.06})(TiO_3)$	1.0681	1.0887	1.93	56.5607	60.8432	7.57
187081	Neutron	$(Ba_{0.91}Ca_{0.11})(TiO_3)$	1.0041	1.0092	0.50	8.0088	8.4251	5.20
152277	Neutron	$Pb(VO_3)$	1.2295	1.1837	3.72	100.6168	100.9659	0.35
187635	Neutron	$Pb(VO_3)$	1.2210	1.1791	3.43	100.2324	99.7261	0.51
169589	Neutron	$(Bi_{0.6}Pb_{0.4})((Fe_{0.6}Ti_{0.4})O_3)$	1.1624	1.1623	0.01	86.8166	87.3904	0.66
169590	Neutron	$(Bi_{0.5}Pb_{0.5})((Fe_{0.5}Ti_{0.5})O_3)$	1.1352	1.1407	0.49	80.4405	80.4774	0.05
169591	Neutron	$(Bi_{0.4}Pb_{0.6})((Fe_{0.4}Ti_{0.6})O_3)$	1.1167	1.1218	0.45	76.9254	75.7234	1.56
169592	Neutron	$(Bi_{0.3}Pb_{0.7})((Fe_{0.3}Ti_{0.7})O_3)$	1.0963	1.1054	0.82	70.2720	70.2110	0.09
169593	Neutron	$(Bi_{0.2}Pb_{0.8})((Fe_{0.2}Ti_{0.8})O_3)$	1.0821	1.0907	0.80	66.3100	65.8954	0.63
169594	Neutron	$(Bi_{0.1}Pb_{0.9})((Fe_{0.1}Ti_{0.9})O_3)$	1.0709	1.0777	0.63	62.4753	61.9738	0.80
188784	Neutron	$(Ba_{0.95}Sr_{0.05})(TiO_3)$	1.0093	1.0085	0.08	8.8597	15.7734	78.04
188785	Neutron	$(Ba_{0.9}Sr_{0.1})(TiO_3)$	1.0080	1.0070	0.10	8.6757	14.0620	62.08
188786	Neutron	$(Ba_{0.85}Sr_{0.15})(TiO_3)$	1.0068	1.0052	0.16	12.7429	12.3027	3.45

245945	Synchrotron	$BaTiO_3$	1.0082	1.0105	0.22	6.4205	14.3440	123.41
150086	XRD	$(Pb_{0.85}La_{0.1})(TiO_3)$	1.0306	1.0322	0.15	48.0853	38.8828	19.14
90693	XRD	$PbTiO_3$	1.0591	1.0646	0.52	63.8469	56.9976	10.73
189383	XRD	$(Ba_{0.94}La_{0.04})(TiO_3)$	1.0000	1.0047	0.47	0.0000	-	0.00
189384	XRD	$(Ba_{0.9}La_{0.067})(TiO_3)$	1.0000	1.0023	0.23	0.0000	-	0.00
161710	XRD	$(Pb_{0.95}Bi_{0.05})(TiO_3)$	1.0556	1.0604	0.46	63.0335	55.2667	12.32
161711	XRD	$(Pb_{0.9}Bi_{0.1})(TiO_3)$	1.0517	1.0556	0.37	67.4114	53.2604	20.99
150087	XRD	$(Pb_{0.775}La_{0.15})(TiO_3)$	1.0204	1.0243	0.39	40.9570	29.1703	28.78
150088	XRD	$(Pb_{0.7}La_{0.2})(TiO_3)$	1.0120	1.0161	0.41	37.1237	19.3274	47.94
150089	XRD	$(Pb_{0.625}La_{0.25})(TiO_3)$	1.0049	1.0082	0.33	25.8963	9.4963	63.33
150085	XRD	$Pb_{0.925}La_{0.05}TiO_3$	1.0413	1.0441	0.27	53.1718	46.9430	11.71

$$p\left[\frac{\mu C}{cm^2}\right] = -800467.451 + 3410445.611\left(\frac{c}{a}\right) - 5806887.936\left(\frac{c}{a}\right)^2 + 4938557.817\left(\frac{c}{a}\right)^3 - 2097541.606\left(\frac{c}{a}\right)^4 + 355895.421\left(\frac{c}{a}\right)^5 \quad (4.14)$$

As can be seen in Figure 4.9 and Table 4.4, most of the data points which show significant error are based on structural parameters determined via XRD. As XRD is insensitive to oxygen positions, the experimental values of polarization for these compositions is likely to contain a great amount of uncertainty, thereby explaining the errors observed in this work.

There are three additional positional parameters which define the structure of *P*4*mm* perovskites: the B-cation *z* displacement in the 1b site and the *z* displacement of anions in both 2c and 1b sites; however, tetragonality is clearly the dominating effect in ultimately determining polarization. It is likely that larger charge differences between B cation and anion result in smaller displacements and, consequently, smaller tetragonalities; therefore, tetragonality itself must be a function of charge and *z*. For this reason, using tetragonality alone to model polarization results in a very good approximation (Fig. 4.9). Expanding this model to include compositions in other systems would require additional data; but it is reasonable to assume that each system would follow a similar trend.

4.4 Conclusion

A total of 21 compositions in the system $[(Pb_yBa_{1-y})_{(1-3x)}La_{(2x)}]TiO_3$ (y = 0.0, 0.25, 0.5, 0.667, 0.75 and 1.0) (x = 0.0, 0.01, 0.02, 0.03, 0.04 and 0.05) were synthesized via the solid-state mixed-oxide route. LeBail refinements of X-ray diffraction patterns were conducted to observe lattice constants and reveal *c*/*a* ratio trends. A general empirical model, based solely on published ionic radii data, for tetragonal lattice constants of perovskites in *P*4*mm* or *P*4*/mmm* has been proposed. Furthermore, a general empirical model for the unit-cell polarization of $A^{2+}B^{4+}O_3^{2-}$ perovskites has been derived.

4.5 References

[1] C. Jia, V. Nagarajan, J. He, L. Houben, T. Zhao, R. Ramesh, K. Urban, R. Waser, Unit-cell scale mapping of ferroelectricity and tetragonality in epitaxial ultrathin ferroelectric films, Nature Materials 6(1) (2007) 64-69.

[2] A. Bhalla, R. Guo, R. Roy, The perovskite structure - a review of its role in ceramic science and technology, Materials Research Innovations 4(1) (2000) 3-26.

[3] M. Ganguly, S. Rout, T. Sinha, S. Sharma, H. Park, C. Ahn, I. Kim, Characterization and Rietveld Refinement of A-site deficient Lanthanum doped Barium Titanate, Journal of Alloys and Compounds 579 (2013) 473-484.

[4] G. Xiao, M. Cieplak, A. Gavrin, F. Streitz, A. Bakhshai, C. Chien, High-Temperature superconductivity in Tetragonal Perovskite Structures - is Oxygen-Vacancy Order Important, Physical Review Letters 60(14) (1988) 1446-1449.

[5] K. Tolman, R. Ubic, M. Papac, K. Seymour, S. McCormack, W. Kriven, H. Kungl, Structural effect of aliovalent doping in lead perovskites, Journal of Solid State Chemistry **225** (2015) 359-367.

[6] M. Lufaso, P. Woodward, Prediction of the crystal structures of perovskites using the software program SPuDS, Acta Crystallographica Section B-Structural Science 57 (2001) 725-738.

[7] A. Salinas-Sanchez, J. Garcia-Munoz, J. Rodriguez-Carvajal, R. Saez-Puche, J. Martinez, Structural characterization of R_2BaCuO_5 (R = Y, Lu, Yb, Tm, Er, Ho, Dy, Gd, Eu AND Sm) oxides by X-ray and neutron diffraction, Journal of Solid State Chemistry 100(2) (1992) 201-211.

[8] L. Jiang, J. Guo, H. Liu, M. Zhu, X. Zhou, P. Wu, C. Li, Prediction of lattice constant in cubic perovskites, Journal of Physics and Chemistry of Solids 67(7) (2006) 1531-1536.

[9] R. Ubic, Revised method for the prediction of lattice constants in cubic and pseudocubic perovskites, Journal of the American Ceramic Society **90** (10) (2007) 3326-3330.

[10] R. Ubic, G. Subodh, The prediction of lattice constants in orthorhombic perovskites, Journal of Alloys and Compounds 488(1) (2009) 374-379.

[11] A. Kumar, A. Verma, Lattice constant of orthorhomic perovskite solids, Journal of Alloys and Compounds 480(2) (2009) 650-657.

[12] R. Pearson, The 2nd-order Jahn-Teller effect, Theochem-Journal of Molecular Structure 12(AUG) (1983) 25-34.

[13] M. Kunz, I. Brown, Out-of-center distortions around octahedrally coordinated d(0) transition-metals, Journal of Solid State Chemistry 115(2) (1995) 395-406.

[14] I.D. Brown, K.R. Poeppelmeier, Bond Valences, Springer Berlin Heidelberg, Berlin, 2014.

[15] R. Shpanchenko, V. Chernaya, A. Tsirlin, P. Chizhov, D. Sklovsky, E. Antipov, E. Khlybov, V. Pomjakushin, A. Balagurov, J. Medvedeva, E. Kaul, C. Geibel, Synthesis, structure, and properties of new perovskite PbVO3, Chemistry of Materials 16(17) (2004) 3267-3273.

[16] T. Qi, I. Grinberg, A. Rappe, Correlations between tetragonality, polarization, and ionic displacement in PbTiO3-derived ferroelectric perovskite solid solutions, Physical Review B 82(13) (2010).

[17] A. Kumar, S.R. Bhardwaj, Lattice Constants of Tetragonal Perovskite Structured Solids, AIP Conference Proceedings 1393(Dec.) (2011) 201-202.

[18] R. Shannon, Revised Effective Ionic-Radii and Systematic Studies of Interatomic Distances in Halides and Chalcogenides, Acta Crystallographica Section a **32** (SEP1) (1976) 751-767.

[19] V. Goldschmidt, The laws of crystal chemistry, Naturwissenschaften **14** (1926) 477-485.

[20] R. Ubic, K. Tolman, K. Talley, B. Joshi, J. Schmidt, E. Faulkner, J. Owens, M. Papac, A. Garland, C. Rumrill, K. Chan, N. Lundy, H. Kungl, Lattice-constant prediction and effect of vacancies in aliovalently doped perovskites, Journal of Alloys and Compounds **644** (2015) 982-995.

[21] R. Ubic, G. Subodh, M.T. Sebastian, Effective size of vacancies in the $Sr_{1-3x/2}Ce_xTiO3$ superstructure, Ceramic Transactions 204 (2009) 177-185.

[22] R. Ubic, K. Tolman, K. Chan, N. Lundy, S. Letourneau, W. Kriven, Effective size of vacancies in aliovalently doped $SrTiO_3$ perovskites, Journal of Alloys and Compounds **575** (2013) 239-245.

[23] L. Finger, D. Cox, A. Jephcoat, A Correction for Powder Diffraction Peak Asymmetry Due to Axial Divergence, Journal of Applied Crystallography **27** (1994) 892-900.

[24] S. Diodati, L. Nodari, M. Natile, U. Russo, E. Tondello, L. Lutterotti, S. Gross, Highly crystalline strontium ferrites SrFeO3-delta: an easy and effective wet-chemistry synthesis, Dalton Transactions 41(18) (2012) 5517-5525.

[25] H. Jin-Fan, N. Xing, B.J. Chun, W. Jing-He, Syntheses, structures and properties of some new composition perovskite compounds: $Sr_{0.6}Bi_{0.4}FeO_{2.7}$, $Sr_{1-x}Bi_xFeO_{3-y}$ and $Ba_{1.55}Pt_{0.5}Mn_2O_6$, Chinese Journal of Structural Chemistry 13(5) (1994) 350-359.

[26] S. Aruna, N. Kini, S. Shetty, K. Rajam, Synthesis of nanocrystalline CeAlO3 by solution-combustion route, Materials Chemistry and Physics 119(3) (2010) 485-489.

[27] C. Jun, X. Xianran, Y. Ranbo, L. Guirong, W. Li, C.X. Long, Structural investigations on ferroelectric $Pb_{1-3x/2}La_xTiO_3$ using the X-ray Rietveld method, Journal of Materials Research 19(12) (2004) 3614-3619.

[28] R. Ranjan, A. Kalyani, R. Garg, P. Krishna, Structure and phase transition of the (1-x)PbTiO3-(x)BiAlO3 system, Solid State Communications 149(45-46) (2009) 2098-2101.

[29] J. Joseph, T. Vimala, V. Sivasubramanian, V. Murthy, Structural investigations on Pb(ZrxT1-x)O-3 solid solutions using the X-ray Rietveld method, Journal of Materials Science 35(6) (2000) 1571-1575.

[30] G. Rossetti, M. Rodriguez, A. Navrotsky, L. Cross, R. Newnham, Structure of the defect perovskite ($Pb_{0.85}$ $La_{0.10}$)TiO_3 between 10 and 1023 K, Journal of Applied Physics 77(4) (1995) 1683-1689.

[31] P. Hu, Z. Cao, J. Chen, J. Deng, C. Sun, R. Yu, X. Xing, Structure and negative thermal expansion of Pb1-xBixTiO3, Materials Letters 62(30) (2008) 4585-4587.

[32] A. Chandra, D. Pandey, Evolution of crystallographic phases in the system (Pb1-xCax)TiO3: A Rietveld study, Journal of Materials Research 18(2) (2003) 407-414.

[33] M. Sindhu, N. Ahlawat, S. Sanghi, R. Kumari, A. Agarwal, Crystal structure refinement and investigation of electrically heterogeneous microstructure of single phased Sr substituted BaTiO3 ceramics, Journal of Alloys and Compounds 575 (2013) 109-114.

[34] T. Plutenko, O. V'yunov, A. Belous, Synthesis and electrical characteristics of (1-x)BaTiO3-xK(0.5)Bi(0.5)TiO(3) PTCR ceramics, Materials Chemistry and Physics 136(1) (2012) 167-172.

CHAPTER FIVE: CONCLUSIONS AND FUTURE WORK

5.1 Concluding Remarks

Chapter one described the perovskites generally. Perovskites comprise the largest range of functional materials of any other material classification, including: high-temperature insulators/capacitors, superconductors, dielectric resonators, pyroelectrics, piezoelectrics, ionic conductors, photovoltaics, *etc*. Predictive models based on empirical evidence are powerful tools; however, no models have existed previously for perovskites with A-cation deficiencies, cation ordering, or tetragonality. This work focused primarily on the effective size of A-site vacancies and the structural effects of A-site point defect chemistry, A- and B-site cation ordering, and tetragonal distortions. This work removes some of the guesswork from the development of new perovskites. The models developed in this work were based on experimental data generated from diffraction and refinements performed as part of this work coupled with reported experimental data from published scientific literature.

Chapter two explored various system-specific studies of extrinsic vacancies in perovskites in terms of the effective size of vacancies. The structural effects of aliovalent doping in five typical oxide perovskite systems ($CaTiO_3$, $SrTiO_3$, $BaTiO_3$, $PbTiO_3$, and $Pb(Zr_{0.6}Ti_{0.4})O_3$) were studied. Samples synthesized via solid-state reactions were checked for phase purity using X-ray diffraction, scanning electron microscopy, and either energy dispersive spectroscopy or wavelength dispersive spectroscopy. Structural parameters were characterized using X-ray, electron, and/or time-of-flight neutron diffraction data.

Quantitative diffraction data were collected and refined in order to develop empirical descriptions of the effects of A-site point defect concentrations. A predictive model for pseudocubic lattice constants was developed which relates stoichiometry to the effective sizes of ionic species and vacancies. The same model can be used to calculate values of tolerance factor which better predict perovskite stability and structure in terms of octahedral tilting than does the traditional definition. A predictive model was derived for the pseudocubic lattice constant of $A_{1-3x}Ln_{2x}BX_3$ perovskites, based solely on published ionic radii data, and applied with great accuracy to many such perovskite systems. Using this model it is also possible to calculate the effective size of anions and A-site cation vacancies as well as to semiquantify the effects of both B-site cation ordering and second-order Jahn Teller distortions. A lower limit for the tolerance factor of oxide perovskites is proposed ($t = 0.8465$).

Chapter three examined complex perovskites which contain cation ordering. Perovskites with multiple cation species sharing the A or B sites may form superstructures in which the A- and/or B-site is non-randomly shared by more than one ionic species. Ordering generally involves a lowering of symmetry; however, such ordering is not always complete or spatially extensive. It can exist in varying degrees from perfectly ordered to near completely random (*i.e.*, disordered) and can extend uniformly throughout an entire crystal or exist only in short-range nanodomains. The model developed in chapter two is used to predict cation ordering. Several well-known examples of B-site ordered perovskites were examined and shown to result in volume shrinkage upon ordering. Furthermore, four samples in the $Na_{(1-3x)/2}La_{(1+x)/2}TiO_3$ system (x = 0, 0.0533, 0.1733 and 0.225) and $Ba(Mg_{1/3}Ta_{2/3})O_3$ were synthesized using a conventional solid-state mixed-oxide method.

$Ba(Mg_{1/3}Ta_{2/3})O_3$ showed a decreasing unit cell volume with annealing due to increasing B-site ordering. On the other hand, a short-range ordered structure of $Na_{0.5}La_{0.5}TiO_3$ was observed via electron diffraction and predicted via an empirical model, which also suggests an unexpected volume increase upon ordering. First-principles calculations using density functional theory support these conclusions. Even though thermodynamics dictates that a finite concentration of vacancies exists even at $x = 0$, there can be no 1:1 long-range vacancy ordering at this or other low-x compositions where the presence of vacancies is nonstoichiometric. Perovskites in the $Na_{(1-3x)/2}La_{(1+x)/2}TiO_3$ system have an A-site ordered layered structure, and the degree of cation order decreases as x increases. Similar A-site ordering and volume expansion has been inferred from previously reported models of $Li_{(1-3x)/2}La_{(1+x)/2}TiO_3$ and both $(Na_{0.5}La_{0.5})(Mg_{0.5}W_{0.5})O_3$ and $(K_{0.5}La_{0.5})(Mg_{0.5}W_{0.5})O_3$. The implication of this empirical modeling method is that it may be possible to predict the degree of cation ordering in complex perovskite systems from Shannon data and experimentally-derived pseudocubic lattice constants alone. It may also be possible to predict the degree of volume expansion/contraction, which has implications for functional properties, especially ionic conduction.

Chapter four proposed a predictive model for tetragonality. Samples of $[(Pb_yBa_{1-y})_{(1-3x)}La_{(2x)}]TiO_3$ were synthesized and X-ray diffraction refinements were conducted in order to measure lattice constants. Further data from open literature were used in order to reveal tetragonality trends. These trends were combined with a model for unit-cell volume in order to derive a generalized empirical predictive model for tetragonal lattice constants of perovskites in either *P*4*mm* or *P*4*/mmm*, based solely on published ionic radii data. This model was extended to include the resultant unit-cell dipole moment. A total of 21 compositions in the system $[(Pb_yBa_{1-y})_{(1-3x)}La_{(2x)}]TiO_3$ (y = 0.0, 0.25, 0.5, 0.667, 0.75 and 1.0) (x = 0.0, 0.01, 0.02, 0.03, 0.04 and 0.05) were synthesized via the solid-state mixed-oxide route. LeBail refinements of X-ray diffraction patterns were conducted to observe lattice constants and reveal *c*/*a* ratio trends. A general empirical model, based solely on published ionic radii data, for tetragonal lattice constants of perovskites in *P*4*mm* or *P*4*/mmm* has been proposed. Furthermore, a general empirical model for the unit-cell polarization of $A^{2+}B^{4+}O_3^{2-}$ perovskites has been derived based on tetragonality alone.

5.2 Future Work

5.2.1 Extend A-site vacancy model to include perovskites with $r_A < 1.34$ Å (Ca^{2+})

MgTiO₃ is ilmenite not perovskite and even though MgSiO₃ is a perovskite, it is challenging to synthesize without getting an amorphous phase. By substituting Mg onto the Ca site in $(Ca_{1-y}Mg_y)_{1-3x}La_{2x}TiO_3$ ($0 \le x \le ⅓$ $0 < y \le 1$) it can effectively reduce r_A until a perovskite would no longer be stable.

5.2.2 Extend A-site vacancy model with thermal variations

This work was solely based on characterizing samples at room temperature and ambient pressure. Thermal variations can vastly change ionic sizes; however, the degree of change in these systems in this work are still unknown. In order to quantify these changes, it will be necessary to establish empirical models for effective ionic sizes as a function of temperature by calculating bond lengths from in-situ x-ray or neutron-diffraction experiments. This additional information could enable this modeling technique to predict important phase-transition temperatures like the ferroelectric T_C.

5.2.3 Extend A-site vacancy model to non-titanates

This work is based heavily on titanates and it is desirable to extend the model beyond titanates. $(Pb_{1-3x}La_{2x})(Zr_yTi_{1-y})O_3$ ($0 \leq x \leq ⅓$ $0 < y \leq 1$) is an appropriate candidate to extend the model beyond titanates while simultaneously achieving a consistent link to the titanate model. The question of SOJT distortion has an additional relevance in that hybrid organic-inorganic semiconductors like α-$HC(NH_2)_2PbI_3$ of interest for perovskite solar cells with a 1:2 B-site ordered structure despite having a single B-site cation species. It is possible that the reported existence of two or three crystallographically inequivalent Pb cations can be explained by inequivalent SOJT distortions, although this hypothesis is still highly speculative.

5.2.4 Extend model to perovskites with chemical ordering on B

B-site ordered perovskites are used as dielectrics, piezoelectrics, ferroelectrics, and optoelectronics; y*et al*iovalent doping creates the same A-site vacancies as in other systems. The $[(Ca,Sr,Ba)_{1-3x}La_{2x}](Mg_{½}W_{½})O_3$ system will allow the effect of B-site ordering on effective ionic sizes and cell volume to be studied as a function of r_A and therefore t as the host crystal changes from $Fm\overline{3}m$ (A=Ba) to $I4/m$ (A=Sr) to $P2_1/n$ (A=Ca). If the SOJT distortions caused by W^{6+} are too strong to independently model the effect of ordering, another system like $Sr_{1-3x}La_{2x}(Mg_{⅓}Nb_{⅔})O_3$ can be used in which the degree of B-O covalency and so SOJT distortion should be less, may be substituted. A data-mining approach will also be employed in all available databases (*e.g.*, ICSD, COD, PDF-4+) for structural information on perovskites with B-site ordering. Although crystallographic models exist for >100 perovskites with B-site ordering, there are few systematic studies of the effects of order on cell volume or packing fraction; nevertheless, the existing data will be analyzed according to the model in order to generalize and refine it. Data will be categorized by t and B-site chemistry, including ordering type (*e.g.*, 1:1 or 1:2) and analyzed for quantifiable trends using simple mathematical tools (*e.g.*, Mathematica).

5.2.5 Create an empirical model for the effect of anion vacancies

Oxygen vacancies are ubiquitous in engineered ceramics and are typically mobile devices, which is useful for ionic-conductor applications but deleterious to other dielectric applications. The effect of oxygen vacancies on structure can be studied using a prototype system in which they can be engineered independently of other defects without relying on chemical reduction. For example, $LaAlO_3$ can be doped with small amounts of Ca^{2+} to produce up to 17% oxygen vacancies whilst retaining full occupancy on both A- and B-cation sublattices. The $(Ca_{6z}La_{1-6z})AlO_{3(1-z)}$ $(0 \leq z \leq {}^1/_6)$ system allows for the study of oxygen vacancies independent of A-site vacancies and without reliance on chemical reduction. The cations Ca^{2+} and La^{3+} are well matched in size so should cause minimal lattice distortion and maximize solubility.

5.2.6 Study the interplay of simultaneous vacancies on both A and X

Simultaneous A- and O-site defects can be engineered in $(Ca_xLa_{1-xy})AlO_{3+x-3xy/2}$, $(0 \leq x \leq 1\ 1 \leq y \leq 1/x)$ by formulating $LaAlO_3$ with $CaCO_3$ in a different way than above, which may only be stable for low values of x, but could theoretically produce up to 50% A-site and 33% oxygen vacancies. Compositions for which $y = 1$ or $x = 0$ yield *only* oxygen vacancies. It is also possible to use different compositions with different tolerance factors to achieve the same $[V_A]$ or $[V_O]$. Using this system has the additional advantages of being able to study the effects of oxygen vacancies on structure both with and without A-site vacancies.

5.2.7 Use model to predict non-cubic perovskite distortions (*i.e.*, predict whether the compound will be cubic, tetragonal, trigonal, or orthorhombic and estimate the magnitude of the distortion).

It should be possible to derive mathematical models for unit-cell distortions. Chapter four shows this for tetragonally distorted perovskites in *P*4*mm* or *P*4*/mmm*. A similar model can be developed for trigonally distorted perovskites, which actually constitutes a much larger group of perovskites. Phase transitions could thus be predicted, for example, by following *c*/*a* or α_r as a function of *x* or *temperature* (see 5.2.2).